

¹ A Search in the Two-Photon Final State for
² Evidence of New Particle Production in pp
³ Collisions at $\sqrt{s} = 7$ TeV

⁴ Rachel P. Yohay
University of Virginia
`rpy3y@virginia.edu`

⁵ June 13, 2012

6 Contents

7	1	Introduction	4
8	2	Motivation for Physics Beyond the Standard Model	7
9	2.1	The Standard Model and Electroweak Symmetry Breaking	8
10	2.2	Implications of the Higgs Mechanism	12
11	2.3	Addressing Problems of the Standard Model with Supersymmetry . .	14
12	3	The Supersymmetric Extension to the Standard Model	18
13	3.1	Supermultiplet Representation	18
14	3.2	The Unbroken SUSY Lagrangian	19
15	3.3	Soft SUSY Breaking	25
16	3.4	Gauge-Mediated SUSY Breaking	28
17	3.5	Phenomenology of General Gauge Mediation	31
18	3.6	Experimental Status of SUSY	34
19	4	The Large Hadron Collider	40
20	4.1	Design Considerations and Performance Limitations	41
21	4.2	Beam Injection	44
22	4.3	Magnets and Cryogenics	46
23	4.4	Radiofrequency Cavities	49

²⁴	5 The Compact Muon Solenoid Experiment	51
²⁵	5.1 The Detectors and Their Operating Principles	55
²⁶	5.1.1 Tracking System	55
²⁷	5.1.2 Electromagnetic Calorimeter	64
²⁸	5.1.3 Hadronic Calorimeter	69
²⁹	5.1.4 Muon System	73
³⁰	5.2 Triggering, Data Acquisition, and Data Transfer	78
³¹	5.2.1 Level 1 and High Level Trigger Systems	78
³²	5.2.2 Data Acquisition System	82
³³	5.2.3 Data Processing and Transfer to Computing Centers	85
³⁴	6 Event Selection	88
³⁵	6.1 Object Reconstruction	89
³⁶	6.1.1 Photons	89
³⁷	6.1.2 Electrons	102
³⁸	6.1.3 Jets and Missing Transverse Energy	102
³⁹	6.2 HLT	109
⁴⁰	6.3 Event Quality	112
⁴¹	6.4 Photon Identification Efficiency	114
⁴²	6.4.1 Tag and Probe Method	115
⁴³	6.4.2 Photon Efficiency Scale Factor $\epsilon_e^{\text{data}}/\epsilon_e^{\text{MC}}$	121
⁴⁴	7 Data Analysis	124
⁴⁵	7.1 Modeling the QCD Background	128
⁴⁶	7.1.1 Outline of the Procedure	128
⁴⁷	7.1.2 Reweighting	129
⁴⁸	7.1.3 Normalization	140
⁴⁹	7.2 Modeling the Electroweak Background	140

50	7.3 Errors on the Background Prediction	146
51	7.4 Results	152
52	8 Interpretation of Results in Terms of GMSB Models	158
53	8.1 Simplified Models	158
54	8.2 Upper Limit Calculation and Model Exclusion	160
55	8.2.1 Signal Acceptance \times Efficiency	160
56	8.2.2 CL_s and the Profile Likelihood Test Statistic	164
57	8.3 Cross Section Upper Limits	171
58	8.4 Exclusion Contours	172
59	9 Conclusion	177
60	A Monte Carlo Samples	179
61	A.1 List of Samples	179
62	A.2 Explanation of Naming Conventions	180

⁶³ Chapter 1

⁶⁴ Introduction

⁶⁵ Although the Standard Model of particle physics has passed every experimental test
⁶⁶ to date, it leaves some very fundamental questions unanswered. Why do particles have
⁶⁷ mass? Why are their masses so different? Up to what energy scale is the Standard
⁶⁸ Model a valid description of nature? Many competing theories have been proposed to
⁶⁹ answer these questions. Establishing the existence of any one of them requires careful
⁷⁰ searches for deviations from Standard Model predictions of particle production or
⁷¹ decay rates. The stellar performance of the Large Hadron Collider, the 7 TeV center-
⁷² of-mass energy proton collider located at the European Organization for Nuclear
⁷³ Research (CERN) in Geneva, Switzerland, presents a golden opportunity to do such
⁷⁴ a search for evidence of new physical phenomena.

⁷⁵ One nearly universal prediction of theories of physics beyond the Standard Model
⁷⁶ is that at a high enough collision energy, heavy particles introduced by the new theory
⁷⁷ will be produced. The heavy particles will then decay, leading to distinctive signatures
⁷⁸ in the hermetic detectors that completely surround the collision points. By comparing
⁷⁹ the observed rate of processes with a particular signature to the expected rate from
⁸⁰ the Standard Model alone, the existence of a particular theory of new physics can be
⁸¹ confirmed or ruled out.

This thesis presents a search for evidence of new heavy particles decaying to a final state with two photons, jets, and a striking momentum imbalance that implies the existence of a new kind of particle that can easily pass through matter without leaving a trace. The signature is motivated by theories that incorporate supersymmetry, a new symmetry of nature that predicts supersymmetric antiparticles to the known particles, just as charge symmetry predicts a positively charged antiparticle for every negatively charged particle and vice versa. Supersymmetry can provide answers to all of the questions posed in the first paragraph. Besides its theoretical motivation, the choice of signature is also driven by the low rate of expected Standard Model background.

The search is performed at the Compact Muon Solenoid experiment, a detector capable of identifying photons, electrons, muons, quark jets, τ leptons, and momentum imbalances with high efficiency. The central feature of the experiment is a superconducting solenoid, which, at a length of 13 m and a diameter of 7 m [1], is one of the largest superconducting magnets ever built. By bending the paths of charged particles in the final state under the Lorentz force, the magnetic field produced by the solenoid allows charged particle momenta to be accurately measured. Highly granular calorimeters sit inside the solenoid for the purpose of measuring the energy of neutral final state particles.

This thesis is organized as follows. Chapters 2 and 3 motivate the search for physics beyond the Standard Model and the specific signature of two photons, as well as give an overview of the Standard Model and supersymmetric theoretical frameworks. A description is given of the Large Hadron Collider in Chapter 4 and the Compact Muon Solenoid detector in Chapter 5. Chapters 6 and 7 explain in detail the experimental techniques used in the search. Chapter 6 shows how collisions that are likely to have produced a new particle are selected from the enormous amount of data collected, then Chapter 7 shows the data analysis in detail and presents the results. An interpretation

¹⁰⁹ of the results in terms of new physics models is given in Chapter 8. Finally, the thesis
¹¹⁰ is concluded in Chapter 9.

¹¹¹ Chapter 2

¹¹² Motivation for Physics Beyond the ¹¹³ Standard Model

¹¹⁴ In the 1960s, Sheldon Glashow, Steven Weinberg, and Abdus Salam proposed a math-
¹¹⁵ ematical framework that unified the electromagnetic and weak forces at an energy
¹¹⁶ scale in the hundreds of GeV/c, as well as a mechanism for breaking the electroweak
¹¹⁷ symmetry at low energies [2]. At the same time, Murray Gell-Mann introduced the
¹¹⁸ concept of quarks to describe hadron spectroscopy, a concept that would later grow
¹¹⁹ into quantum chromodynamics (QCD), the full theory of the strong force [3]. These
¹²⁰ two key developments motivated the unified representation of particle physics as a set
¹²¹ of fields whose dynamics are invariant under the Standard Model (SM) gauge group

$$SU(3)_C \otimes SU(2)_L \otimes U(1)_Y \quad (2.1)$$

¹²² where $SU(3)_C$ describes the quark QCD interactions, $SU(2)_L$ describes the weak
¹²³ interactions among quarks and leptons, and $U(1)_Y$ describes the electromagnetic in-
¹²⁴ teraction.

¹²⁵ The Standard Model has been an extremely successful predictor of particle pro-
¹²⁶ duction and interaction cross-sections and decay rates, as well as of the exact masses

¹²⁷ of the electroweak force carriers. The case for the validity of the Standard Model was
¹²⁸ bolstered by the many precision QCD and electroweak measurements carried out at
¹²⁹ the Large Electron-Positron (LEP) collider, which ran from 1989-2000 at center-of-
¹³⁰ mass energies between 65 and 104 GeV/ c [4]. Figure 2.1 shows some of the highlights
¹³¹ of the LEP program.

¹³² However, there are still deep theoretical problems with the Standard Model,
¹³³ stemming from the introduction of the Higgs scalar into the theory to break elec-
¹³⁴ troweak symmetry [5]. Since the Higgs self-energy diagram is quadratically sensitive
¹³⁵ to the ultraviolet cutoff scale, and assuming that there are no new important en-
¹³⁶ ergy scales of physics between the weak scale ($\mathcal{O}(10^2 \text{ GeV}/c)$) and the Planck scale
¹³⁷ ($\mathcal{O}(10^{19} \text{ GeV}/c)$), in order to be consistent with experimental measurements, this dia-
¹³⁸ gram must include a remarkable 17-orders-of-magnitude cancellation that is otherwise
¹³⁹ poorly motivated [6]. The quest to find new physics at an intermediate energy scale
¹⁴⁰ between the weak and Planck scales, and thus extend the Standard Model, was the
¹⁴¹ driving force behind the construction of the Large Hadron Collider (LHC) in 2009,
¹⁴² the world's highest energy particle accelerator to date.

¹⁴³ Section 2.1 of this chapter gives a brief overview of the Standard Model and
¹⁴⁴ electroweak symmetry breaking. Sections 2.2 and 2.3 examine the issues raised by
¹⁴⁵ electroweak symmetry breaking that the Standard Model is as yet ill-prepared to
¹⁴⁶ address.

¹⁴⁷ **2.1 The Standard Model and Electroweak Symme- ¹⁴⁸ try Breaking**

¹⁴⁹ All of the elementary matter particles (fermions)—quarks, charged leptons, and neutrinos—
¹⁵⁰ can be put in fundamental representations of the SM gauge groups. The fermion con-
¹⁵¹ tent of the Standard Model is summarized in Table 2.1. The left-handed doublets are

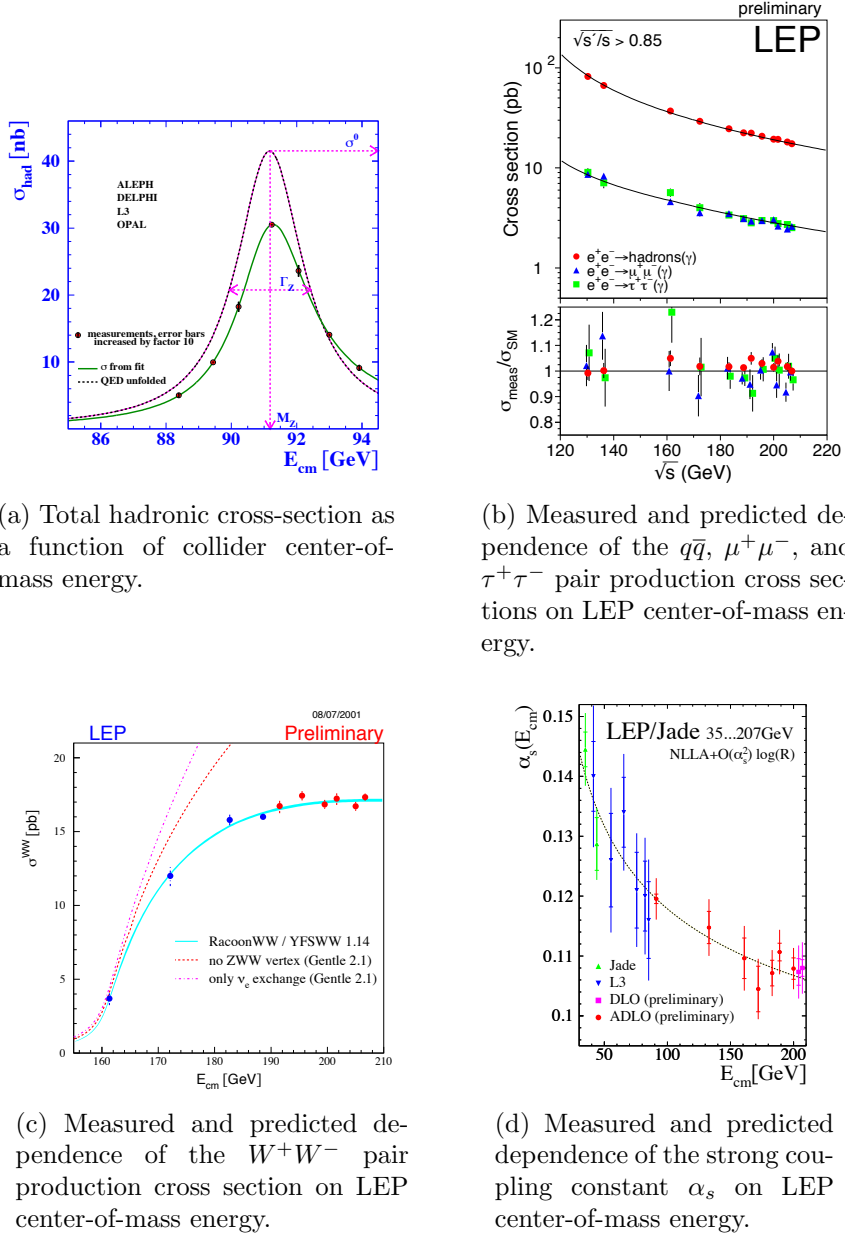


Figure 2.1: Selected LEP measurements demonstrating its contribution to the precise understanding of the Standard Model. Reprinted from ref. [4].

₁₅₂ analogous to the spinors of non-relativistic quantum mechanics, with the z component of “weak isospin” I_3 equal to $+1/2(-1/2)$ for the upper(lower) component of the ₁₅₃ doublet.
₁₅₄

Table 2.1: Fermion content of the Standard Model.

Type	Notation	Representation under $SU(3)_C \otimes SU(2)_L \otimes U(1)_Y$	Couples to
Left-handed quark doublet	$\begin{pmatrix} u_L \\ d_L \\ c_L \\ s_L \\ b_L \\ t_L \end{pmatrix}$	(3, 2, $\frac{1}{6}$)	g, W, Z, γ
Right-handed up-type quark singlet	$\begin{pmatrix} u_R^\dagger \\ c_R^\dagger \\ b_R^\dagger \end{pmatrix}$	($\bar{3}$, 1, $-\frac{2}{3}$)	g, γ
Right-handed down-type quark singlet	$\begin{pmatrix} d_R^\dagger \\ s_R^\dagger \\ t_R^\dagger \end{pmatrix}$	($\bar{3}$, 1, $\frac{1}{3}$)	g, γ
Left-handed lepton doublet	$\begin{pmatrix} \bar{\nu}_{eL} \\ e_L \\ \bar{\nu}_{\mu L} \\ \mu_L \\ \bar{\nu}_{\tau L} \\ \tau_L \end{pmatrix}$	(1, 2, $-\frac{1}{2}$)	W, Z, γ^a
Right-handed charged lepton singlet	$\begin{pmatrix} e_R^\dagger \\ \mu_R^\dagger \\ \tau_R^\dagger \end{pmatrix}$	($\bar{1}$, 1, 1)	γ

^aExcept for neutrinos, which have zero electric charge.

₁₅₅ There are two types of weak interactions: flavor-changing charged currents, in
₁₅₆ which an up-type and down-type quark or charged lepton and neutrino couple to
₁₅₇ a charged W , and neutral currents, in which a fermion couples to another of the
₁₅₈ same flavor and to a neutral Z . The charged current interaction is maximally parity
₁₅₉ violating—it only couples left-handed fermion doublets. The neutral current inter-
₁₆₀ action has a term coupling left-handed doublets and a term coupling right-handed
₁₆₁ singlets. There are no mass terms of the form $m_f^2(f_L \bar{f}_R + f_R \bar{f}_L)$ in the electroweak

162 part of the Lagrangian, as these would violate gauge invariance [7]. The simplest
 163 way to link the left-handed and right-handed fermions is via a Yukawa interaction
 164 $-\xi [\bar{f}_R(\phi^\dagger f_L) + (\bar{f}_L \phi) f_R]$ where ϕ is a doublet of complex scalar fields [7].

165 The fermion interaction part of the Lagrangian is [7]

$$\begin{aligned}\mathcal{L}_{\text{int}} = & \bar{f}_R i\gamma^\mu (\partial_\mu + i\frac{g_Y}{2} A_\mu Y) f_R \\ & + \bar{f}_L i\gamma^\mu (\partial_\mu + i\frac{g_Y}{2} A_\mu Y + i\frac{g_L}{2} \vec{\tau} \cdot \vec{b}_\mu) f_L\end{aligned}\quad (2.2)$$

166 where g_Y and g_L are the electromagnetic and weak coupling constants, respectively;
 167 Y is the weak hypercharge; A_μ is the EM gauge field; \vec{b}_μ is a three-component
 168 vector of weak gauge fields; and $\vec{\tau}$ is a three-component vector of the three Pauli
 169 matrices. Before electroweak symmetry breaking, the three weak gauge fields and the
 170 one EM gauge field are massless. The three weak gauge fields correspond to the three
 171 generators (the Pauli matrices) of $SU(2)_L$. The one EM gauge field corresponds to the
 172 one generator (the real scalar Y) of $U(1)_Y$, where $Y = 2(Q - I_3)$ (Q is electric charge).
 173 For the $SU(3)_C$ part of the Lagrangian, there are eight massless gauge fields (the
 174 gluons) corresponding to the eight generators of $SU(3)_C$ (the Gell-Mann matrices).

175 To break the electroweak symmetry implicit in the massless gauge bosons, a dou-
 176 blet of complex scalar fields (the Higgs) is introduced. It has a potential [7]

$$V(\phi^\dagger \phi) = \mu^2 \phi^\dagger \phi + |\lambda| (\phi^\dagger \phi)^2. \quad (2.3)$$

177 Since $\mu^2 < 0$, the potential has the shape of a sombrero, as shown in Figure 2.2.
 178 At the minimum of the potential, the scalar fields are not zero, but have some positive
 179 vacuum expectation value (VEV) (it can be chosen such that one component is zero
 180 and the other is $\sqrt{-\mu^2/2|\lambda|}$). Nature spontaneously chooses one of the infinitely many

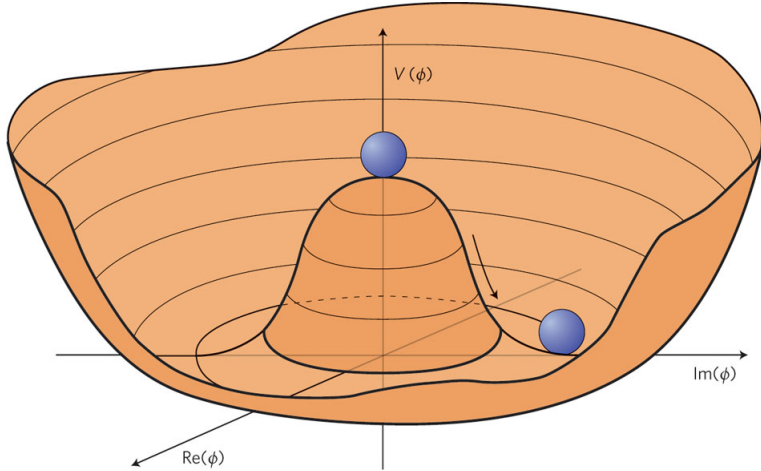


Figure 2.2: Higgs potential (the sombrero) as a function of the real and imaginary parts of the complex scalar field. The movement of the balls shows that the symmetry $\phi = 0$ is spontaneously broken, the stable vacuum state of nature being somewhere along the circle of minimum potential. Reprinted from Fig. 1 of ref. [8].

181 vacua along the circle of minimum V in $(\Re[\phi], \Im[\phi])$ space.

182 Expanding ϕ about its VEV v in the Lagrangian introduces one massive scalar, the
183 Higgs, and new mass terms for the gauge bosons. However, the terms with positive
184 mass are not the original b_1 , b_2 , b_3 , and A (spacetime indices dropped), but the
185 observable W^\pm and Z^0 . The W^\pm are linear combinations of b_1 and b_2 . The Z^0 is
186 one of the linear combinations of b_3 and A , the other being the massless photon γ .
187 After electroweak symmetry breaking (EWSB), the only remaining symmetry of the
188 vacuum is electric charge, because the value of the electric charge operator acting on
189 the Higgs VEV is zero. As expected, there is one massless photon in the SM to reflect
190 this symmetry. The SM fermions can also acquire masses as a by-product of the Higgs
191 mechanism via Yukawa terms.

192 2.2 Implications of the Higgs Mechanism

193 Before the formulation of the Higgs mechanism, physicists suspected that a heavy
194 boson mediated the weak force from observations of β decay, but had no way of

195 putting a mass term into the Lagrangian without breaking gauge symmetry. The
 196 Higgs mechanism of EWSB provided a way to generate masses for the $SU(2)_L$ gauge
 197 bosons. Furthermore, it predicted the W and Z masses in terms of g_L , g_Y , and v . g_L
 198 and g_Y could be measured in scattering experiments, and in 1983 the W and Z were
 199 first observed at the Super Proton-Antiproton Synchrotron (Sp \bar{p} S) at the European
 200 Organization for Nuclear Research (CERN) in Geneva, Switzerland [9, 10]. Crucially,
 201 the values of the coupling constants and the gauge boson masses predict that the
 202 Higgs VEV should be 246 GeV, so the Higgs mass should not be too much different
 203 than that if λ is to remain small enough to do perturbation theory [11].

204 The Higgs mechanism raises some interesting questions that cannot be immedi-
 205 ately answered by SM physics. First of all, why should μ^2 be negative? The form of
 206 the Higgs potential given in Eq. 2.3 is about the simplest renormalizable form that
 207 can be written for a scalar field, but the choice of $\mu^2 < 0$ is completely arbitrary.
 208 Second, how can the hierarchy problem be avoided?

209 The Higgs mass squared receives one-loop corrections from all the particles it
 210 couples to; namely, all particles with mass. Because the Higgs is a scalar particle, one-
 211 loop corrections are proportional to Λ_{UV}^2 , where Λ_{UV} is the ultraviolet cutoff energy of
 212 the loop integral. Λ_{UV} can be interpreted as the energy at which the SM can no longer
 213 describe particle physics and non-SM physics takes over. Ideally, Λ_{UV} is something
 214 like the Planck scale. However, taking $\Lambda_{\text{UV}} = M_{\text{Planck}}$ implies that in order to keep the
 215 Higgs mass of order a few hundred GeV, as required by experimental tests of EWSB, a
 216 very large and precise counterterm must be applied at all orders in perturbation theory
 217 to the bare m_H^2 . The quadratic sensitivity of the Higgs mass to the cutoff scale and the
 218 extremely fine-tuned counterterms it necessitates is called the hierarchy problem. SM
 219 fermions do not experience this problem because chiral symmetry prevents explicit
 220 fermion mass terms at any order, so by dimensional analysis, fermion masses can only
 221 be sensitive to $\ln \frac{\Lambda_{\text{UV}}}{\Lambda_{\text{other}}}$.

²²² One of the most elegant ways to address these problems is to incorporate *super-*
²²³ *symmetry* (SUSY) into the SM. Supersymmetry is new fundamental symmetry of
²²⁴ nature between bosons and fermions, and will be discussed more thoroughly in Chap-
²²⁵ ter 3. The next section just briefly describes how supersymmetry can mitigate some
²²⁶ of the problems of the Higgs mechanism.

²²⁷ 2.3 Addressing Problems of the Standard Model ²²⁸ with Supersymmetry

²²⁹ As in the ordinary Standard Model, the couplings and masses in supersymmetric
²³⁰ theory can be imposed at the supersymmetric scale and evolved down to the weak
²³¹ scale by use of renormalization group equations. For many typical supersymmetric
²³² scenarios (like the one shown in Figure 2.3), μ^2 is positive at the supersymmetric
²³³ scale but runs negative at the weak scale, leading to precisely the conditions needed
²³⁴ for EWSB. This is a consequence of the fact that the evolution of m_H^2 depends on the
²³⁵ top quark Yukawa coupling, which, since the top is very heavy compared to the other
²³⁶ quarks ($m_t \sim 42m_b$, $m_t \sim 136m_c$ [13]), is large. In some sense, then, supersymmetry
²³⁷ not only provides the conditions for EWSB, but also explains why the top quark must
²³⁸ be so much heavier than the other quarks.

²³⁹ SUSY's greatest strength, however, comes from the way it elegantly solves the
²⁴⁰ hierarchy problem. The Higgs squared mass corrections from fermion loops take the
²⁴¹ form [12]

$$\Delta m_H^2 = -\frac{|\lambda_F|^2}{8\pi^2} \Lambda_{\text{UV}}^2 + \dots \quad (2.4)$$

²⁴² while the corrections from scalar loops would take the form [12]

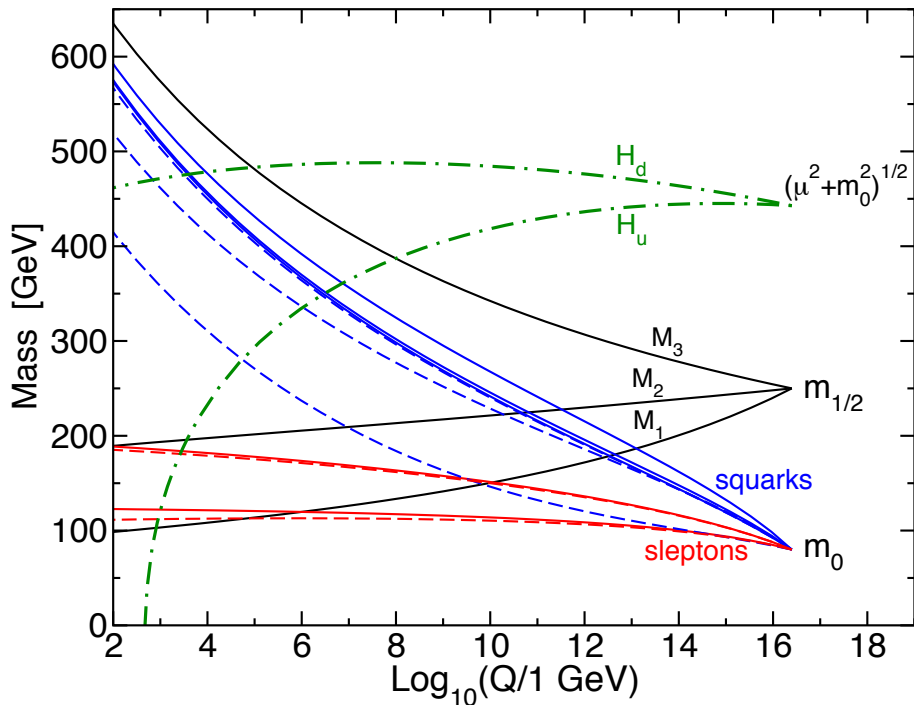


Figure 2.3: Predicted evolution of the free parameters of supersymmetry as a function of renormalization scale for a representative set of SUSY parameters. Note the dash-dotted line marked “ H_u ” that goes negative at ~ 1 TeV; this indicates μ^2 running negative. Reprinted from Fig. 7.4 of ref. [12].

$$\Delta m_H^2 = \frac{|\lambda_S|^2}{16\pi^2} \Lambda_{\text{UV}}^2 + \dots \quad (2.5)$$

where the ellipsis indicates terms proportional to $\ln \Lambda_{\text{UV}}$ that do not pose a problem for the validity of the SM up to the Planck scale. Since the fermion and scalar contributions have opposite signs, if each SM fermion were accompanied by two as-yet undiscovered scalar particles with $\lambda_S = |\lambda_F|^2$, then the problematic quadratic terms in Eqs. 2.4 and 2.5 would exactly cancel. This is precisely the foundation of supersymmetry: for each fermion, there is a supersymmetric partner boson. This would remove the hierarchy problem altogether, and is the main reason physicists are eager to find evidence for the existence of supersymmetry at the LHC.

In addition to providing some rationale for the Higgs mechanism, SUSY makes two other very desirable predictions. The first is that the strong, weak, and electromagnetic coupling constants will exactly unify at an energy scale of 10^{16} GeV/ c , as shown in Figure 2.4. Unification of forces is not required by any experimental consideration, but is an elegant result nonetheless. The second prediction of SUSY, explained in more detail in Sec. 3.5, is the existence of a new stable particle, undiscovered as of yet because of its extremely feeble interactions with ordinary matter. This particle might be what astronomers have observed as dark matter. In fact, regardless of any theory, searches for evidence of dark matter at colliders are well motivated by suggestions from astronomy that some or all of the dark matter should have a mass at the weak scale [14].

Everything discussed in this chapter assumes that the Higgs mechanism is indeed the origin of EWSB. It is important to remember that no experimental observation to date unequivocally establishes the existence of the Higgs scalar, although small excesses recently unearthed in the LHC data [15, 16] tentatively suggest a Higgs mass

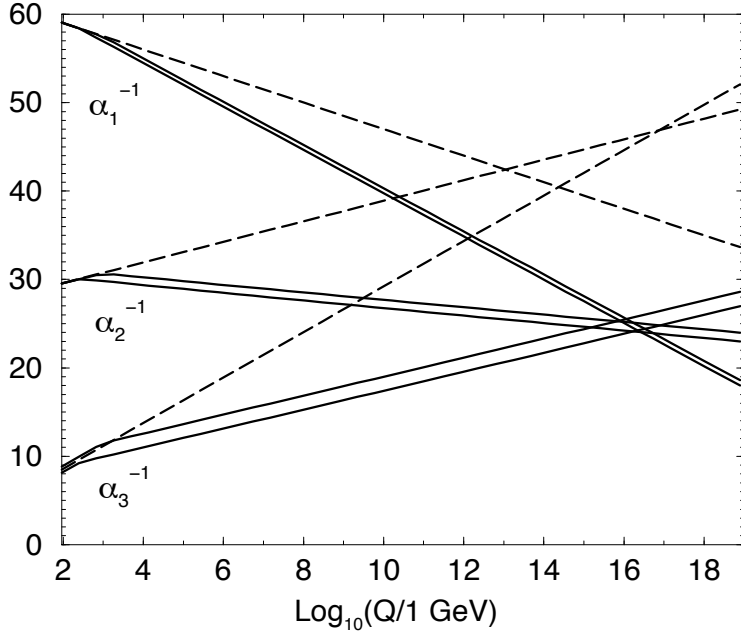


Figure 2.4: Inverse gauge couplings as a function of renormalization scale for the Standard Model assumption (dotted lines) and the SUSY assumption (solid lines; the double lines represent variations in SUSY parameters and in $\alpha_S(m_Z)$). Reprinted from Fig. 5.8 of ref. [12].

of ~ 125 GeV. The discovery of the Higgs scalar would place an important restriction on the types of SUSY theories that might be consistent with experiment. Operating at a 7 TeV center-of-mass energy, the LHC can thoroughly probe the scale of EWSB and the expected mass range of the Higgs, as well as the mass range of supersymmetric particles if SUSY is the solution to the hierarchy problem. Therefore, discovering or excluding SUSY is a key goal of the LHC physics program. The next chapter discusses SUSY more formally and shows what phenomenological consequences it entails.

²⁷³ Chapter 3

²⁷⁴ ²⁷⁵ The Supersymmetric Extension to the Standard Model

²⁷⁶ The following introduction to SUSY focuses primarily on the aspects of the formalism that are relevant to phenomenology. In particular, most of the details of SUSY breaking (about which there is little theoretical consensus) are omitted, except where they are relevant to experiment. The notation is similar to that used in refs. [6] and [12], and much of the information presented is culled from those references.

²⁸¹ 3.1 Supermultiplet Representation

²⁸² The Standard Model is extended to include supersymmetry by the introduction of a supersymmetry transformation that takes fermionic states to bosonic states and vice versa. The resulting model is called the *supersymmetric Standard Model*. In analogy with the known symmetries of the Standard Model, the SUSY transformation has associated generators that obey defining commutation and anticommutation relations, and a fundamental representation. All SM particles and their *superpartners* fall into one of two *supermultiplet* representations. Using the property of SUSY that

$$n_F = n_B, \quad (3.1)$$

289 where n_F is the number of fermionic degrees of freedom per supermultiplet and n_B is
 290 the number of bosonic degrees of freedom, the two types of supermultiplets are

- 291 1. *Chiral supermultiplets*: Weyl fermions (two helicity states $\Rightarrow n_F = 2$) associated
 292 with complex scalar fields (with two real components $\Rightarrow n_B = 2$)
- 293 2. *Gauge supermultiplets*: Spin-1 vector bosons (two helicity states $\Rightarrow n_B = 2$)
 294 associated with Weyl fermions (two helicity states $\Rightarrow n_F = 2$)

295 In the gauge supermultiplet, the vector boson is assumed massless (i.e. before
 296 EWSB generates a mass for it). Since the superpartners to the SM particles have not
 297 yet been discovered, they must be significantly heavier than their SM counterparts.
 298 Unbroken SUSY predicts that the SM particles and their superpartners must have
 299 exactly the same mass, so ultimately a mechanism for SUSY breaking, in addition to
 300 EWSB, must be introduced to generate masses for the superpartners (see Sec. 3.3).
 301 Tables 3.1 and 3.2 show the chiral and gauge supermultiplets of the supersymmetric
 302 Standard Model, respectively. Note that the scalar partners to the SM fermions are
 303 denoted by placing an “s” in front of their names, while the chiral fermion partners
 304 to the SM gauge bosons are denoted by appending “ino” to their names.

305 3.2 The Unbroken SUSY Lagrangian

306 The first piece of the full unbroken SUSY Lagrangian density consists of the kinetic
 307 and interacting terms related to the chiral supermultiplets. As explained in Sec. 3.1, a
 308 chiral supermultiplet consists of Weyl fermions ψ (the ordinary fermion) and complex
 309 scalars ϕ (the sfermion). For a collection of such chiral supermultiplets, the Lagrangian
 310 is

Table 3.1: Chiral supermultiplets of the supersymmetric Standard Model. In the last column, the first number refers to the supermultiplet representation under $SU(3)_C$ (e.g. **3** means it has color charge and feels QCD), the second number refers to the representation under $SU(2)_L$ (e.g. **2** means it has weak isospin and feels the weak interaction), and the third number is the value of the hypercharge. A bar over a number refers to the adjoint representation. **1** means that the supermultiplet is not charged under that group, and thus does not feel the associated force (for example, the right-handed fermion singlets do not feel the weak interaction). Adapted from Table 1.1 of ref. [12].

Type of supermultiplet	Notation	Spin-0 component	Spin-1/2 component	Representation under $SU(3)_C \otimes SU(2)_L \otimes U(1)_Y$
Left-handed quark/squark doublet ($\times 3$ families)	Q	$(\tilde{u}_L \tilde{d}_L)$	$(u_L d_L)$	$(\mathbf{3}, \mathbf{2}, \frac{1}{6})$
Right-handed up-type quark/squark singlet ($\times 3$ families)	\bar{u}	\tilde{u}_R^*	u_R^\dagger	$(\overline{\mathbf{3}}, \mathbf{1}, -\frac{2}{3})$
Right-handed down-type quark/squark singlet ($\times 3$ families)	\bar{d}	\tilde{d}_R^*	d_R^\dagger	$(\overline{\mathbf{3}}, \mathbf{1}, \frac{1}{3})$
Left-handed lepton/slepton doublet ($\times 3$ families)	L	$(\tilde{\nu}_{eL} \tilde{e}_L)$	$(\bar{\nu}_{eL} e_L)$	$(\mathbf{1}, \mathbf{2}, -\frac{1}{2})$
Right-handed lepton/slepton singlet ($\times 3$ families)	\bar{e}	\tilde{e}_R^*	e_R^\dagger	$(\overline{\mathbf{1}}, \mathbf{1}, 1)$
Up-type Higgs/Higgsino doublet	H_u	$(H_u^+ H_u^0)$	$(\tilde{H}_u^+ \tilde{H}_u^0)$	$(\mathbf{1}, \mathbf{2}, \frac{1}{2})$
Down-type Higgs/Higgsino doublet	H_d	$(H_d^0 H_d^-)$	$(\tilde{H}_d^0 \tilde{H}_d^-)$	$(\mathbf{1}, \mathbf{2}, -\frac{1}{2})$

Table 3.2: Gauge supermultiplets of the supersymmetric Standard Model. Adapted from Table 1.2 of ref. [12].

Type of supermultiplet	Spin-1/2 component	Spin-1 component	Representation under $SU(3)_C \otimes SU(2)_L \otimes U(1)_Y$
Gluon/gluino	\tilde{g}	g	(8, 1, 0)
W/wino	$\widetilde{W}^\pm \widetilde{W}^0$	$W^\pm W^0$	(1, 3, 0)
B/bino	\tilde{B}^0	B^0	(1, 1, 0)

$$\begin{aligned} \mathcal{L}_{\text{chiral}} = & -\partial^\mu \phi^{*i} \partial_\mu \phi_i - V_{\text{chiral}}(\phi, \phi^*) - i\psi^{\dagger i} \bar{\sigma}^\mu \partial_\mu \psi_i - \frac{1}{2} M^{ij} \psi_i \psi_j \\ & - \frac{1}{2} M_{ij}^* \psi^{\dagger i} \psi^{\dagger j} - \frac{1}{2} y^{ijk} \phi_i \psi_j \psi_k - \frac{1}{2} y_{ijk}^* \phi^{*i} \psi^{\dagger j} \psi^{\dagger k} \end{aligned} \quad (3.2)$$

where i runs over all supermultiplets in Table 3.1, $\bar{\sigma}^\mu$ are the negative of the Pauli matrices (except for $\sigma^0 = \bar{\sigma}^0$), M^{ij} is a mass matrix for the fermions, y^{ijk} are the Yukawa couplings between one scalar and two spinor fields, and $V_{\text{chiral}}(\phi, \phi^*)$ is the scalar potential

$$\begin{aligned} V_{\text{chiral}}(\phi, \phi^*) = & M_{ik}^* M^{kj} \phi^{*i} \phi_j + \frac{1}{2} M^{in} y_{jkn}^* \phi_i \phi^{*j} \phi^{*k} \\ & + \frac{1}{2} M_{in}^* y^{jkn} \phi^{*i} \phi_j \phi_k + \frac{1}{4} y^{ijn} y_{klm}^* \phi_i \phi_j \phi^{*k} \phi^{*l}. \end{aligned} \quad (3.3)$$

The Lagrangian can also be written as the kinetic terms plus derivatives of the *superpotential* W :

$$\begin{aligned} \mathcal{L}_{\text{chiral}} = & -\partial^\mu \phi^{*i} \partial_\mu \phi_i - i\psi^{\dagger i} \bar{\sigma}^\mu \partial_\mu \psi_i \\ & - \frac{1}{2} \left(\frac{\delta^2 W}{\delta \phi^i \delta \phi^j} \psi_i \psi_j + \frac{\delta^2 W^*}{\delta \phi_i \delta \phi_j} \psi^{\dagger i} \psi^{\dagger j} \right) - \frac{\delta W}{\delta \phi^i} \frac{\delta W^*}{\delta \phi_i} \end{aligned} \quad (3.4)$$

³¹⁷ where

$$W = M^{ij} \phi_i \phi_j + \frac{1}{6} y^{ijk} \phi_i \phi_j \phi_k. \quad (3.5)$$

³¹⁸ The second part of the Lagrangian involves the gauge supermultiplets. In terms
³¹⁹ of the spin-1 ordinary gauge boson A_μ^a and the spin-1/2 Weyl spinor gaugino λ^a of
³²⁰ the gauge supermultiplet, where a runs over the number of generators for the SM
³²¹ subgroup (i.e. 1-8 for $SU(3)_C$, 1-3 for $SU(2)_L$, and 1 for $U(1)_Y$), this part of the
³²² Lagrangian is

$$\mathcal{L}_{\text{gauge}} = -\frac{1}{4} F_{\mu\nu}^a F^{\mu\nu a} - i \lambda^a \bar{\sigma}^\mu D_\mu \lambda^a + \frac{1}{2} D^a D^a \quad (3.6)$$

³²³ where

$$F_{\mu\nu}^a = \partial_\mu A_\nu^a - \partial_\nu A_\mu^a + g f^{abc} A_\mu^b A_\nu^c \quad (3.7)$$

³²⁴ (g is the coupling constant and f^{abc} are the structure constants for the particular SM
³²⁵ gauge group),

$$D_\mu \lambda^a = \partial_\mu \lambda^a + g f^{abc} A_\mu^b \lambda^c, \quad (3.8)$$

³²⁶ and D^a is an auxiliary field that is introduced as a bookkeeping tool to keep the
³²⁷ fermionic and bosonic degrees of freedom equal both on- and off-shell. There is no
³²⁸ kinetic term for D^a in the Lagrangian, so therefore it does not propagate or represent

³²⁹ any real particle. Its equation of motion, from $\delta\mathcal{L}/\delta D^a = 0$, yields a simple algebraic
³³⁰ expression for D^a that can be used to eliminate it from the Lagrangian if desired.

³³¹ To build a fully supersymmetric and gauge-invariant Lagrangian, the ordinary
³³² derivatives in $\mathcal{L}_{\text{chiral}}$ (Eq. 3.2) must be replaced by covariant derivatives

$$D_\mu \phi_i = \partial_\mu \phi_i - ig A_\mu^a (T^a \phi)_i \quad (3.9)$$

$$D_\mu \phi^{*i} = \partial_\mu \phi^{*i} + ig A_\mu^a (\phi^* T^a)^i \quad (3.10)$$

$$D_\mu \psi_i = \partial_\mu \psi_i - ig A_\mu^a (T^a \psi)_i. \quad (3.11)$$

³³³ This leads to the full Lagrangian

$$\begin{aligned} \mathcal{L} &= \mathcal{L}_{\text{chiral}} + \mathcal{L}_{\text{gauge}} \\ &\quad - \sqrt{2} g (\phi^{*i} T^a \psi_i) \lambda^a - \sqrt{2} g \lambda^{\dagger a} (\psi^{\dagger i} T^a \phi_i) + g (\phi^{*i} T^a \phi_i) D^a \\ &= -\partial^\mu \phi^{*i} \partial_\mu \phi_i - i \psi^{\dagger i} \bar{\sigma}^\mu \partial_\mu \psi_i + ig \partial^\mu \phi^{*i} A_\mu^a (T^a \phi)_i - ig \partial_\mu \phi_i A^{\mu a} (\phi^* T^a)^i \\ &\quad - g^2 A^{\mu a} (\phi^* T^a)^i A_\mu^a (T^a \phi)_i - g \psi^{\dagger i} \bar{\sigma}^\mu A_\mu^a (T^a \psi)_i - V_{\text{chiral}}(\phi, \phi^*) \\ &\quad - \frac{1}{2} M^{ij} \psi_i \psi_j - \frac{1}{2} M_{ij}^* \psi^{\dagger i} \psi^{\dagger j} - \frac{1}{2} y^{ijk} \phi_i \psi_j \psi_k - \frac{1}{2} y_{ijk}^* \phi^{*i} \psi^{\dagger j} \psi^{\dagger k} \\ &\quad - \frac{1}{4} F_{\mu\nu}^a F^{\mu\nu a} - i \lambda^{\dagger a} \bar{\sigma}^\mu \partial_\mu \lambda^a - ig \lambda^{\dagger a} \bar{\sigma}^\mu f^{abc} A_\mu^b \lambda^c + \frac{1}{2} D^a D^a \\ &\quad - \sqrt{2} g (\phi^{*i} T^a \psi_i) \lambda^a - \sqrt{2} g \lambda^{\dagger a} (\psi^{\dagger i} T^a \phi_i) + g (\phi^{*i} T^a \phi_i) D^a. \end{aligned} \quad (3.12)$$

³³⁴ Writing out $F_{\mu\nu}^a$ and $V_{\text{chiral}}(\phi, \phi^*)$ explicitly combining the D^a terms using the equation
³³⁵ of motion $D^a = -g \phi^{*i} T^a \phi_i$, and rearranging some terms, the final unbroken SUSY
³³⁶ Lagrangian is

$$\begin{aligned}
\mathcal{L} = & -\partial^\mu \phi^{*i} \partial_\mu \phi_i - i\psi^{\dagger i} \bar{\sigma}^\mu \partial_\mu \psi_i \\
& - \frac{1}{4} (\partial_\mu A_\nu^a - \partial_\nu A_\mu^a) (\partial^\mu A^{\nu a} - \partial^\nu A^{\mu a}) - i\lambda^{\dagger a} \bar{\sigma}^\mu \partial_\mu \lambda^a \\
& - M_{ik}^* M^{kj} \phi^{*i} \phi_j - \frac{1}{2} M^{ij} \psi_i \psi_j - \frac{1}{2} M_{ij}^* \psi^{\dagger i} \psi^{\dagger j} \\
& + ig \partial^\mu \phi^{*i} A_\mu^a (T^a \phi)_i - ig \partial_\mu \phi_i A^{\mu a} (\phi^* T^a)^i - g \psi^{\dagger i} \bar{\sigma}^\mu A_\mu^a (T^a \psi)_i \\
& - ig \lambda^{\dagger a} \bar{\sigma}^\mu f^{abc} A_\mu^b \lambda^c \\
& - \frac{1}{4} g f^{abc} [(\partial_\mu A_\nu^a - \partial_\nu A_\mu^a) A^{\mu b} A^{\nu c} + A_\mu^b A_\nu^c (\partial^\mu A^{\nu a} - \partial^\nu A^{\mu a})] \\
& - \frac{1}{2} M_{in}^* y^{jkn} \phi^{*i} \phi_j \phi_k - \frac{1}{2} M^{in} y_{jkn}^* \phi_i \phi^{*j} \phi^{*k} \\
& - \frac{1}{2} y^{ijk} \phi_i \psi_j \psi_k - \frac{1}{2} y_{ijk}^* \phi^{*i} \psi^{\dagger j} \psi^{\dagger k} \\
& - \sqrt{2} g (\phi^{*i} T^a \psi_i) \lambda^a - \sqrt{2} g \lambda^{\dagger a} (\psi^{\dagger i} T^a \phi_i) \\
& - g^2 A^{\mu a} (\phi^* T^a)^i A_\mu^a (T^a \phi)_i - \frac{1}{4} g^2 f^{abc} A_\mu^b A_\nu^c f^{abc} A^{\mu b} A^{\nu c} \\
& - \frac{1}{4} y^{ijn} y_{kln}^* \phi_i \phi_j \phi^{*k} \phi^{*l} - \frac{1}{2} g^2 (\phi^{*i} T^a \phi_i)^2.
\end{aligned} \tag{3.13}$$

³³⁷ The above Lagrangian applies to chiral supermultiplets interacting with one kind
³³⁸ of gauge supermultiplet (i.e. one SM gauge group). In the general case, there are
³³⁹ additional terms corresponding to interactions with all three SM gauge groups.

³⁴⁰ The following list gives a description of the terms in Eq. 3.13:

- ³⁴¹ • First two lines: kinetic terms for the four types of fields ϕ_i , ψ_i , A_μ^a , and λ^a
- ³⁴² • Third line: mass terms for the ϕ_i and ψ_i (see Figs. 3.1(a) and 3.1(b))
- ³⁴³ • Fourth and fifth lines: cubic couplings in which ϕ_i , ψ_i , or λ^a radiates an A_μ^a (see
³⁴⁴ Figs. 3.1(c), 3.1(d), and 3.1(e))
- ³⁴⁵ • Sixth line: triple gauge boson couplings (see Fig. 3.1(f))
- ³⁴⁶ • Seventh line: triple sfermion couplings (see Fig. 3.1(g))

- 347 • Eighth line: cubic couplings in which ψ_i radiates a ϕ_i (see Fig. 3.1(h))
- 348 • Ninth line: ϕ_i - ψ_i - λ^a vertices (see Fig. 3.1(i))
- 349 • 10th line: A_μ^a - A_μ^a - ϕ_i - ϕ_i and quadruple gauge boson couplings (see Figs. 3.1(j)
350 and 3.1(k))
- 351 • 11th line: ϕ_i^4 vertices (see Figs. 3.1(l) and 3.1(m))

352 3.3 Soft SUSY Breaking

353 Since quadratic divergences in sfermion masses vanish to all orders in perturbation
 354 theory in plain unbroken SUSY [12] due to the presence of gauge and Yukawa in-
 355 teractions with the necessary relationships between coupling constants (i.e. chiral
 356 symmetry inherited from the partner fermion protects the sfermion masses, as ex-
 357 plained in Sec. 2.2), it is desirable that the terms that break SUSY not disturb this
 358 property. In addition, SUSY should be broken spontaneously, as electroweak symme-
 359 try is broken in the Standard Model, so that it is only made manifest at high energies.
 360 To satisfy these constraints, SUSY-breaking terms are simply added to the unbroken
 361 SUSY Lagrangian in Eq. 3.13 such that $\mathcal{L}_{\text{total}} = \mathcal{L}_{\text{unbroken}} + \mathcal{L}_{\text{breaking}}$. The coefficients
 362 of terms in $\mathcal{L}_{\text{breaking}}$ must have positive mass dimension in order not to contribute
 363 quadratically divergent loop corrections to the scalar masses (like the Higgs mass);
 364 i.e. to not create a hierarchy problem (Sec. 2.2) for the scalars.¹ This form of SUSY

¹This point can be argued via dimensional analysis. Radiative corrections take the form Δm_S^2 , where m_S is the mass of the scalar particle in question. The dimensions of Δm_S^2 are mass². Δm_S^2 is proportional to some coupling constant or mass coefficient k multiplied by a function of Λ_{UV} , the high energy cutoff scale. The function of Λ_{UV} is determined by a loop integral, and thus typically takes the form Λ_{UV}^2 (quadratically divergent) or $\ln \frac{\Lambda_{\text{UV}}}{m_{\text{low}}}$ (logarithmically divergent, where m_{low} is some other lower-mass scale in the problem). Now, if k already contributes at least one power of mass to Δm_S^2 , then the high-energy behavior—the function of Λ_{UV} —can only contribute at most one power of the dimensionful parameter Λ_{UV} . However, there are typically no loop integrals that diverge linearly in Λ_{UV} , so by forcing k to have positive mass dimension, the form of the radiative corrections contributed by SUSY-breaking terms is limited to $\Delta m_S^2 \sim m_{\text{low}}^2 \ln \frac{\Lambda_{\text{UV}}}{m_{\text{low}}}$. In effect, the possibility of dangerous corrections proportional to Λ_{UV}^2 is excluded by dimensional analysis if the requirement that k contribute at least one power of mass is enforced.

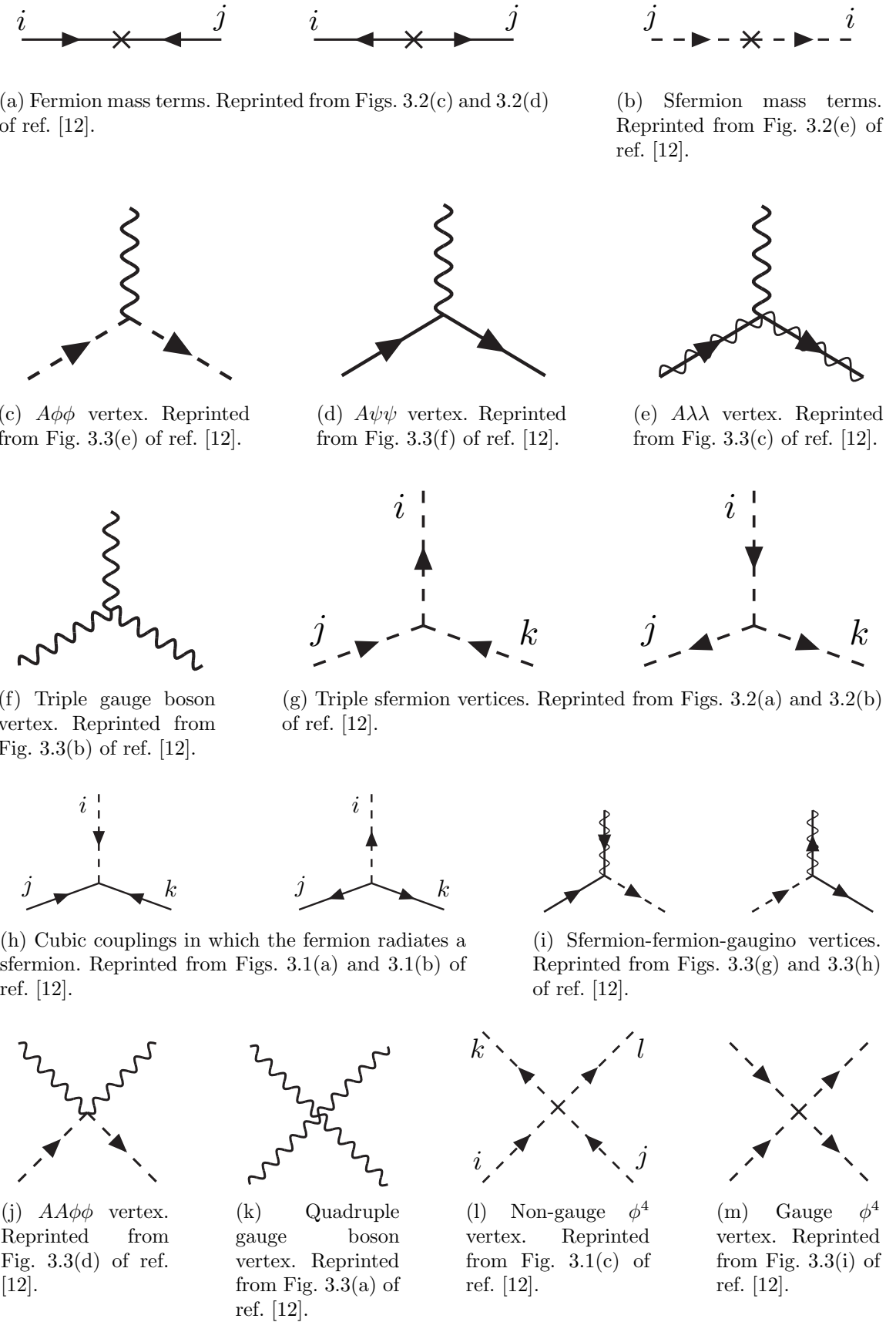


Figure 3.1: Interactions in the unbroken SUSY Lagrangian.

³⁶⁵ breaking is called *soft*, and all coefficients of soft SUSY breaking terms are expected
³⁶⁶ to be of order m_{soft} or m_{soft}^2 .

³⁶⁷ Soft SUSY breaking terms give masses to the sfermions and gauginos and introduce
³⁶⁸ a cubic sfermion vertex. The soft terms are given by

$$\begin{aligned} \mathcal{L}_{\text{soft}} = & -\frac{1}{2}(M_3\tilde{g}^a\tilde{g}^a + M_2\tilde{W}^a\tilde{W}^a + M_1\tilde{B}\tilde{B} + \text{h.c.}) \\ & - (a_u^{ij}\tilde{u}_{Ri}^*\tilde{Q}_jH_u - a_d^{ij}\tilde{d}_{Ri}^*\tilde{Q}_jH_d - a_e^{ij}\tilde{e}_{Ri}^*\tilde{L}_jH_d + \text{h.c.}) \\ & - m_{\tilde{Q}_{ij}}^2\tilde{Q}_i^\dagger\tilde{Q}_j - m_{\tilde{L}_{ij}}^2\tilde{L}_i^\dagger\tilde{L}_j \\ & - m_{\tilde{u}_{ij}}^2\tilde{u}_{Ri}\tilde{u}_{Rj}^* - m_{\tilde{d}_{ij}}^2\tilde{d}_{Ri}\tilde{d}_{Rj}^* - m_{\tilde{e}_{ij}}^2\tilde{e}_{Ri}\tilde{e}_{Rj}^* \\ & - m_{H_u}^2H_u^*H_u - m_{H_d}^2H_d^*H_d - (bH_uH_d + \text{h.c.}) \end{aligned} \quad (3.14)$$

³⁶⁹ where a runs from 1-8 for \tilde{g}^a and from 1-3 for \tilde{W}^a , and i, j run over the three families.
³⁷⁰ The color indices are not shown. The first line of Eq. 3.14 contains the gaugino mass
³⁷¹ terms. The second line contains cubic scalar couplings that contribute to mixing
³⁷² between the left- and right-handed third generation sfermions (it is assumed in the
³⁷³ supersymmetric Standard Model that the a_u^{ij} , a_d^{ij} , and a_e^{ij} are negligible unless $i =$
³⁷⁴ $j = 3$). The third and fourth lines of Eq. 3.14 contain squark and slepton mass terms,
³⁷⁵ and finally the last line contains the Higgs mass terms.

³⁷⁶ Many viable models of achieving soft SUSY breaking have been studied over the
³⁷⁷ last 30 years. For an overview, see Sec. 6 of ref. [12]. However, this thesis will only cover
³⁷⁸ *gauge-mediated SUSY breaking* (GMSB), because the two-photon search performed
³⁷⁹ is far more sensitive to this model than to other models of SUSY breaking.

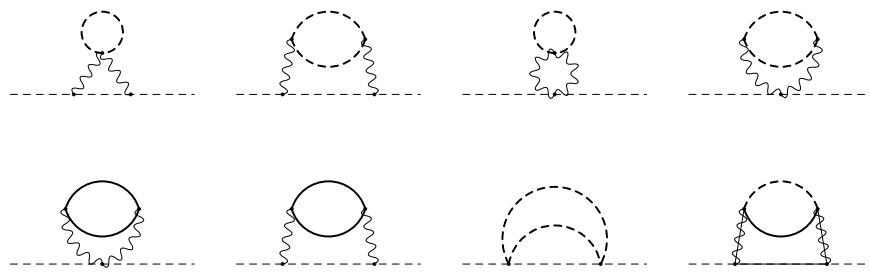
380 3.4 Gauge-Mediated SUSY Breaking

381 In gauge-mediated models [17], “hidden” fields spontaneously break the supersymme-
 382 try of very heavy chiral *messenger* supermultiplets. There are a number of competing
 383 models (see ref. [17]) that attempt to explain the precise mechanism of spontaneous
 384 SUSY breaking, but fortunately the details of those models mostly decouple from the
 385 phenomenology of GMSB. The messengers then communicate the SUSY breaking
 386 to the sparticles via self-energy loop diagrams of gauge interaction strength (i.e. via
 387 vertices like those shown in Figs. 3.1(c), 3.1(d), 3.1(i), 3.1(j), and 3.1(m), which are
 388 proportional to the SM gauge couplings constants). The messengers are very heavy,
 389 so they cannot be detected in current collider experiments. Feynman diagrams corre-
 390 sponding to gaugino and sfermion mass terms are shown in Figure 3.2.

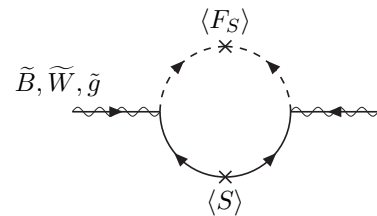
391 Historically, GMSB and gravity-mediated SUSY breaking, or mSUGRA [18], have
 392 been the two most thoroughly experimentally studied scenarios of SUSY breaking.
 393 One advantage of GMSB over mSUGRA is that it naturally suppresses flavor vio-
 394 lation, a generic prediction of supersymmetry. Flavor violation is introduced in the
 395 scalar³ couplings and sfermion mass terms of $\mathcal{L}_{\text{soft}}$ (second, third, and fourth lines of
 396 Eq. 3.14). Since a_u^{ij} , a_d^{ij} , a_e^{ij} , $m_{\tilde{Q}ij}$, $m_{\tilde{L}ij}$, $m_{\tilde{u}ij}$, $m_{\tilde{d}ij}$, and $m_{\tilde{e}ij}$ are matrices in family
 397 space, any nonzero off-diagonal elements will lead to mixing between sfermions of
 398 different families. This can lead, for example, to contributions to the diagram $\mu \rightarrow e\gamma$
 399 (Figure 3.3) exceeding the experimental bounds. To avoid this disaster, *universality*
 400 conditions are assumed:

$$\mathbf{m}_{\tilde{\mathbf{Q}}}^2 = m_{\tilde{Q}}^2 \mathbf{1}, \mathbf{m}_{\tilde{\mathbf{L}}}^2 = m_{\tilde{L}}^2 \mathbf{1}, \mathbf{m}_{\tilde{\mathbf{u}}}^2 = m_{\tilde{u}}^2 \mathbf{1}, \mathbf{m}_{\tilde{\mathbf{d}}}^2 = m_{\tilde{d}}^2 \mathbf{1}, \mathbf{m}_{\tilde{\mathbf{e}}}^2 = m_{\tilde{e}}^2 \mathbf{1} \quad (3.15)$$

401 i.e. all sfermion mass matrices arising from the soft terms are assumed to be propor-
 402 tional to the unit matrix $\mathbf{1}$, such that there can be no flavor mixing from these terms



(a) Sfermion mass terms. Heavy dashed lines denote messenger sfermions; solid lines denote messenger fermions. Reprinted from Fig. 6.4 of ref. [12].



(b) Gaugino mass term. The $\langle S \rangle$ part of the loop is a messenger fermion contribution; the $\langle F_S \rangle$ part is a messenger sfermion contribution. Reprinted from Fig. 6.3 of ref. [12].

Figure 3.2: Contributions to sfermion and gaugino masses from loop interactions with messenger particles in the GMSB framework.

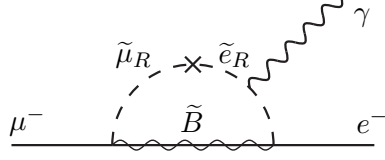


Figure 3.3: Possible contribution to $\mu \rightarrow e\gamma$ from $m_{\tilde{e}ij}$ soft term. Reprinted from Fig. 5.6(a) of ref. [12].

and contributions to flavor-changing processes are drastically reduced.² In mSUGRA models, universality is assumed from the beginning, while in GMSB it is a natural consequence of the fact that the sparticle-messenger vertices are the ordinary flavor-blind gauge couplings that prevent things like flavor-changing neutral currents.

In minimal GMSB (mGMSB), there are four messenger supermultiplets q, \bar{q}, l, \bar{l} providing the messenger (s)quarks and (s)leptons. There is one breaking scale Λ . The gaugino masses computed from diagrams like Fig. 3.2(b) are given by

$$M_a = \frac{\alpha_a}{4\pi} \Lambda \quad (3.16)$$

where a runs from 1-3 and the α_a are the SM gauge coupling constants. The sfermion masses computed from diagrams like Fig. 3.2(a) are given by

$$m_{\phi_i}^2 = 2\Lambda^2 \sum_{a=1}^3 \left(\frac{\alpha_a}{4\pi}\right)^2 C_a(i) \quad (3.17)$$

where $C_a(i)$ are group theory factors that are identical for all particles residing in the same type of supermultiplet (e.g. for all left-handed (s)quarks or left-handed (s)leptons). As explained in the previous paragraph, the gaugino and sfermion masses do not depend on fermion family.

²Universality also includes some assumptions about the form of a_{uij} , a_{dij} , and a_{eij} and the stipulation that the soft terms not introduce any CP-violating phases.

416 In recent years, much theoretical progress has been made in unifying models of
 417 gauge mediation and developing less restrictive models than mGMSB. *General gauge*
 418 *mediation* (GGM) [19] retains the essential features of mGMSB, such as flavor de-
 419 generacy and communication of SUSY breaking via messengers, but does not make
 420 assumptions about the specific messenger sector or SUSY breaking scale. Many dif-
 421 ferent collider final states can be interpreted in terms of GGM, and conversely, GGM
 422 implies a wealth of signatures, only a small fraction of which have been searched for
 423 at colliders [20, 21, 22]. The following section discusses the aspects of GGM collider
 424 phenomenology relevant to this thesis.

425 3.5 Phenomenology of General Gauge Mediation

426 The main distinguishing feature of all GMSB phenomenology is that the gravitino \tilde{G} is
 427 very light (eV-keV). In general, the gravitino mass is proportional to $\langle F \rangle / M_P$, where
 428 $\langle F \rangle$ is the vacuum expectation value (VEV) of a field F that spontaneously breaks
 429 SUSY in the vacuum state and M_P is the Planck mass. In GGM models, $\langle F \rangle \sim 10^8$
 430 GeV, leading to a very light gravitino. In contrast, mSUGRA predicts $\langle F \rangle \sim 10^{20}$
 431 GeV. The fact that the gravitino is so much lighter than any other particles in the
 432 supersymmetric Standard Model, and that it interacts only gravitationally (and thus
 433 extremely feebly), leads to two important phenomenological consequences:

- 434 1. All sparticle decay chains in GMSB end with the production of a gravitino.
 435 2. The gravitino escapes 4π , hermetic collider detectors without interacting, leav-
 436 ing a signature of “missing” momentum transverse to the beam direction.

437 Even if the gravitino were lighter than any other sparticle, but heavier than an
 438 ordinary SM particle, it still could not decay to the SM particle due to *R-parity*. R-
 439 parity is a conserved quantity of the supersymmetric Standard Model introduced to

440 enforce baryon and lepton number conservation, which would otherwise be generically
 441 allowed at levels in conflict with experiment (e.g. the non-observation of baryon-
 442 and lepton-number-violating proton decay). All sparticles have R-parity -1, while all
 443 ordinary SM particles have R-parity +1, and R-parity conservation dictates that at
 444 any vertex, the product of the R-parities of each leg must be +1. This leads to two
 445 more important consequences:

- 446 1. Since conservation of energy only allows it to decay to ordinary SM particles,
 447 but R-parity prevents a sparticle-particle-particle vertex, the *lightest supersym-
 448 metric particle* (LSP) must be absolutely stable. All sparticle decays proceed
 449 through the *next-to-lightest supersymmetric particle* (NLSP), which in turn de-
 450 cays to the LSP. The fact that it is stable and only gravitationally interacting
 451 makes the gravitino a candidate dark matter particle (see Sec. 3.6).
- 452 2. In colliders, sparticles are produced in pairs (particle + particle \rightarrow sparticle +
 453 sparticle).

454 In GMSB, then, the gravitino is the LSP. If the NLSP is a gaugino,³ then the
 455 possible decays depend on mixing among the gauginos. The four neutral gauginos
 456 $\tilde{H}_u^0, \tilde{H}_d^0, \tilde{B}, \tilde{W}^0$ mix into four *neutralino* mass eigenstates $\tilde{\chi}_1^0, \tilde{\chi}_2^0, \tilde{\chi}_3^0, \tilde{\chi}_4^0$, and the four
 457 charged gauginos $\tilde{H}_u^+, \tilde{H}_d^-, \tilde{W}^+, \tilde{W}^-$ mix into two *chargino* mass eigenstates $\tilde{\chi}_1^\pm, \tilde{\chi}_2^\pm$
 458 (two mass eigenstates each with two possible charges = four particles). In the limit
 459 that EWSB effects are small, the neutralino and chargino masses can be written as
 460 the gauge eigenstate masses plus a small perturbation:

³In principle, the NLSP could be anything, but in most popular GGM models, it is either a gaugino or a stau. The stau NLSP search is not the subject of this thesis, so it will not be considered in this section.

$$m_{\tilde{\chi}_1^0} = M_1 - \frac{m_Z^2 \sin^2 \theta_W (M_1 + \mu \sin 2\beta)}{\mu^2 - M_1^2} + \dots \quad (3.18)$$

$$m_{\tilde{\chi}_2^0} = M_2 - \frac{m_W^2 (M_2 + \mu \sin 2\beta)}{\mu^2 - M_2^2} + \dots \quad (3.19)$$

$$m_{\tilde{\chi}_3^0} = |\mu| + \frac{m_Z^2 (\text{sgn}(\mu) - \sin 2\beta)(\mu + M_1 \cos^2 \theta_W + M_2 \sin^2 \theta_W)}{2(\mu + M_1)(\mu + M_2)} + \dots \quad (3.20)$$

$$m_{\tilde{\chi}_4^0} = |\mu| + \frac{m_Z^2 (\text{sgn}(\mu) + \sin 2\beta)(\mu - M_1 \cos^2 \theta_W - M_2 \sin^2 \theta_W)}{2(\mu - M_1)(\mu - M_2)} + \dots \quad (3.21)$$

$$m_{\tilde{\chi}_1^\pm} = M_2 - \frac{m_W^2 (M_2 + \mu \sin 2\beta)}{\mu^2 - M_2^2} + \dots \quad (3.22)$$

$$m_{\tilde{\chi}_2^\pm} = |\mu| + \frac{m_W^2 \text{sgn}(\mu)(\mu + M_2 \sin 2\beta)}{\mu^2 - M_2^2} + \dots \quad (3.23)$$

461 where $\tan \beta = \langle H_u^0 \rangle / \langle H_d^0 \rangle$.

462 The two scenarios studied in ref. [22] are the following:

463 • **Bino NLSP:** $M_1 \sim$ few hundred GeV, $M_2, |\mu| \gg M_1$. All but the lightest
464 neutralino (Eq. 3.18) are effectively inaccessible at the LHC due to their large
465 masses. The NLSP can always decay to $\gamma + \tilde{G}$, and if it is heavy enough, to
466 $Z + \tilde{G}$ or $H + \tilde{G}$.

467 • **Wino NLSP:** $M_2 \sim$ few hundred GeV, $M_1, |\mu| \gg M_2$. The lightest neutralino
468 (Eq. 3.18) and the lightest chargino (Eq. 3.22) are nearly degenerate in mass,
469 and are the only two particles to play a role at the LHC. The decays described
470 in the previous bullet point can happen, as well as chargino decays to $W + \tilde{G}$.

471 The search described in this thesis is optimized for the classic bino NLSP decay $\gamma + \tilde{G}$,
472 but sensitivity to the wino co-NLSP scenario is also studied (see Chapter 8).

473 Since strong production of SUSY particles, for instance via $gg \rightarrow \tilde{g}\tilde{g}$, dominates
474 over electroweak production, for instance via $q\bar{q} \rightarrow \tilde{\chi}_1^\pm \tilde{\chi}_1^\mp$, at the LHC due to the
475 enhanced gg parton luminosity over the $q\bar{q}$ parton luminosity, early LHC searches are
476 particularly sensitive to light squarks and gluinos. General gauge mediation makes no

⁴⁷⁷ a priori restrictions on the mass splitting between the strongly interacting sparticles
⁴⁷⁸ and the weakly interacting sparticles, so models with light squarks and gluinos are
⁴⁷⁹ viable. In fact, such models could not be probed as well at the Tevatron⁴ as they are
⁴⁸⁰ at the LHC due to the aforementioned parton luminosities.

⁴⁸¹ Typical LHC signatures of the bino and wino NLSP scenarios are shown in Fig-
⁴⁸² ure 3.4.

⁴⁸³ 3.6 Experimental Status of SUSY

⁴⁸⁴ Collider searches for evidence of supersymmetry began in earnest in the 1980s [24]
⁴⁸⁵ and continue to this day. Most recently, the LHC and Tevatron experiments have set
⁴⁸⁶ the strictest limits on a variety of SUSY breaking scenarios, including GMSB and
⁴⁸⁷ mSUGRA.

⁴⁸⁸ Figure 3.5 shows the current limits set by the CMS experiment on the mSUGRA
⁴⁸⁹ model (with $\tan \beta = 10$) in the m_0 - $m_{1/2}$ plane. (Note that although the plot is trun-
⁴⁹⁰ cated at $m_0 = 1000 \text{ GeV}/c^2$, some searches are sensitive out to $m_0 \sim 2000 \text{ GeV}/c^2$.)
⁴⁹¹ Although the LHC has pushed m_0 above $\sim 1 \text{ TeV}/c^2$ for $m_{1/2}$ up to $\sim 400 \text{ GeV}/c^2$,
⁴⁹² casting some doubt onto the theory's prospects for solving the hierarchy problem,
⁴⁹³ there is still a sizable chunk of mSUGRA parameter space that is not ruled out by
⁴⁹⁴ collider experiments. Furthermore, parts of the CMS unexplored regions overlap with
⁴⁹⁵ areas allowed by astrophysics experiments [25].

Removed

⁴⁹⁶ Figure 3.6 shows the most up-to-date limit (using 1 fb^{-1} of integrated luminosity CMS
⁴⁹⁷ collected by the ATLAS experiment [27] at the LHC) on the Snowmass Points and Moriond
⁴⁹⁸ Slopes (SPS) model of mGMSB, dubbed SPS8 [28]. In general, the lifetime of the result
⁴⁹⁹ lightest neutralino in GMSB models can take on any value between hundreds of
⁵⁰⁰ nanometers to a few kilometers depending on the mass of the lightest neutralino and

⁴Located on the Fermilab site in Batavia, Illinois, the Tevatron was a proton-antiproton collider operating at 1.96 TeV center-of-mass energy. The Tevatron ran from 1987 to 2011 [23].

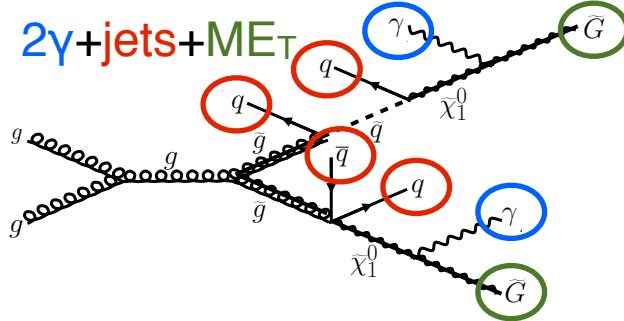
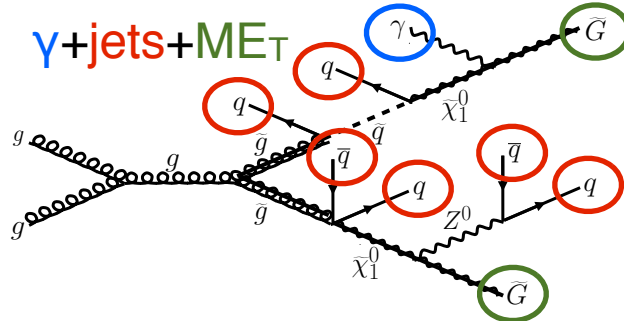
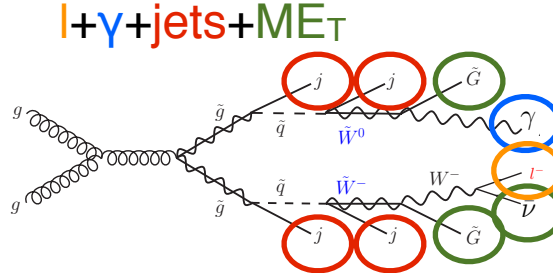
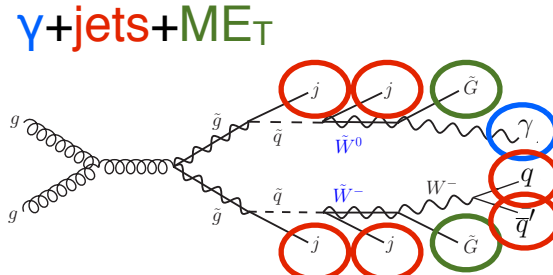
(a) Two gluinos each decay via $\tilde{\chi}_1^0 \rightarrow \gamma \tilde{G}$.(b) One gluino decays via $\tilde{\chi}_1^0 \rightarrow \gamma \tilde{G}$, the other via $\tilde{\chi}_1^0 \rightarrow Z(\rightarrow q\bar{q})\tilde{G}$.(c) One gluino decays via $\tilde{\chi}_1^0 \rightarrow \gamma \tilde{G}$, the other via $\chi_1^\pm \rightarrow W^\pm(\rightarrow l^\pm \nu_l)\tilde{G}$.(d) One gluino decays via $\tilde{\chi}_1^0 \rightarrow \gamma \tilde{G}$, the other via $\chi_1^\pm \rightarrow W^\pm(\rightarrow q\bar{q}')\tilde{G}$.

Figure 3.4: Typical LHC signatures of the bino and wino NLSP scenarios.

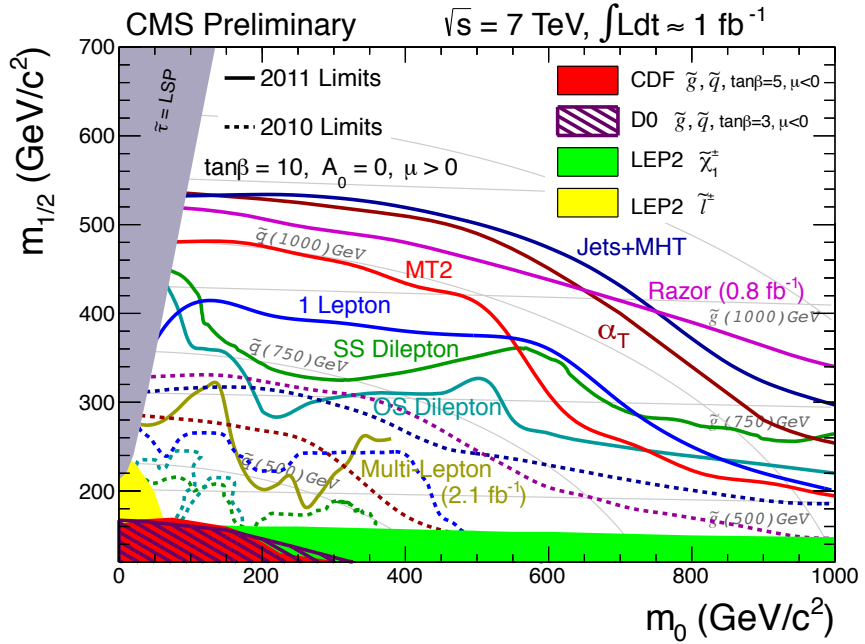


Figure 3.5: CMS limits on mSUGRA with $\tan\beta = 10$, corresponding to a model with third-generation squarks and sfermions somewhat lighter than their first- and second-generation counterparts. The limits set by individual searches are shown as separate colored lines. Solid lines refer to 2011 searches (i.e. using an integrated luminosity of $\sim 1 \text{ fb}^{-1}$), while dashed lines refer to 2010 searches ($\sim 36 \text{ pb}^{-1}$). Reprinted from ref. [26].

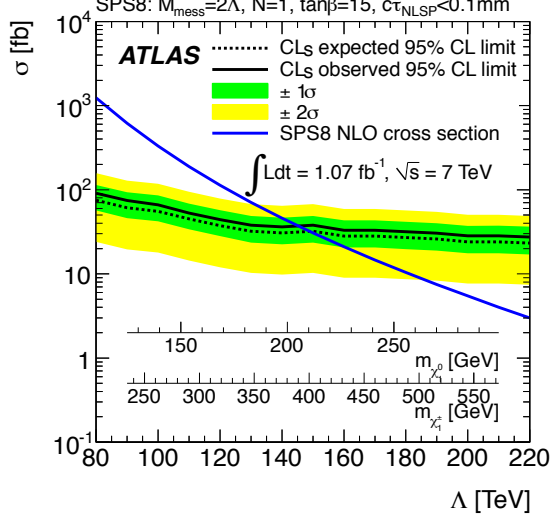


Figure 3.6: ATLAS cross section upper limit on the SPS8 [28] model of mGMSB as a function of SUSY breaking scale Λ , lightest neutralino mass $m_{\tilde{\chi}_1^0}$, or lightest chargino mass $m_{\tilde{\chi}_1^\pm}$. Values of Λ , $m_{\tilde{\chi}_1^0}$, or $m_{\tilde{\chi}_1^\pm}$ below the intersection point between the blue (predicted SPS8 cross section) and black (observed cross section upper limit) curves are excluded. The model parameters listed above the plot are defined in Secs. 3.4 and 3.5, except for τ_{NLSP} , which is the neutralino lifetime. Reprinted from ref. [20].

501 the SUSY breaking scale [12]. The search published in ref. [20] (from which Fig. 3.6 is
 502 culled) considers only *prompt* neutralino variants, i.e. with neutralino lifetime short
 503 enough that the distance traveled by the neutralino before decay cannot be resolved
 504 by the detector. The most recent limits on non-prompt SPS8-style neutralino models
 505 were set by the Collider Detector at Fermilab (CDF) collaboration with 570 pb^{-1} ,
 506 and are shown in Figure 3.7 [21].

507 Finally, if the gravitino is to make up some or all of the dark matter, constraints
 508 on the form of gauge mediation must come from cosmological considerations and
 509 astronomical observations. The gravitino in gauge mediation models is usually very
 510 light ($\mathcal{O}(\text{eV-MeV})$) because it is proportional to the SUSY breaking scale divided
 511 by the Planck mass, and in GMSB the breaking scale is typically only of order a
 512 few hundred TeV ([12] and Sec. 3.5). A light, highly relativistic dark matter particle
 513 might have been produced, for instance, in the early, radiation-dominated period
 514 of the universe [30]. This *warm dark matter* (WDM) may be responsible for all of

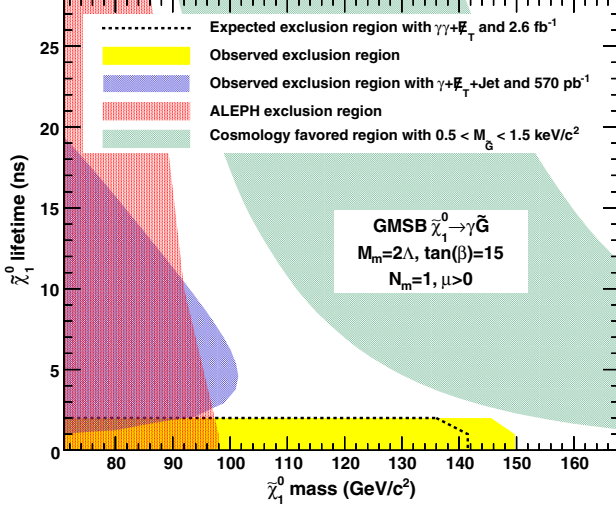


Figure 3.7: CDF exclusion contour in the $\tau_{\tilde{\chi}_1^0}$ - $m_{\tilde{\chi}_1^0}$ plane, where $\tau_{\tilde{\chi}_1^0}$ is the lifetime of the neutralino. Reprinted from ref. [21].

the dark matter needed to account for galactic structure, or it may share the duties with *cold dark matter* (CDM, weakly interacting particles with masses in the GeV range). In any viable model, the predicted relic density of the dark matter species must match the observed value of $\Omega h^2 \sim 0.1$ [31]. For many GMSB models, this measurement constrains the gravitino mass to the keV range [32]. This constraint, however, does not translate into a very strong bound on the lifetime of the lightest neutralino. Using the following equation (taken from [32]):

$$\tau_{\tilde{\chi}_1^0} \sim 130 \left(\frac{100 \text{ GeV}}{m_{\tilde{\chi}_1^0}} \right)^5 \left(\frac{\sqrt{\langle F \rangle}}{100 \text{ TeV}} \right)^4 \mu \text{m} \quad (3.24)$$

and applying the gravitino mass constraint $\sqrt{\langle F \rangle} \lesssim 3000 \text{ TeV}$ (cf. the first paragraph of Sec. 3.5 with $m_{\tilde{G}} \sim \text{keV}$) and $m_{\tilde{\chi}_1^0} = 100 \text{ GeV}$, the upper bound on the neutralino lifetime is 100 meters. For $\sqrt{\langle F \rangle} \sim 100 \text{ TeV}$, the neutralino lifetime is detectable on collider time scales.

Recently, a lower bound on the WDM particle mass in either pure warm or mixed warm and cold dark matter scenarios was set using observations of the Lyman- α forest. For pure WDM, $m_{\text{WDM}} > 8 \text{ keV}$, while for some mixed WDM-CDM scenarios,

529 $m_{\text{WDM}} > 1.1\text{-}1.5 \text{ keV}$ [30, 33]. These bounds and others have motivated the develop-
530 ment of more complicated gauge mediation models [33].

531 However, rather than focus on a specific GMSB model, of which there are many,
532 the search detailed in the following chapters is interpreted in a minimally model
533 dependent way. With this approach, the results can be applied to many competing
534 models. The remainder of this thesis is devoted to the experimental details of the
535 search, analysis strategy, and presentation of the results. The work described in this
536 thesis forms the basis for the CMS public result “Search for Supersymmetry in Events
537 with Photons and Missing Energy” [29], published in April 2012 (see Chapters 7 and 8
538 for results). Ref. [29] contains the best limits on bino-like NLSP and wino-like NLSP
539 GGM models to date.

540 **Chapter 4**

541 **The Large Hadron Collider**

542 At a 2010-2011 energy of 3.5 TeV/beam (7 TeV/beam design [34]) and maximum
543 instantaneous luminosity of $3.55 \times 10^{33} \text{ cm}^{-2} \text{ s}^{-1}$ [35] ($10^{34} \text{ cm}^{-2} \text{ s}^{-1}$ design [34]),
544 the CERN Large Hadron Collider (LHC) is the highest energy and highest intensity
545 proton-proton collider ever built. Its purpose is to allow the four LHC experiments to
546 explore TeV scale physics. For CMS and ATLAS, this implies examining the origins of
547 EWSB via searches for the SM Higgs boson and physical phenomena not predicted by
548 the SM that may explain the mass hierarchy in the SM. It also includes searches for
549 possible dark matter candidates that are often proposed to have masses at the weak
550 scale. The LHC needs to provide high energy proton collisions because the masses
551 of the sought-after particles are higher than those already incorporated into the SM.
552 It must also provide an unprecedented collision rate because signatures of the Higgs
553 boson and physics beyond the SM are very rare compared to SM processes.

554 The rest of this chapter is devoted to an overview of the LHC machine. Section
555 4.1 gives the overall layout of the machine and design choices made in light of
556 energy and luminosity demands. Section 4.2 describes the LHC injection scheme. The
557 different types of magnets and their functions is illustrated in Section 4.3, and finally
558 the radiofrequency cavities are covered in Section 4.4. Unless otherwise noted, all

559 information in this chapter comes from ref. [34].

560 4.1 Design Considerations and Performance Lim- 561 itations

562 The layout of the 26.7-km long [36] LHC ring, located \sim 100 m underground on the
563 border between France and Switzerland northwest of Geneva, is shown in Figure 4.1.
564 The two circulating beams of protons travel in opposite directions, colliding only at
565 the experimental points. There are eight straight sections, each \sim 528 m long, and
566 eight arcs, each made of 23 106.9-m long arc cells. Beam crossings occur in four of
567 the straight sections. The arcs contain six 14.3-m long dipole magnets, the cryogenics
568 to cool the magnets, and short straight sections (SSS) with focusing and corrector
569 magnets. The high luminosity experiments CMS and ATLAS are located diametrically
570 opposite each other on the ring, ensuring that in principle each should receive the
571 same integrated luminosity from the LHC.

572 To achieve a maximum energy per beam of 7 TeV, the peak magnetic field pro-
573 duced by the dipole magnets must be 8.33 T, demanding the use of superconducting
574 technology. Due to the like charges of the two beams, two separate magnet systems
575 and evacuated beam pipes must be used to accelerate the protons in opposite direc-
576 tions. Space limitations in the LHC tunnel, which was previously used for the LEP
577 collider, prevent the installation of two separate rings of magnets, so each dipole in-
578 stead contains two beam pipe bores and two sets of superconducting coils to produce
579 two fields in opposite directions. In order to safely operate the magnets at 8.33 T,
580 the cryogenic bath temperature is chosen to be 1.9 K, colder than any other acceler-
581 ator cryogen and well below the critical temperature of the niobium-titanium (NbTi)
582 superconducting wires of 9.2 K [39]. The extremely low bath temperature leads to
583 a lessened heat capacity in the wires and consequently a lower energy threshold for

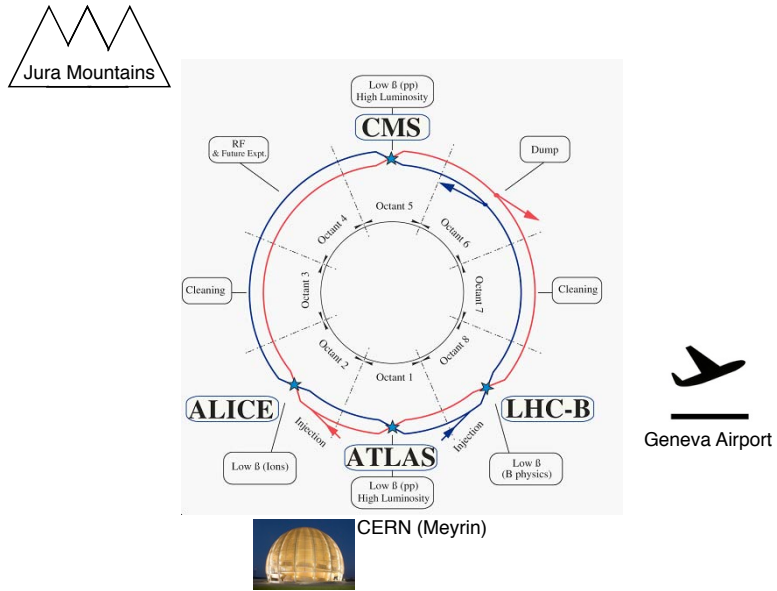


Figure 4.1: Bird's-eye view of the LHC ring, showing the locations of the experiments and local landmarks. Arrows show the beam direction. The ring figure is reprinted from Fig. 2.1 of ref. [34]. The CERN Globe of Innovation photo comes from ref. [37] and the airplane cartoon comes from ref. [38].

584 triggering a quench, so movements and heat dissipation within the cables must be
 585 controlled more tightly than in previous accelerators.

586 The LHC beams are arranged in bunches of protons, with each bunch separated
 587 by an integer multiple of the 25 ns minimum bunch spacing. The machine luminosity
 588 L is given by

$$L = \frac{N_b^2 n_b f_{\text{rev}} \gamma_r}{4\pi \epsilon_n \beta^*} F \quad (4.1)$$

589 where N_b is the number of protons per bunch (squared for the two beams), n_b is
 590 the number of bunches per beam, f_{rev} is the bunch revolution frequency, γ_r is the
 591 relativistic γ of the protons, ϵ_n is the normalized transverse beam emittance, β^* is
 592 the value of the β function at the collision point, and F is a geometrical factor less
 593 than one related to the *crossing angle* of the bunches with respect to the horizontal

594 (ATLAS) or vertical (CMS) planes and the beam size. The normalized transverse
 595 beam emittance is a measure of the RMS spread of the beam in the plane transverse
 596 to its direction of motion, irrespective of its energy. A smaller emittance implies that
 597 particles are squeezed into a smaller area in phase space, leading to larger luminosity.
 598 The β function is defined as the square of the transverse beam size divided by the
 599 emittance. It describes the oscillations of the transverse beam size as a function of
 600 position in the ring. To achieve high luminosity, β^* is the minimum of the β function,
 601 and it is related to the focusing strength of the triplet magnets near the interaction
 602 points. In accelerating sections of the ring, the β function gets large so that the proton
 603 momenta may be more uniform. Each piece of the luminosity is limited by safety or
 604 design considerations.

605 Above some saturated bunch intensity, nonlinear beam-beam interactions experi-
 606 enced by the protons during collisions cause the luminosity to scale as N_b , not N_b^2
 607 [40]. The scale of these interactions is set by N_b/ϵ_n , and the size of the beam pipe and
 608 maximum β function limit ϵ_n to $3.75 \mu\text{m}$. Instabilities are also introduced through
 609 interactions between the protons and the wall of the beam pipe that scale with the
 610 beam current. Last but not least, the beam dump and magnet safety systems limit the
 611 total stored energy in the ring. For these reasons, the maximum number of bunches
 612 is limited to 1.15×10^{11} . In bunches of this proton multiplicity, the average num-
 613 ber of proton-proton collisions per bunch crossing, or *pileup*, in CMS and ATLAS is
 614 approximately 20. This unprecedented level of pileup poses unique triggering, event
 615 reconstruction, and analysis challenges for the experiments.

616 n_b can range from zero to 2808 and had a maximum of ~ 1400 in 2011, corre-
 617 sponding to 50 ns bunch spacing. f_{rev} is set by the circumference of the ring to 11.2
 618 kHz [41]. γ_r is set by the beam energy, which was 3.5 TeV in 2011.

619 The mechanical aperture of the triplet assemblies of quadrupole magnets limit
 620 the minimum β^* to 0.55 [41] and maximum crossing angle to $285 \mu\text{rad}$ [41] at the

The LHC injection complex

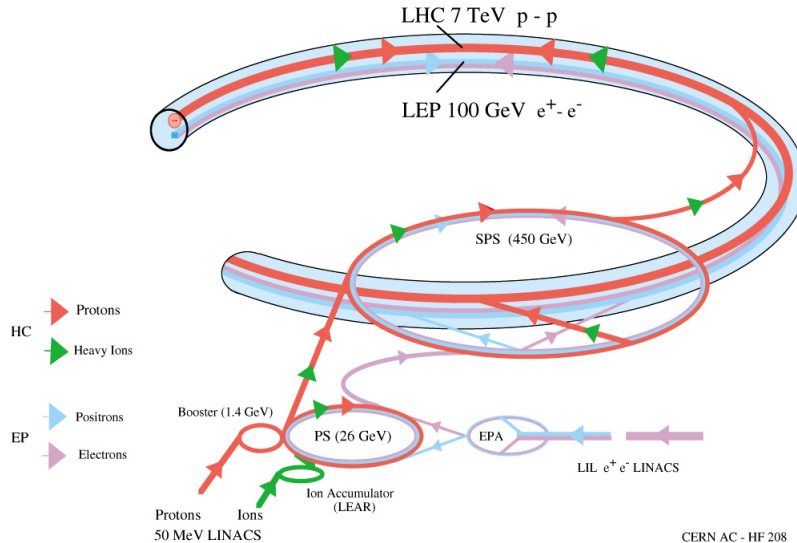


Figure 4.2: Overview of the LHC injector complex at CERN [42].

621 interaction points. The purpose of the crossing angle is to prevent parasitic collisions
 622 in the 23-m length of shared beam pipe upstream and downstream of the interaction
 623 points.

624 4.2 Beam Injection

625 The ultimate source of protons for the LHC is a bottle of hydrogen connected to the
 626 CERN Linac2 linear accelerator, which accelerates the protons up to 50 MeV. From
 627 there they enter the Proton Synchrotron Booster (PSB), which accelerates them to
 628 1.4 GeV, and then the Proton Synchrotron (PS) itself, which brings them to 25 GeV.
 629 The Super Proton Synchrotron (SPS) is the next stage, accelerating the protons to
 630 an energy of 450 GeV. Finally, they leave the SPS and enter the LHC, where they are
 631 accelerated to the desired beam energy (3.5 TeV in 2011). An overview of the LHC
 632 injector complex is shown in Figure 4.2.

633 The 25-ns spaced bunches (or 50 ns for 2011 operation) are produced in trains
 634 of 72 in the PS via a process of splitting six initial bunches into 12 smaller bunches

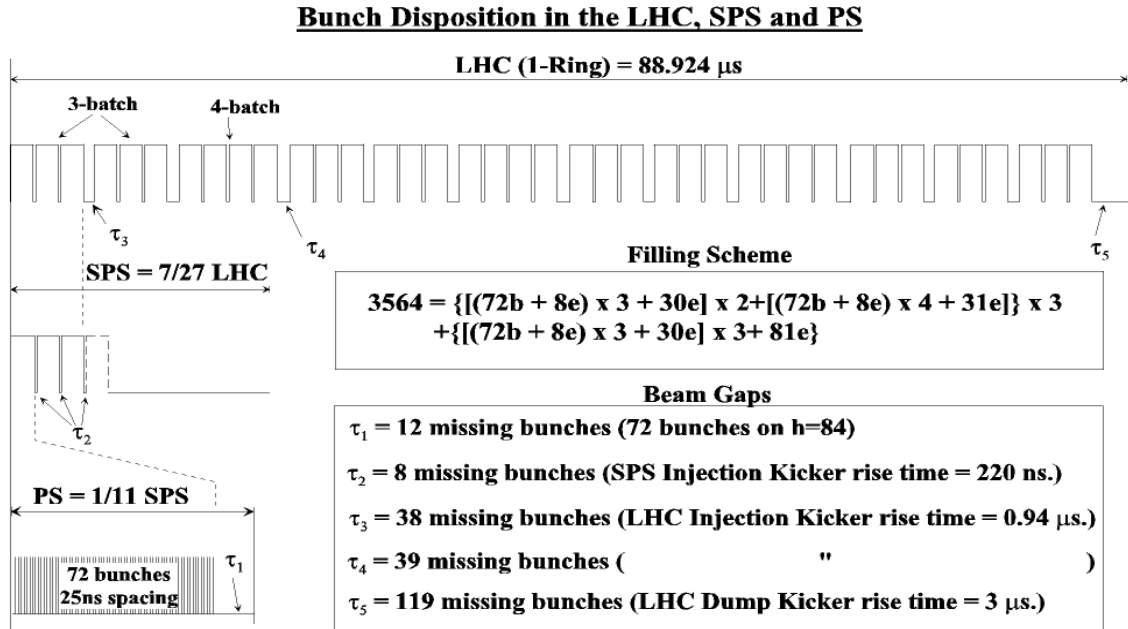


Figure 4.3: LHC injection scheme. Reprinted from Fig. 12.2 of ref. [34].

at specified points along the ring. At the end of each train is a 300 ns (12 bunch) gap, which is an artifact of the splitting process. The SPS is limited by its maximum allowed bunch intensity to storing three or four PS trains at a time. There is an 220 ns (8 bunch) gap at the end of each train due to the SPS injection kicker rise time. The LHC is filled three or four trains at a time from the SPS. At the end of each three-train and four-train group is a gap of 0.94 μ s (38 or 39 bunches) due to the LHC injection kicker rise time. Finally, at the end of an entire 88.924- μ s long LHC orbit is a gap of 3 μ s (119 bunches), known as the *abort gap*, to allow for the LHC dump kicker rise time. The injection scheme is shown in Figure 4.3.

LHC injection occurs at points 2 and 8. At the intersection of the SPS-LHC transfer line and the LHC beam pipe are five septum magnets that deflect the bunches 12 mrad horizontally into orbit. The septum magnets have a gap into which the beam is injected as well as two separate holes for the circulating beams, as shown in Figure 4.4. Four kicker magnets then deflect the bunches 0.85 mrad vertically into orbit. The kicker magnets supply a pulsed magnetic field with a 0.94 μ s rise time

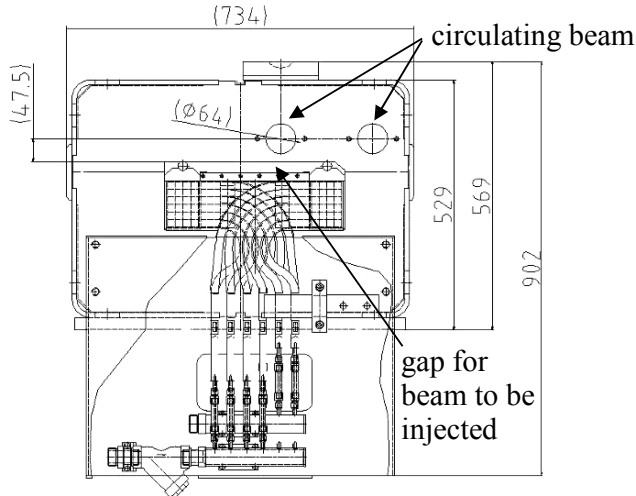


Figure 4.4: Cross-sectional view of septum magnet (beam direction is into or out of the page) showing the holes for the circulating beams and the separate gap for injected particles. Reprinted from Fig. 11.2 of ref. [34].

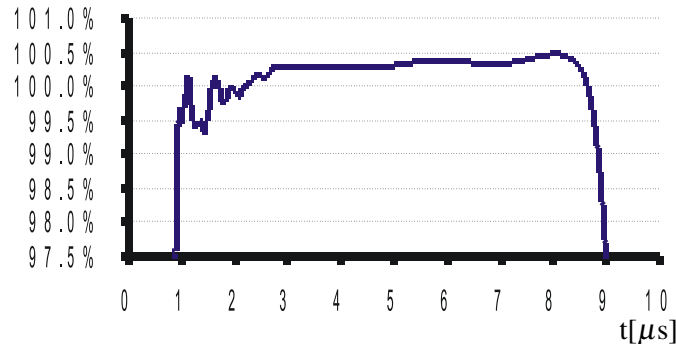


Figure 4.5: LHC injection kicker pulse shape. The y -axis measures percentage of maximum current. Reprinted from Fig. 11.7 of ref. [34].

650 (see Fig. 4.3) and a 5.84(7.86) μs flat top for three-train(four-train) injection (see
 651 Figure 4.5). To limit emittance growth at injection due to over- or under-kicking the
 652 injected bunches such that they miss the core of the LHC orbit, the kicker current is
 653 limited to $< 0.5\%$ flat top ripple in any direction.

654 4.3 Magnets and Cryogenics

655 There are 1232 twin-bore dipole magnets along the LHC ring used for establishing
 656 the circular orbit of the protons. They consist of two evacuated beam pipes, each

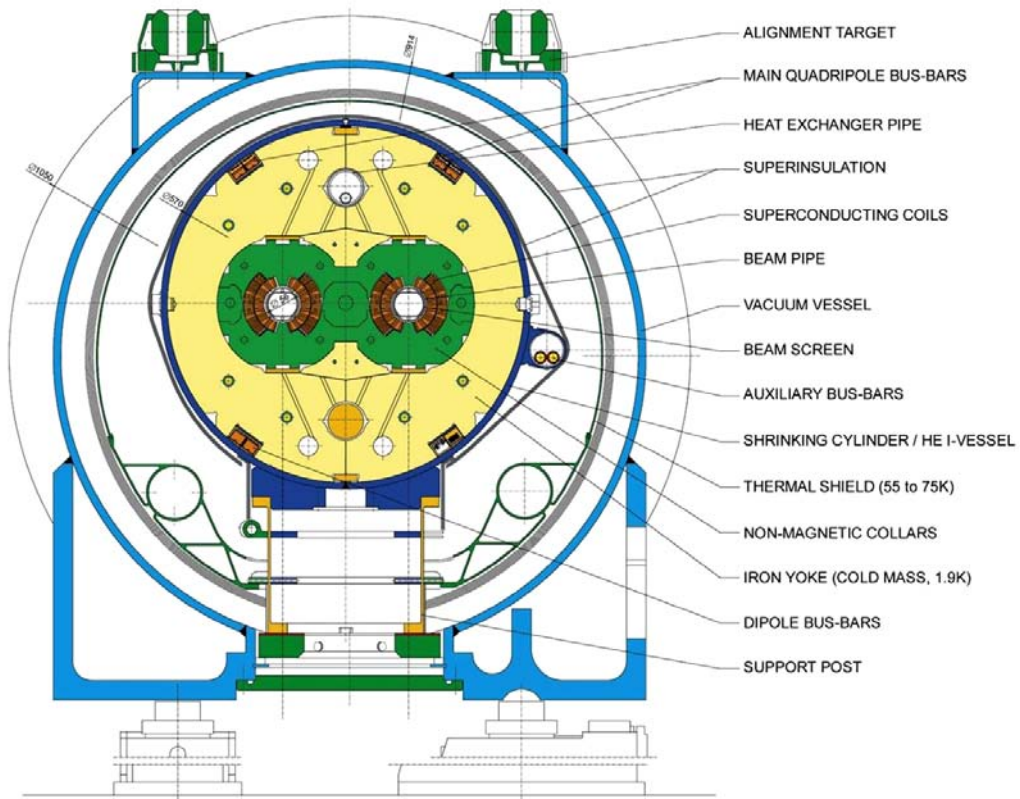


Figure 4.6: Cross-sectional view of LHC dipole + cryostat. Reprinted from Fig. 3.3 of ref. [34].

657 flanked by its own set of superconducting coils, inside an iron yoke which serves as
658 the 1.9 K cold mass. The entire assembly sits inside a helium vessel, which is itself
659 surrounded by a vacuum chamber thermally insulating the cold mass from the room
660 temperature LHC cavern. The entire dipole + cryostat device is \sim 16.5 m long and
661 weighs about 27.5 t. A cross-sectional view of the dipole is given in Figure 4.6.

To provide a centripetal Lorentz force on the protons, the dipole field points vertically up or down, depending on the sense of the beam. The magnetic field lines for a single beam pipe are shown in Figure 4.7. Figure 4.8 shows the coil windings in two bores. To provide the correct field direction, the coils are wound around blocks that are ~ 14 m long (the length of the dipole), so that each winding has a circumference of ~ 28 m.

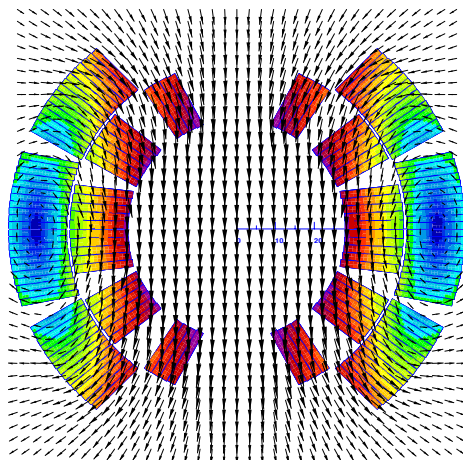


Figure 4.7: Magnetic field lines of the dipole field. The beam direction is into the page. Reprinted from Fig. 4 of ref. [43].

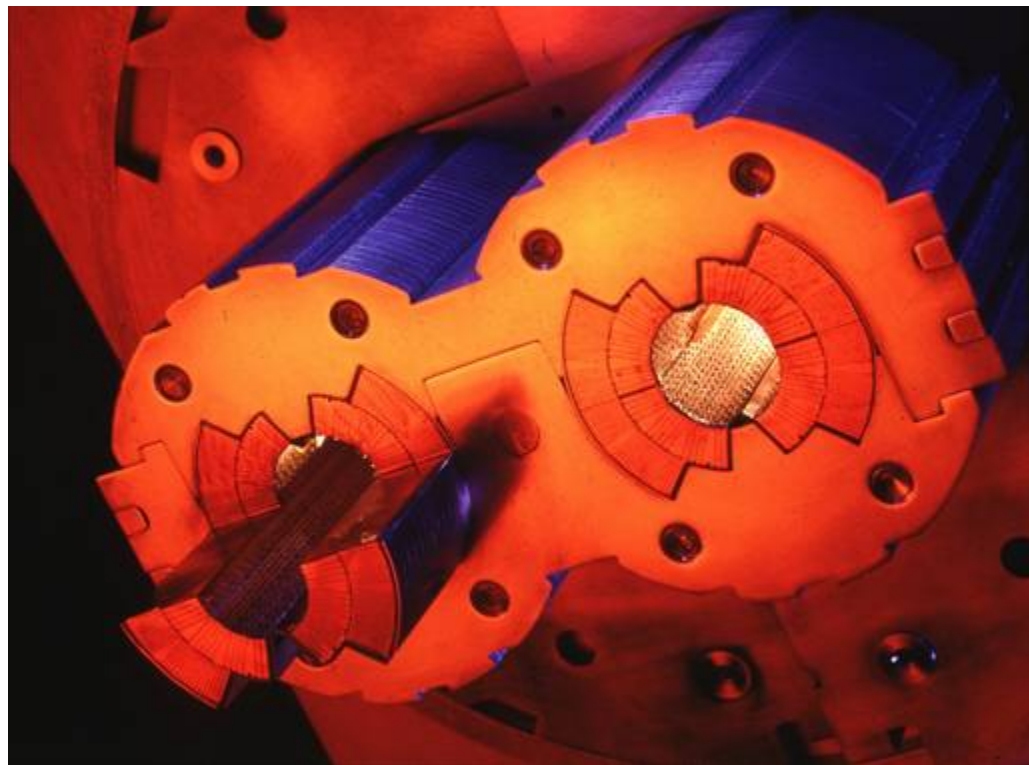


Figure 4.8: Superconducting coils in a twin-bore dipole [44].

668 In addition to the dipoles, a number of different types of orbit corrector magnets
 669 are installed throughout the ring. The main quadrupole magnets, as well as higher
 670 order field corrector magnets, are located in the arcs and short straight sections. The
 671 function of these magnets is to provide fine grained control over the magnetic field
 672 in order to keep the bunches in the proper orbit and control the emittance and β
 673 functions.

674 In the straight sections, there are four specialized types of magnets related to SPS
 675 extraction and bringing the beams into collision. Matching section quadrupoles near
 676 the transfer lines help to match the injected bunch orbit to the circulating bunch orbit.
 677 Dispersion suppressors, consisting of dipoles and quadrupoles, help to reduce beam
 678 dispersion near the collision points due to off-momentum protons. Matching section
 679 separation dipoles control the separation between the two beams near the collision
 680 points. The magnets that perform the final squeeze of the beams before collision,
 681 called the low- β inner triplets, must provide a very high field gradient of 215 T/m,
 682 withstand a high radiation dose, and sustain high heat loads in the superconducting
 683 coils.

684 The superfluid helium cryogen is delivered to the magnets via a distribution line
 685 from the main refrigerator. A cross section of the LHC tunnel, showing the cryogen
 686 delivery apparatus for a dipole, is shown in Figure 4.9.

687 4.4 Radiofrequency Cavities

688 LHC bunches are captured and accelerated in 400 MHz superconducting radiofre-
 689 quency (RF) cavities. 400 MHz defines the bunch length of $\lesssim 2$ ns. As bunches pass
 690 through the cavities, the oscillating electric field is at its peak and accelerates the
 691 protons through a potential difference of 2 MV per cavity (16 MV per turn). The
 692 finite bunch length is due to particles that arrive out of phase with the electric field

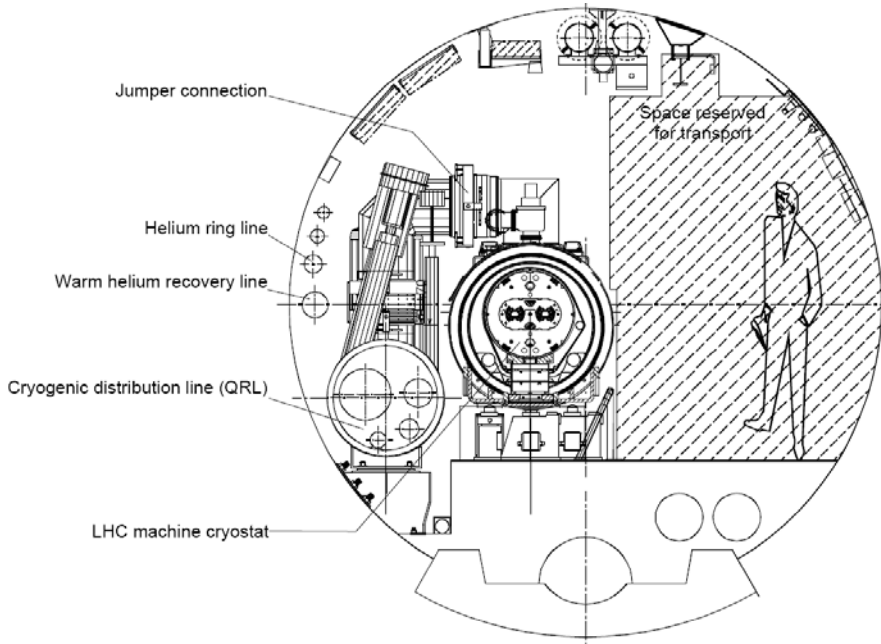


Figure 4.9: Cross section of the LHC tunnel, showing the cryogen delivery apparatus for a dipole. Reprinted from Fig. 7.1 of ref. [34].

693 due to deviations in their momenta from the nominal. During a ramp of the beam
 694 energy from 450 GeV to 3.5 or 7 TeV, bunches repeatedly travel around the ring, re-
 695 ceiving an energy kick each time, until the desired energy is reached. Feedback from
 696 the RF accelerating system causes an increase in magnet current to keep the bunches
 697 in a fixed orbit.

698 Superconducting material (niobium) coats the cylindrical walls of the cavity. RF
 699 power is coupled to the cavity via a klystron. The RF electric field standing wave is set
 700 up across the cavity in the beam direction. The transverse magnetic field dissipates
 701 some energy into the walls, but much less than in a normal conducting cavity.

702 **Chapter 5**

703 **The Compact Muon Solenoid**
704 **Experiment**

705 The Compact Muon Solenoid (CMS) detector sits at point 5 of the LHC ring, diamet-
706 rically opposite the ATLAS detector at point 1. It is a 4π hermetic general purpose
707 detector, meaning that it has the capability to detect charged and neutral hadrons,
708 photons, electrons, muons, taus, neutrinos, and non-Standard-Model particles pre-
709 dicted to escape the detector with good efficiency over a large range of rapidity.
710 Its main distinguishing feature is a superconducting solenoid that provides a 3.8T
711 magnetic field parallel to the beam line. This strong magnetic field allows precise de-
712 termination of the momentum and charge of muons and electrons up to a momentum
713 of ~ 1 TeV.

714 The origin of the CMS coordinate system is at the nominal interaction point. The
715 y -axis points skyward, the x -axis points towards the center of the LHC ring, and
716 the z -axis points counterclockwise along the LHC ring. r denotes radial distances
717 from the beam line, ϕ is the azimuthal angle measured with respect to the positive
718 x -axis, and θ is the polar angle measured with respect to the positive z -axis. The
719 *pseudorapidity* η is defined as $\eta = -\ln \tan(\theta/2)$, and is a good approximation to

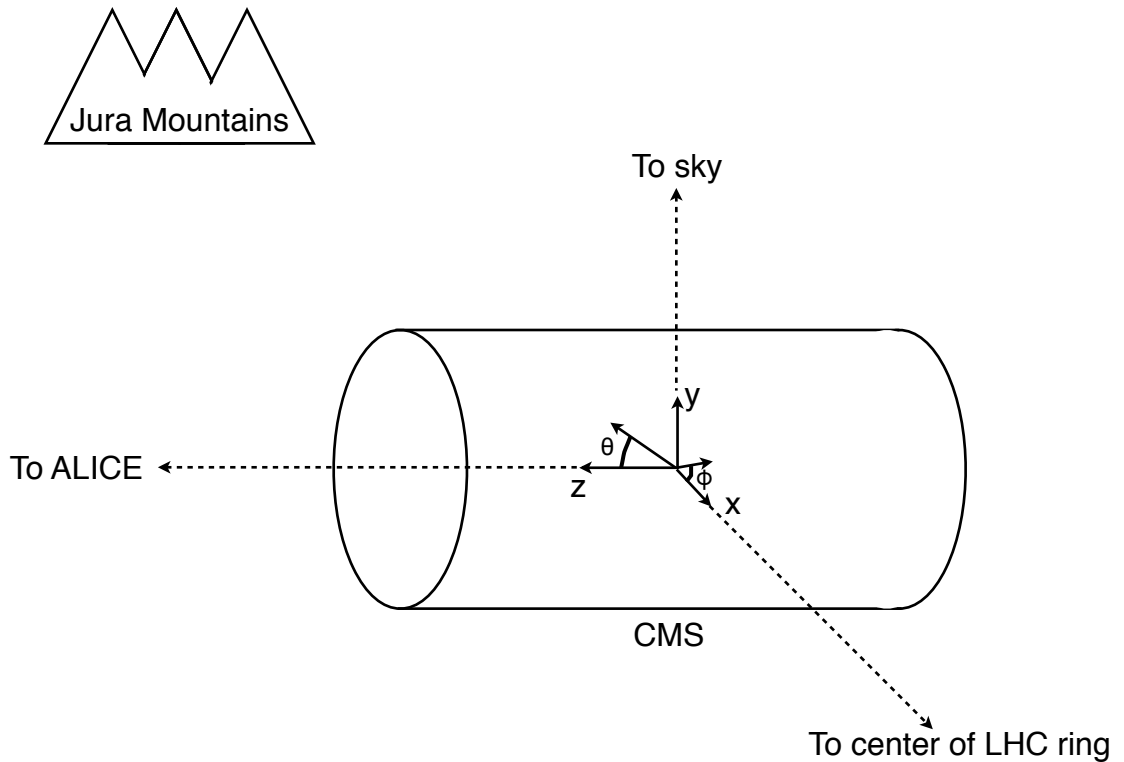


Figure 5.1: CMS coordinate system.

720 rapidity $y = (1/2) \ln((E + p_z c)/(E - p_z c))$ for relativistic particles. The transverse
 721 momentum and energy (p_T and E_T) of a particle are defined as $p_T = p \cos \phi$ and
 722 $E_T = E \cos \phi$, where p and E are the magnitude of the particle's momentum vector
 723 and the particle's total energy, respectively. A depiction of the CMS coordinate system
 724 is shown in Figure 5.1.

725 The CMS sub-detectors are arranged in concentric cylindrical layers, plus “end-
 726 caps,” around the beam line, as shown in Figure 5.2. Closest to the beam line are
 727 three layers of silicon pixel detectors, with the innermost at radius 4.4 cm and out-
 728 ermost at radius 10.2 cm [45]. Including the pixel endcaps, the total pixel coverage

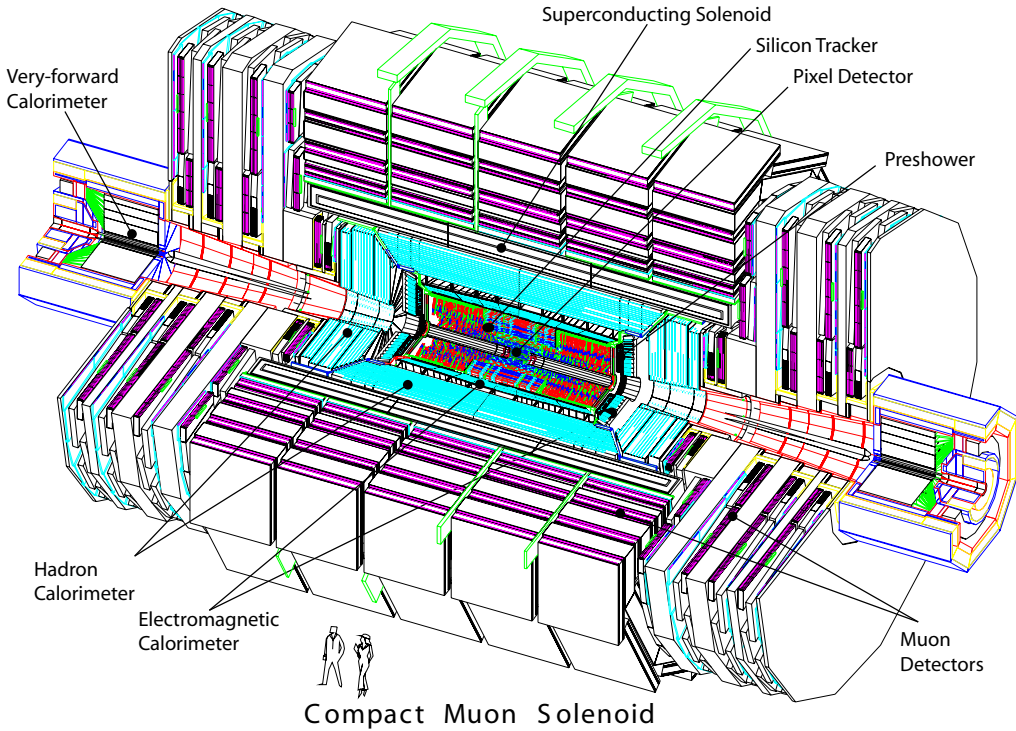


Figure 5.2: Cutaway view of CMS. Reprinted from Fig. 1.1 of ref. [45].

729 extends to $\eta = 2.5$ [45]. The pixel detector plays an important role in determining the
 730 proton-proton interaction position (*beam spot*) and the impact parameters of charged
 731 particle trajectories, and is critical for the measurement of decay positions some dis-
 732 tance from the beam spot (*displaced vertices*), such as those due to the showering and
 733 hadronization of a b quark.

734 The 10 next layers of CMS are comprised of silicon microstrip detectors, with the
 735 outermost layer at a radius of 1.3 m from the beam line [45]. As for the pixel detectors,
 736 the silicon strip endcaps extend tracking coverage to $\eta = 2.5$. The silicon microstrip
 737 layers are the workhorse of the CMS tracking system, and provide excellent charged
 738 particle momentum resolution and track finding efficiency.

739 Outside the tracking detectors are the calorimeters, starting with the single-layer
 740 lead tungstate crystal electromagnetic calorimeter at a radius of 1.3 m from the beam
 741 line (location of crystal front faces) [45]. Each crystal is 23 cm long, corresponding

742 to 25.8 radiation lengths (X_0) [45]. The crystal dimensions are such that most of one
 743 electromagnetic shower, and no more, can be contained in a single crystal, leading to
 744 excellent energy resolution for photons and electrons. The electromagnetic calorime-
 745 ter radial and endcap layers cover a pseudorapidity range up to 3.0. A lead/silicon
 746 sampling calorimeter sits in front of the crystal endcaps to provide better rejection
 747 of neutral pions.

748 The last layer of calorimetry inside the solenoid is the brass/scintillator sampling
 749 hadronic calorimeter, which has a radial extent from 1.77-2.95 m [45]. The hadronic
 750 barrel and endcap calorimeters cover up to $|\eta| = 3.0$, while the iron/quartz-fiber for-
 751 ward hadronic calorimeter covers the region $3.0 \leq |\eta| \leq 5.2$.¹ There is one more
 752 layer of hadronic calorimetry outside the solenoid in $|\eta| < 1.3$ which, together with
 753 the layers inside the solenoid, provides approximately 12 hadronic interaction lengths
 754 of instrumented absorber. Because of its large $|\eta|$ coverage and depth, the hadronic
 755 calorimeter provides good missing transverse energy resolution and accurate measure-
 756 ments of high energy jets.

757 The iron return yoke of the solenoidal magnetic field is interleaved with muon
 758 detectors from 4.1-7.4 m in r and 6.6-10.6 m in z , providing muon detection up to
 759 $|\eta| = 2.4$ [45]. In the barrel region of $|\eta| < 1.2$, drift tubes are used to read out the
 760 muon tracks, while in the endcaps cathode strip chambers are used. Due to their
 761 speed, resistive plate chambers are used throughout the muon system to provide
 762 an independent trigger and timing measurement. Combining the tracker and muon
 763 system hits, the momenta and charge of muons up to $p_T = 1$ TeV can be precisely
 764 reconstructed.

765 A longitudinal quarter cross-sectional view of CMS is shown in Figure 5.3. The
 766 remainder of this chapter is devoted to explaining the CMS subdetectors and readout

¹The Centauro and Strange Object Research (CASTOR) and Zero Degree Calorimeter (ZDC) detectors provide additional calorimetry beyond $|\eta| = 5.2$. However, they are mainly used in the heavy ion and diffractive physics programs of CMS, and play no role in the detection of heavy SUSY particles. Therefore, they will not be discussed here.

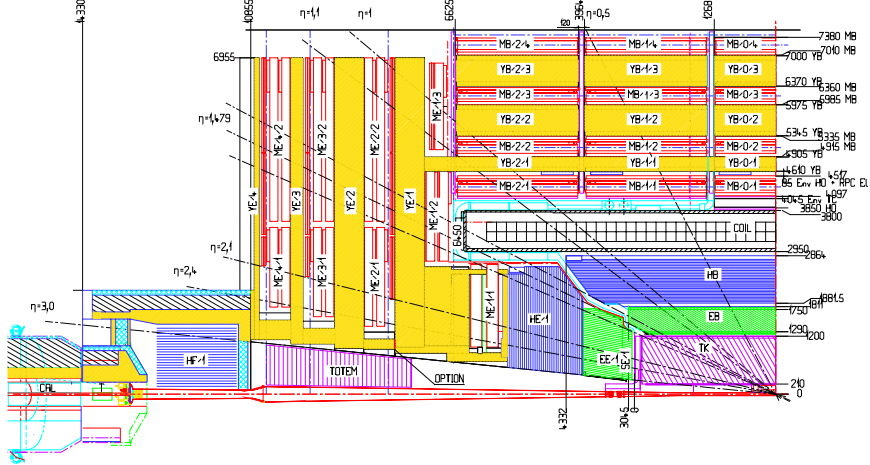


Figure 5.3: Longitudinal quarter cross-sectional view of CMS. The nominal interaction point is at the lower right-hand corner of the drawing. The tracker is shown in purple diagonal hashing, the electromagnetic calorimeter in green, the hadronic calorimeter in blue, and the muon stations in red. The solenoid is shown in black and white and labeled COIL, and the magnet return yoke is shown in yellow. Radial and longitudinal distances are measured in millimeters. Reprinted from Fig. CP 1 of ref. [46].

systems. Section 5.1 describes the subdetector technologies and performance benchmarks, while Section 5.2 details the CMS trigger and data acquisition systems and framework for promptly reconstructing and transferring data worldwide. For a thorough description of CMS, see ref. [45]. Unless otherwise noted, all information in this chapter comes from ref. [45].

5.1 The Detectors and Their Operating Principles

5.1.1 Tracking System

Given the LHC design instantaneous luminosity, efficient reconstruction of charged particle tracks from transverse momenta of 1 GeV up to 1 TeV can only be achieved with a low occupancy tracker. For $r < 10$ cm, the hit rate density is highest, leading to the choice of $100 \mu\text{m} \times 150 \mu\text{m}$ silicon pixel sensors for hit detection. For $20 \text{ cm} < r < 110 \text{ cm}$, the lower hit rate allows the use of silicon strips, with length along z of

779 order centimeters and length along the $r \cdot \phi$ curve of order hundreds of microns. This
 780 design leads to a pixel hit occupancy of $\sim 10^{-4}$ /pixel/BX and a strip hit occupancy
 781 of $\sim 10^{-2}$ /pixel/BX, where BX refers to 1 LHC bunch crossing.

782 As radiation dose from hadrons accumulates over the lifetime of the tracker, silicon
 783 leakage current through the semiconductor junctions increases, heating up the sensors.
 784 Since the leakage current itself depends on temperature, this can lead to *thermal*
 785 *runaway* that damages the detector. To avoid this, the tracker must be cooled to
 786 approximately -10°C . Operating at this temperature, the signal:noise ratio in the
 787 silicon sensors is 10:1, and should remain at that level over the 10-year lifetime of the
 788 tracker.

789 At its thickest ($|\eta| \sim 1.5$), the tracker depth (including services) is $\sim 1.8X_0$,
 790 and the depth falls off to $\sim 1X_0$ in thinner areas. Unfortunately, the large mass of
 791 the tracker degrades somewhat the performance of the electromagnetic calorimeter
 792 behind it, as $\sim 50\%$ of photons will convert to e^+e^- pairs in the tracker.

793 Pixel Detector

794 A longitudinal quarter view of the three barrel pixel (BPix) layers and two forward
 795 pixel (FPix) disks is shown in Figure 5.4. There are 768 BPix modules in total.
 796 Each BPix layer is divided into 32 ϕ -wedges, with eight modules per wedge arranged
 797 end-to-end in z . The ϕ -wedges operate nearly independently in terms of clock and
 798 readout. Each FPix disk consists of 24 ϕ -wedges, with pie-shaped modules attached
 799 to the front and back of the disk, for a total of 192 modules. The front- and back-side
 800 modules of the FPix disks are constructed of different sized *plaquettes*, or multi-pixel
 801 sensor chips, such that the gaps in the front-side module are covered by plaquette
 802 area in the back-side module and vice versa. An illustration of the BPix and FPix
 803 mechanical layouts is given in Figure 5.5.

804 Since the electric field in the depletion region of the BPix sensors is perpendicular

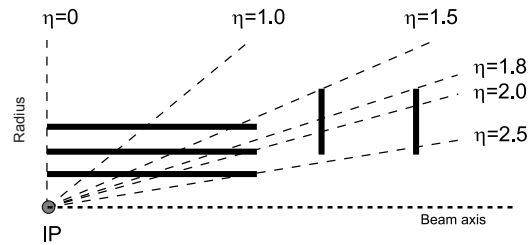
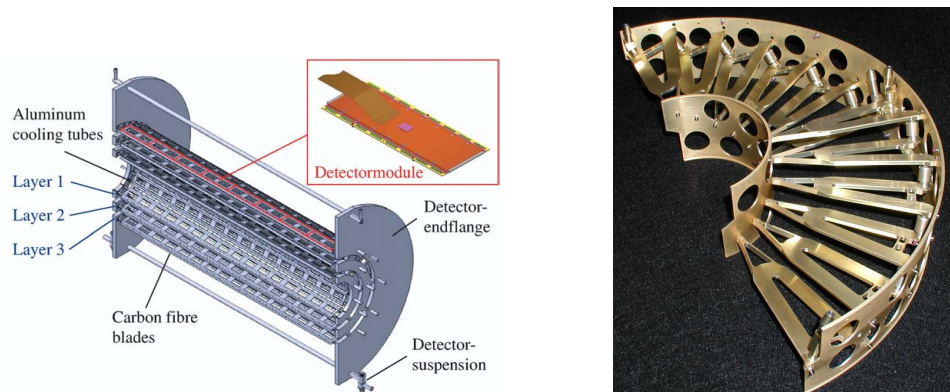


Figure 5.4: Longitudinal quarter view of the pixel detector. Reprinted from Fig. 3.6 of ref. [45].



(a) Cutaway view of the barrel pixel layers, showing the three layers and the eight end-to-end modules along z . Reprinted from Fig. 3.11 of ref. [45].

(b) Half-disk of the forward pixel detector, showing the 12 pie-shaped module mounts. Reprinted from Fig. 3.15 of ref. [45].

Figure 5.5: BPix and FPix mechanical structures.

805 (i.e. pointing along r) to the magnetic field of CMS (i.e. pointing along z), the charge
 806 carriers in the silicon experience a Lorentz drift along ϕ . The multi-pixel sensor pitch
 807 is such that this causes the charge from one particle hit to be shared among multiple
 808 pixels. Particle hits are reconstructed reading out the analog pixel signal and inter-
 809 polating between signals in multiple pixels. This method achieves a $15\text{-}20 \mu\text{m}$ spatial
 810 resolution, which is comparable to the sensor pitch. To induce this effect in FPix,
 811 the sensor wedges are tilted by the approximate BPix Lorentz angle of 20° [47] with
 812 respect to the y -axis.

813 Each multi-pixel sensor consists of an array of 52×80 n-type pixels implanted onto
 814 an n-type substrate with $320 \mu\text{m}$ thickness. The other face of the substrate is covered
 815 with a thin layer of p-type semiconductor. Except for the outer edges, which are held
 816 at ground potential to prevent sparking between the sensor edges and the connected
 817 readout chip [48], the p-side is reverse biased at 150 V (BPix) or 300 V (FPix). The
 818 pixels are held at ground potential. A particle entering through the p-side will cause
 819 a burst of current to flow across the p-n junction. The charge will be collected by the
 820 pixels, which are bump-bonded to the readout. The BPix and FPix sensors employ
 821 slightly different technologies for electrically isolating the individual pixels, but both
 822 rely on the idea of surrounding the pixels with a p-type material to provide a p-n
 823 junction that acts as a barrier to current flow.

824 Each 52×80 pixel sensor is bump bonded to a readout chip (ROC). The ROCs
 825 provide zero suppression and amplify, buffer, and communicate the signals from the
 826 sensors. A single token bit manager (TBM) controls ~ 16 ROCs in the barrel or ~ 24
 827 ROCs in the endcaps. Its purpose is to distribute the clock and trigger to the ROCs
 828 (the latter initiates a transmission of the signal further upstream to be assembled
 829 into the full event readout of CMS). The clock and trigger are supplied by the pixel
 830 front end controller (pFEC), which interfaces to the central clock and data acquisition
 831 systems. Analog signals that are collected from the pixel front ends are digitized by

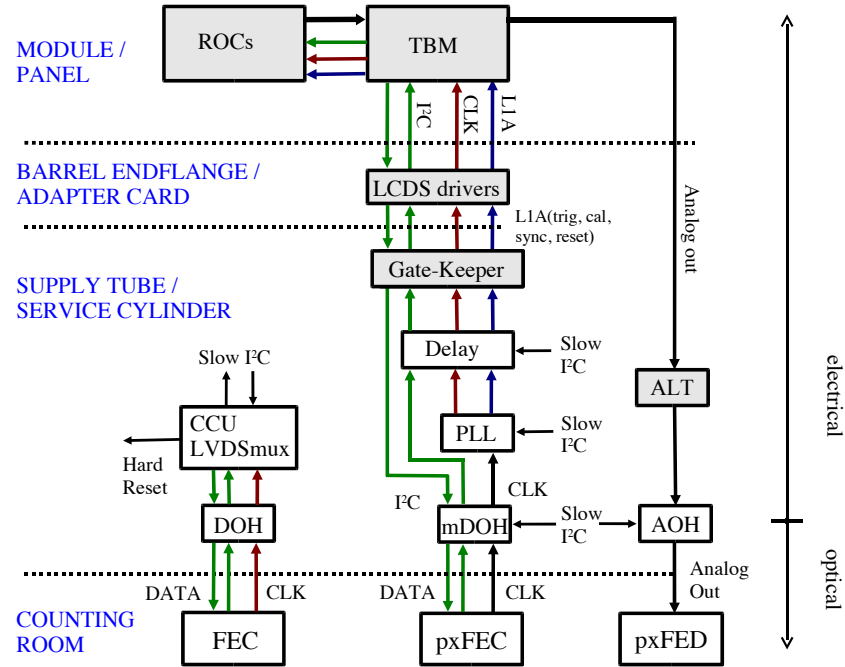


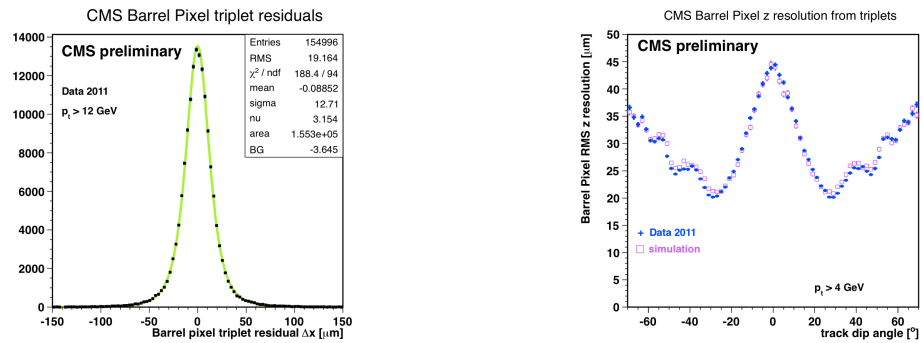
Figure 5.6: Pixel control and readout system. Reprinted from Fig. 3.9 of ref. [45].

832 the pixel front end digitizer (pxFED). A diagram of the readout system is shown in
 833 Figure 5.6.

834 Figure 5.7 shows some results highlighting the performance of the pixel detector.

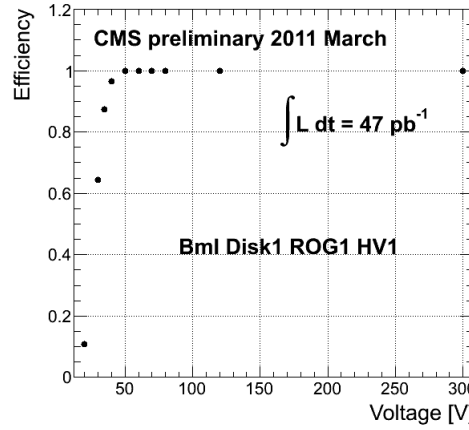
835 Silicon Strip Tracker

836 The silicon strip tracker is divided into four parts: the inner barrel (TIB) and inner
 837 disks (TID), covering the radial extent $20 \text{ cm} < r < 55 \text{ cm}$ and z extent $80 \text{ cm} <$
 838 $|z| < 90 \text{ cm}$; and the outer barrel (TOB) and endcap (TEC), covering the radial
 839 extent $61 \text{ cm} < r < 108 \text{ cm}$ and z extent $124 \text{ cm} < |z| < 282 \text{ cm}$. A number of the
 840 tracker layers and endcaps hold double-sided strip modules (shown as double lines
 841 in Figure 5.8), with the rear module tilted at an angle of 100 mrad with respect to
 842 the front module, to provide a measurement in two coordinates. There are a total of
 843 15,148 modules in the tracker, arranged as shown in the longitudinal cross-sectional
 844 view of Fig. 5.8. For the TIB and TOB, the modules are arranged in straight rows



(a) BPix hit resolution in the $r \cdot \phi$ coordinate [49].

(b) BPix hit resolution in the z coordinate vs. track dip angle, showing the effect of charge sharing on resolution [50].



(c) Pixel reconstruction efficiency vs. bias voltage for a group of three wedges in FPix [51].

Figure 5.7: Pixel detector performance highlights.

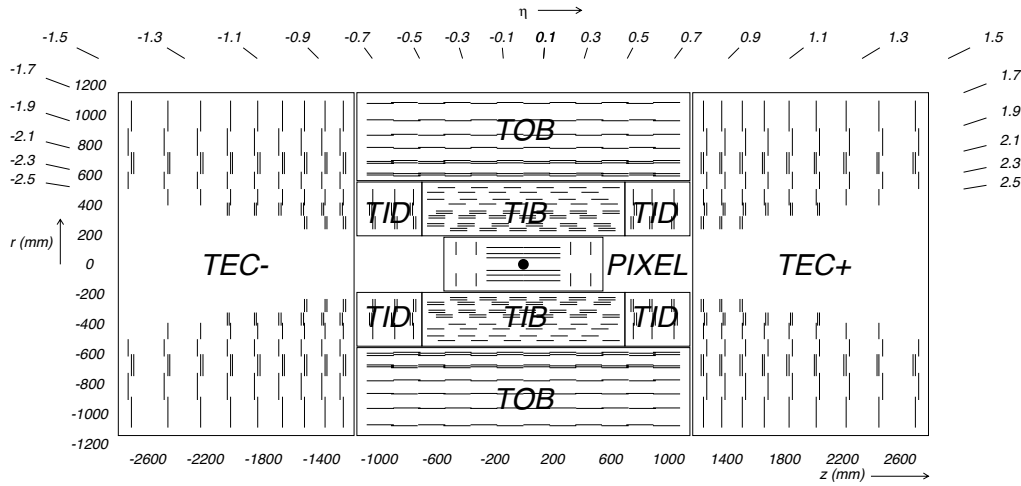


Figure 5.8: Longitudinal cross section of the silicon strip detector. Reprinted from Fig. 3.1 of ref. [45].

845 end-to-end along z , with repeating rows covering the full 2π extent in ϕ . In each of the
 846 TID disks, the modules are arranged into three concentric circular rings of increasing
 847 r . In the TEC, the modules are affixed to ϕ -wedges called *petals*. One side of the TEC
 848 and its petal structure is shown in Figure 5.9.

849 Like the pixels, the strip sensors generate a signal when current flows across a
 850 p-n junction in response to interaction with a charged particle. Whereas the pixels
 851 are n-type implants on an n-type substrate, with a solid p-type rear layer to which
 852 the high voltage is connected, the strips are p-type implants on an n-type substrate,
 853 with a solid n-type rear layer connecting to the high voltage. The p-n junction in the
 854 strip sensors is at the strip-substrate boundary, whereas in the pixel sensors it is at
 855 the boundary between the rear layer and the substrate. Each sensor has either 512
 856 or 768 electrically isolated strips, with pitch varying from 80-205 μm depending on
 857 location. Strip lengths in z range from ~ 10 to ~ 25 cm. Thin (320 μm) sensors are
 858 used in the TIB, TID, and inner four rings of the TEC, while thick (500 μm) sensors
 859 are used in the TOB and the outer rings of the TEC. The thicker sensors compensate
 860 for the increased strip capacitance (and hence electronics noise) of the longer strips
 861 in the outer layers/disk of the tracker such that strip signal:noise is maintained above

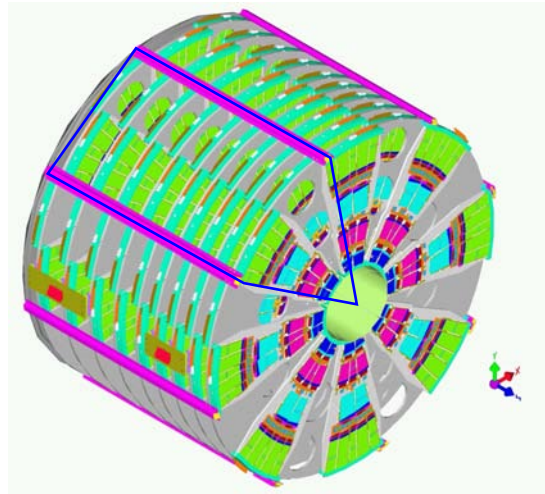


Figure 5.9: View of one tracker endcap, with the outline of a petal shown in blue. There are nine petals per wedge-shaped sector (one per TEC disk). Reprinted from Fig. 3.30 of ref. [45].

862 10 everywhere.

863 The strips are wire bonded to a front end readout chip called the APV25. The
 864 APV25 amplifies and shapes the strip signals before sending the full analog pulse
 865 information to an APVMUX, which multiplexes the output of two APV25s. Then,
 866 the electrical signal from the APVMUX is sent differentially a few centimeters to an
 867 optical driver, where it is converted to an optical signal and sent to one of the 450
 868 front end drivers (FEDs). The FEDs convert the signal back to an electrical pulse
 869 and digitize it for use in the global event assembly. As for the pixels, analog readout
 870 is used on detector so that hit reconstruction may benefit from charge sharing.

871 Clock, trigger, and control signals are sent from the front end controllers (FECs)
 872 to phase locked loop (PLL) chips on the front ends. The FECs interface to the global
 873 clock and trigger system. Four or six APV25s, an APVMUX, and a PLL chip all sit on
 874 a *hybrid*, two which one thin or two thick sensors are also affixed. The sensor-hybrid
 875 combination and its frame form a module. Figure 5.10 shows a diagram of a module,
 876 while Figure 5.11 shows a block diagram of the strip readout architecture.

877 As an example of the strip capabilities, strip hit resolution and signal:noise mea-

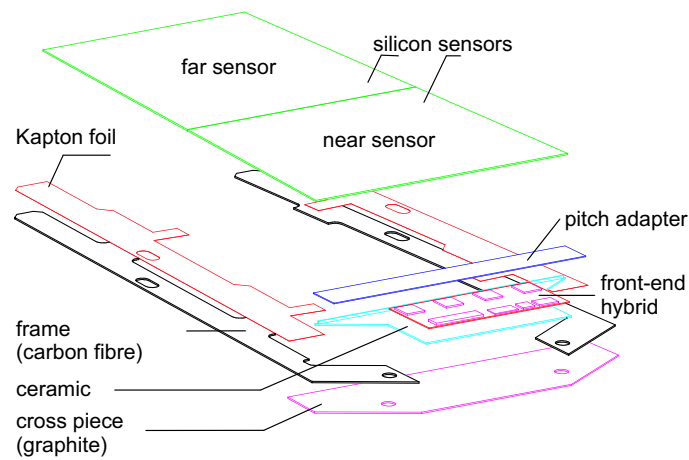


Figure 5.10: Exploded view of a strip module with two sensors. Reprinted from Fig. 3.22 of ref. [45].

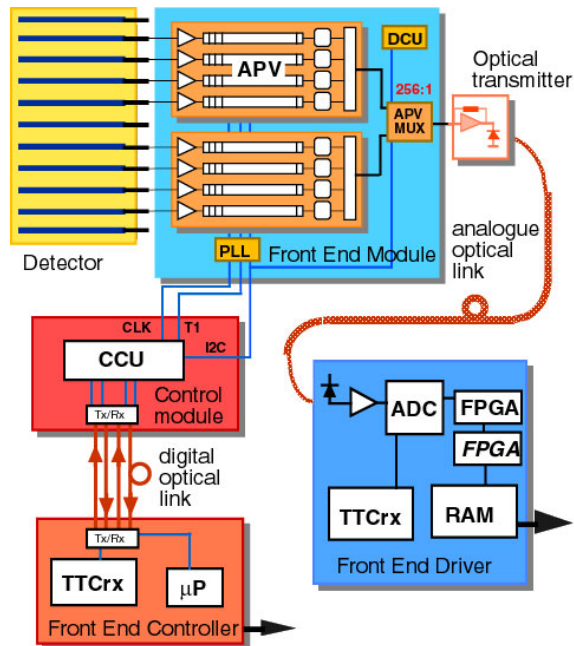


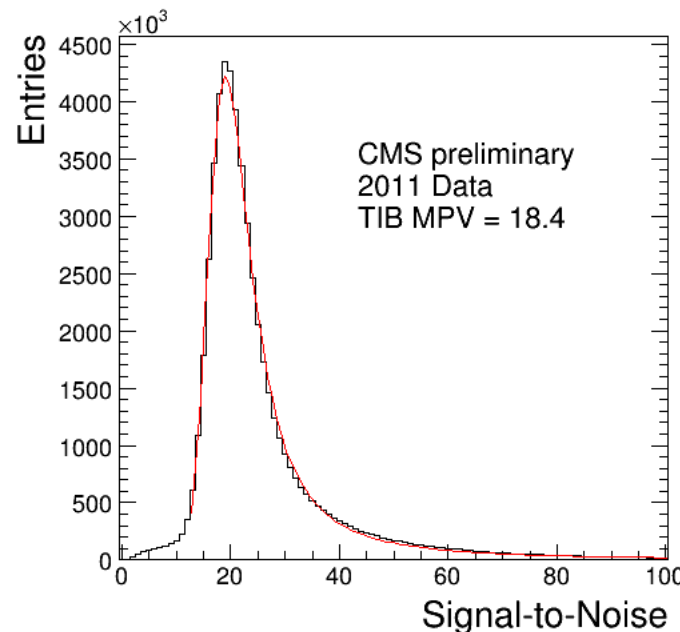
Figure 5.11: Block diagram of the strip readout architecture. Reprinted from Fig. 3.20 of ref. [45].

surements are shown in Figure 5.12. The entire pixel + strip tracker has been used successfully in the reconstruction of primary and secondary vertices, electrons, muons, tau decays, and charm and bottom hadron decays. In addition, the superior performance of the tracker over the hadronic calorimeter for low energy charged hadrons has been exploited in the the particle flow jet and \cancel{E}_T reconstruction technique (see Sec. 6.1.3). The CMS silicon strips, as well as the pixels, are well aligned and operating at close to design performance.

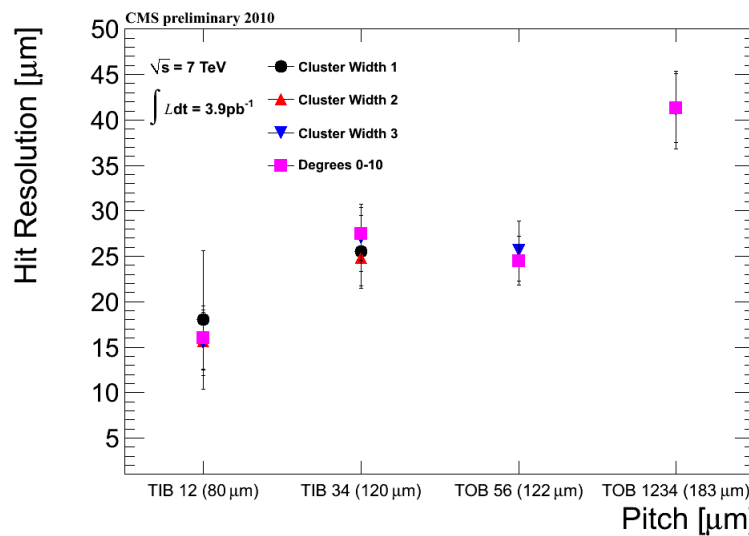
5.1.2 Electromagnetic Calorimeter

The electromagnetic calorimeter (ECAL) is composed of 68,524 lead tungstate (PbWO_4) crystals, divided into one barrel (EB) layer and two endcap (EE) disks. In EB, there are 1700 crystals per *supermodule* (SM), arranged in a 20×85 grid in $\phi \times \eta$. Two SMs are laid out end-to-end to form one row at fixed ϕ , with a total of 18 rows needed to cover the entire 2π extent in ϕ . The SMs may be operated independently. In EE, the independent unit is a wedge-shaped sector, with nine sectors covering each endcap side. The 7,324 EE crystals are divided approximately evenly between the 18 EE sectors. A two-layer preshower detector is placed in front of the EE disks, each layer consisting of a lead absorber followed by 1.9 mm pitch silicon strip detectors (the strips in the first layer are rotated 90° with respect to the second layer). The ECAL layout is shown in Figure 5.13.

The electromagnetic energy resolution can be parametrized as $(\sigma/E)^2 = (S/\sqrt{E})^2 + (N/E)^2 + (C)^2$, where S characterizes the size of photostatistical fluctuations, N characterizes the contribution from electronics noise, and C is a constant accounting for imperfect intercalibration between crystals, non-uniformity of crystal performance, and incomplete shower containment within one crystal. The design goal of the ECAL is to achieve $C = 0.5\%$. Therefore, fast, dense, and relatively radiation hard PbWO_4 was chosen as the crystal material. When a photon or electron strikes the crystal, it



(a) TIB signal:noise [52].



(b) TIB and TOB hit resolution as a function of strip pitch [53].

Figure 5.12: Strip detector performance highlights.

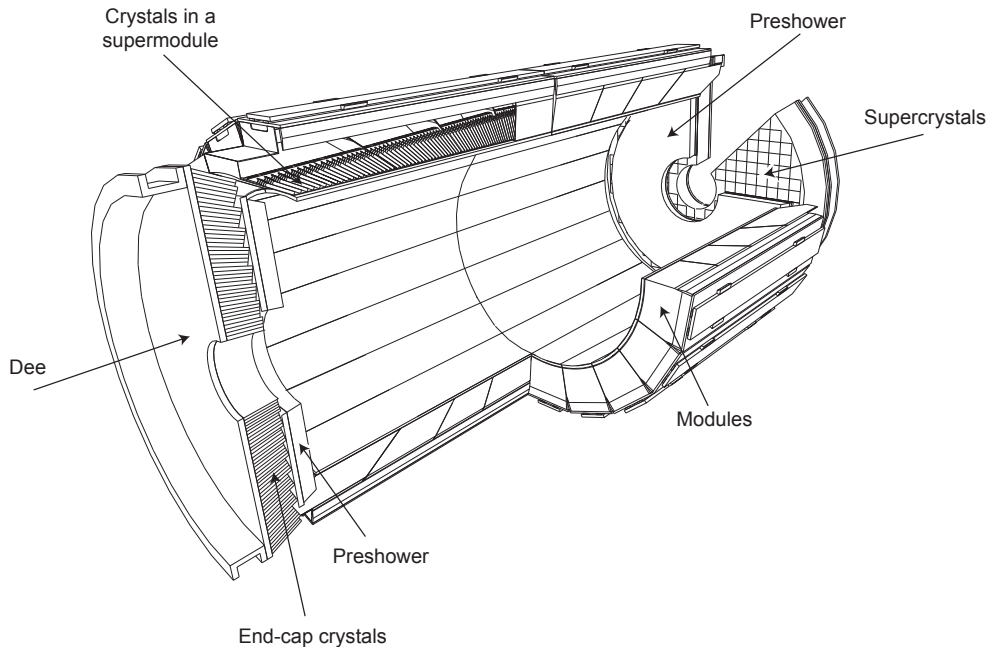


Figure 5.13: Layout of the ECAL detector. Reprinted from Fig. 4.5 of ref. [45].

904 initiates an electromagnetic (EM) shower. Due to the density, short radiation length,
 905 and small Molière radius of PbWO_4 , nearly the entirety of an EM shower can be
 906 contained in a single 23-cm long crystal with front face dimensions $2.2 \text{ cm} \times 2.2 \text{ cm}$.
 907 The crystals scintillate in the blue-green part of the spectrum, emitting $\sim 80\%$ of the
 908 scintillation light within 25 ns. Light is transmitted along the length of the crystals
 909 and collected at the rear with avalanche photodiodes (semiconductor diodes) in EB or
 910 vacuum phototriodes (conventional photomultipliers) in EE. Since the light output is
 911 low and varies with temperature, the crystals must be kept precisely at 18°C . The EB
 912 and EE crystals, which are slightly tapered to match the lateral shower development,
 913 are shown in Figure 5.14.

914 For each trigger, 10 samples, each separated by 25 ns, are read out. The 10-sample
 915 pulse is amplified and shaped by a multi-gain preamplifier (MGPA) residing on a very
 916 front end (VFE) card serving five crystals. The MGPA can switch between gains 1,
 917 6, and 12 to avoid saturation of the electronics, and affords a dynamic range up to

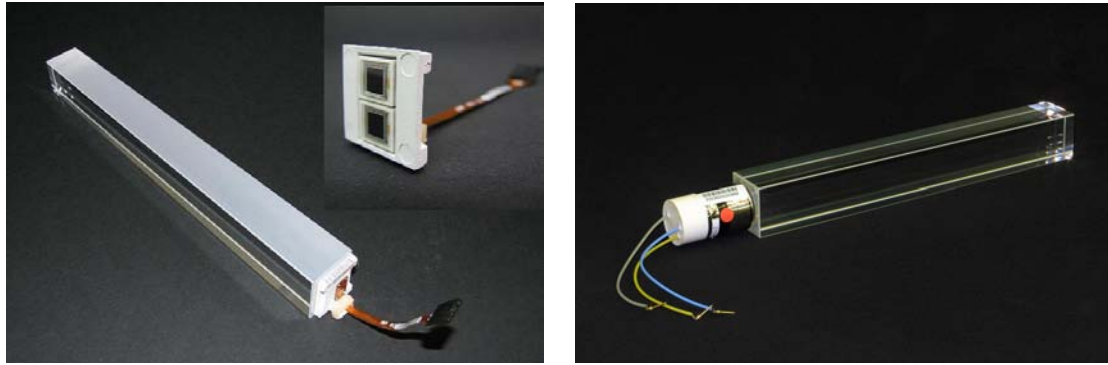


Figure 5.14: Left: EB crystal with attached APD. Right: EE crystal with attached VPT. Reprinted from Fig. 4.2 of ref. [45].

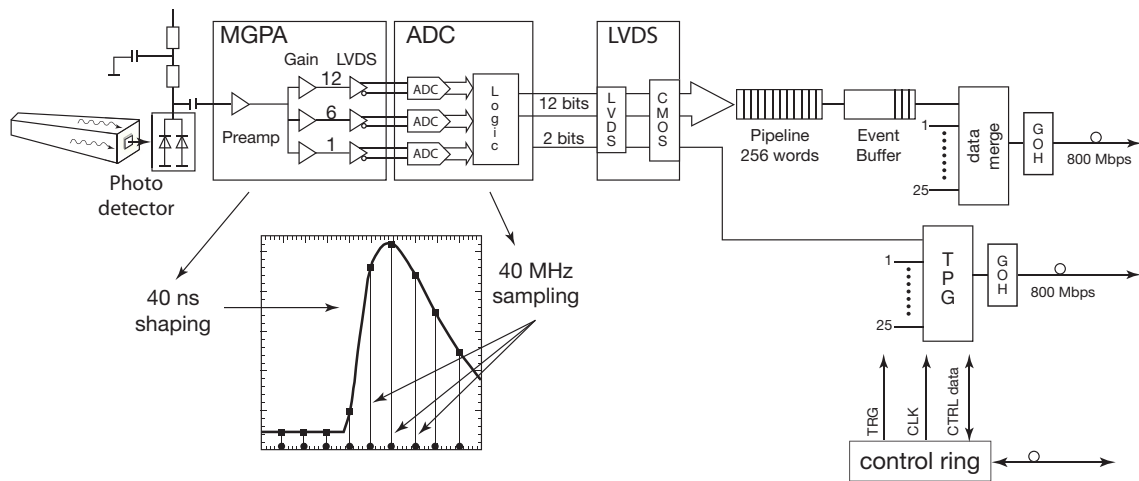


Figure 5.15: Flow chart of the crystal readout, showing the 10-sample pulse shape. Reprinted from Fig. 4.9 of ref. [45].

918 3 TeV. The samples are digitized on the VFE card, then sent to the front end (FE)
 919 card serving five VFEs. Digitized samples are buffered in the FE card until receipt
 920 of a trigger, when they are sent over an optical link to the data concentrator card
 921 (DCC) that interfaces to the global DAQ. The DCC interfaces to the *selective readout*
 922 processor, which decides whether a crystal should be read out with or without zero
 923 suppression based on its proximity to a high-energy hit. The clock is transmitted to
 924 the FE cards from the Clock and Control System (CCS) boards. A flow chart of the
 925 crystal readout is given in Figure 5.15.

At each bunch crossing, the trigger concentrator cards (TCC) of the ECAL compute *trigger primitives* from 5×5 non-overlapping transverse energy sums (in the endcaps the geometry is not always 5×5). This information, along with a special bit in EB only characterizing the transverse shower profile that is used for rejection of anomalous APD hits (see Sec. 6.1.1), is transmitted from the TCCs to the synchronization and link boards (SLBs), and then on to the global trigger system. The trigger decision is communicated to the DCCs, which request the buffered data from the front ends if the decision is affirmative.

Despite the radiation hardness of lead tungstate relative to other types of crystals, it still suffers from transparency loss due to radiation-induced lattice damage, as shown in Figure 5.16. In addition, any unforeseen change in the gains of the MGPAs and VPTs, or in the pedestal levels, will degrade the energy resolution. For this reason, a continuously running calibration system is installed with the ECAL. The system makes use of the LHC abort gaps to read out the pedestal levels, test pulses fired into the MGPAs, and laser (EB and EE) or LED (EE only) pulses fired into the crystals at regular intervals. Laser and LED events are used to compute corrections to the crystal gains for transparency loss, while the other types of calibration events serve to monitor changes in the electronics performance due to magnetic field or high voltage cycling. The mean time between transparency measurements is ~ 40 minutes. Figure 5.17 shows the architecture of the laser monitoring system.

The current ECAL energy resolution is somewhat worse than the design goal of 0.5%. An incomplete understanding of (a) the transparency loss and (b) the photon conversion and electron bremsstrahlung processes in the $\sim 1X_0$ of tracker material in front of the ECAL are the main limiting factors in improving the resolution. However, as more data accumulate, more refined models of transparency loss and EM interactions in the tracker can be built, leading to better resolution. Energy resolution vs. $|\eta|$ can be seen in Figure 5.18.

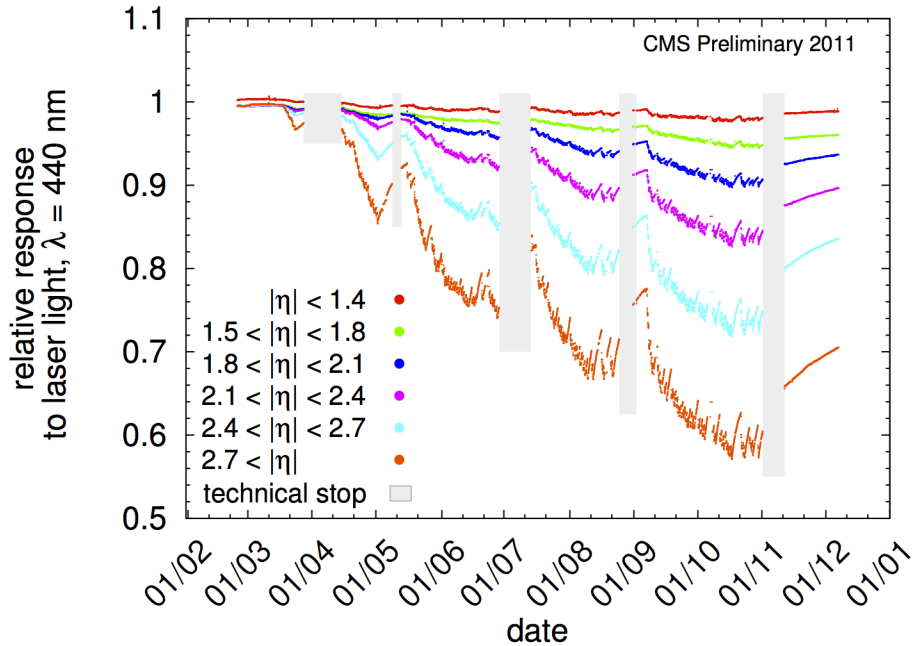


Figure 5.16: Relative response of the crystals to blue laser pulses from February 1, 2011 to January 1, 2012 [54]. Technical stops, during which the LHC is turned off for maintenance and development, are shown in gray. These periods of inactivity correspond to growth in the crystal response, as radiation damage recovery occurs.

953 The 10-sample readout coupled with the fast scintillation time of lead tungstate
 954 allows for a very precise reconstruction of the time of ECAL hits. ECAL timing is used
 955 for searches for long-lived particles that decay to photons or jets, such as long-lived
 956 neutralinos in GMSB [?]. Figure 5.19 shows the timing resolution in EE.

957 5.1.3 Hadronic Calorimeter

958 The CMS hadronic calorimeter (HCAL) has four parts: HCAL barrel (HB), HCAL
 959 endcap (HE), and HCAL outer (HO), which all utilize the same brass absorber /
 960 plastic scintillator sandwich technology; and HCAL forward (HF), which is a Čerenkov
 961 detector made of quartz fibers. A quarter longitudinal cross-sectional view of HCAL
 962 is shown in Figure 5.20. Like EB, HB is formed of 36 ϕ -wedges (18 cover 2π in positive
 963 η , 18 cover 2π in negative η). Each wedge is divided into 16 along η and four along
 964 ϕ , for a total of 64 readout towers per wedge (compare 1700 individually read out

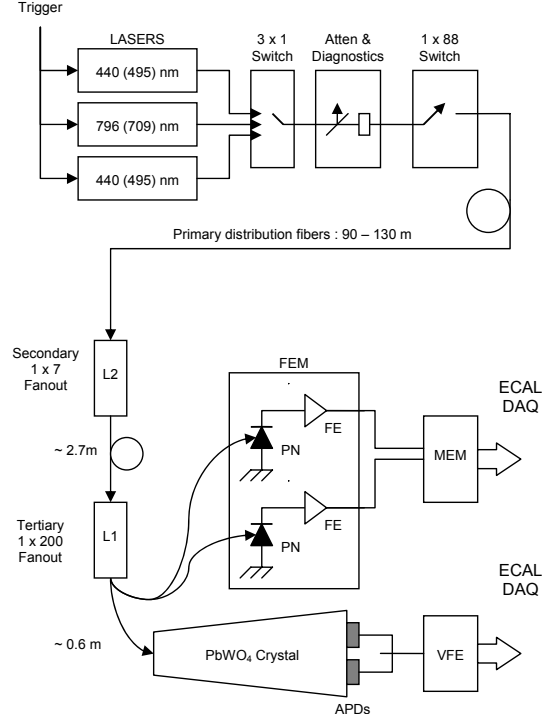


Figure 5.17: Architecture of the laser monitoring system. Reprinted from Fig. 4.16 of ref. [45].

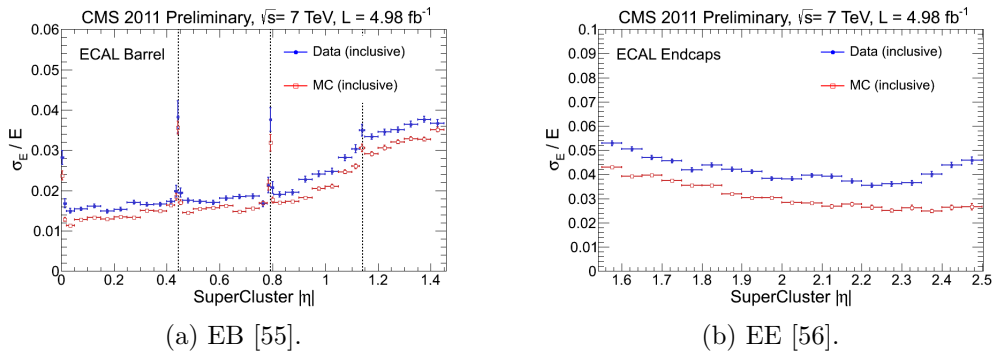


Figure 5.18: Energy resolution vs. $|\eta|$ for Z decay electrons for data (filled blue circles) and MC (empty red squares). The dotted lines show the locations of module gaps (three per SM).

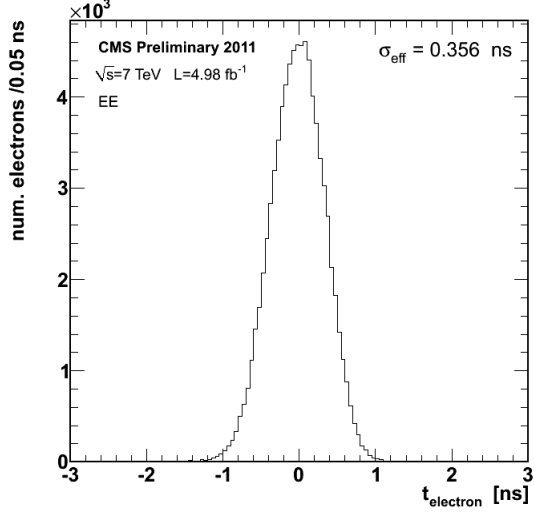


Figure 5.19: Distribution of reconstructed times of Z decay electrons in EE [57].

965 crystals per EB wedge). HE is divided into 36 ϕ -wedges containing 38 readout towers
 966 each. HO consists of five rings around HB and HE distributed symmetrically along z .
 967 There are 72 ϕ -slices per ring, with each ϕ -slice further divided into 5, 6, or 8 along
 968 z depending on ring. The HF fibers are distributed within the steel absorber. HF is
 969 divided into 18 ϕ -wedges per endcap side, each containing 24 readout towers. All HB
 970 towers have a single readout channel except for the two in each wedge at highest $|\eta|$,
 971 which are segmented into two longitudinal layers for readout. In HE, all towers have
 972 two longitudinal readout layers, except for the three rings of towers closest to the
 973 beam line, which have three. There are also two longitudinal depths of HF fibers.

974 HB, HE, and HO are all sampling calorimeters consisting of alternating layers of
 975 brass absorber and plastic scintillator. The absorber initiates the hadronic shower,
 976 and as shower particles travel through the scintillator the scintillation light is read
 977 out by wavelength-shifting (WLS) fibers connected to the scintillator tiles.² The full
 978 development of the shower is sampled by the layers of instrumented scintillator. The
 979 scintillator tiles are staggered so that there are no cracks in coverage along the direc-

²By contrast, in the ECAL, the crystal material acts as both absorber and scintillator, greatly reducing the contribution to energy resolution from sampling fluctuations.

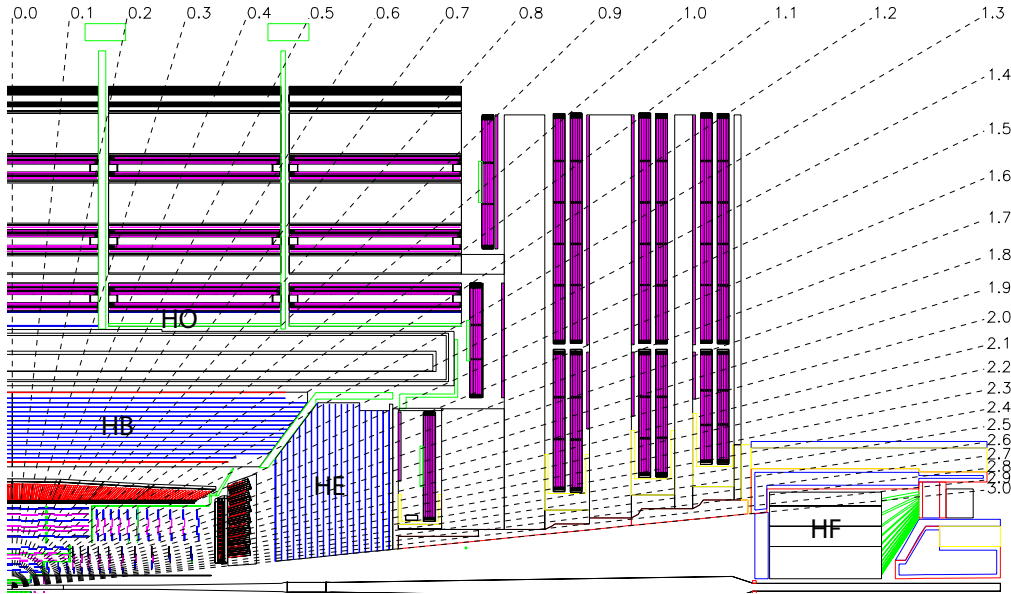


Figure 5.20: Quarter longitudinal cross-sectional view of HCAL (and muon stations in purple). Reprinted from Fig. 5.1 of ref. [45].

tion projected back to the beam spot. Light output from all tiles in a single readout tower is collected via the WLS fibers and merged into a single signal that is amplified by a hybrid photodiode (HPD). A diagram of the optical readout of HB (similar for HE and HO) is shown in Figure 5.21.

Due to the extremely harsh radiation environment near the beam line, HF is constructed of a 1.2-m thick, 1.7-m long ring of steel absorber with radiation hard quartz fibers distributed within the steel and running parallel to the beam line. Hadronic showers develop in the steel and are sampled in the quartz fibers when charged shower particles hit the the fibers and emit Čerenkov light. The light is transmitted by total internal reflection down the fibers to a photomultiplier tube (PMT), where the signals from all fibers in an HF tower are merged into one. Since only relativistic particles emit Čerenkov light in these fibers, it is mostly the EM component of the hadronic shower, consisting of neutral pions decaying to photons that interact electromagnetically with the absorber, that is sampled [58]. The charged hadrons produced in hadronic showers are typically too slow to generate Čerenkov light. Figure 5.22

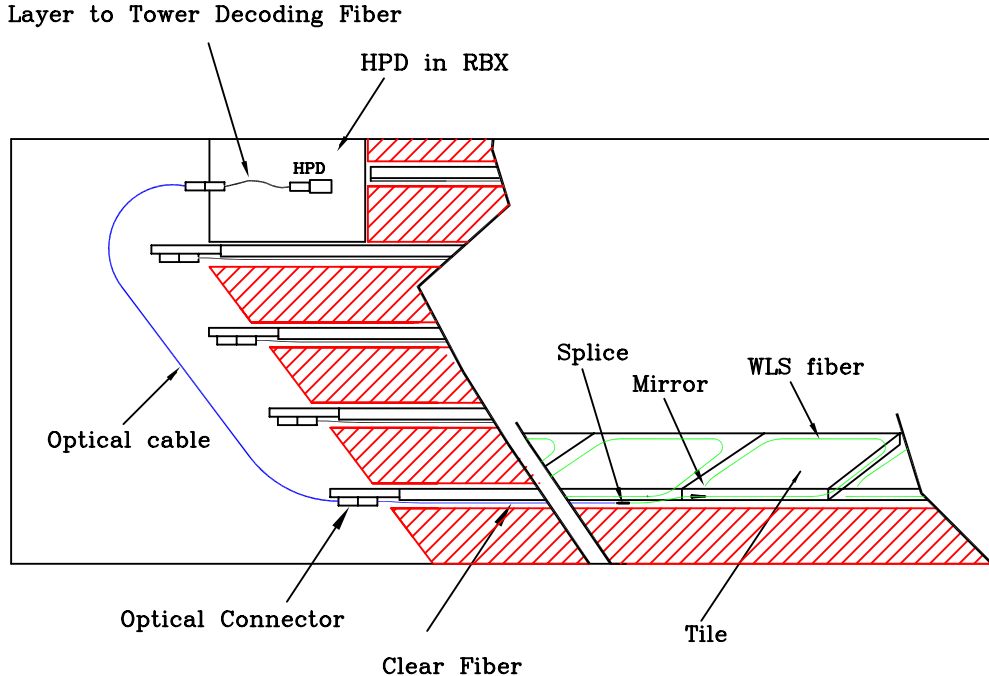


Figure 5.21: Diagram of the optical readout of HB. Reprinted from Fig. 5.7 of ref. [45].

995 shows a cross-sectional view of one side of HF.

996 Electrical signals from either HPDs (HB/HE/HO) or PMTs (HF) are digitized on
 997 the front ends by means of a fast charge-integrating ADC. The digitized signals are
 998 sent off-detector to the HCAL Trigger/Read-Out (HTR) boards, where they await a
 999 trigger decision. If the trigger is accepted, the signals are sent on to the HCAL data
 1000 concentrator cards (DCCs), which interface to the global DAQ system. HCAL trigger
 1001 primitives, consisting of transverse energy sums over an entire tower, are calculated
 1002 in the HTR boards and sent to the global trigger system.

1003 Selected HCAL performance results can be seen in Figure 5.23.

1004 5.1.4 Muon System

1005 Beginning at a radius of ~ 10 interaction lengths from the beam line, where all parti-
 1006 cles except muons should have been stopped by the HCAL, are the muon chambers,
 1007 interspersed with the iron return yoke of the CMS magnetic field. Three technologies

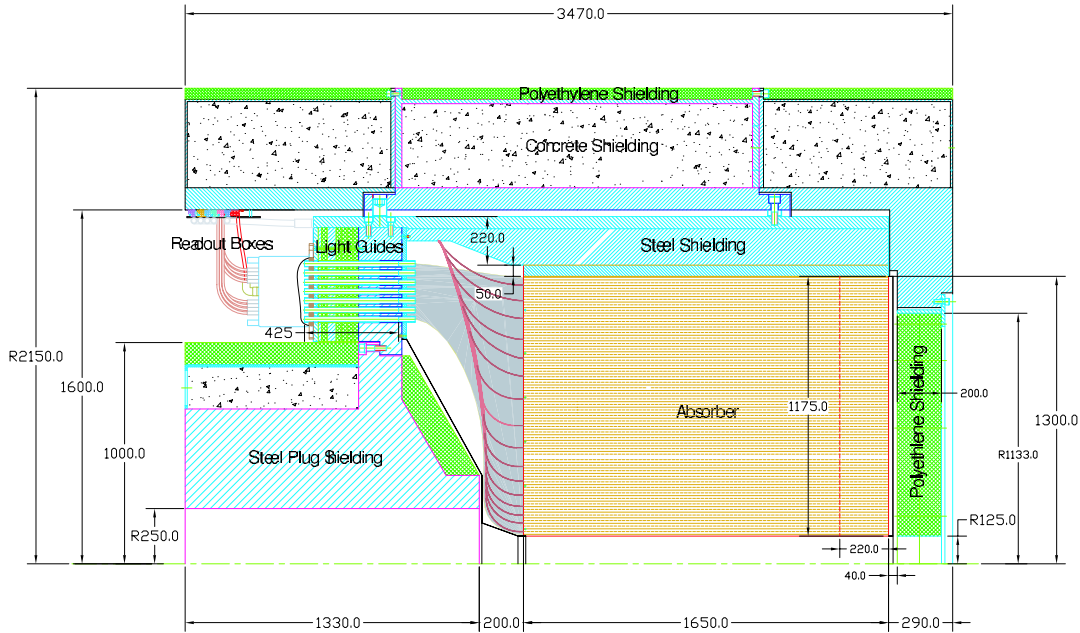
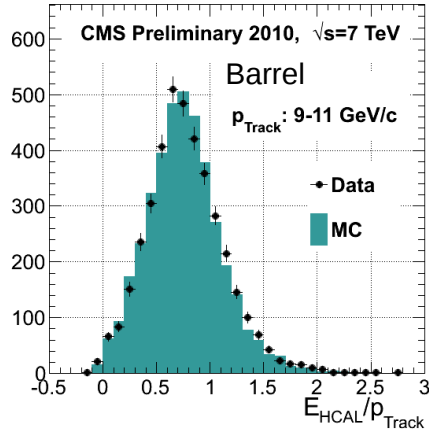


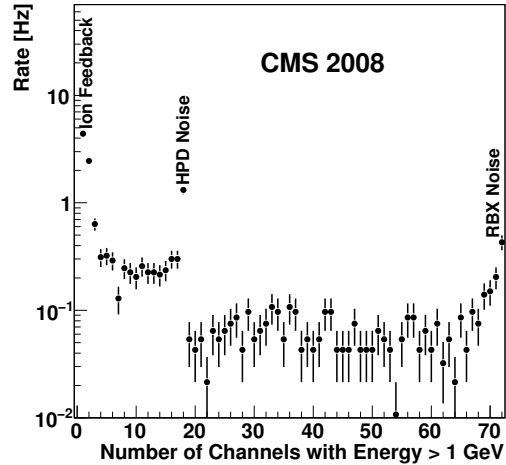
Figure 5.22: Cross-sectional view of one side of HF. The z -axis is horizontal. Reprinted from Fig. 5.28 of ref. [45].

1008 are employed: drift tubes in the barrel section (MB), cathode strip chambers (CSCs)
 1009 in the endcap section (ME), and resistive plate chambers (RPCs) in both sections to
 1010 provide an independent trigger with superior time resolution. There are four barrel
 1011 layers of stations extending out to $|\eta| = 1.2$. Each endcap consists of five disks of
 1012 stations as shown in Figure 5.24b, covering $1.4 < |\eta| < 2.4$. RPCs populate the barrel
 1013 and endcap muon systems alongside the DT chambers and CSCs. Since they have
 1014 time resolution much better than a few ns, they are used to assign the bunch crossing
 1015 of muon tracks and provide a p_T trigger with sharp turn-on.

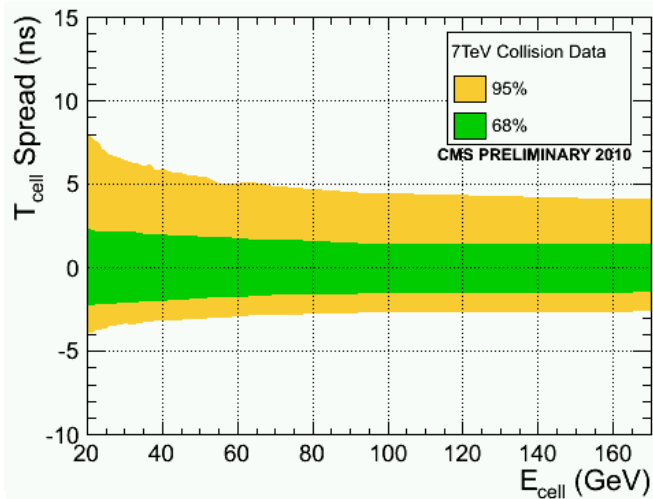
1016 Each DT chamber consists of two $r \cdot \phi$ superlayers (SLs) and optionally one z
 1017 SL (in all chambers except those in the fourth layer). The SLs contain four rows of
 1018 drift tubes, with the rows staggered such that there are no gaps in the coverage. The
 1019 $r \cdot \phi$ SLs have the tube axis parallel to the beam line, while the z SL is perpendicular
 1020 to the beam line. The tubes are ~ 2.4 m in length and $13 \text{ mm} \times 42 \text{ mm}$ in cross
 1021 section. Each chamber therefore records eight $r \cdot \phi$ tracking points and optionally four



(a) Data/MC comparison of HB response to charged tracks of 9-11 GeV/c momentum [59].

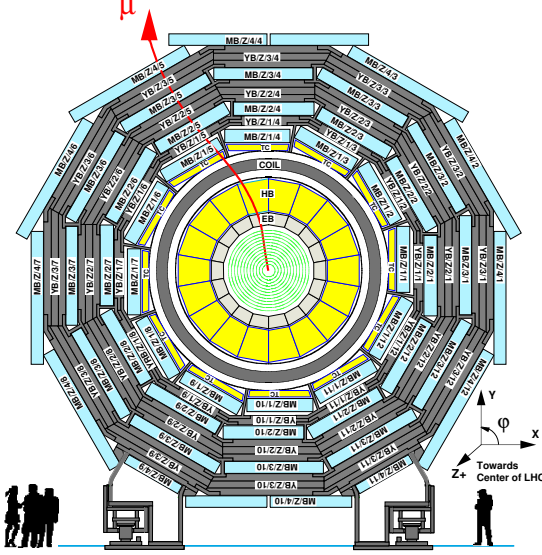


(b) Distribution of tower multiplicity, clearly showing three peaks in rate corresponding to noise sources (see Sec. 6.3) [100].

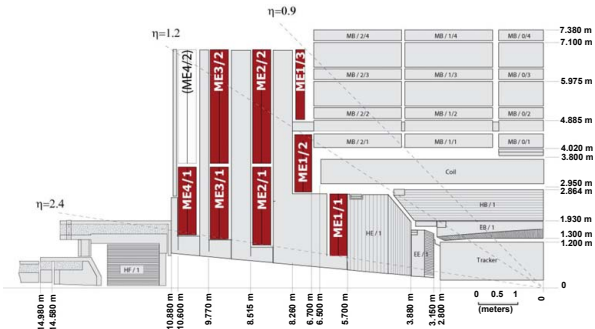


(c) Timing resolution vs. tower energy [59].

Figure 5.23: Selected HCAL performance results.



(a) One of the five wheels of MB, showing the four layers of muon stations. The five wheels are spaced symmetrically in z about $z = 0$. As a muon traverses the muon detectors, its curvature in the transverse plane changes direction and magnitude due to the magnetic field in the return yoke, which is of opposite sign and reduced strength relative to the field within the solenoid volume. Reprinted from Fig. 7.3 of ref. [45].



(b) Quarter longitudinal cross section of CMS highlighting the location of the ME disks. Reprinted from Fig. 7.47 of ref. [45].

Figure 5.24: View of the MB and ME layout in CMS.

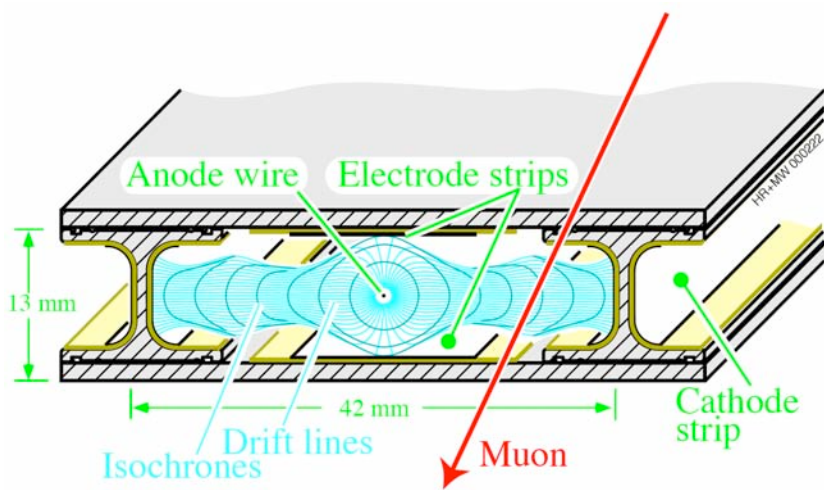


Figure 5.25: Electric field lines within a drift tube as well as the contours of equal drift time. Reprinted from Fig. 7.5 of ref. [45].

1022 z tracking points. The tubes are filled with an 85%Ar + 15% CO₂ gas mixture. An
 1023 anode wire at 3600 V runs the length of the tube, while the walls are covered with
 1024 electrodes held at 1800 V or -1200 V depending on wall. When a muon passes through
 1025 the tube, it ionizes the gas atoms. The liberated electrons drift along the electric field
 1026 lines created by the electrodes to the anode, which is read out. Figure 5.25 shows
 1027 the electric field lines within a drift tube as well as the contours of equal drift time.
 1028 The maximum drift time is 380 ns.

1029 CSCs consist of alternating layers of cathode strips (four planes oriented along r)
 1030 and anode wires (three planes oriented along ϕ). A 40%Ar + 50%CO₂ + 10%CF₄ gas
 1031 mixture fills the space between two successive planes, forming six gas gaps. When a
 1032 muon ionizes the gas atoms, the positive ions drift toward the anode and are read
 1033 out to provide a measurement of r , just as in the DTs. However, an image charge is
 1034 induced on the cathode strips, which is also read out to provide a measurement of ϕ .
 1035 The wires are spaced 3.2 mm apart. The cathode strips have pitch varying from 8.4
 1036 mm at the end closest to the beam line to 16 mm at the other end, and are spaced
 1037 0.5 mm apart. A trapezoidal CSC is shown in Figure 5.26.

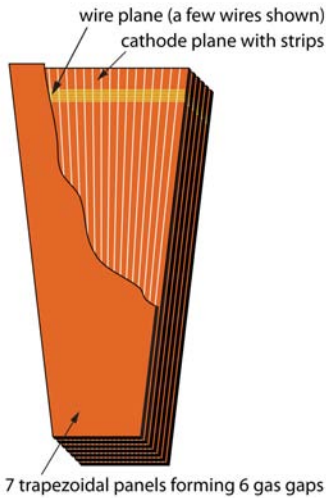


Figure 5.26: CSC wedge, showing the cathode and wire planes. Reprinted from Fig. 7.49 of ref. [45].

1038 Track stubs from the muon system are combined with tracks from the tracking
 1039 system to form more precise muon tracks than either system could form alone, as
 1040 shown in Figure 5.27. This leads to extremely good di-muon invariant mass resolution
 1041 (Figure 5.28) over a large p_T range.

1042 **5.2 Triggering, Data Acquisition, and Data Trans-** 1043 **fer**

1044 **5.2.1 Level 1 and High Level Trigger Systems**

1045 The Level-1 (L1) trigger system, which encompasses dedicated hardware processors
 1046 to construct trigger objects (typically high p_T jets, electrons, photons, taus, and
 1047 muons) out of the calorimeter and muon hits, distributes a L1 accept or reject to all
 1048 subdetectors at the LHC bunch crossing frequency of 40 MHz. Further data filtering
 1049 is performed by the High Level Trigger (HLT) system, a farm of ~ 1000 commercially
 1050 available processors running a slimmed down version of the CMS event reconstruction

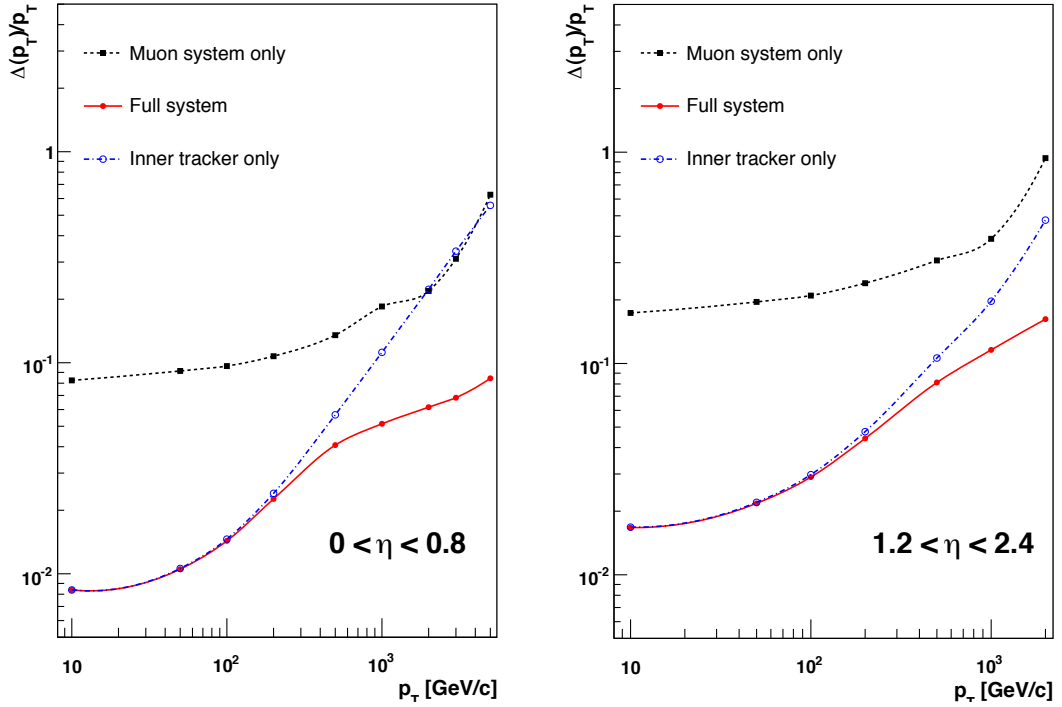


Figure 5.27: Muon p_T resolution as a function of muon p_T for tracker information only (blue), muon information only (black), and both tracker and muon information combined (red). Reprinted from Fig. 1.2 of ref. [45].

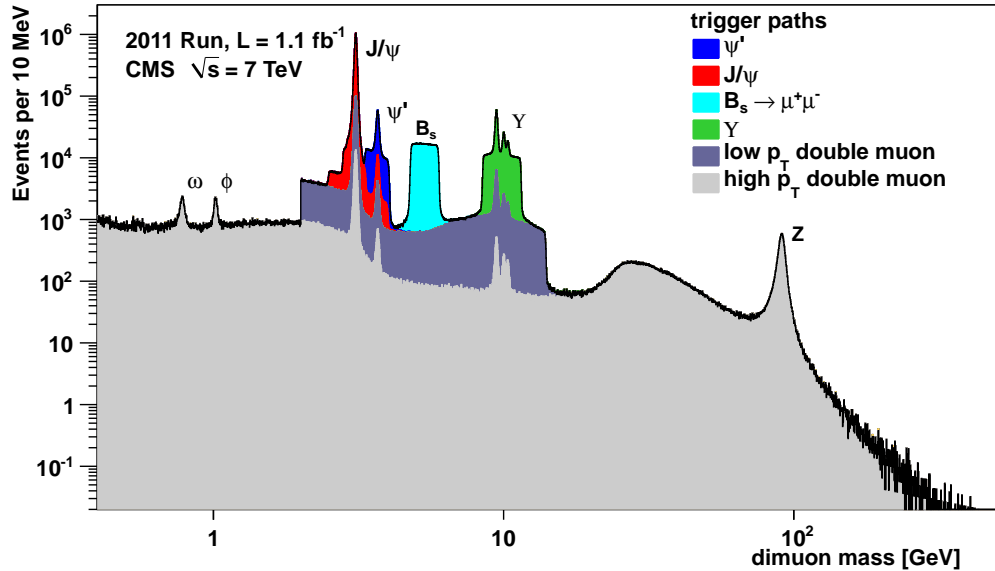


Figure 5.28: Di-muon invariant mass spectrum broken down by trigger path [60]. The light(dark) gray regions show the contribution from high- p_T (low- p_T) di-muon triggers. Note that no $B_s \rightarrow \mu^+\mu^-$ decays have been observed [61]; the light blue region just shows the amount of triggers dedicated to the $B_s \rightarrow \mu^+\mu^-$ search.

1051 software CMSSW. The data rate received by the HLT is ~ 100 kHz; the output rate of
 1052 events permanently written to disk is ~ 100 Hz. An L1 trigger *latency* (time between
 1053 the collision and the distribution of the L1 decision to the subdetectors) of $3.2\ \mu\text{s}$ is
 1054 achieved via the use of fast electronics and sufficiently deep buffers to pipeline trigger
 1055 primitives waiting to be analyzed. This latency corresponds to the length of the LHC
 1056 abort gap, so in principle CMS may be operated with zero *dead time* (during which
 1057 LHC bunches are missed because the L1 system is blocked while processing other
 1058 triggers).

1059 At the bottom, the L1 trigger consists of trigger primitive generators (TPGs) in
 1060 the calorimeter and muon systems that send E_T sums or muon track stubs to the
 1061 regional calorimeter trigger (RCT) or muon track finders, respectively. The EB TPG
 1062 also sends a *fine grain veto bit* [63], which encodes information about the EM shower
 1063 pattern in the 5×5 array of crystals, and is used to reject anomalous signals (see
 1064 Sec. 6.1.1). The RCT, DT track finder (DTTF), and CSC track finder (CSCTF) sort
 1065 and rank the regional trigger primitives based on p_T and quality. The ranked RCT
 1066 candidates and muon track stubs are sent to the global calorimeter trigger (GMT)
 1067 and global muon trigger (GMT), respectively, where high-level objects like isolated
 1068 and non-isolated muons and EM candidates, jets, taus, and \cancel{E}_T are constructed from
 1069 all the regional inputs and ranked. Calorimeter isolation sums for muons are also
 1070 sent from the RCT to the GMT. The highest ranked global objects are sent to the
 1071 global trigger (GT), which sits at the top of the L1 trigger. The GT issues the final
 1072 L1 accept or reject to all subdetectors based on a comparison of the GMT and GCT
 1073 candidates with the requirements of its programmed trigger menu. A block diagram
 1074 of the L1 trigger is shown in Figure 5.29.

1075 A region in the RCT consists of a matrix of 4×4 trigger towers. A trigger tower
 1076 in EB/HB is one HCAL tower + the 5×5 matrix of ECAL crystals in front of it;
 1077 in EE/HE the idea is similar but the counting of crystals and HE towers is slightly

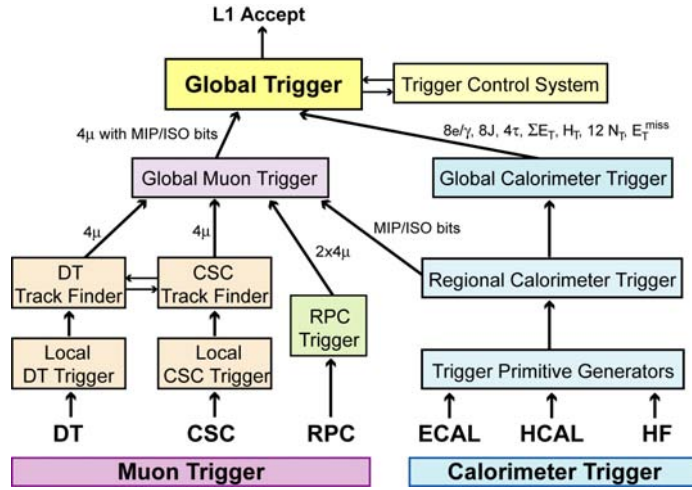


Figure 5.29: Block diagram of the L1 trigger. Reprinted from Fig. 8.1 of ref. [45].

more complicated. An EM RCT candidate is built around a high E_T seed tower.
 The E_T of the candidate is the sum of the tower E_T and the E_T of its highest- E_T
 broad side neighbor (see Figure 5.30 for a definition of the broad side neighbors). Two
 isolation criteria are defined based on (a) the ratio of the EM energy to the HCAL
 energy in the tower and (b) the shower shape. For a non-isolated EM candidate, the
 highest- E_T broad side neighboring tower must pass these two isolation criteria; for
 an isolated EM candidate, all eight neighboring towers must pass the criteria, and there
 must also be at least one quiet corner with the E_T of all five towers in the corner
 below some threshold (see Fig. 5.30). The process is repeated until four isolated and
 four non-isolated EM candidates are found, starting with the highest- E_T tower in the
 region and moving down in tower E_T . An RCT region is flagged as consistent with
 tau decay only if the pattern of tower transverse energy sums defines at most a 2×2
 matrix of energetic towers within the 4×4 RCT region.

From the tower transverse energy sums, eight EM candidates, and tau flag received
 from each RCT, the GCT computes the total E_T in the calorimeter (and the total E_T
 above some programmable threshold, called H_T), and the \not{E}_T . It also classifies the
 towers into jets and determines the globally highest ranked isolated and non-isolated

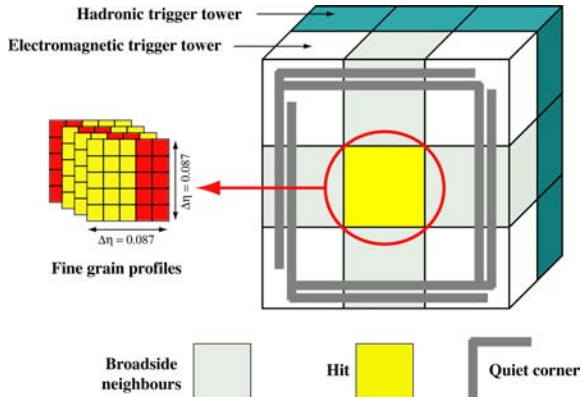


Figure 5.30: Geometry of an EM RCT candidate. Reprinted from Fig. 8.2 of ref. [45].

1095 EM candidates. The jet finding uses a clustering algorithm based on the energy of a
 1096 sub-cluster with respect to its neighbors [62]. Jets are classified as tau decays if all
 1097 of the RCT regions participating in the jet clustering had energy patterns consistent
 1098 with tau decay. Counts of jets above 12 different programmable E_T thresholds are
 1099 calculated. The jet counts, energy sums, E_T , and highest ranked EM candidates
 1100 are sent to the GT, where the final L1 decision is taken and transmitted to the sub-
 1101 detectors. The GT can execute a maximum of 128 trigger algorithms in parallel. If
 1102 any one of these algorithms yields an accept, the event is accepted, and all trigger
 1103 information is sent on to the HLT for further filtering. The double-photon HLT paths
 1104 used in this analysis (see Sec. 6.2) require isolated L1 seeds (i.e. EM candidates built
 1105 by the RCT) with $E_T > 12$ or 20 GeV, depending on path.

1106 No muon triggers are used in the two-photon analysis. A description of the muon
 1107 trigger system can be found in ref.[45].

1108 5.2.2 Data Acquisition System

1109 The CMS data acquisition (DAQ) system takes event fragments (calorimeter hits,
 1110 track hits, etc.) from each of the 626 subdetector front end drivers (FEDs), assembles
 1111 them into a data structure representing the full event, and sends the event on to

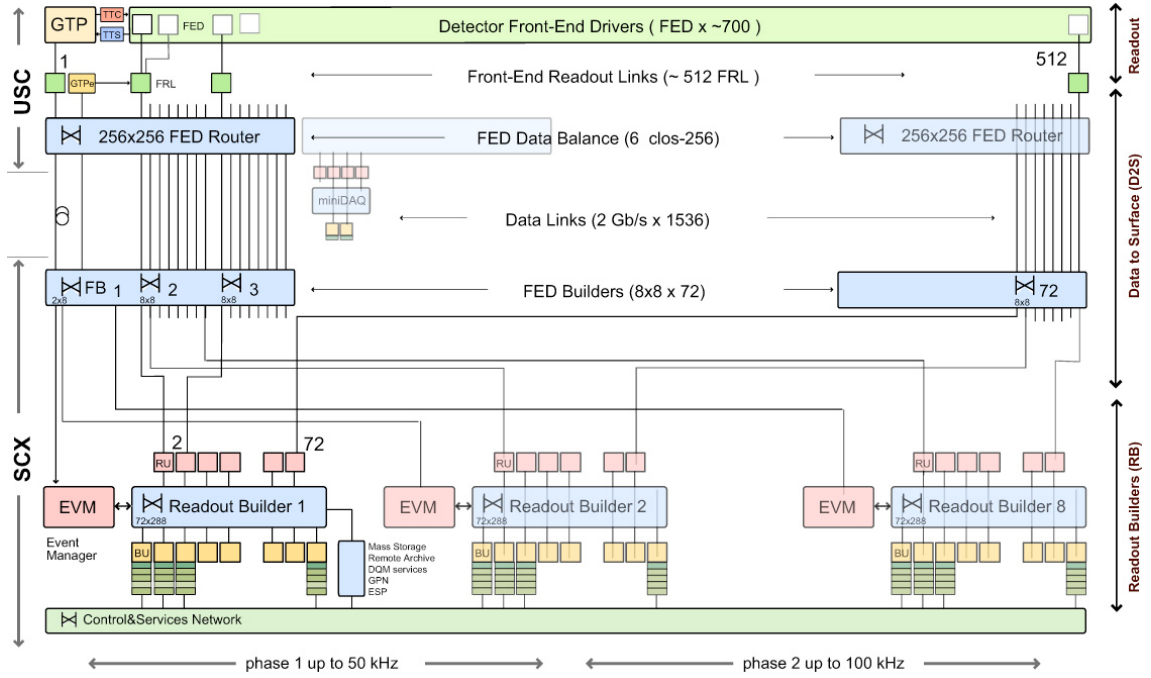


Figure 5.31: Diagram of the DAQ system. The identical event builder systems, shown as inputs and outputs to the boxes labeled “Readout Builder 1”, “Readout Builder 2”, etc., represent the eight slices. Within one slice, data can flow from the detector front ends to the readout systems to the builder network (which assembles the event fragments) to the filter systems (HLT) independently of the other slices. Reprinted from Fig. 9.8 of ref. [45].

the HLT for further filtering. The DAQ must operate at an input rate of ~ 100 GB/s, corresponding to an input rate from the L1 trigger of ~ 100 kHz. To facilitate expansion of the system as the need arises, the DAQ is composed of eight nearly independent slices. Each slice functions as a smaller version of the whole DAQ that can handle an input event rate up to ~ 12.5 kHz. A diagram of the DAQ system, showing schematically the eight slices, is given in Figure 5.31.

Data from the front ends is collected by the FEDs and pushed to the front end readout links (FRLs), which may take inputs from up to two FEDs simultaneously. The FRLs check for transmission errors, generate event fragments with size ~ 2 kB, buffer the fragments in 64 kB memories, and finally send them to the FED builders. The FEDs, FRLs, and FED builders are located in the underground control room.

1123 The 72 FED builders each construct one ~ 16 kB *super-fragment* from the input
 1124 event fragments, then send the super-fragment on to a readout unit (RU) located in
 1125 the surface control room ~ 80 m away. Super-fragments belonging to the same event
 1126 are sent to RUs in the same DAQ slice. There are 72 RUs per readout builder, one
 1127 for each super-fragment of an event, with each DAQ slice built around one readout
 1128 builder (see Fig. 5.31). Each readout builder hosts a number of builder units (BUs)
 1129 that perform the final integration of super-fragments into complete events.

1130 Resource brokers (RBs) in the HLT filter farm request complete events from the
 1131 BUs and distribute those events to the filter units (FUs) for HLT selection. If an
 1132 event passes any one of the HLT paths in the predefined menu, it is sent back to
 1133 the RB for transfer to the storage manager (SM). The SM nodes transfer accepted
 1134 events to the CERN Tier-0 prompt reconstruction facility for unpacking of the raw
 1135 data into ROOT [64] files that can be accessed by physicists wishing analyze the data.
 1136 The lag time between recording of an event in the DAQ and availability of the fully
 1137 reconstructed event for analysis is typically 48 hours.

1138 If the buffers of the upstream DAQ elements (the filter farm, readout builders,
 1139 FED builders, or FRLs) are full, those elements will not request new events from
 1140 downstream. This can lead to a buildup of events in the downstream element buffers,
 1141 *back-pressuring* all the way down to the FEDs themselves. The CMS trigger throttling
 1142 system (TTS) consists of dedicated lines between the FEDs and the GT for the
 1143 purpose of sending predefined signals to the GT about the state of the FED buffers.
 1144 If the buffer of a particular FED is getting full, it can alert the GT to reduce the
 1145 trigger rate so as to prevent FED buffer overflows and loss of time synchronization
 1146 between event fragments. The TTS latency is $\sim 1\mu\text{s}$. Causes of back-pressure (hence
 1147 dead time) include: problems with the FED electronics (in this case, the upstream
 1148 elements request events but the FEDs have trouble sending them), increases in the
 1149 L1 accept rate (perhaps due to a noisy detector channel) beyond what the upstream

1150 DAQ elements can handle, increases in the event size due to high pileup or a poor
 1151 quality beam that scrapes against the beam pipe, failures of the DAQ transmission
 1152 lines or DAQ hardware such that events are not requested from the FEDs fast enough,
 1153 or bottlenecks at the SM nodes or filter farm due to hardware failures or large event
 1154 sizes.

1155 All components of the DAQ, from the FEDs up to the SMs, are controlled by
 1156 cross-platform DAQ (XDAQ) [65] processes, or *executives*. The Simple Object Access
 1157 Protocol (SOAP) [66] protocol is used to transmit control and monitoring data be-
 1158 tween XDAQ-enabled devices and to the end user, who can view the running of a
 1159 XDAQ executive via a Web interface called HyperDAQ [67]. The Run Control and
 1160 Monitoring System (RCMS) handles the configuration and control of all XDAQ exec-
 1161 utives via a hierarchical structure. At the top of the hierarchy is the Level-0 *function*
 1162 *manager* (FM), controlling the Level-1 sub-detector FMs, which in turn control their
 1163 Level-2 system-specific XDAQ executives. The central DAQ and L1 trigger each have
 1164 their own Level-1 FM. A unit of data acquisition, called a *run*, may be configured,
 1165 started, and stopped by an end user interacting with the RCMS Web interface.

1166 5.2.3 Data Processing and Transfer to Computing Centers

1167 Data leaving the filter farm are grouped into datasets based on HLT path, i.e. there
 1168 are different datasets for events passing diphoton triggers, jet triggers, muon + elec-
 1169 tron triggers, etc. At the Tier-0 facility, the datasets go through three levels of
 1170 processing to create three *data tiers*. The first layer produces RAW data by unpack-
 1171 ing the detector byte streams sent from the DAQ and L1 trigger into data structures
 1172 holding the ADC counts recorded for each channel of the detector, digitized trigger
 1173 primitives, and the L1 decision. A single event has ~ 1.5 MB of RAW data. The next
 1174 layer of processing is the reconstruction, which forms channel energies in GeV, ap-
 1175 plies calibrations, and creates high-level objects like photons, electrons, muons, taus,

jets, E_T , and charged tracks. The RECO data tier occupies ~ 0.5 MB per event.
 Finally, analysis object data (AOD) is a subset of the RECO data, comprising the
 high-level objects but usually excluding the individual channel hit information if it is
 not associated to a physics object. This tier occupies ~ 0.1 MB per event. One copy
 of the RAW data is stored permanently at CERN and another copy is distributed
 amongst the Tier-1 facilities (see below) for permanent storage. Changes in the re-
 construction algorithms periodically require reprocessing of the RAW data to form a
 new RECO tier. In general, only the AOD tier is available to physicists wishing to
 perform analyses due to the smaller size and faster replication and transfer time of
 AOD with respect to RAW or RECO.

There are three tiers of computing and data storage sites within the Worldwide
 LHC Computing Grid (WLCG) [68]. The tier closest to CMS is Tier-0, which is
 located at CERN and performs archiving of the RAW data, prompt reconstruction
 of the data within ~ 48 hours of its being collected, and transferral of copies of the
 RECO datasets to Tier-1 facilities. There are a few Tier-1 centers worldwide, hosted
 by national computing facilities and laboratories. They store parts of the RAW dataset
 and copies of the RECO datasets, participate in subsequent reconstruction passes
 after the prompt reconstruction at Tier-0, and ship AOD datasets upon request to the
 Tier-2 centers. Analysts interact primarily with the Tier-2 centers, which store AOD
 datasets and run batch processing queues for running analysis jobs over the datasets.
 Different layers of WLCG software control data transfer between sites, data storage,
 and batch processing. A diagram of the WLCG tier system is given in Figure 5.32.

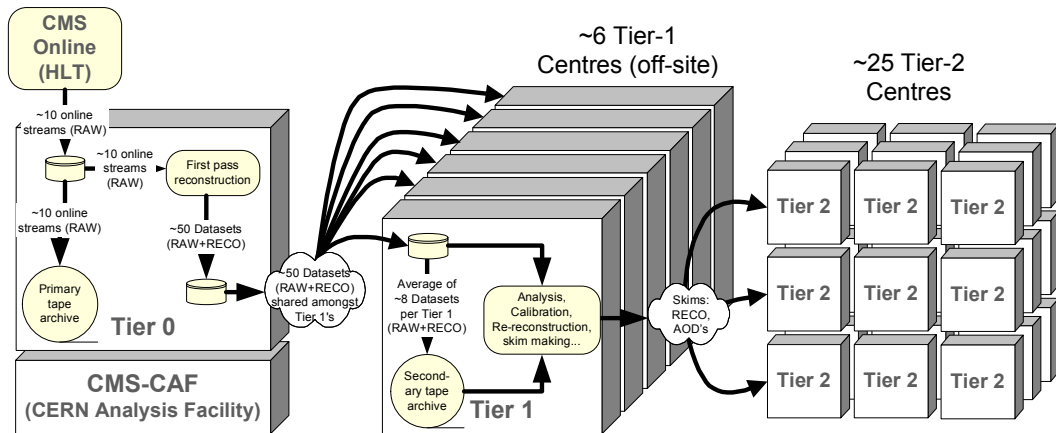


Figure 5.32: Diagram of the WLCG tier system showing data archival and reconstruction at each tier along with data transfer between tiers. Reprinted from Fig. 11.2 of ref. [45].

1198

Chapter 6

1199

Event Selection

1200 In keeping with the phenomenology described in Sec. 3.5, the candidate GGM events
1201 selected in this search consist of two high- E_T photons and a significant momentum
1202 imbalance transverse to the beam, indicating the production of an escaping gravitino.
1203 This momentum imbalance is usually referred to as *missing transverse energy* and is
1204 denoted by the symbols \cancel{E}_T or ME_T . The GGM signature is shown in Figure 6.1.

1205 However, in order to use real CMS data (as opposed to simulation) to derive
1206 predictions for the backgrounds to the search, *control samples* that are not expected
1207 to contain any GGM signal events and are distinct from the *candidate* two-photon
1208 sample must be collected from the LHC data. These samples consist of different
1209 numerical combinations of photons, electrons, and jets, and are explained in more
1210 detail in Chapter 7. Since this search is performed in the high- E_T tail of the \cancel{E}_T
1211 distribution, where adequate detector simulation is very difficult, it is advantageous
1212 to use *data-driven* background estimates, which capture the true detector response,
1213 over numbers derived from simulation.

1214 In the following sections, the reconstruction of photons, electrons, jets, and \cancel{E}_T
1215 is explained. Sec. 6.1 begins with an explanation of the high level reconstruction.
1216 It is followed by Sec. 6.2, which describes the triggers used to collect the candidate

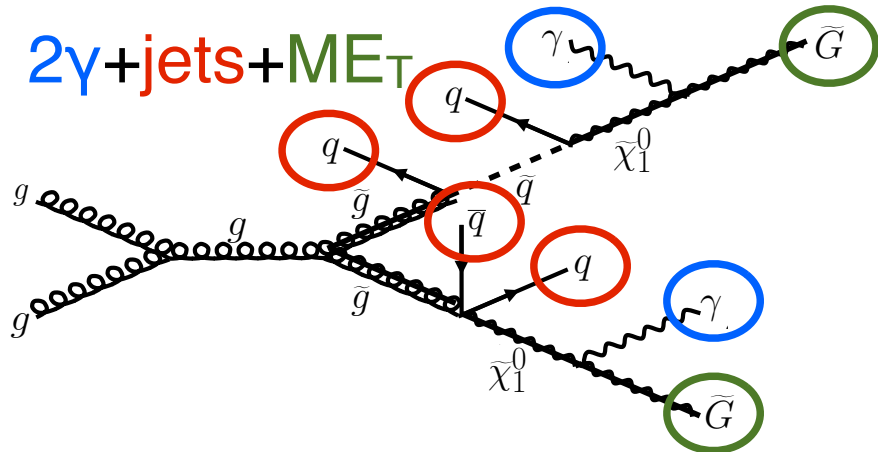


Figure 6.1: Two gluinos each decay via $\tilde{\chi}_1^0 \rightarrow \gamma \tilde{G}$.

and control samples. Sec. 6.3 describes event cleaning cuts that are applied to the candidate and control samples. Finally, the chapter concludes with a measurement of the photon identification efficiency in Sec. 6.4.

6.1 Object Reconstruction

This section describes the *offline* object reconstruction, i.e. the reconstruction of particle objects from events that have already been triggered and written to permanent storage, as opposed to the building of trigger objects explained in Secs. 5.2.1 and 6.2.

6.1.1 Photons

Uncalibrated EB/EE Hits

Photon reconstruction begins with the ADC count value for each of the 10 recorded time samples per ECAL crystal per trigger. To construct an *uncalibrated hit*, the gain (1, 6, or 12; see Sec. 5.1.2) of each sample is determined and the ADC count value scaled appropriately. The pedestal is estimated from the average of the first three samples, which, for a properly timed in hit, should contain no signal. This

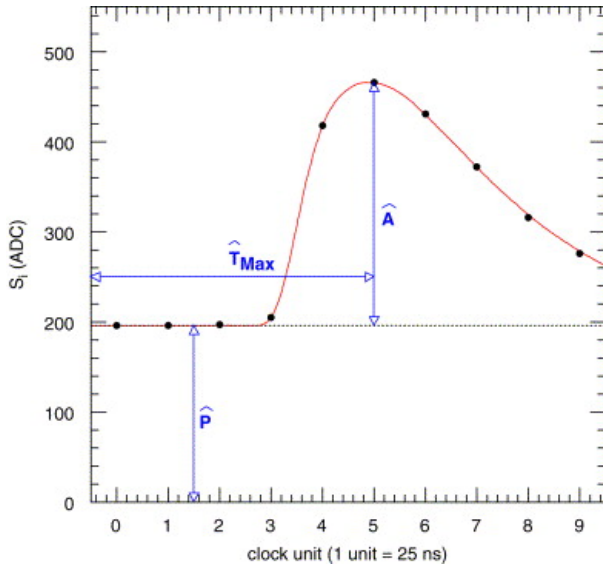


Figure 6.2: Typical ECAL channel pulse shape. \hat{P} is the pedestal value, \hat{A} is the pulse amplitude, and \hat{T}_{\max} is the hit time. The red line is the assumed pulse shape from which the weights are derived. Reprinted from ref. [69].

pedestal value is subtracted from the rest of the samples. Finally, the amplitude of the pulse is reconstructed using a predetermined weight for each sample [69]. The weights correspond to the pulse shape expected from the MGPA and shaping circuit response. The time of the hit is also reconstructed using the ratios between neighboring time samples [70]. A typical ECAL channel pulse shape is shown in Figure 6.2.

Calibrated EB/EE Hits

In the next phase of the photon reconstruction, calibrations are applied to the uncalibrated hits to form *calibrated hits* with energy measured in GeV. Channels are excluded from seeding calibrated hits if

- they are excessively noisy,
- they are stuck in fixed gain (i.e. the MGPA gain does not change properly to avoid saturation),
- they are totally dead,

- 1244 • they have one or more neighboring dead channels, or
 1245 • they do not have good trigger primitives (i.e. trigger primitive is missing, satu-
 1246 rated, or *spike-like*; cf. Secs. 5.1.2 and 5.2.1).

Added

1247 *ECAL spikes* are hits in which low energy protons and heavy ions from jets ionize [this](#)
 1248 in the sensitive volume of the EB APD (Sec. 5.1.2), causing the APD to register a [para-](#)
 1249 fake large-amplitude hit. Because they are not the result of a real electromagnetic [graph](#)
 1250 shower, spikes tend to be isolated. They may also appear to arrive early or late with [and the](#)
 1251 respect to the nominal bunch crossing. Most spikes are reconstructed with a hit time [next](#)
 1252 ~10 ns earlier than real EM hits because unlike real hits, whose pulse shapes include [about](#)
 1253 the time constant associated with crystal scintillation, the reconstructed spikes only [spikes](#)
 1254 involve the rise time of the electronics. There also is a long tail of late arriving spikes
 1255 due to slow neutrons from jets [71].

1256 Because of their particular timing and topological characteristics, cuts have been
 1257 developed to effectively identify and reject spike-like hits. This analysis utilizes both
 1258 the “Swiss cross” cut $1 - E_4/E_1 > 0.95$, where E_1 is the energy of the spike candidate
 1259 crystal and E_4 is the sum of the energies in the four crystals whose edges are next to
 1260 the four edges of the spike candidate crystal, and a timing cut $t \geq 3$ ns, to flag spikes.
 1261 More information about these cuts can be found in ref. [71]. A simpler algorithm
 1262 using the fine grain veto bit of the ECAL L1 TPG (Sec. 5.2.1) is used to reject spikes
 1263 at the trigger level.

1264 In addition to the trigger primitives, no uncalibrated hits that are spike-like are
 1265 eligible for calibration. The calibrations applied are corrections to account for crystal
 1266 transparency and VPT photocathode loss (leading to signal loss), measured continu-
 1267 ously by the laser/LED system; energy intercalibrations (relative energy calibration
 1268 between crystals); absolute scale calibrations between ADC counts and GeV;¹ and

¹The ADC-GeV scale factors (one for EB and one for EE) are defined such that the sum of fully calibrated and scaled hits in a particular 5×5 cluster of crystals (plus the associated energy deposited in ES) is 50 GeV for a 50 GeV incident unconverted photon [72].

1269 time intercalibrations (relative time calibration between crystals).

1270 The ECAL crystals were pre-calibrated before installation in CMS using labora-
1271 tory light yield and photodetector gain measurements [73]. In addition, some EB and
1272 EE crystals were intercalibrated using test beams [74], and all EB crystals were inter-
1273 calibrated with cosmic ray muons [75]. EE precalibrations were validated with LHC
1274 *splash events* in 2009 [75, 76], in which the beam was dumped onto a collimator ap-
1275 proximately 150 meters upstream of CMS, causing a spray of muons to enter CMS at
1276 one endcap and exit at the other. Splash events were also used to derive time intercal-
1277 ibration constants. Before colliding beam operations commenced, the intercalibration
1278 precision was estimated to be 0.5%-2.2% in EB and 1%-5% in EE [77].

1279 Three calibration methods were employed once colliding beam operations began:

- 1280 • ϕ symmetry relative calibration between crystals, exploiting the azimuthal sym-
1281 metry of CMS
- 1282 • π^0 and η relative calibration between crystals, using the diphoton decays of
1283 these particles
- 1284 • E/p absolute calibration, comparing the momentum measured in the tracker p
1285 to the energy measured in the ECAL E of a sample of electrons from Z decay

1286 By September 2011, the intercalibration precision in EB was measured to be be-
1287 tween 0.3% and 1.1% using the π^0/η method [78]. Figure 6.3 shows the improvement
1288 in Z reconstruction from pre-LHC calibration constants to the latest π^0/η -derived
1289 constants.

1290 Calibrated ES Hits

Added

1291 ES calibrated hits are formed from the three samples read out per sensor. Just as in the paren-
1292 case of EB/EE crystals, ES uncalibrated hits are gain-adjusted, pedestal-subtracted, thetical
remark

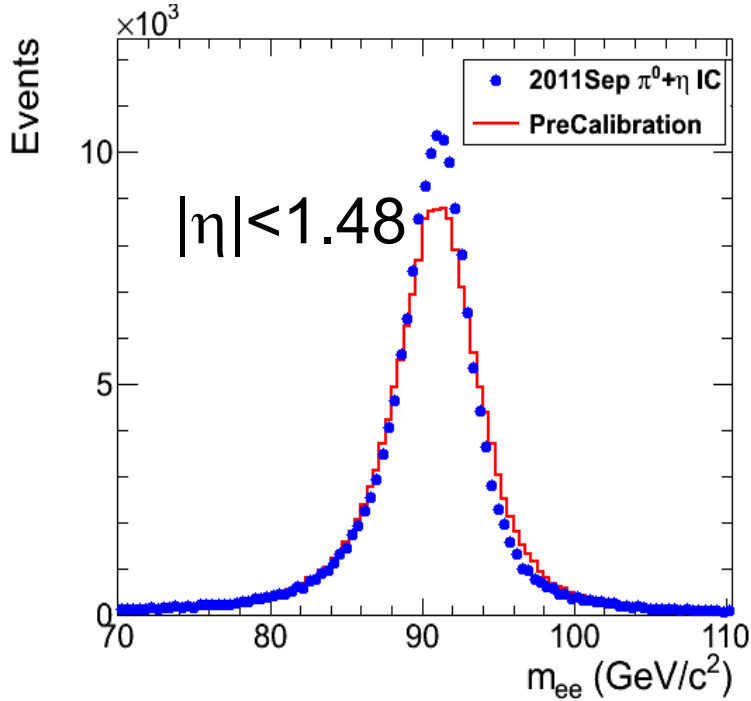


Figure 6.3: Z peak reconstructed using pre-LHC calibration constants (red) or September 2011 π^0/η -derived intercalibration constants (blue). Reprinted from ref. [78].

1293 and reconstructed using weights. To make a calibrated ES hit, intercalibration con-
 1294 stants, angle correction constants (for the non-uniformity of sensor angle with respect
 1295 to the vertical across ES), and a MIP-GeV absolute scale factor are applied.

1296 **Clustering**

1297 After calibrated ECAL hits are formed, they must be clustered into shapes that
 1298 represent the energy deposit from a single particle. *Basic clusters* are formed around
 1299 seed hits, defined as a hit that

- 1300 • has calibrated $E_T > 1(0.18)$ GeV in EB(EE),
- 1301 • does not originate from a dead channel or one with faulty hardware,
- 1302 • is not poorly calibrated,

- 1303 ● was reconstructed with the standard algorithm (i.e. not a special recovery algo-
- 1304 rithm for channels with subpar data integrity),
- 1305 ● is not saturated,
- 1306 ● is not spike-like, and
- 1307 ● is in time (EB).

1308 EB basic clusters are formed around the seeds via the *hybrid* algorithm, while EE
 1309 basic clusters are formed with the `multi5x5` algorithm [79]. In addition to handling
 1310 non-radiating electrons and unconverted photons, both algorithms are designed to also
 1311 recover all of the energy associated with electron bremsstrahlung deposits and photon
 1312 conversions. The geometry of the CMS magnetic field means that bremsstrahlung
 1313 and conversions will tend to spread the shower out in ϕ , not η . Both algorithms
 1314 work by forming basic clusters around seeds, then combining the basic clusters into
 1315 *superclusters* (SC) by searching in a window extended in the ϕ direction for all basic
 1316 clusters consistent with bremsstrahlung radiation from the primary electron, or with
 1317 a photon conversion. Figure 6.4 illustrates the hybrid algorithm in EB. In EE, the
 1318 energy deposited in ES must also be added into the total clustered energy sum.

1319 Figure 6.5 shows the effect of superclustering on $Z \rightarrow ee$ reconstruction.

1320 **Supercluster Corrections**

1321 The total clustered ECAL energy is defined as

$$E = F \times \sum_{i=1}^{n_{\text{crystal}}} G \times c_i \times A_i \quad (6.1)$$

1322 where G is the ADC-GeV or MIP-GeV scale factor, c_i are the intercalibration con-
 1323 stants, A_i is the uncalibrated hit amplitude in ADC counts, and F is a SC correction

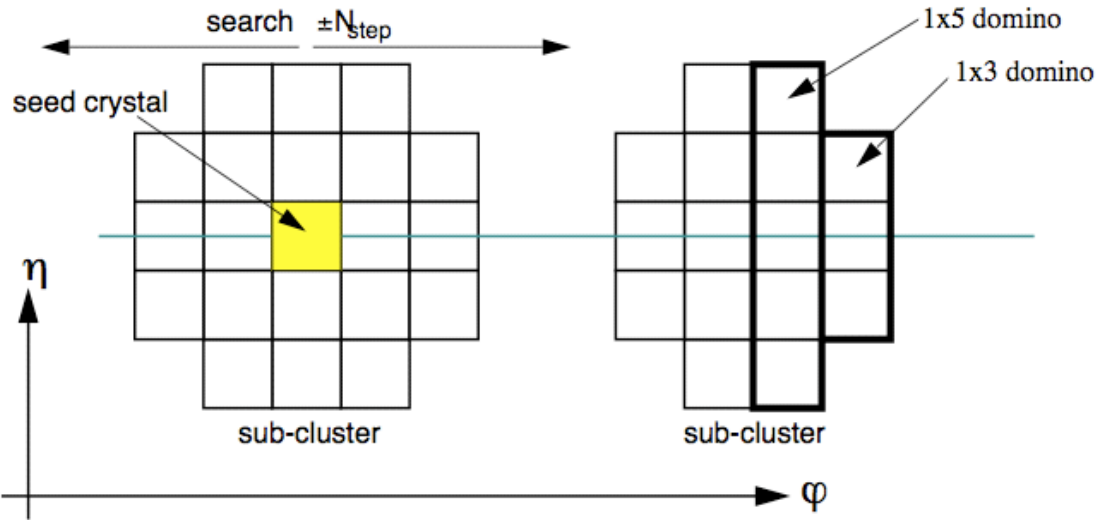


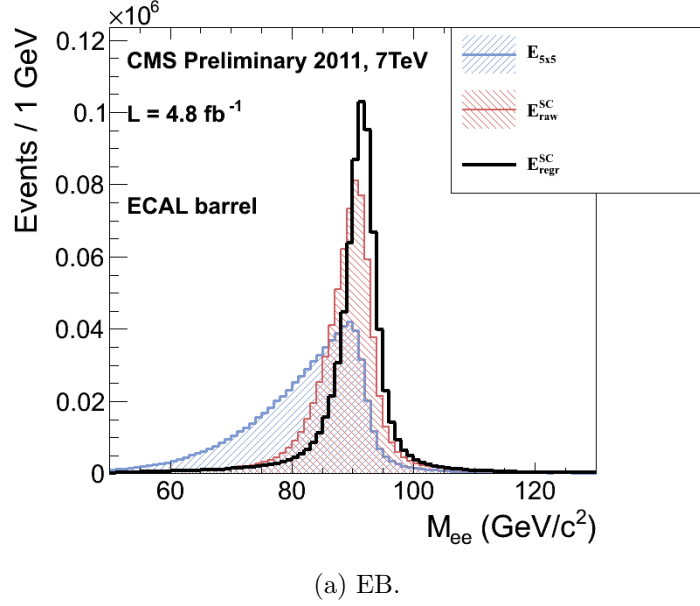
Figure 6.4: Hybrid algorithm in EB. The shower extent is constant in η (five crystals), but spreads out in ϕ as the two sub-clusters (or basic clusters) are grouped into the same supercluster. The maximum extent in ϕ is 17 crystals. Reprinted from ref. [79].

1324 factor. G and c_i were explained in Sec. 6.1.1. F is a product of three factors for hybrid
1325 SCs (two for `multi5x5` SCs in EE, items 2 and 3 below) [79]:

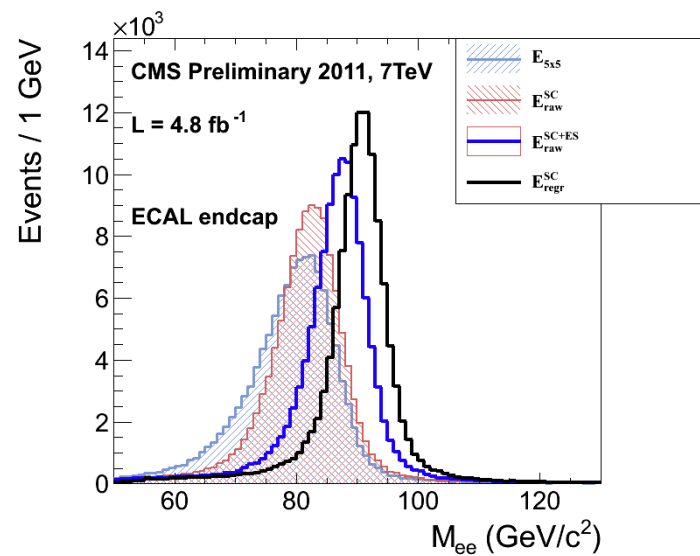
- 1326 1. $C_{\text{EB}}(\eta)$, which compensates for lateral energy leakage due to the crystal off-
1327 pointing in EB only. These corrections are taken from MC simulation [79] and
1328 were confirmed in test beams [74].
- 1329 2. $f(\text{brem})$, which corrects for biases in the clustering algorithms for showers char-
1330 acterized by differing amounts of bremsstrahlung. These corrections are taken
1331 from MC simulation [79].
- 1332 3. Residual correction $f(E_T, \eta)$, due to the variation in η of detector material
1333 traversed by a primary electron or photon, and to any residual E_T dependence
1334 of the reconstruction. These corrections are determined from MC and validated
1335 on $Z \rightarrow ee$ data samples [80].

Changed

1336 As a benchmark of ECAL calibration performance, the extra energy smearing in
1337 MC needed to achieve data/MC agreement in the Z width was between $\sim 0.9\%$ (in



(a) EB.



(b) EE.

Figure 6.5: Z peak reconstructed in the dielectron channel for different kinds of clustering. The constituent hits were calibrated with the best available intercalibrations and laser calibrations as of December 2011. The light blue histogram shows the reconstruction using a 5×5 energy sum, the red histogram shows the reconstruction using the SC energy for crystals only (the dark blue histogram in the EE plot adds in the energy from ES), and the black histogram shows the reconstruction after the SCs are corrected using a multivariate method [?]. Reprinted from Fig. 30 of ref. [?].

1338 the central part of EB for electrons with little bremsstrahlung) and $\sim 3.3\%$ (in the
1339 outer part of EE for heavily radiating electrons) [81].

1340 **From Supercluster to Photon**

1341 The CMS photon object is any SC with $E_T > 10$ GeV and $H/E < 0.5$, unless the SC
1342 $E_T > 100$ GeV, in which case the H/E requirement is dropped. H/E is defined as the
1343 ratio of energy in the HCAL in a 0.15 cone around the SC centroid, directly behind
1344 the SC, to the SC energy. SCs with $R9 > 0.94(0.95)$ in EB(EE), where $R9$ is defined
1345 as the ratio of the energy in the central 3×3 cluster of crystals divided by the SC
1346 energy $E_{3 \times 3}/E_{\text{SC}}$, are the best calibrated and most accurate type of electromagnetic
1347 shower. Therefore, for these objects, the photon energy is defined as the energy sum
1348 of the fully calibrated hits in the central 5×5 cluster around the seed (with $C_{\text{EB}}(\eta)$
1349 applied for EB photons). For all other SCs, the photon energy is equal to the fully
1350 corrected SC energy (cf. Sec. 6.1.1).

Reorganized

1351 In this search, candidate photons and *fake photons* (f , “fakes”) are further selected next 3
1352 according to the criteria listed in Table 6.1. Fakes are used in the determination of para-
1353 the QCD background, as explained in Chapter 7. graphs;

Table 6.1: Selection criteria for photons and fakes. “Pixel seed,” I_{comb} , and $\sigma_{i\eta i\eta}$ are edited
defined in the text.

Variable	Cut (γ)	Cut (f)
SC $ \eta $	< 1.4442	< 1.4442
H/E	< 0.05	< 0.05
$R9$	< 1	< 1
Has pixel seed	No	No
$I_{\text{comb}}, \sigma_{i\eta i\eta}$	< 6 GeV AND < 0.011	$(\geq 6 \text{ AND } < 20 \text{ GeV}) \text{ OR } \geq 0.011$

1354 I_{comb} is defined as

Updated
effective
area

$$I_{\text{comb}} = I_{\text{ECAL}} - 0.093\rho + I_{\text{HCAL}} - 0.0281\rho + I_{\text{track}} \quad (6.2)$$

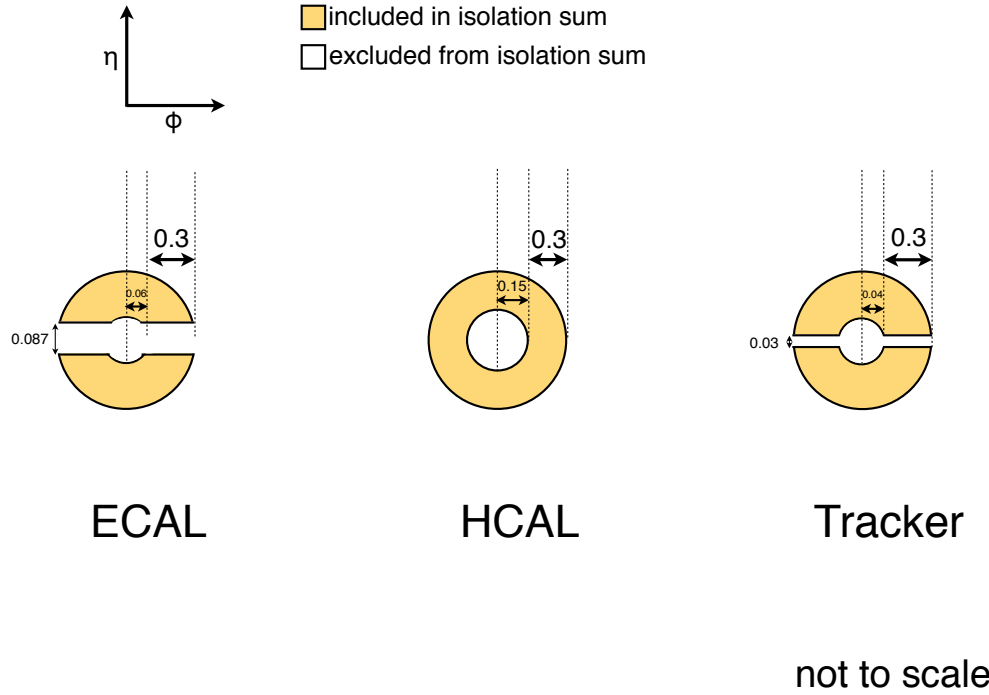


Figure 6.6: ECAL, HCAL, and track isolation cones.

1355 where I_{ECAL} , I_{HCAL} , and I_{track} are E_T sums in the annular regions defined in Figure 6.6
 1356 and ρ is the average pileup energy density in the calorimeters (per unit $\eta \cdot \phi$, or unit
 1357 calorimeter surface area) as measured with the Fastjet algorithm [82, 83]. ρ is constant
 1358 over the η range of the calorimeter. Note that the ECAL and track isolation veto
 1359 strips at constant η ensure that the isolation cuts are similarly efficient for converted
 1360 photons, radiating electrons, and unconverted photons.

1361 $\sigma_{i\eta i\eta}$ is the log energy weighted extent of the shower in η and is defined as

Added

$$\sigma_{i\eta i\eta} = \frac{\sum_{i=1}^{25} w_i (\eta_i - \bar{\eta})^2}{\sum_{i=1}^{25} w_i} \quad (6.3)$$

$\sigma_{i\eta i\eta}$

**defini-
tion**

1362 where the sums run over the 5×5 matrix of crystals surrounding the seed, $w_i =$
 1363 $\max(0, 4.7 + \ln(E_i/E))$, E_i is the energy of the i^{th} crystal, E is the total energy in the

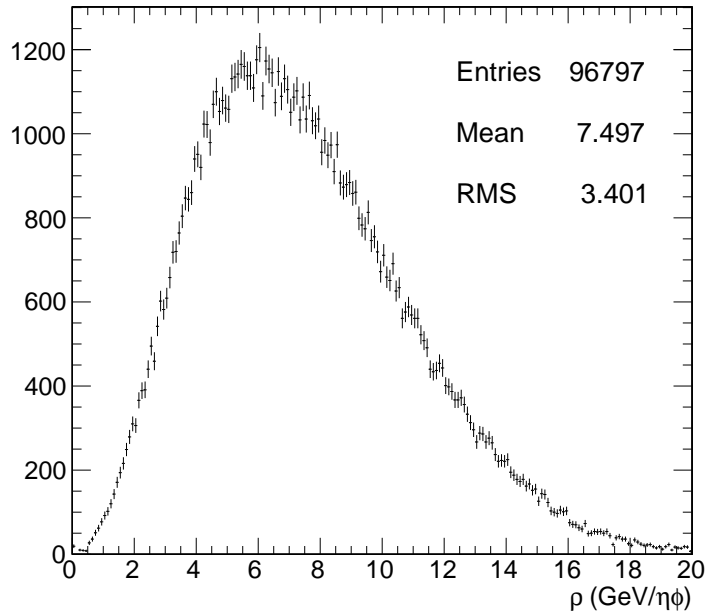


Figure 6.7: ρ distribution for a sample of two-photon events, with at least one 40 GeV and one 25 GeV photon, passing the selection requirements in Table 6.1 and the trigger requirements in Table 6.3. This sample covers the full 2011 dataset of 4.7 fb^{-1} .

1364 25 crystals, η_i is the offset in η of the i^{th} crystal from the seed, and $\bar{\eta}$ is the weighted
 1365 average η of the 25 crystals (using the w_i as weights) [84]. Changed

1366 Figure 6.7 shows the ρ distribution for a sample of two-photon events, with at average
 1367 least one 40 GeV and one 25 GeV photon, passing the selection requirements in ρ ; up-
 1368 Table 6.1 and the trigger requirements in Table 6.3. This sample represents the full dated
 1369 2011 dataset of 4.7 fb^{-1} . Since the average ρ is $\sim 7.5 \text{ GeV}$, and there is a long tail fig. 6.7
 1370 above this average value, it is necessary to subtract pileup energy from the ECAL
 1371 and HCAL isolation cones to recover otherwise clean photons in events with large
 1372 pileup. The ECAL and HCAL *effective areas* of 0.093 and 0.0281, respectively, are
 1373 calculated by fitting the average ECAL or HCAL isolation energy vs. ρ in a sample
 1374 of $Z \rightarrow ee$ events to a straight line. The slope of the line—which has the units of $\eta \cdot \phi$,
 1375 or area—is the effective area. New

1376 The cut on combined isolation of 6 GeV (Table 6.1) is the result of an S/\sqrt{B}

S \sqrt{B} Vs ComblsoDR03

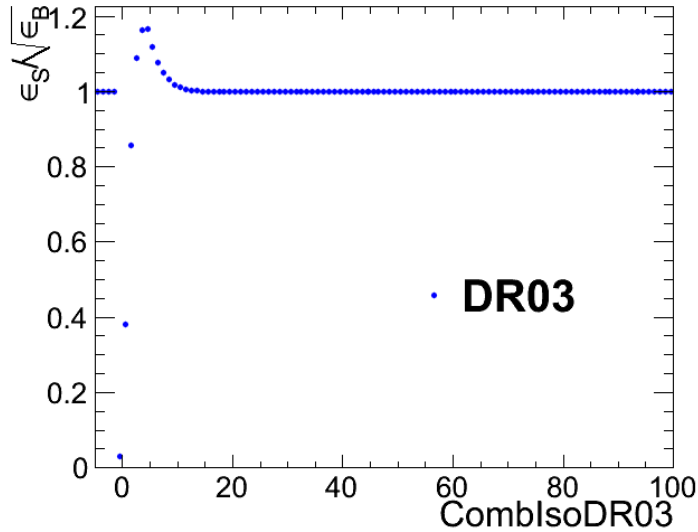


Figure 6.8: S/\sqrt{B} (S and B defined in the text) vs. I_{comb} . “DR03” in the legend indicates that this combined isolation was calculated in $\Delta R = 0.3$ cones, as used throughout this analysis. Reprinted from Fig. 7 of ref. [85].

1377 optimization procedure [85]. S is a sample of photons in simulated GGM events that
 1378 are products of neutralino decay, while B is a sample of photons matched to generated
 1379 hadronic jets in simulated QCD events. Figure 6.8 shows the value of S/\sqrt{B} vs.
 1380 combined isolation, in particular the pronounced peak around 6 GeV.

1381 The upper bound on fake photon combined isolation guarantees that poorly iso-
 1382 lated dijet events, with \cancel{E}_T resolution dissimilar to the candidate diphoton events,
 1383 do not enter the ff sample. The exact value of 20 GeV (cf. Table 6.1) arises from
 1384 a low- \cancel{E}_T $ff/\gamma\gamma \chi^2$ optimization procedure [85]. Figure 6.9 shows the value of the
 1385 Neyman’s χ^2 between the ff and $\gamma\gamma \cancel{E}_T$ distributions, truncated at either 25 or 50
 1386 GeV, vs. upper bound on fake combined isolation. As shown in the figure, 20 GeV
 1387 keeps the χ^2 small while also being large enough that a sufficient number of ff events
 1388 may be collected.

1389 Finally, a “pixel seed” is defined as a hit in the pixel detector consistent with a

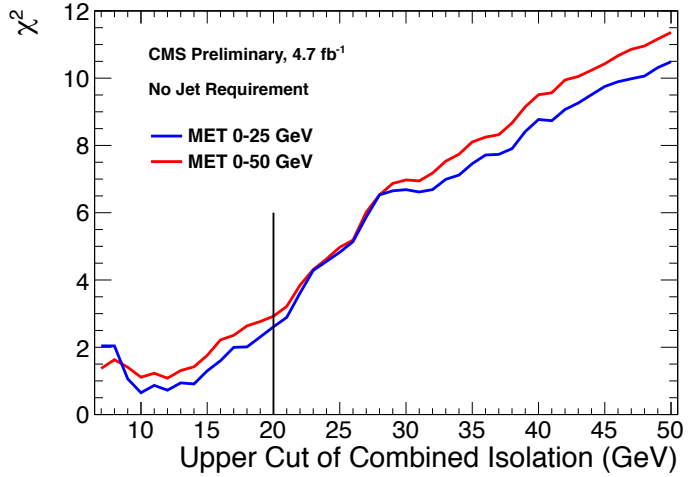
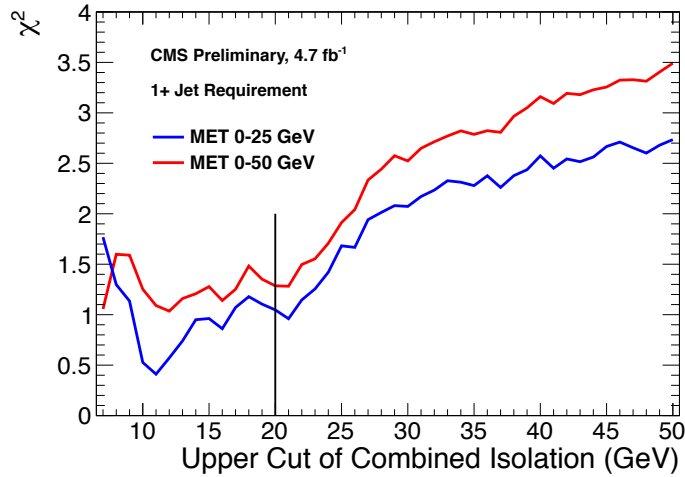
(a) Events with ≥ 0 jets.(b) Events with ≥ 1 jet.

Figure 6.9: Neyman's χ^2 between the ff and $\gamma\gamma$ \cancel{E}_T distributions, truncated at either 25 (red) or 50 (blue) GeV, vs. upper bound on fake combined isolation. A jet is defined as in Table 6.2, but with the ΔR cleaning criteria of Table 6.2 applied to the two primary EM objects and all additional electrons, photons, and fake photons. The full reweighting and normalization procedure is employed in the \cancel{E}_T calculation (see Sec. 7.1). Reprinted from Fig. 9 of ref. [85].

1390 track extrapolated from the position of the ECAL SC back to the primary vertex.
 1391 Real photons, having no charge and therefore no bending in the magnetic field, should
 1392 not have a pixel seed.

1393 6.1.2 Electrons

1394 Electrons are reconstructed identically to photons, except that in the electron case
 1395 the presence of a pixel seed is enforced, rather than vetoed.² Photons and electrons
 1396 are defined by very similar criteria so that $Z \rightarrow ee$ events can be used to model
 1397 the QCD background in the two-photon sample without introducing any bias in the
 1398 electron energy measurement (cf. Sec. 7.1).

1399 6.1.3 Jets and Missing Transverse Energy

1400 Particle Flow

1401 In this analysis, jets and \cancel{E}_T are formed from *particle flow* (PF) candidates. The parti-
 1402 cle flow algorithm [89, 90] uses information from all CMS subdetectors to reconstruct
 1403 as accurately as possible the positions and momenta of all visible jet constituents,
 1404 exploiting the fine granularity of the tracker and ECAL to achieve a greatly improved
 1405 momentum resolution over calorimeter-only jets [91]. The PF algorithm is summa-
 1406 rized below [92].

1407 1. Reconstruct the fundamental detector objects via iterative procedures

- 1408 • Tracks in the inner silicon layers
 - 1409 – High efficiency and low fake rate for charged hadrons in jets

²In many CMS analyses, electrons are reconstructed very differently from photons. In particular, a special tracking algorithm [88] is used to best follow a radiating electron. However, in this analysis, the electron tracking is not used.

- 1410 – Relaxed primary vertex constraint allows photon conversions, parti-
 1411 cles originating from nuclear interactions in the silicon, and long-lived
 1412 particles to be reconstructed
- 1413 • Calorimeter clusters
- 1414 • Muon tracks in the outer muon layers
- 1415 2. Create a “block” of linked fundamental objects
- 1416 • Link silicon tracks to calorimeter clusters via $\Delta R_{\text{track-cluster}}$ (account for
 1417 electron bremsstrahlung)
- 1418 • Link clusters in one calorimeter layer to clusters in a separate layer via
 1419 $\Delta R_{\text{cluster-cluster}}$
- 1420 • Link silicon tracks to muon tracks via global track χ^2
- 1421 3. ID the particles in the block
- 1422 • If global (silicon + muon layers) muon p_T is compatible with silicon track
 1423 p_T , ID as a muon and remove corresponding tracks from block
- 1424 • ID electron tracks via special algorithm and removed all corresponding
 1425 tracks and cluster from block
- 1426 • Remove fake tracks from the block
- 1427 • Allow multiple tracks to be associated to one HCAL cluster, but not mul-
 1428 tiple HCAL clusters to be associated to one track—for each track, keep
 1429 only the HCAL cluster link that is closest in ΔR to the track
- 1430 • If the cluster energy is significantly larger then the energy of the linked
 1431 tracks, ID as a PF photon or PF neutral hadron
- 1432 • If the cluster is not linked to a track, ID as a PF photon or PF neutral
 1433 hadron

- 1434 • If the cluster energy is smaller than the energy of the linked tracks, ID
 1435 each track as a PF charged hadron

1436 **Jets**

1437 PF candidates are clustered into jets by means of the anti- k_T algorithm with $R = 0.5$
 1438 [93]. In this algorithm, all possible pairs of PF candidates i, j are looped over, and
 1439 the pairs that minimize the distance variable

$$d_{ij} = \frac{\Delta R_{ij}^2}{R^2 \max(k_{Ti}^2, k_{Tj}^2)} \quad (6.4)$$

1440 are clustered together, where k_{Ti} is the transverse momentum of PF candidate i . The
 1441 process is repeated, using the pairwise-clustered PF candidates as input objects to
 1442 the next round of clustering, until $d_{ij} > 1/k_{Ti}^2$ for all pairs of clustered PF candidates
 1443 [94]. An illustration is given in Figure 6.10. The anti- k_T algorithm is infrared and Added
 1444 collinear safe, leading to well-behaved theoretical predictions and ease of comparison refer-
 1445 between data and MC simulation. It also tends to form circular jets, making it easy ence to
 1446 for experimental effects such as expected out-of-cone energy and fiducial acceptance Fig. 6.10
 1447 to be measured or simulated. For these reasons, the anti- k_T jet clustering algorithm
 1448 was chosen for this analysis.

1449 Once jets are found, they must be corrected for biases in the energy measurement
 1450 due to non-compensation [95], invisible energy (lost to overcoming nuclear binding
 1451 energy, in neutrinos, or in unclustered muons, for example) [95], detector geometry
 1452 and cracks [96], zero suppression and trigger inefficiencies [97], pileup, and effects of
 1453 the clustering algorithm [96]. Four multiplicative correction factors are applied to the
 1454 raw jet four-momentum p_μ^{raw} [91]:

- 1455 • $C_{\text{offset}}(p_T^{\text{raw}})$, which accounts for extra energy due to noise, pileup, and the un-

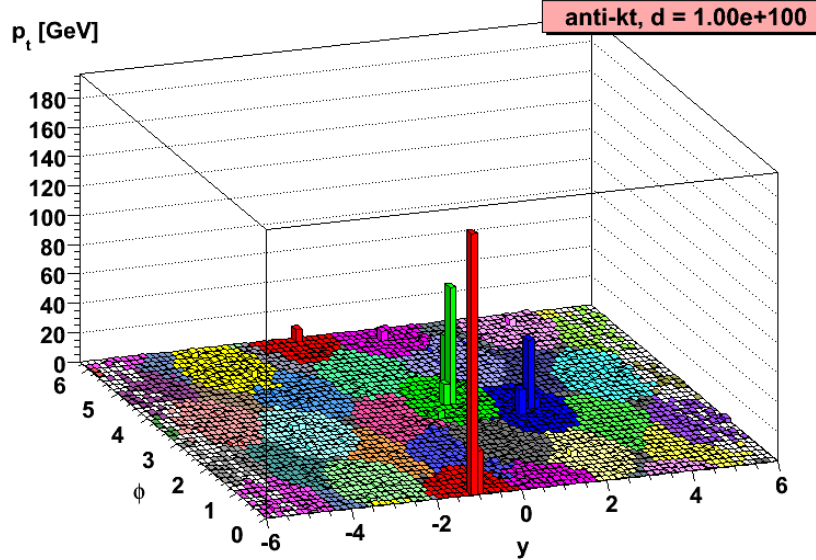


Figure 6.10: Example event display showing jets clustered via the anti- k_T algorithm. y is pseudorapidity. Reprinted from slide 85 of ref. [94].

- 1456 derlying event;
- 1457 • $C_{\text{MC}}(C_{\text{offset}}p_T^{\text{raw}}, \eta)$, which is derived from MC and accounts for most of the p_T
1458 and η dependence;
- 1459 • $C_{\text{rel}}(\eta)$, which accounts for the remaining differences in uniformity over the
1460 entire calorimeter between data and MC; and
- 1461 • $C_{\text{abs}}(C_{\text{rel}}C_{\text{MC}}C_{\text{offset}}p_T^{\text{raw}})$, which accounts for the remaining differences in linear-
1462 ity over the full p_T range between data and MC.

1463 Figure 6.11 shows the total jet energy correction factor $C_{\text{offset}}C_{\text{MC}}C_{\text{rel}}C_{\text{abs}}$ vs. η
1464 for jets reconstructed with the anti- k_T algorithm, $R = 0.5$. The PF jet corrections
1465 are more uniform across η than those of CALO jets (composed of simple calorimeter
1466 towers) or JPT jets (Jet Plus Tracks; composed of calorimeter energies replaced,
1467 where possible, with matching track p_T) [98]. In addition, for p_T in the range 30-200
1468 GeV and $|\eta|$ up to 2.0, the PF jet energy correction uncertainty is lower than that of
1469 the other two types of jets, and never exceeds $\sim 3\%$ [91]. The superior performance

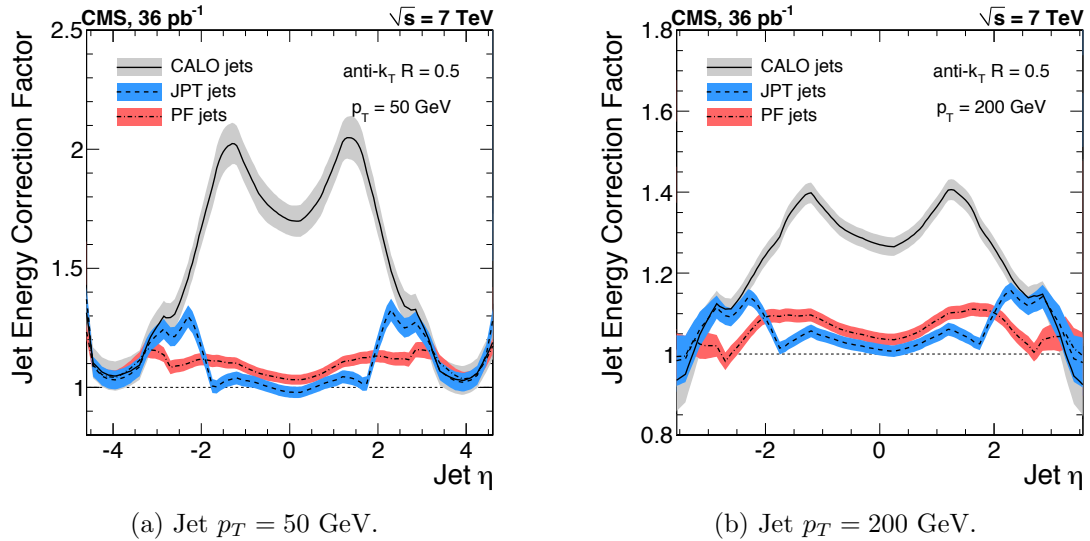


Figure 6.11: Total jet energy correction factor $C_{\text{offset}}C_{\text{MC}}C_{\text{rel}}C_{\text{abs}}$ vs. η , including uncertainty band, for jets reconstructed with the anti- k_T algorithm, $R = 0.5$. Reprinted from Fig. 26 of ref. [91].

¹⁴⁷⁰ of PF jets motivates their use in this search.

¹⁴⁷¹ In this analysis, candidate and QCD control events are binned by number of jets
¹⁴⁷² satisfying the criteria in Table 6.2.

¹⁴⁷³ Missing Transverse Energy

¹⁴⁷⁴ To be consistent with the jet reconstruction, \cancel{E}_T in this analysis is also reconstructed
¹⁴⁷⁵ from PF candidates. Raw \cancel{E}_T is defined as

$$\cancel{E}_{T\text{raw}} = \left| - \sum_{i=1}^{n_{\text{PF}}} \vec{p}_{Ti} \right| \quad (6.5)$$

¹⁴⁷⁶ where n_{PF} is the number of PF candidates in the event. $\cancel{E}_{T\text{raw}}$ may be corrected for
¹⁴⁷⁷ the same effects that necessitate jet corrections, since $\cancel{E}_{T\text{raw}}$ is usually the result of jet
¹⁴⁷⁸ mis-measurement (except, of course, in electroweak physics processes that include an
¹⁴⁷⁹ energetic neutrino, or SUSY production). CMS *Type-I* \cancel{E}_T corrections simply involve

Table 6.2: Definition of HB/HE hadronic jets.

Variable	Cut
Algorithm	L1FastL2L3Residual corrected PF
p_T	$> 30 \text{ GeV}$
$ \eta $	< 2.6
Neutral hadronic energy fraction	< 0.99
Neutral electromagnetic energy fraction	< 0.99
Number of constituents	> 1
Charged hadronic energy	$> 0.0 \text{ GeV}$ if $ \eta < 2.4$
Number of charged hadrons	> 0 if $ \eta < 2.4$
Charged electromagnetic energy fraction	< 0.99 if $ \eta < 2.4$
ΔR to nearest PF electron ^a , muon ^b , or one of the two primary EM objects	> 0.5

^aA PF electron is defined as an electron reconstructed with the PF algorithm [86] with $p_T > 15 \text{ GeV}$, $|\eta| < 2.6$, and $(I_{\text{charged}} + I_{\text{photon}} + I_{\text{neutral}})/p_T < 0.2$, where $I_{\text{charged}}(I_{\text{photon}})(I_{\text{neutral}})$ is the sum of PF charged hadron(PF photon)(PF neutral hadron) momenta in a $\Delta R = 0.4$ cone around the PF electron.

^bMuons are reconstructed [87] from a combination of muon station and inner tracker hits. Here, a muon must have track $\chi^2 < 10$, at least one good muon station hit, inner track transverse impact parameter $< 0.02 \text{ cm}$, inner track longitudinal impact parameter $< 0.5 \text{ cm}$, $p_T > 15 \text{ GeV}$, $|\eta| < 2.6$, and $(I_{\text{ECAL}} + I_{\text{HCAL}} + I_{\text{track}})/p_T < 0.2$, where $I_{\text{ECAL}}(I_{\text{HCAL}})(I_{\text{track}})$ is the sum of ECAL(HCAL)(track) momenta in a $\Delta R = 0.3$ cone around the muon.

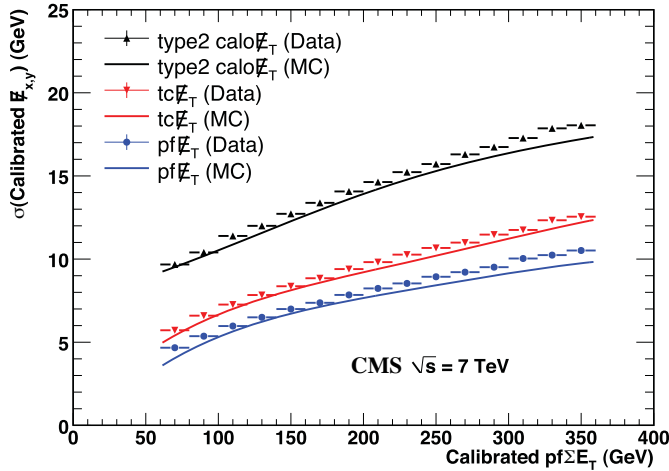


Figure 6.12: σ of a Gaussian fit to the x- and y-components of calibrated E_T vs. the calibrated PF E_T sum in a sample of events containing at least two jets with $p_T > 25$ GeV. σ is calibrated such that the E_T scale is equal for all three algorithms. PF $\sum E_T$ is corrected, on average, to the particle level using a Pythia v8 simulation [99]. The blue markers (data) and line (MC) refer to PF jets. Reprinted from Fig. 13 of ref. [97].

replacing the PF jets with their corrected energies (cf. Sec 6.1.3) and recalculating E_T . Only jets with electromagnetic fraction (EMF) below 90% and $p_T > 20$ GeV are replaced. This ensures that very electromagnetic jets (as well as isolated leptons, which also receive no correction), which consist chiefly of neutral pions and are measured accurately by the ECAL, do not receive a correction derived for jets with a large fraction of their energy in charged hadrons. In addition, the p_T cut guarantees that jet corrections are only applied where they are known to within a few percent. For this search, the level of agreement between the SM background estimate and the two-photon search sample in a low- E_T control region is the same regardless of whether the E_T is corrected or not, so for simplicity the Type-I E_T corrections are not used (see Sec. 7.3).

Figure 6.12 shows the σ of a Gaussian fit to the x- and y-components of calibrated E_T vs. the calibrated PF E_T sum in a sample of events containing at least two jets with $p_T > 25$ GeV. Again, PF E_T outperforms E_T constructed of calorimeter towers or track-corrected calorimeter deposits.

1495 **6.2 HLT**

1496 From the objects described in Sec. 6.1, four samples of events are formed:

- 1497 • $\gamma\gamma$ candidate sample, in which the two highest E_T objects are photons,
- 1498 • $e\gamma$ control sample, in which the two highest E_T objects are one electron and
1499 one photon,
- 1500 • ee control sample, in which the two highest E_T objects are electrons, and
- 1501 • ff control sample, in which the two highest E_T objects are fakes.

1502 In all samples, the leading EM object is required to have offline reconstructed $E_T > 40$
1503 GeV, while the trailing EM object is required to have offline reconstructed $E_T > 25$
1504 GeV. The high level triggers used to select the four samples, by run range, are listed
1505 in Table 6.3. No trigger is prescaled.

1506 Each piece of the HLT path name is defined as follows.

- 1507 • **Photon**: Energy deposit in the ECAL that fired an L1 trigger (cf. Sec. 5.2.1).
1508 For **Photon26_IsoVL_Photon18**, the L1 seed E_T threshold is 12 GeV, while for Switched
HLT
1509 all other triggers in Table 6.3 it is 20 GeV (cf. Sec. 5.2.1).
path
names
to ver-
batim
font and
added
refer-
ence
to L1
section
- 1510 • Integer following the word **Photon**: E_T threshold in GeV for offline reconstructed
1511 photon, using the full photon reconstruction of Sec. 6.1.1 minus the laser cali-
1512 brations and assuming the primary vertex at (0, 0, 0).
- 1513 • **CaloIdL**: For EB photons, $H/E < 0.15$ and $\sigma_{inj} < 0.014$.
- 1514 • **IsoVL**: $I_{ECAL} < 0.012E_T + 6$ GeV, $I_{HCAL} < 0.005E_T + 4$ GeV, and $I_{track} <$
1515 $0.002E_T + 4$ GeV.
- 1516 • **R9Id**: $R9 > 0.8$.

Table 6.3: HLT paths triggered by the $\gamma\gamma$, $e\gamma$, ee , and ff samples, by run range. No triggers are prescaled.

Run range	$\gamma\gamma$	$e\gamma$	ee	ff
160404-163261	Photon26_ IsoVL_ Photon18	Photon26_ IsoVL_ Photon18	Photon26_ IsoVL_ Photon18	Photon26_ IsoVL_ Photon18
161216-166967	Photon36_ CaloIdL_ Photon22_ CaloIdL	Photon36_ CaloIdL_ Photon22_ CaloIdL	Photon36_ CaloIdL_ Photon22_ CaloIdL	Photon36_ CaloIdL_ Photon22_ CaloIdL
166347-180252	Photon36_ CaloIdL_ IsoVL_ Photon22_ CaloIdL_ IsoVL	Photon36_ CaloIdL_ IsoVL_ Photon22_ CaloIdL_ IsoVL	Photon36_ CaloIdL_ IsoVL_ Photon22_ CaloIdL_ IsoVL	Photon36_ CaloIdL_ IsoVL_ Photon22_ CaloIdL_ IsoVL Photon36_ CaloIdL_ IsoVL_ Photon22_ R9Id Photon36_ R9Id_ Photon22_ CaloIdL_ IsoVL Photon36_ R9Id_ Photon22_ R9Id

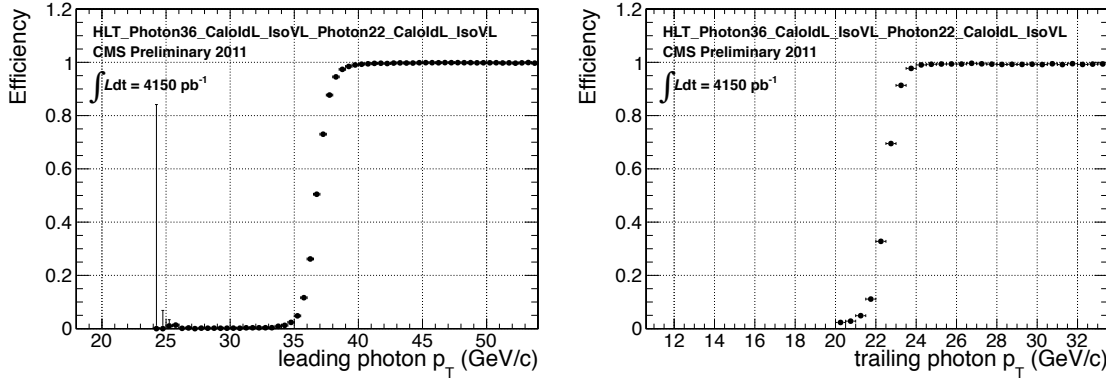


Figure 6.13: Efficiency of `HLT_Photon36_CaloIdL_IsoVL_Photon22_CaloIdL_IsoVL` for offline selected leading photon (left) and trailing photon (right) vs. photon p_T . Reprinted from Fig. 2 of ref. [85].

1517 In addition, the versions of `HLT_Photon26_IsoVL_Photon18` and
 1518 `Photon36_CaloIdL_Photon22_CaloIdL` that were active during runs 160404-163268
 1519 included a cut $E_{\max}/E_{5\times 5} < 0.98$ for spike rejection. E_{\max} is the energy in the highest
 1520 energy crystal of the EM cluster and $E_{5\times 5}$ is the energy in the 5×5 crystal matrix
 1521 around the seed crystal. For runs after 163268, Swiss cross spike rejection of individual
 1522 crystals from HLT quantities was performed (cf. Sec. 6.1.1). All information about the
 1523 evolution of the CMS HLT settings can be found in the HLT configuration browser
 1524 at <http://j2eeps.cern.ch/cms-project-confdb-hltdev/browser/>.

1525 As an example of the naming convention just described, the HLT path

1526 `Photon36_CaloIdL_IsoVL_Photon22_R9Id` is fired if one photon is found with $E_T >$
 1527 36 GeV passing the CaloIdL and IsoVL requirements, and another is found with
 1528 $E_T > 22$ GeV passing the R9Id requirement.

1529 For the offline E_T cuts described in this section, the triggers are $> 99\%$ efficient,
 1530 as shown in Figure 6.13 [85]. The efficiencies are measured with respect to triggers
 1531 with lower E_T thresholds.

Switched
 HLT
 path
 names
 to ver-
 batim
 font
 Switched
 HLT
 path
 names
 to ver-
 batim
 font
 Added
 HLT ef-
 ficiency
 discus-
 sion

1532 6.3 Event Quality

1533 To suppress instrumental backgrounds, a set of event quality cuts are applied to the
 1534 $\gamma\gamma$, $e\gamma$, ee , and ff samples. First, all events are required to pass a good run selection,
 1535 as determined by the CMS Physics Validation Team [101]. The good run selection
 1536 excludes luminosity sections during which a sufficient part of the CMS detector was
 1537 unpowered or malfunctioning. Such conditions could occur if, for example, a high
 1538 voltage supply trips off in the middle of a run, or a DAQ error corrupts data quality
 1539 but is not spotted until after the data have been collected. The severity of a detec-
 1540 tor problem is judged by its effect on a wide range of analyses and reconstruction
 1541 algorithms. Of the $\sim 5 \text{ fb}^{-1}$ of integrated luminosity delivered by the LHC in 2011,
 1542 4.68 fb^{-1} passed the good run selection. This analysis is performed on the entire 2011
 1543 certified dataset.

1544 Second, all events must contain at least one good interaction vertex. The criteria
 1545 for a good vertex are:

- 1546 • $\chi^2 \neq 0$ OR $\text{ndof} \neq 0$ OR $N_{\text{tracks}} \neq 0$, where χ^2 and ndof are calculated for the
 1547 track fit to the vertex, and N_{tracks} is the number of tracks in the vertex fit
- 1548 • $\text{ndof} > 4$
- 1549 • $|z| < 24 \text{ cm}$, where z is the z -coordinate of the vertex position
- 1550 • $|\rho| < 2 \text{ cm}$, where ρ is the transverse displacement of the vertex position from
 1551 the beam line

1552 The good vertex requirement eliminates non-collision backgrounds such as beam
 1553 scraping, beam halo, cosmic muon interactions, and instrumental effects.

1554 Third, the two electromagnetic objects in the $\gamma\gamma$, $e\gamma$, ee , and ff events must
 1555 be separated in ϕ by at least 0.05. This requirement protects against beam halo
 1556 bremsstrahlung, in which a halo muon traveling parallel to the beam line radiates an

1557 energetic photon while itself depositing a large amount of energy in the ECAL. In
 1558 this case, the two ECAL hits would likely be at the same ϕ (and ρ).

1559 Fourth, the two EM objects must be separated in R by at least 0.6. Since the
 1560 isolation cone size used is 0.3, this ensures that the isolation energy of one EM object
 1561 cannot be in the veto strip (Fig. 6.6) of the other.

1562 Finally, the $\gamma\gamma$, $e\gamma$, ee , and ff events must pass an HCAL noise filter and ECAL
 1563 dead channel filter. The HCAL noise filter guarantees that all HCAL reconstructed
 1564 hits are inconsistent with any noise source. Noise sources [100] include:

- 1565 • Ion feedback in the HPDs absent any true incident photons, in which a thermal
 1566 electron ionizes a molecule in the HPD acceleration gap, faking a real signal
- 1567 • HPD discharge affecting nearly all channels in the same HPD [102], partially
 1568 explained by the effect of the 4 T CMS magnetic field on the flashover voltage
 1569 of the dielectric [104]
- 1570 • Concurrent signals in nearly all 72 channels of a single RBX, as yet unexplained
- 1571 • HF PMT window hits (as opposed to the usual quartz fiber hits)
- 1572 • ADC saturation

1573 Since HCAL noise may induce fake jets or E_T , events are rejected if any of the
 1574 following criteria are true:

- 1575 • Any HPD has > 17 hits
- 1576 • A single HPD has > 10 hits, but every other HPD has zero hits
- 1577 • An RBX has > 10 zero-ADC-count hits
- 1578 • Any HB/HE reconstructed hit corresponding to an RBX with > 50 GeV of
 1579 energy fails a two-dimensional cut defined by the variables $(TS4 - TS5)/(TS4 +$

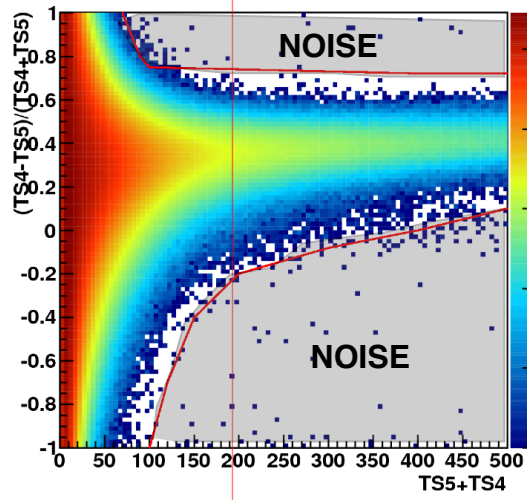


Figure 6.14: $(TS4 - TS5)/(TS4 + TS5)$ vs. $TS4 + TS5$ for a minimum bias sample. HB/HE hits are considered noisy if they lie in the sparsely populated gray region labeled "NOISE" defined by the curved red lines. Adapted from ref. [103].

1580 $TS5)$ vs. $TS4 + TS5$, where $TS4(TS5)$ is the hit amplitude in the fourth(fifth)
 1581 time sample read out for that hit. The cut is defined in Fig. 6.14.

1582 The ECAL dead channel filter is designed to flag events in which significant EM
 1583 energy was deposited in a masked region of the ECAL by using the trigger primitive
 1584 information for the corresponding trigger tower. Energy deposited in a masked region
 1585 of ECAL can cause fake \cancel{E}_T . Events are rejected if the trigger primitive E_T exceeds
 1586 the maximum value of 63.75 GeV in any trigger tower that is masked in the readout.

1587 6.4 Photon Identification Efficiency

1588 In order to determine the cross section (or cross section upper limit) for a GGM
 1589 signal, the photon identification efficiency is needed. Since no suitably large sample
 1590 of $Z \rightarrow \mu\mu\gamma$ events in CMS exists yet, the efficiency calculation relies on the similarity
 1591 between detector response to electrons and photons. A scale factor to correct the MC
 1592 photon ID efficiency to the real photon efficiency for the data is obtained from the
 1593 ratio of the electron efficiency from the data to the electron efficiency from MC.

1594 The different types of photon ID variables—calorimeter and track isolation, ratio of **Removed**
 1595 hadronic to electromagnetic energy of the shower, and transverse shower shape—are **refer-**
 1596 chosen so that their distributions for isolated electrons and photons are similar.³ **ence to**
 1597 The photon selection efficiency is **plots**

$$\epsilon_\gamma = \epsilon_\gamma^{\text{MC}} \times \frac{\epsilon_e^{\text{data}}}{\epsilon_e^{\text{MC}}} \quad (6.6)$$

1598 where

- 1599 • ϵ_γ is the photon ID efficiency in data,
- 1600 • $\epsilon_\gamma^{\text{MC}}$ is the photon ID efficiency in MC,
- 1601 • ϵ_e^{data} is the electron ID efficiency obtained using $Z \rightarrow ee$ electrons in the data
1602 that satisfy the photon ID cuts, and
- 1603 • ϵ_e^{data} is the electron ID efficiency obtained using $Z \rightarrow ee$ electrons in MC that
1604 satisfy the photon ID cuts.

1605 The ratio $\epsilon_e^{\text{data}}/\epsilon_e^{\text{MC}}$ is defined as the scale factor by which the GGM signal MC
 1606 photon ID efficiency must be multiplied to give an estimate of the photon ID efficiency
 1607 in data. The photon ID requirements of Table 6.1 plus the **IsoVL** HLT requirement
 1608 described in Sec. 6.2 and Table 6.3 are repeated in Table 6.4.

1609 6.4.1 Tag and Probe Method

1610 A *tag and probe* method using Z events is utilized to measure the efficiency of the
 1611 photon ID cuts in Table 6.1. The tag is a well-identified electron. The probe, by
 1612 contrast, is as loosely identified as possible, and all tags must pass the probe criteria

³ $R9$ differs between photons and radiating electrons, but the requirement $R9 < 1$ is loose enough not to introduce problems with the use of electrons to measure the photon ID efficiency.

1613 in addition to the stringent tag criteria. The tag and probe criteria used in this study
1614 are shown in Table 6.5.

1615 The invariant mass of the tag and probe are required to be within a narrow window
1616 around Z mass. Assuming that the probabilities of the tag and probe legs of the Z
1617 decay to pass the photon ID cuts are uncorrelated, the efficiency can be estimated as

$$\epsilon = \frac{N_{\text{tag-pass}}}{N_{\text{tag-pass}} + N_{\text{tag-fail}}} \quad (6.7)$$

1618 where $N_{\text{tag-pass}}$ is the number of tag-probe pairs in which the probe leg passes the
1619 photon ID cuts under study and $N_{\text{tag-fail}}$ is the number of tag-probe pairs in which
1620 the probe leg fails the cuts. Implicit in these definitions is a double counting of pairs
1621 in which both electrons pass the tag and probe criteria [106]. In addition, in the rare
1622 circumstance (less than 1% in MC [106]) that two or more probes may be matched
1623 to one tag, the pair with invariant mass closest to the Z mass is chosen.

1624 In practice, $N_{\text{tag-pass}}$ and $N_{\text{tag-fail}}$ are returned by a simultaneous unbinned maxi-
1625 mum likelihood fit to the invariant mass distributions of tag-pass and tag-fail events,
1626 with appropriate signal and background PDF assumptions. The fit form used is

Table 6.4: Candidate photon ID requirements.

Variable	Cut
I_{ECAL}	$< 0.012E_T + 6 \text{ GeV}$
I_{HCAL}	$< 0.005E_T + 4 \text{ GeV}$
I_{track}	$< 0.002E_T + 4 \text{ GeV}$
H/E	< 0.05
$\sigma_{i\eta i\eta}$	< 0.011
$I_{\text{ECAL}} - 0.0792\rho + I_{\text{HCAL}} - 0.0252\rho + I_{\text{track}}$	$< 6 \text{ GeV}$
$R9$	< 1

Table 6.5: Tag and probe criteria. The superscript 0.4 indicates that the isolation variable was calculated in a cone of $\Delta R = 0.4$ around the photon candidate. The isolations without superscripts use the standard $\Delta R = 0.3$ cones.

Variable	Cut	
	Tag	Probe
RECO object	photon	photon
HLT	HLT_Ele17_CaloIdVT_CaloIsoVT_TrkIdT_TrkIsoVT_SC8_Mass30_v* (must have fired the 17 GeV leg)	—
H/E	< 0.05	< 0.15
$I_{\text{ECAL}}^{0.4}$	$< 0.006E_T + 4.2 \text{ GeV}$	—
$I_{\text{HCAL}}^{0.4}$	$< 0.0025E_T + 2.2 \text{ GeV}$	—
$I_{\text{track}}^{0.4}$	$< 0.001E_T + 2.0 \text{ GeV}$	—
E_T	$> 25 \text{ GeV}$	—
SC E_T	—	$> 15 \text{ GeV}$
SC $ \eta $	< 1.4442	< 1.4442
$\sigma_{i\eta i\eta}$	< 0.009	—
Has pixel seed	Yes	—
Track match type	General track ^a	—
Track match ΔR	< 0.04	—
Track match p_T	$> 15 \text{ GeV}$	—
Track match $ \eta $	< 1.479	—

^aA general track is reconstructed with the CMS standard combinatorial track finder [105].

$$\begin{aligned} f_{\text{tag-pass}}(m_{\text{tag-pass}}) &= \epsilon N_S f_S^{\text{pass}}(m_{\text{tag-pass}}) + N_B^{\text{pass}} f_B^{\text{pass}}(m_{\text{tag-pass}}) \\ f_{\text{tag-fail}}(m_{\text{tag-fail}}) &= (1 - \epsilon) N_S f_S^{\text{fail}}(m_{\text{tag-fail}}) + N_B^{\text{fail}} f_B^{\text{fail}}(m_{\text{tag-fail}}) \end{aligned} \quad (6.8)$$

where $f_{\text{tag-pass}}(m_{\text{tag-pass}})$ and $f_{\text{tag-fail}}(m_{\text{tag-fail}})$ are the tag-pass and tag-fail PDFs, respectively; ϵ is the efficiency; N_S is the total number of Z signal events summed over both samples; $f_S^{\text{pass}}(m_{\text{tag-pass}})$ and $f_S^{\text{fail}}(m_{\text{tag-fail}})$ are the tag-pass and tag-fail signal PDFs, respectively; N_B^{pass} and N_B^{fail} are the numbers of background events in the tag-pass and tag-fail samples, respectively; and $f_B^{\text{pass}}(m_{\text{tag-pass}})$ and $f_B^{\text{fail}}(m_{\text{tag-fail}})$ are the tag-pass and tag-fail background PDFs, respectively. This particular implementation of the tag and probe methodology is based on tag `CMSSW_4_2_5` of the CMSSW package `PhysicsTools/TagAndProbe`, and uses the MINUIT2 [107] library, as coded in RooFit [108], for the likelihood maximization. For this study, CMSSWv4.2.8 was used.

For both samples, the signal shape is assumed to be a Crystal Ball function [109] convoluted with the Z generated lineshape, while the background shape is a PDF that describes the falling background as well as the kinematic turn-on at low invariant mass. The background PDF, called `RooCMSShape` [106], is given by

$$f_{\text{RooCMSShape}}(x) = \begin{cases} 1e20 & \text{for } (x - \mu)\gamma < -70 \\ 0 & \text{for } (x - \mu)\gamma > 70 \\ \text{erfc}((\alpha - x)\beta) \exp(-(x - \mu)\gamma) & \text{otherwise} \end{cases} \quad (6.9)$$

where α , β , γ , and μ are parameters of the fit, most of which are held fixed. In the three lowest E_T bins, all parameters of the tag-pass and tag-fail background PDFs are left floating, because the effect of the relaxed E_T cuts has a significant effect on

1644 the background shape. More details of the signal and background PDFs are given
 1645 in Table 6.6. The fixed signal and background parameter values were determined by
 1646 fitting a small sample ($0.0 \leq \eta < 0.25$) of Fall11 MC signal (DYJetsToLL) and back-
 1647 ground (QCD_Pt-20to30_BCtoE, QCD_Pt-30to80_BCtoE, QCD_Pt-80to170_BCtoE,
 1648 GJet_Pt-20_doubleEMEnriched, WJetsToLNu, TTJets) with parameters left float-
 1649 ing.⁴

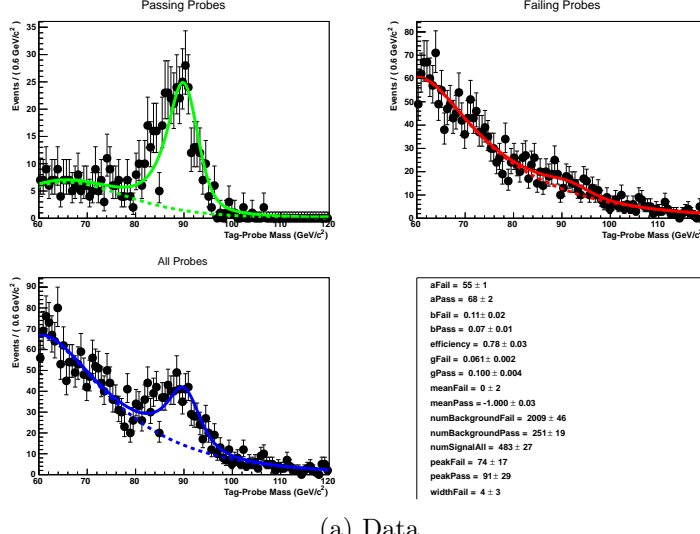
Table 6.6: Parameter values (parameter definitions are in the text) for the signal and background PDFs for the different samples. The background PDF applies to all efficiency bins except the four lowest E_T bins, which use a floating `RooCMSShape` background. When a bracketed range is given, the parameter is allowed to float within that range. When a constant is given, the parameter is fixed to that constant.

PDF	Crystal Ball fit parameters				RooCMSShape fit parameters			
	μ	σ	α	n	μ	α	β	γ
Tag-pass signal	[-1.0, 1.0]	[1.0, 3.0]	0.87	97.0	N/A	N/A	N/A	N/A
Tag-fail signal	[-1.0, 1.0]	[1.0, 3.0]	0.73	134.9	N/A	N/A	N/A	N/A
Tag-pass background	N/A	N/A	N/A	N/A	65.0	61.949	0.04750	0.01908
Tag-fail background	N/A	N/A	N/A	N/A	α	[50.0, 100.0]	0.065	0.048

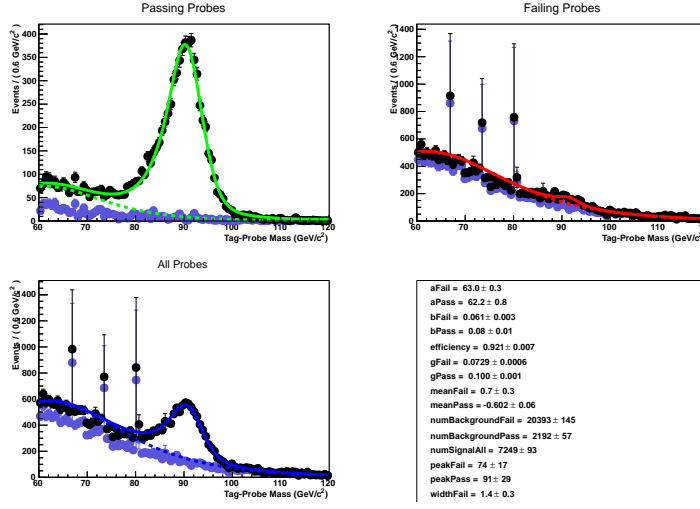
Added

1650 Some fit examples are shown in Figures 6.15 and 6.16. In Fig. 6.15, which shows fits
 1651 fits to data and MC for $15 \text{ GeV} \leq \text{probe } E_T < 20 \text{ GeV}$, the kinematic turn-on is below
 1652 the invariant mass range covered by the plot. The exponentially falling background
 1653 is easily seen underneath the signal, and is especially pronounced in the background-
 1654 dominated tag-fail sample.

⁴See Appendix A for a discussion of the MC samples.



(a) Data.



(b) MC. The purple points are the background MC (photon + jet, W, QCD, and t̄t).

Figure 6.15: Tag and probe invariant mass fits for $15 \text{ GeV} \leq \text{probe } E_T < 20 \text{ GeV}$. Errors are statistical only. The tag-pass fit is shown in green in the upper-left-hand plot, the tag-fail fit in red in the upper-right-hand plot, and a fit to both samples in blue in the lower-left-hand plot. Dotted lines are the background components of the fits; solid lines are signal plus background.

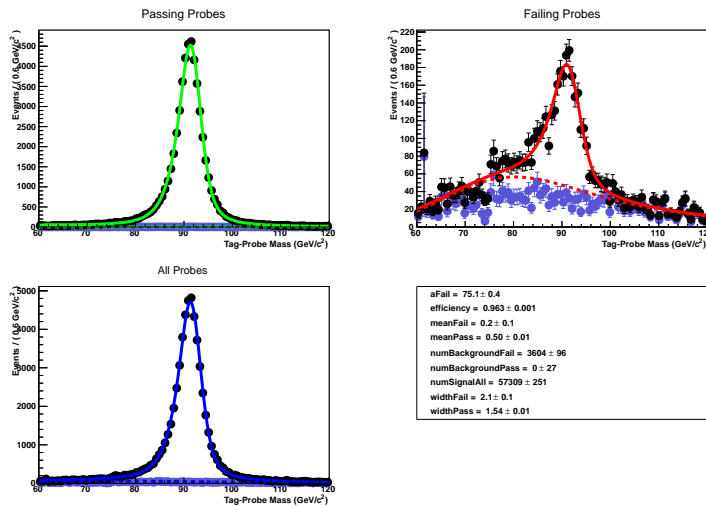
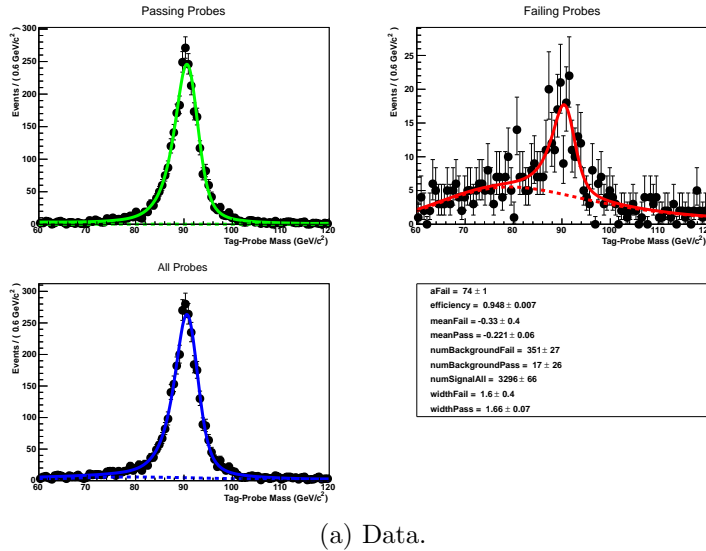


Figure 6.16: Tag and probe invariant mass fits for $-0.25 \leq \text{probe } \eta < -0.5$. Errors are statistical only. The tag-pass fit is shown in green in the upper-left-hand plot, the tag-fail fit in red in the upper-right-hand plot, and a fit to both samples in blue in the lower-left-hand plot. Dotted lines are the background components of the fits; solid lines are signal plus background.

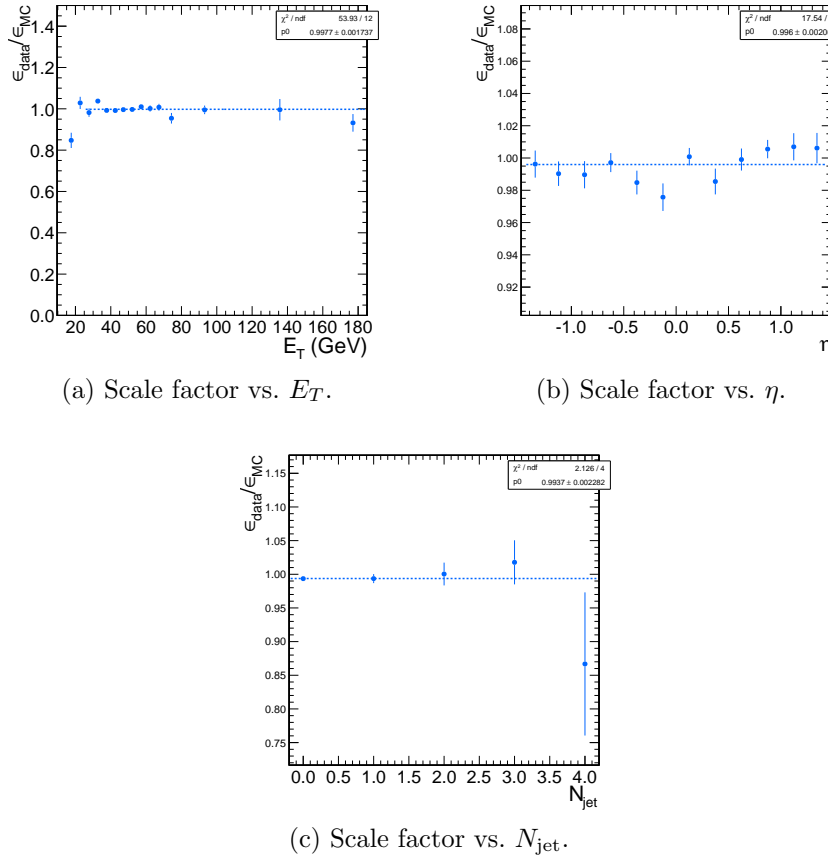


Figure 6.17: Dependence of the photon ID efficiency scale factor on some kinematic variables. Errors are statistical only.

1655 6.4.2 Photon Efficiency Scale Factor $\epsilon_e^{\text{data}}/\epsilon_e^{\text{MC}}$

1656 Figure 6.17 shows the dependence of the photon ID efficiency scale factor $\epsilon_e^{\text{data}}/\epsilon_e^{\text{MC}}$
1657 on E_T , η , and N_{jet} , where jets are defined as in Table 6.2, but with only the two
1658 Z electrons considered as candidates for overlap removal. Errors are statistical only.
1659 There no significant dependence of the scale factor on these variables, so only one
1660 scale factor is computed from the entire dataset.

1661 The effect of pileup is studied by comparing the efficiencies ϵ_e^{data} and ϵ_e^{MC} vs. the
1662 number of primary vertices (N_{PV}) in the event. The efficiency only drops a few percent
1663 for events with large N_{PV} after using pileup-corrected isolation cuts, as can be seen in
1664 Figure 6.18a. The MC tracks the data, and the scale factor is flat vs. N_{PV} , as shown

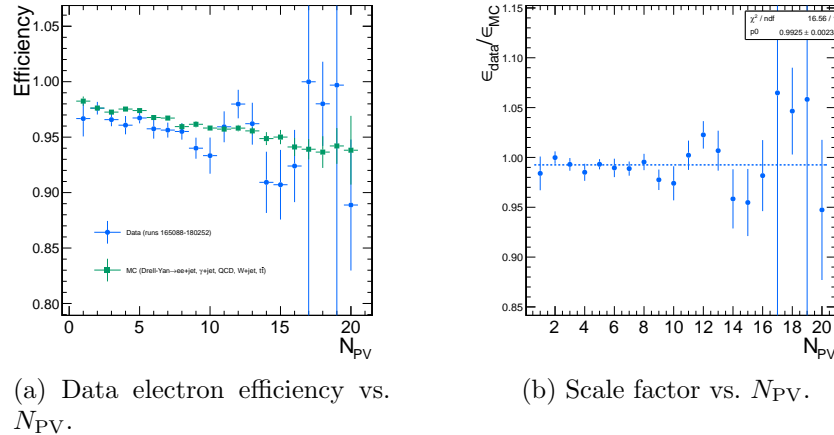


Figure 6.18: Dependence of the photon ID efficiency scale factor on the number of primary vertices per event. Errors are statistical only.

in Fig. 6.18b.

The scale factor is measured to be $\epsilon_e^{\text{data}}/\epsilon_e^{\text{MC}} = 0.994 \pm 0.002(\text{stat.}) \pm 0.035(\text{syst.})$.

Four main sources of systematic error, in addition to the statistical error of 0.2%, were studied.

Different behavior of electrons and photons in MC Even though the photon ID cuts are designed to be similarly efficient for both electrons and photons, there might be a small difference in the performance between the two kinds of particles, e.g. because of electron bremsstrahlung. To check this effect, the MC electron ID efficiency was calculated using a $Z \rightarrow ee$ sample and the MC photon ID efficiency was calculated using a $\gamma + \text{jets}$ sample. Both samples were reconstructed in CMSSWv3.6. Half the difference between these two results, 0.5%, was taken as an error on the scale factor.

Pileup To account for the possibility that the MC simulation may not adequately reproduce the data in a high pileup environment, the data/MC scale factor for events with 1-4 good reconstructed primary vertices was calculated, along with the same for events with ≥ 5 good reconstructed primary vertices. The

Official

result

uses this

syst.

error, so

I am not

recheck-

ing

it

Corrected

some of

these

bullets

1681 difference between the scale factors from both samples, 2.4%, was taken as an
 1682 error on the scale factor from pileup.

1683 **Signal fit over/underestimation** It was found that the signal fit slightly under-
 1684 estimates the data in the tag-pass sample, and slightly overestimates it in the
 1685 tag-fail sample. To cover this effect with a systematic error, the efficiencies in
 1686 data and MC, and then the scale factor, were recalculated using the background
 1687 (from fit) subtracted integrals of the tag-pass and tag-fail distributions, rather
 1688 than the fitted signal yields in those distributions. The difference between the
 1689 scale factor found in this way and the nominal scale factor, 1.9%, was taken as
 1690 an error on the scale factor.

1691 **Signal and background shape assumption** To assess the magnitude of the error
 1692 from the signal and background shape assumptions, the tag-pass and tag-fail
 1693 tail parameters (Crystal Ball α and n) were varied by $\pm 1\sigma$, and the background
 1694 shape was varied between `RooCMSShape`, exponential, power law, and quadratic.
 1695 All possible combinations of varied parameters were generated, and the data and
 1696 MC were refit and new scale factors generated according to those combinations.
 1697 The error was taken as the largest deviation of the scale factor from nominal,
 1698 1.8%.

1699 Finally, the pixel veto efficiency was estimated from MC to be 0.96 ± 0.005 (syst.),
 1700 with error due to varying assumptions of the tracker material distribution [110]. In
 1701 general, the photon ID selection used in this analysis is very efficient for GGM photons
 1702 and robust to pileup, and its efficiency is fairly well measured.

1703

Chapter 7

1704

Data Analysis

1705 The signature of GGM SUSY particle production in this search is an excess of two-
1706 photon events with high \cancel{E}_T . \cancel{E}_T is reconstructed using the particle flow algorithm
1707 as described in Sec. 6.1.3. Candidate two-photon events, as well as control events,
1708 are selected according to the offline object criteria presented in Secs. 6.1.1, 6.1.2,
1709 and 6.1.3; the event quality criteria in Sec. 6.3; and the trigger requirements in Sec. 6.2.
1710 These are summarized in Table 7.1.

Table 7.1: Selection criteria for $\gamma\gamma$, $e\gamma$, ee , and ff events.

Variable	Cut			
	$\gamma\gamma$	$e\gamma$	ee	ff
HLT match	IsoVL	IsoVL	IsoVL	IsoVL R9Id
E_T	$> 40/ > 25 \text{ GeV}$			
$\text{SC } \eta $	< 1.4442	< 1.4442	< 1.4442	< 1.4442
H/E	< 0.05	< 0.05	< 0.05	< 0.05
$R9$	< 1	< 1	< 1	< 1
Pixel seed	No/No	Yes/No	Yes/Yes	No/No
$I_{\text{comb}}, \sigma_{inj\eta}$	$< 6 \text{ GeV} \&& < 0.011$	$< 6 \text{ GeV} \&& < 0.011$	$< 6 \text{ GeV} \&& < 0.011$	$< 20 \text{ GeV} \&& (\geq 6 \text{ GeV} \parallel \geq 0.011)$
JSON	Yes	Yes	Yes	Yes
No. good PVs	≥ 1	≥ 1	≥ 1	≥ 1
ΔR_{EM}	> 0.6	> 0.6	> 0.6	> 0.6
$\Delta\phi_{\text{EM}}$	≥ 0.05	≥ 0.05	≥ 0.05	≥ 0.05

1711 This search utilizes 4.7 fb^{-1} of CMS data collected during the period April-
 1712 December 2011, corresponding to the following datasets [111]:

- 1713 • /Photon/Run2011A-05Jul2011ReReco-ECAL-v1/AOD
- 1714 • /Photon/Run2011A-05Aug2011-v1/AOD
- 1715 • /Photon/Run2011A-03Oct2011-v1/AOD
- 1716 • /Photon/Run2011B-PromptReco-v1/AOD

1717 The search strategy is to model the backgrounds to the GGM SUSY signal using
 1718 \cancel{E}_T shape templates derived from the control samples, and then to look for a high- \cancel{E}_T
 1719 excess above the estimated background in the $\gamma\gamma$ sample. There are two categories
 1720 of backgrounds: QCD processes with no real \cancel{E}_T and electroweak processes with real
 1721 \cancel{E}_T from neutrinos. The relevant QCD background processes are multijet production
 1722 with at least two jets faking photons, photon + jet production with at least one jet
 1723 faking a photon, and diphoton production, and Z production with a radiated photon
 1724 where at least one of the Z decay products (typically a jet) fakes a photon. The
 1725 relevant electroweak background processes, which are small compared to the QCD
 1726 background, involve $W \rightarrow e\nu$ decay with a recoiling jet that fakes a photon or a
 1727 real radiated photon (the W may come from the decay of a top quark in $t\bar{t}$ events).
 1728 In both cases, the electron is misidentified as a photon due to a small inefficiency
 1729 in reconstructing the electron pixel seed. The main diagrams contributing to the
 1730 QCD(electroweak) backgrounds are shown in Figure 7.1(7.2).

1731 Data control samples are used to model all of the backgrounds. The primary
 1732 control sample used to model the QCD background is the ff sample, which is similar
 1733 to the candidate $\gamma\gamma$ sample but with combined isolation or $\sigma_{inj\eta}$ cuts inverted. The cuts
 1734 on these variables are used to distinguish between photons and jets, so by inverting
 1735 those cuts, the resulting ff sample becomes enriched with QCD dijets. Because the

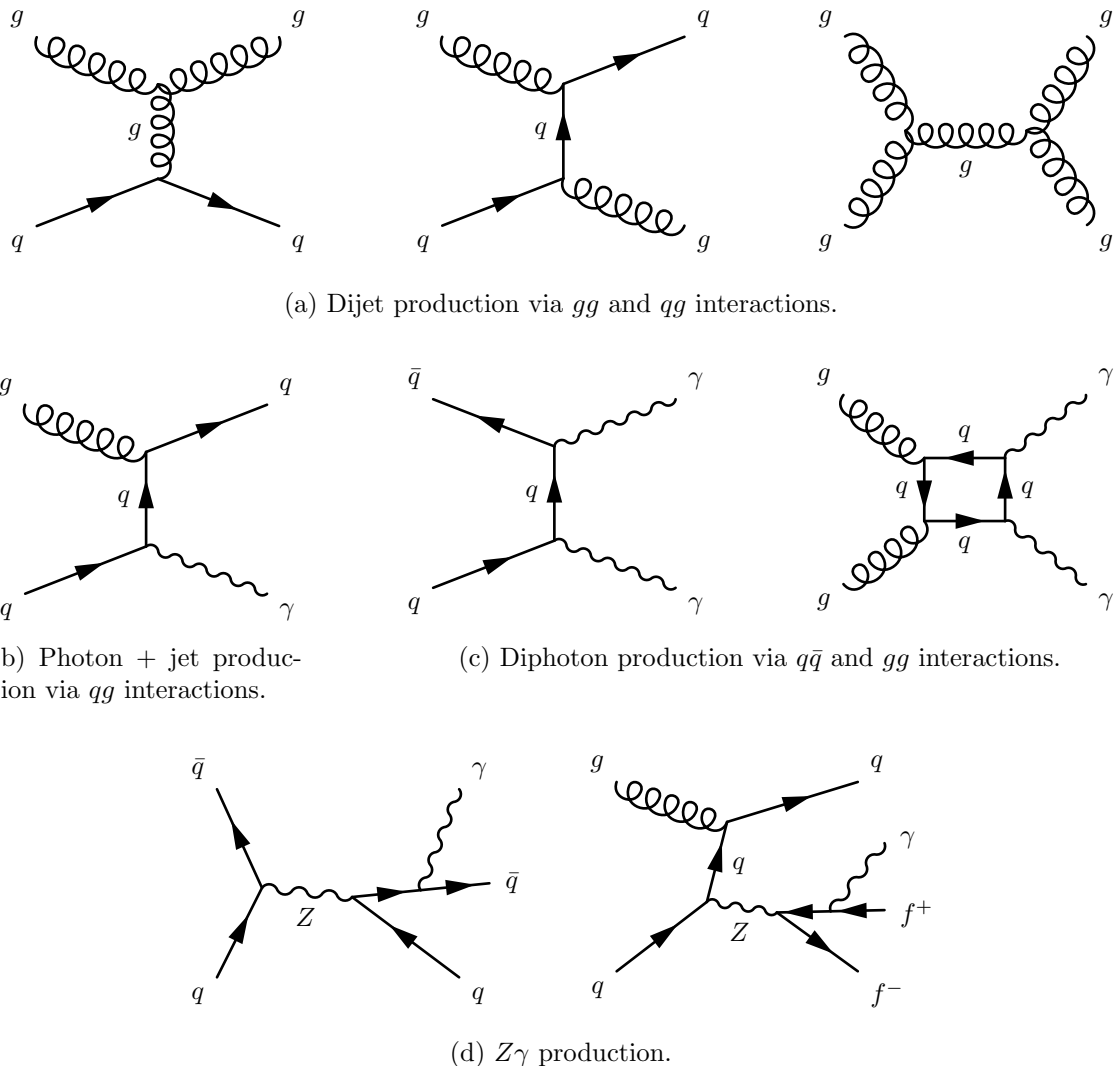


Figure 7.1: Representative Feynman diagrams of some QCD backgrounds to the GGM SUSY search.

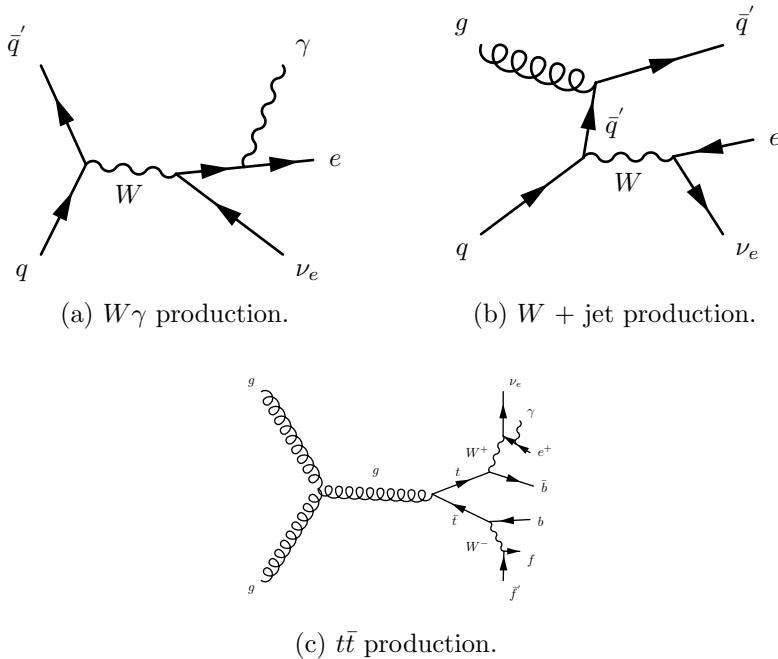


Figure 7.2: Representative Feynman diagrams of some electroweak backgrounds to the GGM SUSY search.

1736 fake photons are still required to pass a tight cut on H/E , they are guaranteed to be
 1737 very electromagnetic jets, with an EM energy scale and resolution similar to that of
 1738 the candidate photons. This insures that the resulting estimate of the \cancel{E}_T shape does
 1739 not have too long of a tail from severe HCAL mis-measurements that are actually
 1740 rare in the $\gamma\gamma$ sample.

1741 As a cross-check, the ee sample is also used to model the QCD background. This
 1742 sample of Z decays should have no true \cancel{E}_T , just like the ff sample, and the electron
 1743 definition (differing from the photon definition only in the presence of a pixel seed)
 1744 insures that the electron energy scale and resolution is similar to that of the photon.

1745 Finally, the $e\gamma$ sample is used to model the electroweak background from $W \rightarrow e\nu$
 1746 decays. The $e\gamma$ \cancel{E}_T distribution is scaled by the electron \rightarrow photon misidentification
 1747 rate to predict the number of $W\gamma$, $W +$ jet, and $t\bar{t}$ events in the $\gamma\gamma$ sample.

1748 The remainder of this chapter describes the data analysis procedures and the final
 1749 results of the search. Sec. 7.1 addresses the QCD background estimation. Sec. 7.2

1750 addresses the electroweak background estimation. The chapter concludes with a dis-
 1751 cussion of systematic errors in Sec. 7.3 and a presentation of the final results in
 1752 Sec. 7.4.

1753 7.1 Modeling the QCD Background

1754 7.1.1 Outline of the Procedure

1755 Due to the fact that the CMS ECAL energy resolution is much better than the
 1756 HCAL energy resolution, the energies of the two candidate photons in the events of
 1757 the $\gamma\gamma$ sample are typically measured to far greater accuracy and precision than the
 1758 energy of the hadronic recoil in those events. Therefore, fake E_T in the $\gamma\gamma$ sample
 1759 is almost entirely the result of hadronic mis-measurement in QCD dijet, photon +
 1760 jet, and diphoton events. The strategy employed to model this background is to find
 1761 a control sample in data consisting of two well-measured EM objects, just like the
 1762 candidate $\gamma\gamma$ sample, and assign each event a weight to account for the underlying
 1763 kinematic differences between the control and candidate samples. Once the reweighted
 1764 E_T spectrum of the control sample is created, it is then normalized in the low- E_T
 1765 region, the assumption being that GGM SUSY does not predict a significant amount
 1766 of events at low E_T . There are three aspects of this QCD background estimation
 1767 procedure that bear highlighting:

1768 **Choice of control sample** Since the underlying cause of E_T in the candidate sam-
 1769 ple is mis-measured hadronic activity, a control sample with similar hadronic
 1770 activity to the candidate sample should be chosen. Hadronic activity refers to
 1771 number of jets, jet E_T , pileup, etc.

1772 **Reweighting** The control sample is reweighted so that its E_T spectrum appears as it
 1773 would if the control sample had the same kinematic properties as the candidate

sample (i.e. particle p_T and η distributions, etc.). By choosing an appropriate control sample and reweighting it, the control \cancel{E}_T distribution should now match both the hadronic activity and the kinematics of the candidate sample.

Normalization Finally, the control E_T distribution is normalized in a region of low \cancel{E}_T , where contamination from the expected GGM SUSY signal is small. This implies an extrapolation of the low- \cancel{E}_T QCD background prediction to the high- \cancel{E}_T signal region.

As explained in the beginning of this chapter, the ff sample is used as the primary QCD control sample, while the ee sample is used as a cross-check. Both samples have two well-measured EM objects per event, no real \cancel{E}_T , and similar hadronic activity to the $\gamma\gamma$ sample. Figure 7.3 shows a comparison of the shapes of some distributions relevant to hadronic activity between the $\gamma\gamma$, ee , and ff samples. In general, the ee sample has less hadronic activity than the $\gamma\gamma$ and ff samples, as shown by the more steeply falling ee distributions in Figs. 7.3a, 7.3b, 7.3c, and 7.3d. In addition to the kinematic reweighting, there is also a reweighting by number of jets per event, which attempts to correct for this difference (see Sec. 7.1.2).

7.1.2 Reweighting

To reweight the control sample events to match the kinematics of the candidate sample events, a weight based on the p_T of the di-EM-object system and the number of jets in the event is used. As explained in Sec. 7.1.1, E_T in the $\gamma\gamma$, ff , and ee samples is due to the poorly measured hadronic recoil off the well-measured di-EM system. Therefore, the p_T of the di-EM system is a good handle on the true magnitude of the hadronic recoil, which affects the measured \cancel{E}_T . The di-EM system is depicted in Figure 7.4. As shown in Figure 7.5, \cancel{E}_T is largely uncorrelated with di-EM p_T , so there is little danger of reweighting away a true signal excess.

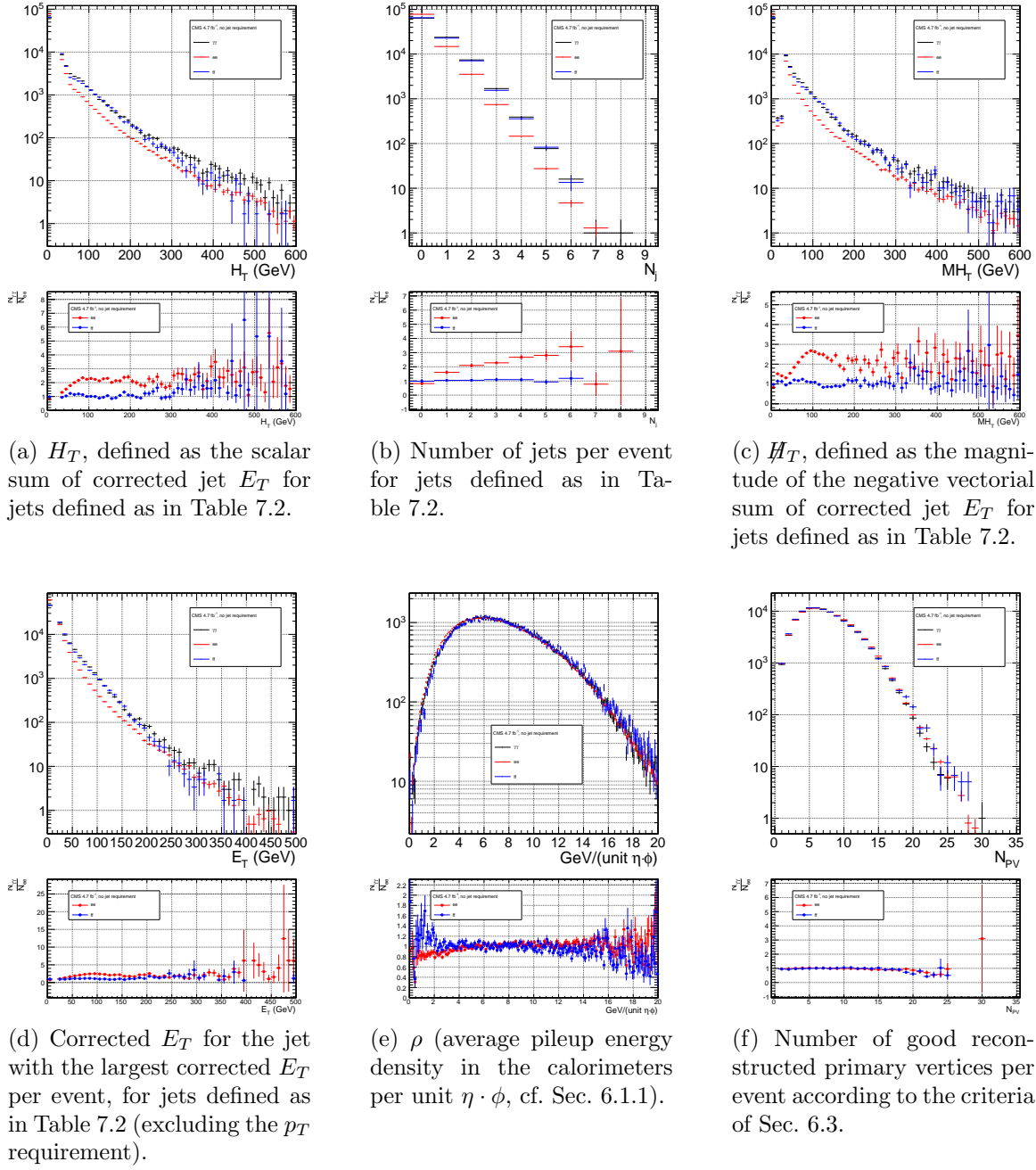


Figure 7.3: Comparison of the shapes of some distributions relevant to hadronic activity between the $\gamma\gamma$, ee ($81 \text{ GeV} \leq m_{ee} < 101 \text{ GeV}$), and ff samples. The ee and ff distributions are normalized to the number of events in the $\gamma\gamma$ distribution. Errors are statistical only.

Table 7.2: Definition of HB/HE/HF hadronic jets.

Variable	Cut
Algorithm	L1FastL2L3Residual corrected PF (cf. Sec. 6.1.3)
p_T	$> 30 \text{ GeV}$
$ \eta $	< 5.0
Neutral hadronic energy fraction	< 0.99
Neutral electromagnetic energy fraction	< 0.99
Number of constituents	> 1
Charged hadronic energy	$> 0.0 \text{ GeV}$ if $ \eta < 2.4$
Number of charged hadrons	> 0 if $ \eta < 2.4$
Charged electromagnetic energy fraction	< 0.99 if $ \eta < 2.4$
ΔR to nearest PF electron ^a , muon ^b , or one of the two primary EM objects	> 0.5

^aA PF electron is defined as an electron reconstructed with the PF algorithm [86] with $p_T > 15 \text{ GeV}$, $|\eta| < 2.6$, and $(I_{\text{charged}} + I_{\text{photon}} + I_{\text{neutral}})/p_T < 0.2$, where $I_{\text{charged}}(I_{\text{photon}})(I_{\text{neutral}})$ is the sum of PF charged hadron(PF photon)(PF neutral hadron) momenta in a $\Delta R = 0.4$ cone around the PF electron.

^bMuons are reconstructed [87] from a combination of muon station and inner tracker hits. Here, a muon must have track $\chi^2 < 10$, at least one good muon station hit, inner track transverse impact parameter $< 0.02 \text{ cm}$, inner track longitudinal impact parameter $< 0.5 \text{ cm}$, $p_T > 15 \text{ GeV}$, $|\eta| < 2.6$, and $(I_{\text{ECAL}} + I_{\text{HCAL}} + I_{\text{track}})/p_T < 0.2$, where $I_{\text{ECAL}}(I_{\text{HCAL}})(I_{\text{track}})$ is the sum of ECAL(HCAL)(track) momenta in a $\Delta R = 0.3$ cone around the muon.

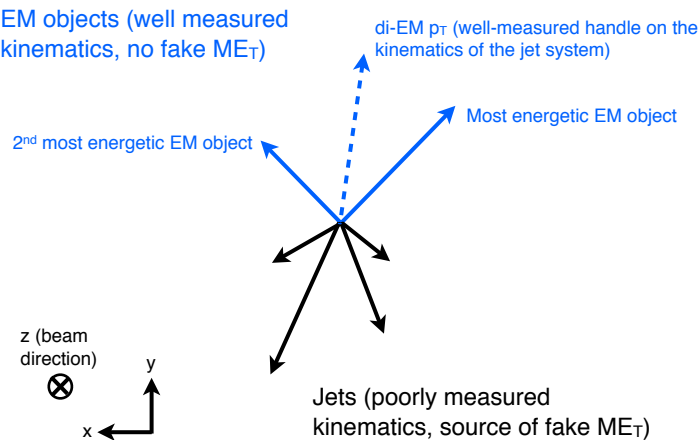


Figure 7.4: Cartoon showing the di-EM system in blue and the hadronic recoil in black. The di-EM p_T (dashed blue line) is used to reweight the control sample kinematic properties to match those of the candidate $\gamma\gamma$ sample.

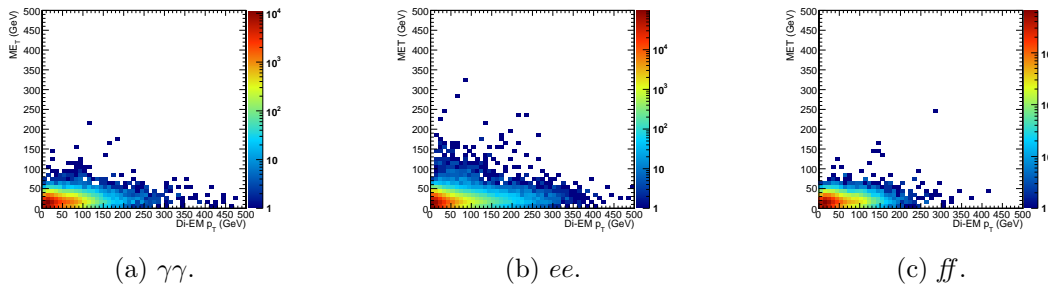


Figure 7.5: \not{E}_T vs. di-EM p_T .

Whereas the di-EM p_T reweighting accounts for differences in production kinematics between the control and $\gamma\gamma$ samples, a simultaneous reweighting based on the number of jets in the event accounts for differences in hadronic activity between the samples, especially between ee and $\gamma\gamma$ (cf. Fig. 7.3). Jets are defined as in Table 6.2. Figure 7.6 shows the effect of reweighting by number of jets per event, which is to increase(decrease) the tail of the $ee(ff)$ E_T spectrum.

1805 Although the electron and photon energies are well measured by the ECAL, the
 1806 ECAL-only measurement of the fake photon energy (cf. Sec 6.1.1) is biased slightly
 1807 low due to the fact that fakes (which are really jets) tend to deposit some energy in
 1808 the HCAL. This can be seen in Figs. 7.7 and 7.8, which show the relative difference
 1809 between the ECAL-only E_T measurement and the PF E_T measurement vs. EMF for
 1810 electrons, photons, and fakes. PF E_T is defined as the L1Fast-corrected E_T of the
 1811 nearest PF jet with $p_T \geq 20$ GeV (i.e., the E_T of the PF jet object reconstructed from
 1812 the same ECAL shower as the fake photon). On average, the fakes tend to deposit
 1813 a few percent more energy in the HCAL than the electrons or photons, which is
 1814 recovered by the PF algorithm. For this reason, the PF p_T is used in the calculation
 1815 of di-EM p_T rather than the ECAL-only p_T .¹ This leads to a modest improvement in
 1816 the agreement between the ee and ff E_T spectra, as shown in Figure 7.9.

1817 The control sample event weights are defined as

¹In the few events ($\mathcal{O}(10^{-3})$) in which two PF jet objects, corresponding to the two electrons or fakes, are not found, the ECAL-only p_T is used.

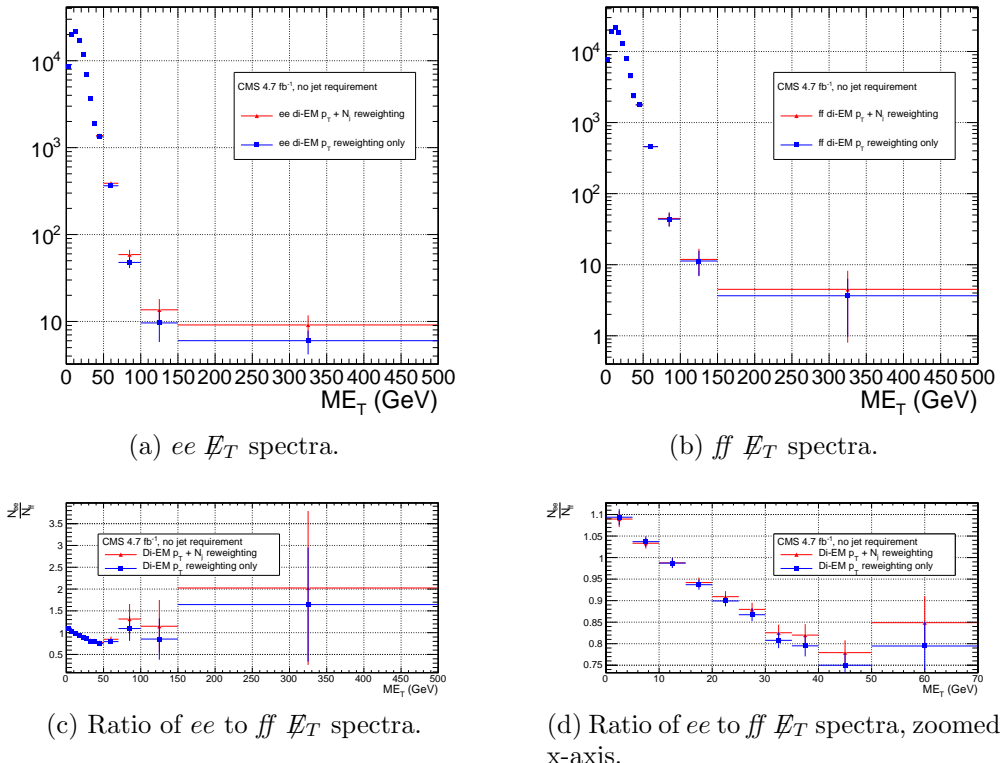


Figure 7.6: \cancel{E}_T spectra of the reweighted ee ($81 \text{ GeV} \leq m_{ee} < 101 \text{ GeV}$) and ff control samples. Blue squares indicate di-EM p_T reweighting only; red triangles indicate di-EM $p_T + \text{number of jets}$ reweighting. PF p_T (cf. p. 132) is used to calculate the di-EM p_T . The full normalization procedure is employed, along with ee sideband subtraction (discussed at the end of this section). Error bars are statistical only.

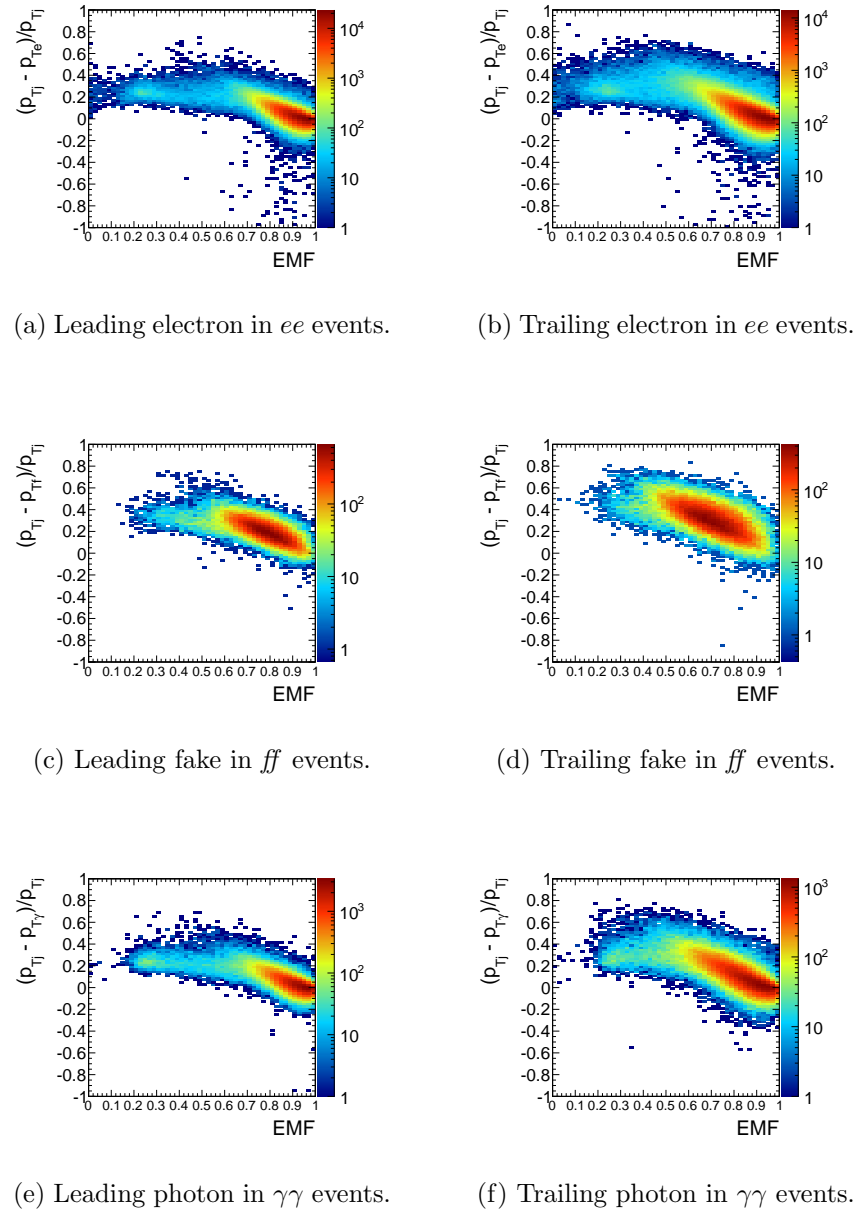


Figure 7.7: Relative difference between the ECAL-only E_T measurement and the PF E_T measurement vs. EMF. PF E_T is defined in the text.

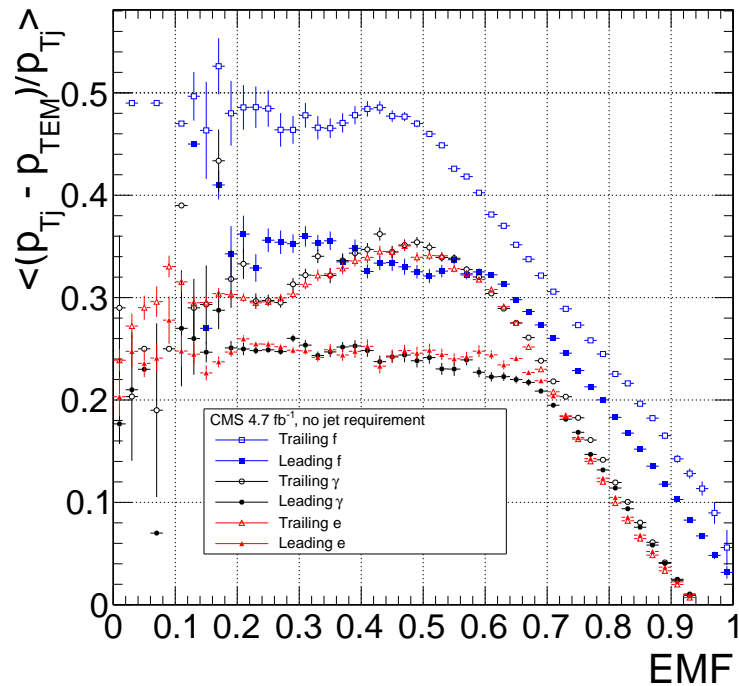


Figure 7.8: Average relative difference between the ECAL-only E_T measurement and the PF E_T measurement vs. EMF for the leading (filled marker) and trailing (open marker) electrons in ee events (red triangles), fakes in ff events (blue squares), and photons in $\gamma\gamma$ events (black circles). These are nothing more than profile histograms of Fig. 7.7. PF E_T is defined in the text. Error bars are statistical only.

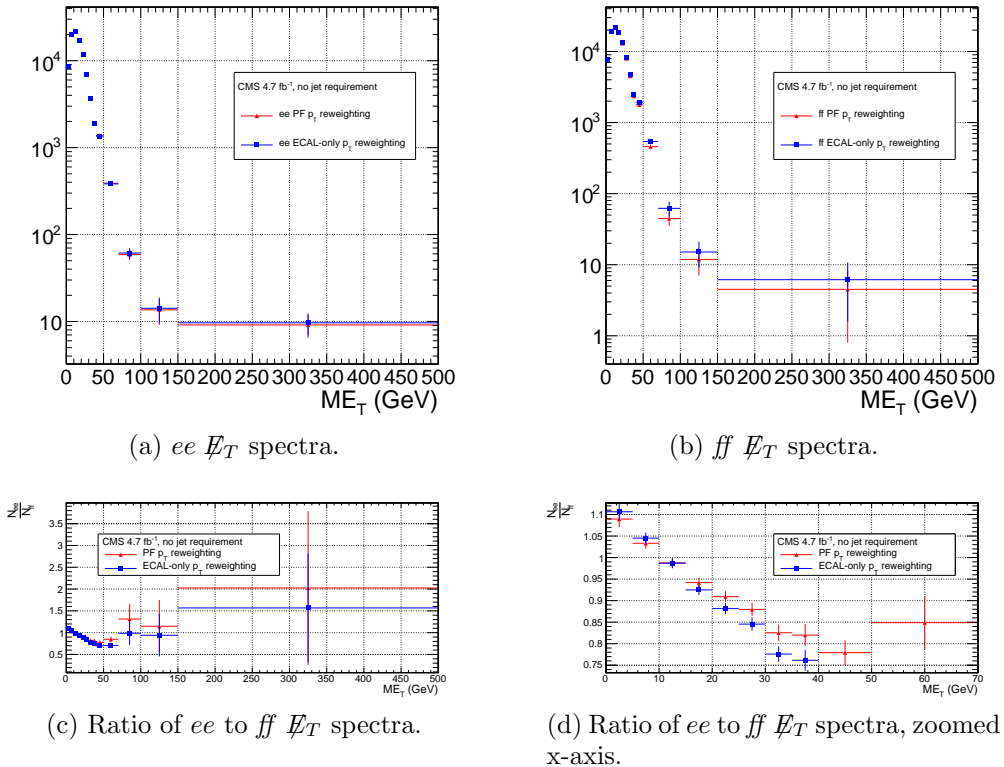


Figure 7.9: E_T spectra of the reweighted ee ($81 \text{ GeV} \leq m_{ee} < 101 \text{ GeV}$) and ff control samples. Blue squares indicate reweighting using the ECAL-only p_T estimate; red triangles indicate reweighting using the PF p_T estimate. The full reweighting and normalization procedure is employed, along with ee sideband subtraction (discussed at the end of this section). Error bars are statistical only.

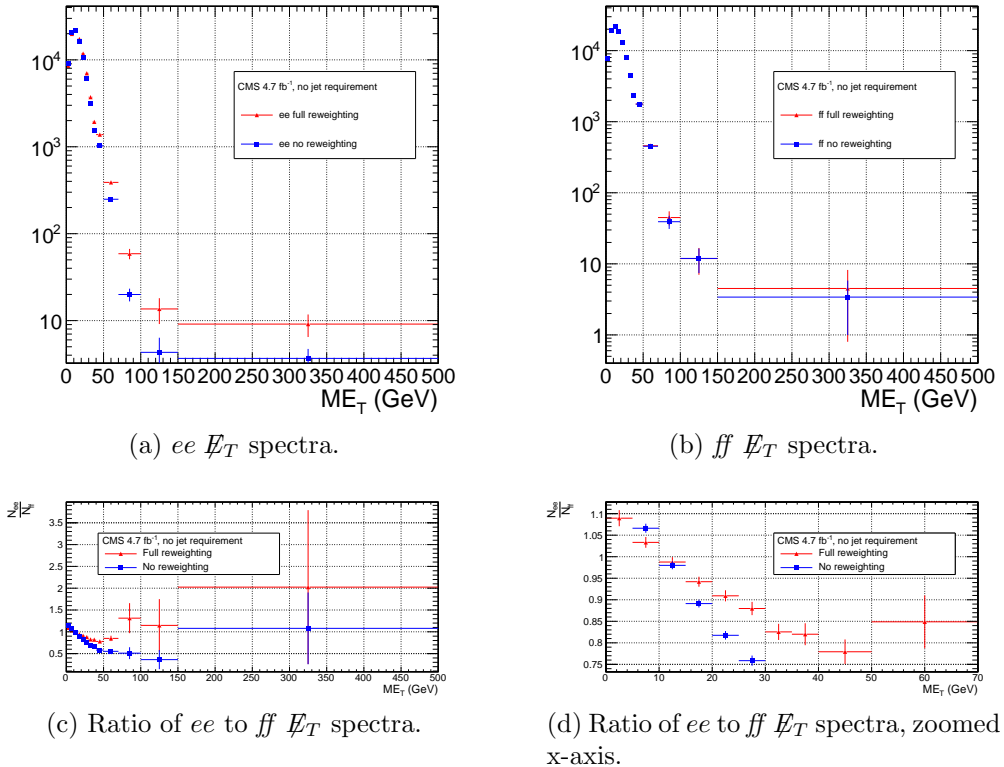


Figure 7.10: \cancel{E}_T spectra of the ee ($81 \text{ GeV} \leq m_{ee} < 101 \text{ GeV}$) and ff control samples. Red triangles indicate full di-EM $p_T +$ number of jets reweighting; blue squares indicate no reweighting. PF p_T (cf. p. 134) is used to calculate the di-EM p_T . The full normalization procedure is employed, along with ee sideband subtraction (discussed at the end of this section). Error bars are statistical only.

$$w_{ij} = \frac{N_{\text{control}}}{N_{\gamma\gamma}} \frac{N_{\gamma\gamma}^{ij}}{N_{\text{control}}^{ij}} \quad (7.1)$$

1818 where i runs over the number of di-EM p_T bins, j runs over the number of jet bins,
 1819 N_{control} is the total number of events in the control sample, $N_{\gamma\gamma}$ is the total number of
 1820 events in the $\gamma\gamma$ sample, $N_{\gamma\gamma}^{ij}$ is the number of $\gamma\gamma$ events in the i^{th} di-EM p_T bin and
 1821 j^{th} jet bin, and N_{control}^{ij} is the number of control sample events in the i^{th} di-EM p_T
 1822 bin and j^{th} jet bin. The effect of the reweighting is more significant for the ee sample
 1823 than for the ff sample, as shown in Figure 7.10.

1824 The ee sample contains a non-negligible background of $t\bar{t}$ events in which both
 1825 W bosons decay to electrons. These events have significant real \cancel{E}_T from the two
 1826 neutrinos (unlike the $\gamma\gamma$ events), and therefore inflate the background estimate at
 1827 high \cancel{E}_T . In order to remove the $t\bar{t}$ contribution from the ee sample, a sideband
 1828 subtraction method is employed.

1829 Only events in the ee sample with $81 \text{ GeV} \leq m_{ee} < 101 \text{ GeV}$, where m_{ee} is the
 1830 di-electron invariant mass, are used in the QCD background estimate. This choice
 1831 maximizes the ratio of Z signal to background. The sidebands used to estimate the
 1832 background contribution within the Z window are defined such that $71 \text{ GeV} \leq m_{ee} <$
 1833 81 GeV and $101 \text{ GeV} \leq m_{ee} < 111 \text{ GeV}$.

1834 The full reweighting procedure is applied to the Z signal region and the two
 1835 sideband regions independently. Only Z signal events are used in the calculation of
 1836 the di-EM p_T weights for the Z signal region, and likewise only the events within
 1837 a given sideband region are used in the calculation of the weights for that region.
 1838 Assuming a constant $t\bar{t}$ background shape, the resulting reweighted sideband \cancel{E}_T
 1839 distributions are added together and subtracted from the reweighted Z signal \cancel{E}_T
 1840 distribution. The sideband subtracted Z signal \cancel{E}_T distribution is then normalized
 1841 as discussed in Secs. 7.1.1 and 7.1.3. The statistical and reweighting error from the
 1842 sideband regions is propagated to the error on the final ee QCD \cancel{E}_T estimate.

1843 The di-EM p_T weights for the two ee sideband regions are shown in Figure 7.11.
 1844 The overall scale of the weights, as well as the trend with di-EM p_T , is similar for
 1845 the two regions (except at high di-EM p_T , where the statistics are poor anyway).
 1846 Figure 7.12 shows the \cancel{E}_T spectra for the two sideband regions and the Z signal
 1847 region after subtraction. The shapes of the spectra indicate that the high- \cancel{E}_T $t\bar{t}$ tail,
 1848 present in the sideband distributions, was successfully subtracted from the Z signal
 1849 distribution.

1850 The ee ($81 \text{ GeV} \leq m_{ee} < 101 \text{ GeV}$), ff , and $\gamma\gamma$ di-EM p_T spectra for events with

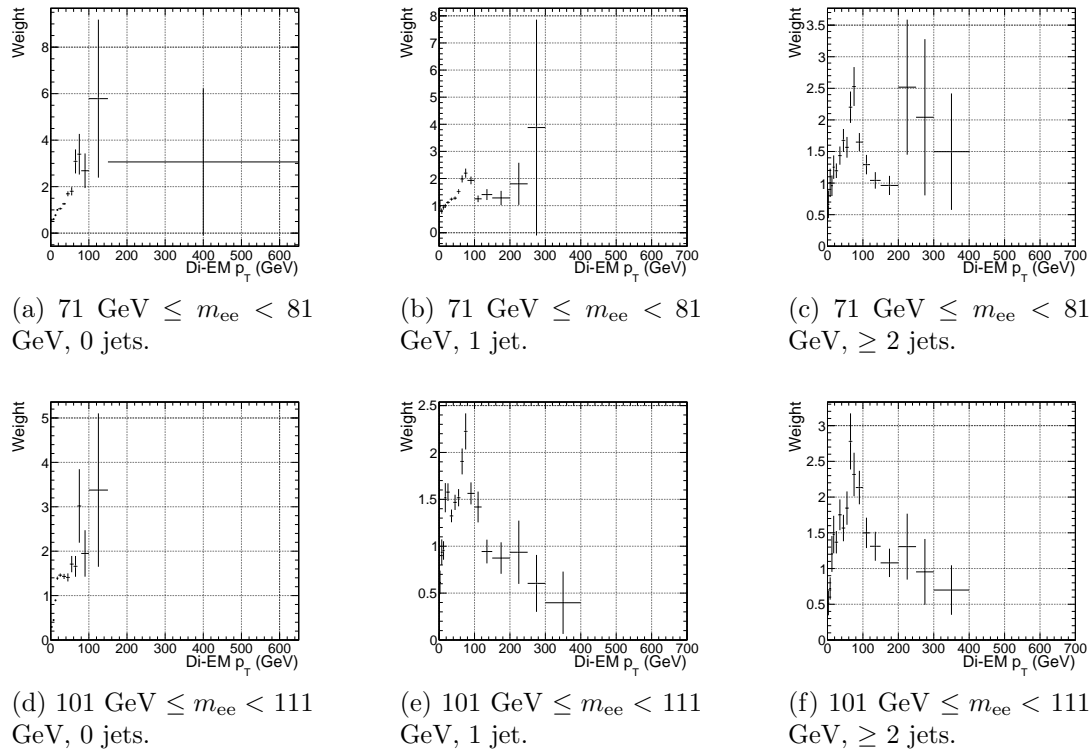


Figure 7.11: ee sideband di-EM p_T weights for events with 0, 1, or ≥ 2 jets (as in Table 6.2). Errors are statistical only.

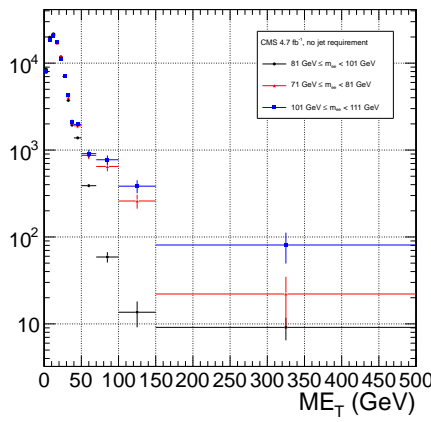


Figure 7.12: E_T spectra of the ee sample for $71 \text{ GeV} \leq m_{ee} < 81 \text{ GeV}$ (red triangles), $81 \text{ GeV} \leq m_{ee} < 101 \text{ GeV}$ (black circles), and $101 \text{ GeV} \leq m_{ee} < 111 \text{ GeV}$ (blue squares). The two sideband distributions (red and blue) and the Z signal distribution (black) are normalized to the total number of $\gamma\gamma$ events. Errors are statistical only.

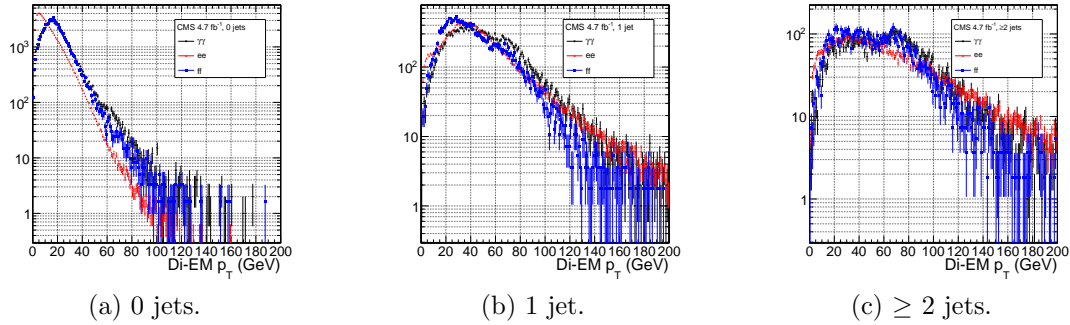


Figure 7.13: ee ($81 \text{ GeV} \leq m_{ee} < 101 \text{ GeV}$) (red triangles), ff (blue squares), and $\gamma\gamma$ (black circles) di-EM p_T spectra for events with 0, 1, or ≥ 2 jets (as in Table 6.2). Errors are statistical only.

1851 0, 1, or ≥ 2 jets (as in Table 6.2) are shown in Figure 7.13. Broad humps in the ff
 1852 and $\gamma\gamma$ spectra are due to kinematic ΔR and p_T turn-ons that are suppressed in the
 1853 ee sample due to the invariant mass cut. Figure 7.14 shows the weights applied to
 1854 the ee ($81 \text{ GeV} \leq m_{ee} < 101 \text{ GeV}$) and ff \cancel{E}_T spectra as a function of di-EM p_T and
 1855 number of jets per event.

1856 7.1.3 Normalization

After reweighting, the \cancel{E}_T distributions of the QCD control samples are normalized to the $\cancel{E}_T < 20$ GeV region of the candidate $\gamma\gamma \cancel{E}_T$ spectrum, where signal contamination is low. The normalization factor is $(N_{\gamma\gamma}^{\cancel{E}_T < 20\text{GeV}} - N_{e\gamma}^{\cancel{E}_T < 20\text{GeV}})/N_{\text{control}}^{\cancel{E}_T < 20\text{GeV}}$, where $N_{e\gamma}^{\cancel{E}_T < 20\text{GeV}}$ is the expected number of electroweak background events with $\cancel{E}_T < 20$ GeV (discussed in Section 7.2).

¹⁸⁶² 7.2 Modeling the Electroweak Background

¹⁸⁶³ $W\gamma$, $W + \text{jet}$, and $t\bar{t}$ processes in which the W decay electron is misidentified as a
¹⁸⁶⁴ photon (due to a failure to properly associate a pixel seed to the electron candidate)
¹⁸⁶⁵ can contribute significantly to the high- \cancel{E}_T tail of the $\gamma\gamma$ \cancel{E}_T spectrum. To estimate

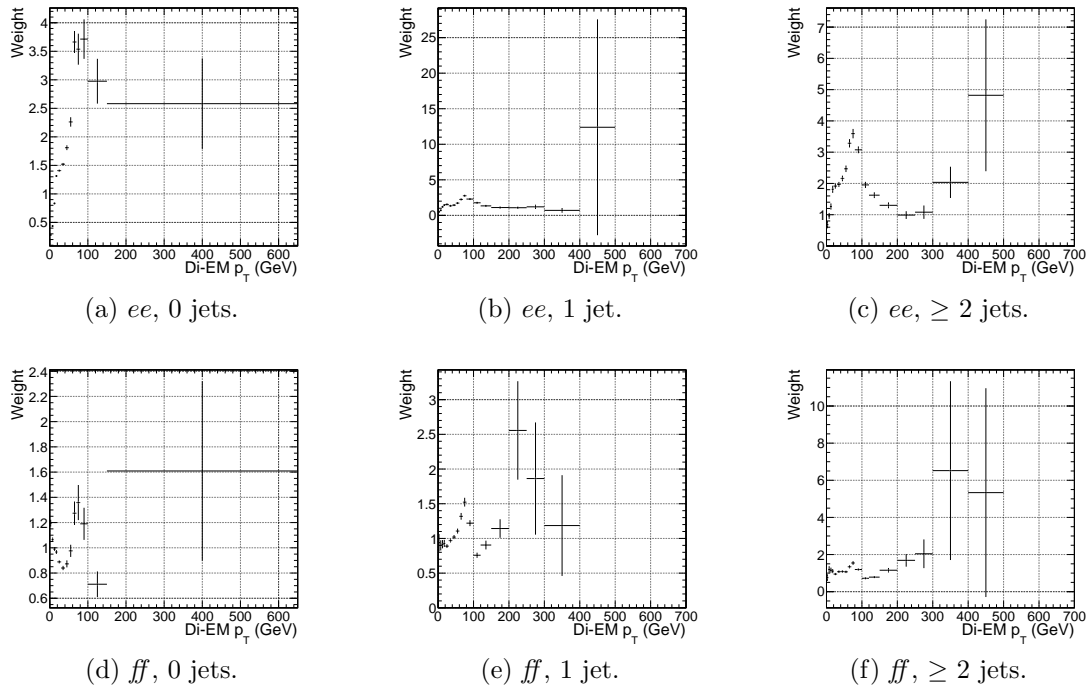


Figure 7.14: ee ($81 \text{ GeV} \leq m_{ee} < 101 \text{ GeV}$) and ff di-EM p_T weights for events with 0, 1, or ≥ 2 jets (as in Table 6.2). Errors are statistical only.

1866 this background, the $e\gamma$ sample, which is enriched in $W \rightarrow e\nu$ decays, is scaled by
 1867 $f_{e \rightarrow \gamma}/(1 - f_{e \rightarrow \gamma})$, where $f_{e \rightarrow \gamma}$ is the rate at which electrons are misidentified as photons.
 1868 The derivation of this scaling factor comes from the two equations

$$N_{e\gamma}^W = f_{e \rightarrow e} N_W \quad (7.2)$$

$$N_{\gamma\gamma}^W = (1 - f_{e \rightarrow e}) N_W \quad (7.3)$$

1869 where $N_{e\gamma}^W$ is the number of W events in the $e\gamma$ sample in which the electron was
 1870 correctly identified, $f_{e \rightarrow e}$ is the probability to correctly identify an electron, N_W is
 1871 the true number of triggered $W \rightarrow e\nu$ events, and $N_{\gamma\gamma}^W$ is the number of W events in
 1872 the $\gamma\gamma$ sample in which the electron was misidentified as a photon. The contribution
 1873 from $Z \rightarrow ee$ can be neglected (i.e. $f_{e \rightarrow \gamma}$ is small and the Z contribution involves
 1874 $f_{e \rightarrow \gamma}^2$, since both electrons have to be misidentified). Since $f_{e \rightarrow e} = 1 - f_{e \rightarrow \gamma}$, solving

1875 for $N_{\gamma\gamma}^W$ gives

$$N_{\gamma\gamma}^W = \frac{f_{e\rightarrow\gamma}}{1 - f_{e\rightarrow\gamma}} N_{e\gamma}^W \quad (7.4)$$

1876 $f_{e\rightarrow\gamma}$ is measured by fitting the Z peaks in the ee and $e\gamma$ samples. The number of
1877 Z events fitted in the ee and $e\gamma$ samples, respectively, is given by

$$N_{ee}^Z = (1 - f_{e\rightarrow\gamma})^2 N_Z \quad (7.5)$$

$$N_{e\gamma}^Z = 2f_{e\rightarrow\gamma}(1 - f_{e\rightarrow\gamma}) N_Z \quad (7.6)$$

1878 where N_Z is the true number of triggered $Z \rightarrow ee$ events. Solving for $f_{e\rightarrow\gamma}$ gives

$$f_{e\rightarrow\gamma} = \frac{N_{e\gamma}^Z}{2N_{ee}^Z + N_{e\gamma}^Z} \quad (7.7)$$

1879 A Crystal Ball function is used to model the Z signal shape in both the ee and
1880 $e\gamma$ samples, while an exponential convoluted with an error function (`RooCMSShape`,
1881 see Sec. 6.4.1) is used to model the background shape. The fixed fit parameters are
1882 identical for the two samples, but the other parameters are allowed to float indepen-
1883 dently. Table 7.3 shows the values and ranges of the fixed and floating fit parameters,
1884 respectively.

1885 Fits to the ee and $e\gamma$ invariant mass spectra are shown in Figure 7.15. Figure 7.16
1886 indicates that the dependence of $f_{e\rightarrow\gamma}$ on the electron p_T and η is small. (Note that all
1887 fit parameters are floating in the p_T -dependent fits.) Therefore, a constant misidenti-
1888 fication rate (derived from all ee and $e\gamma$ events), rather than a p_T - and η -dependent
1889 misidentification rate, is used in the final electroweak background estimate, with the

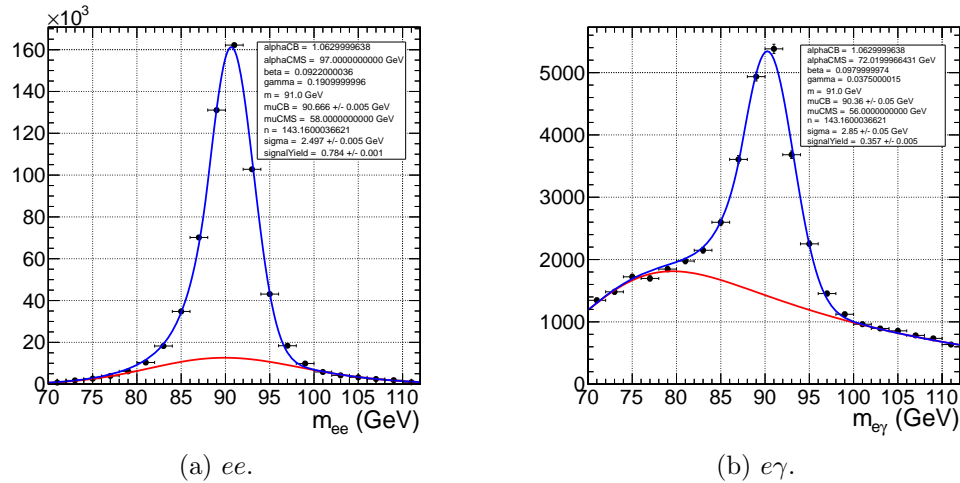


Figure 7.15: Fits to the ee and $e\gamma$ invariant mass spectra using the Crystal Ball RooCMSShape function described in the text and in Table 7.3. The total fit is shown in blue, while the background component is shown in red.

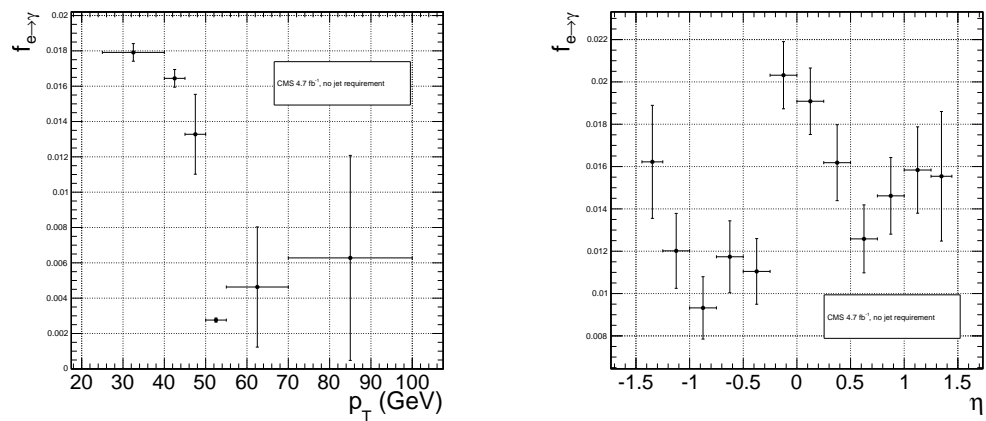
¹⁸⁹⁰ difference between the constant rate and the rate for electrons with p_T between 25
¹⁸⁹¹ and 40 GeV (the range in which the bulk of the trailing photons in the $\gamma\gamma$ sample
¹⁸⁹² lie) taken as a systematic error.

Using the integrals of the Z fits shown in Fig. 7.15, Eq. 7.7, and the p_T systematic discussed above, $f_{e \rightarrow \gamma}$ is calculated to be $0.014 \pm 0.000(\text{stat.}) \pm 0.004(\text{syst.})$. The scaled $e\gamma$ MET distribution is shown in Figure 7.17.

In the 36 pb^{-1} version of this analysis [112], it was shown that the ee sample could
 accurately predict the QCD and real Z contribution to the $e\gamma$ sample at low \cancel{E}_T , and
 that the expectation from $W \rightarrow e\nu$ MC accounted for the remaining W contribution
 at high \cancel{E}_T . A plot of the \cancel{E}_T distributions of the 2010 $e\gamma$ sample and the predicted
 components is shown in Figure 7.18. This exercise helps to validate both the QCD
 and electroweak background prediction methods.

Table 7.3: Parameter values for the signal and background PDFs for the ee and $e\gamma$ samples. When a bracketed range is given, the parameter is allowed to float within that range. When a constant is given, the parameter is fixed to that constant.

PDF	Crystal Ball fit parameters				RooCMSShape fit parameters			
	μ	σ	α	n	μ	α	β	γ
ee signal	[86.2, 96.2]	[1.0, 5.0]	1.063	143.16	N/A	N/A	N/A	N/A
$e\gamma$ signal	[86.2, 96.2]	[1.0, 5.0]	1.063	143.16	N/A	N/A	N/A	N/A
ee background	N/A	N/A	N/A	N/A	58	97.0	0.0922	0.191
$e\gamma$ background	N/A	N/A	N/A	N/A	56	72.02	0.098	0.0375



(a) $f_{e \rightarrow \gamma}$ vs. electron p_T . For the lowest p_T bin, the fit to the $e\gamma$ spectrum does not converge well, so the Z signal fraction is fixed to the value in Fig. 7.15b.

(b) $f_{e \rightarrow \gamma}$ vs. electron η .

Figure 7.16: $f_{e \rightarrow \gamma}$ vs. electron p_T and η .

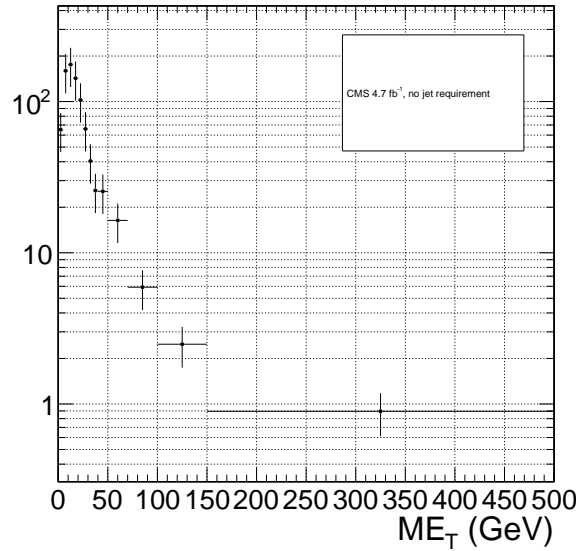


Figure 7.17: \cancel{E}_T spectrum of the $e\gamma$ sample after scaling by $f_{e \rightarrow \gamma}$. The total error on $f_{e \rightarrow \gamma}$ is propagated to the total error on the electroweak background estimate.

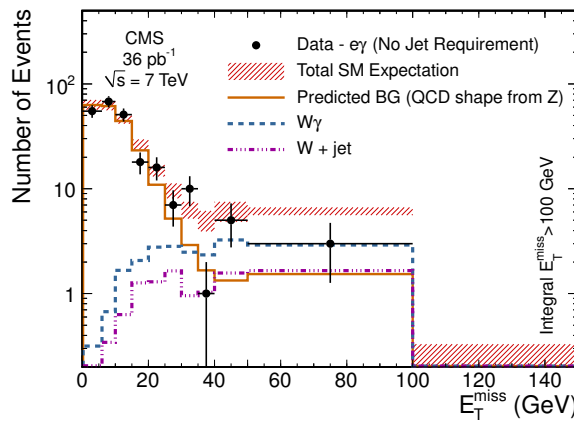


Figure 7.18: \cancel{E}_T spectrum of the $e\gamma$ sample in 36 pb^{-1} of 2010 LHC data scaled by the 2010 measured $f_{e \rightarrow \gamma}$ (black dots), QCD and real Z predicted background from the 2010 ee sample (solid orange line), MC $W + \text{jet}$ estimate (dash-dotted purple line), and MC $W\gamma$ estimate (dashed blue line). The total $e\gamma$ prediction (red band) is the sum of the ee , $W + \text{jet}$, and $W\gamma$ predictions. Reprinted from Fig. 2 of ref. [112].

1902 7.3 Errors on the Background Prediction

1903 The statistical error on the final background estimate in a particular \cancel{E}_T bin comes
 1904 from three sources: the number of control sample events collected in that bin, the
 1905 statistical error on the weights applied to events in that bin, and the statistics of the
 1906 normalization region. In the case of the ee control sample, there are contributions
 1907 from the statistics of the m_{ee} sidebands as well.

1908 In order to estimate the statistical error due to the reweighting procedure, 1000
 1909 toy sets of weights are generated. Each set includes a weight for each (di-EM p_T , N_j)
 1910 bin, with the values picked from a Gaussian distribution with mean and standard
 1911 deviation equal to the observed weight for that bin and its statistical error. The effect
 1912 of reweighting error is not correlated between \cancel{E}_T bins. For each of the 1000 exper-
 1913 iments, the control sample data are reweighted according to the generated weights,
 1914 and the background estimates are calculated for each \cancel{E}_T bin. Since the distribution
 1915 of the toy background estimates follows a Gaussian distribution in each \cancel{E}_T bin, the
 1916 RMS spread of the estimates is taken as the statistical error due to reweighting. This
 1917 procedure is carried out for the ff , ee , low sideband ee , and high sideband ee samples.

1918 The total statistical error on the background estimate per \cancel{E}_T bin is given by

$$\sigma_{\text{stat}}^2 = \sigma_{\text{stat,QCD}}^2 + \sigma_{\text{stat,EW}}^2 \quad (7.8)$$

1919 where $\sigma_{\text{stat,QCD}}^2$ is the square of the total statistical error on the QCD prediction in
 1920 the \cancel{E}_T bin

$$\sigma_{\text{stat,QCD}}^2 = \sigma_{\text{stat},s}^2 + \sigma_{\text{Poisson,QCD}}^2 + \sigma_{\text{reweight},s}^2 + \sigma_{\text{reweight,QCD}}^2 \quad (7.9)$$

1921 and $\sigma_{\text{stat,EW}}$ is the Poisson error on the number of $e\gamma$ events in the \cancel{E}_T bin ($= \sqrt{N_{e\gamma}}$,
 1922 where $N_{e\gamma}$ is the prediction in the \cancel{E}_T bin after scaling by $f_{e\rightarrow\gamma}$). The contributions
 1923 to $\sigma_{\text{stat,QCD}}^2$ are discussed below.

- 1924 • $\sigma_{\text{stat},s}^2$ is the statistical error contributed by the normalization factor s (i.e. from
 1925 Poisson error in the normalization region $\cancel{E}_T < 20$ GeV):

$$\begin{aligned}\sigma_{\text{stat},s}^2 = & \frac{N_{\text{control}}^2}{(N_{\gamma\gamma}^{\text{norm}} - N_{e\gamma}^{\text{norm}})^2} (\sigma_{\text{Poisson},\gamma\gamma}^{\text{norm}})^2 + (\sigma_{\text{Poisson},e\gamma}^{\text{norm}})^2 + \\ & \frac{N_{\text{control}}^2}{(N_{\text{control}}^{\text{norm}})^2} (\sigma_{\text{Poisson,control}}^{\text{norm}})^2\end{aligned}\quad (7.10)$$

1926 where N_{control} is the number of reweighted, normalized events in the \cancel{E}_T bin,
 1927 $N_{\gamma\gamma}^{\text{norm}}$ is the number of $\gamma\gamma$ events in the normalization region, $N_{e\gamma}^{\text{norm}}$ is the num-
 1928 ber of $e\gamma$ events in the normalization region (after scaling by $f_{e\rightarrow\gamma}$), $\sigma_{\text{Poisson},\gamma\gamma}^{\text{norm}}$
 1929 is the Poisson error on the number of $\gamma\gamma$ events in the normalization region
 1930 ($= \sqrt{N_{\gamma\gamma}^{\text{norm}}}$), $\sigma_{\text{Poisson},e\gamma}^{\text{norm}}$ is the Poisson error on the number of $e\gamma$ events in the
 1931 normalization region ($= \sqrt{N_{e\gamma}^{\text{norm}}}$), $N_{\text{control}}^{\text{norm}}$ is the number of QCD control (ee
 1932 or ff) events in the normalization region, and $\sigma_{\text{Poisson,control}}^{\text{norm}}$ is the Poisson error
 1933 on the number of QCD control (ee or ff) events in the normalization region
 1934 ($= \sqrt{\sum_{i=1}^{N_{\text{control}}^{\text{norm}}} w_i^2}$, where w_i is the di-EM p_T weight applied to event i). For
 1935 the ee control region, N_{control} and $N_{\text{control},\text{norm}}$ are sideband subtracted, and
 1936 $\sigma_{\text{Poisson,control}}^{\text{norm}}$ includes the Poisson error on the number of sideband events.

- 1937 • $\sigma_{\text{Poisson,QCD}}$ is the Poisson error due to the number of QCD control (ee or ff)
 1938 events in the \cancel{E}_T bin, equal to $\sqrt{\sum_{i=1}^{N_{\text{control}}^{\text{norm}}} w_i^2}$, where w_i is the di-EM p_T weight
 1939 applied to event i . For the ee control region, $\sigma_{\text{Poisson,QCD}}$ includes the Poisson
 1940 error on the number of subtracted sideband events.
- 1941 • $\sigma_{\text{reweight},s}$ is the error contributed by the control sample reweighting in the nor-

1942 malization region ($= \frac{N_{\text{control}}^2}{(N_{\text{control}}^{\text{norm}})^2} \sigma_{\text{reweight,control}}^{\text{norm}}$). $\sigma_{\text{reweight,control}}^{\text{norm}}$ is the quadrature
 1943 sum of the RMS of the 1000 toy reweighting experiments for each \cancel{E}_T bin in the
 1944 normalization region. For the ee control sample, it also includes (in quadrature)
 1945 the RMS of the toys in the sideband samples.

- 1946 • $\sigma_{\text{reweight,QCD}}$ is the error contributed by the control sample reweighting in the \cancel{E}_T
 1947 bin ($= s\sigma_{\text{reweight,control}}$). $\sigma_{\text{reweight,control}}$ is the RMS of the 1000 toy reweighting
 1948 experiments for the E_T bin. For the ee control sample, it also includes (in
 1949 quadrature) the RMS of the toys in the sideband samples.

1950 The dominant source of systematic error on the background estimate is the slight
 1951 difference in hadronic activity between the ee , ff , and $\gamma\gamma$ samples. This results in a
 1952 small bias (~ 1 GeV) of the ee \cancel{E}_T distribution towards lower values with respect to
 1953 the ff and $\gamma\gamma$ samples, as shown in Figure 7.19. Therefore, the ff sample is used as
 1954 the primary QCD background estimator, and the difference between the ee and ff
 1955 predictions is assigned as an error on the knowledge of the hadronic activity. For \cancel{E}_T
 1956 > 100 GeV, this error amounts to 43% of the total QCD + electroweak background
 1957 estimate.

1958 The second largest source of systematic error comes from the p_T dependence of the
 1959 $e \rightarrow \gamma$ misidentification rate (see 7.2). For $\cancel{E}_T > 100$ GeV, the expected electroweak
 1960 background is 3.4 ± 1.0 events, so this error amounts to 4.8% of the total QCD +
 1961 electroweak background estimate.

1962 The assumption of a constant $t\bar{t}$ and $W + \text{jets}$ background shape under the Z
 1963 peak in the ee sample induces a systematic error on the ee sideband-subtracted back-
 1964 ground prediction. To assess the magnitude of this error, the sideband subtraction
 1965 (see Sec. 7.1.2) is performed once using only the prediction from the high sideband,
 1966 and once using only the prediction from the low sideband. In each of these cases, the
 1967 prediction is weighted by a factor of two, to account for the fact that the sideband
 1968 regions are only half as wide (10 GeV) as the signal region (20 GeV). The maximum

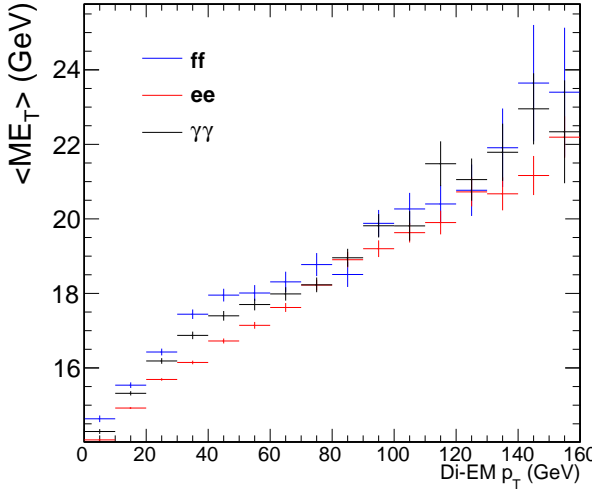


Figure 7.19: Average \mathcal{E}_T vs. di-EM p_T for the ff (blue), ee (red), and $\gamma\gamma$ (black) samples.

1969 variation from the nominal ee estimate is taken as the error, which amounts to 11%
 1970 for $\mathcal{E}_T > 100$ GeV. \mathcal{E}_T distributions using the nominal ee sideband subtraction, the
 1971 low-sideband-only subtraction, and the high-sideband-only subtraction are shown in
 1972 Figure 7.20.

Added

1973 Finally, the few percent error on the jet energy correction factors introduces an this
 1974 error on the final background estimate through (a) the use of the PF p_T to measure para-
 1975 the di-EM p_T , (b) the counting of jets passing a 30 GeV p_T threshold for placement of graph
 1976 the event in an N_j bin for reweighting, and (c) the counting of jets above threshold for
 1977 the ≥ 1 -jet version of the selection. To estimate this error, 100 pseudo-experiments
 1978 are generated with identical properties as the true data sample, except with corrected
 1979 jet energies (in all events) all shifted by an amount $r\sigma(p_T, \eta)$. r is a random number
 1980 drawn from a Gaussian distribution with mean 0 and width 1, and $\sigma(p_T, \eta)$ is the
 1981 uncertainty on the jet energy correction factor (which, like the correction factor itself,
 1982 is a function of p_T and η). The same factor r is applied to all jets in all events in the
 1983 pseudo-experiment because the jet energy correction errors are correlated from jet to
 1984 jet (they result from e.g. uncertainties in MC simulation or uncertainties in ECAL

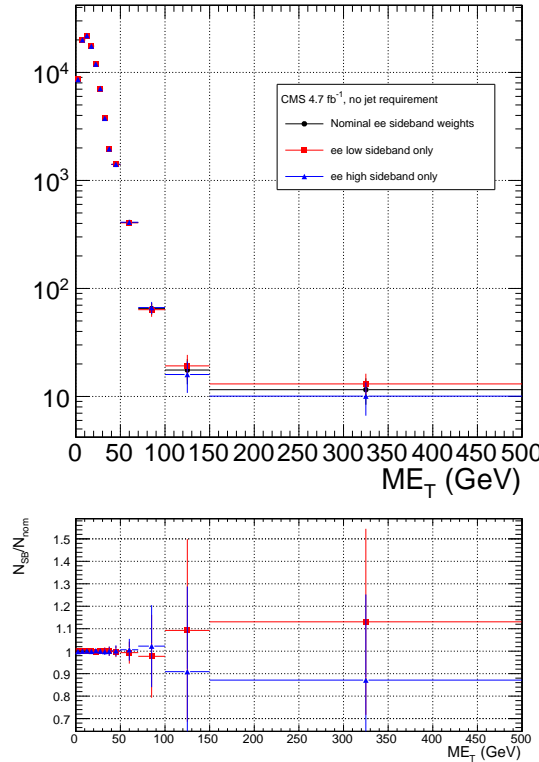


Figure 7.20: ee E_T distributions using the nominal sideband subtraction (black circles), low sideband only (red squares), and high sideband only (blue triangles). The bottom plot shows the ratio of the low sideband distribution to the nominal (red squares) and the ratio of the high sideband distribution to the nominal (blue triangles).

1985 energy scale [91]). The standard error of the mean of the 100 resulting background
 1986 estimates in each relevant E_T bin is taken as the error. The error in each E_T bin is
 1987 assumed to be uncorrelated. This process is repeated for both the inclusive and ≥ 1 -
 1988 jet selections. For $E_T \geq 100$ GeV, the jet energy correction uncertainty is 1.5% (2.2%)
 1989 of the total background for the inclusive (≥ 1 -jet) selection.

1990 The uncertainty in how to define the (di-EM p_T , N_j) bins, especially at high di-
 1991 EM p_T where the statistics are low, is covered by the 1000-toys procedure as long as
 1992 the bins are not too coarse. This is shown in Figure 7.21. If the bins are too coarse,
 1993 the details of the shape of the di-EM p_T spectra are lost, and the reweighting has a
 1994 smaller effect.

1995 The use of uncorrected instead of corrected PF E_T (see Sec. 6.1.3) makes no

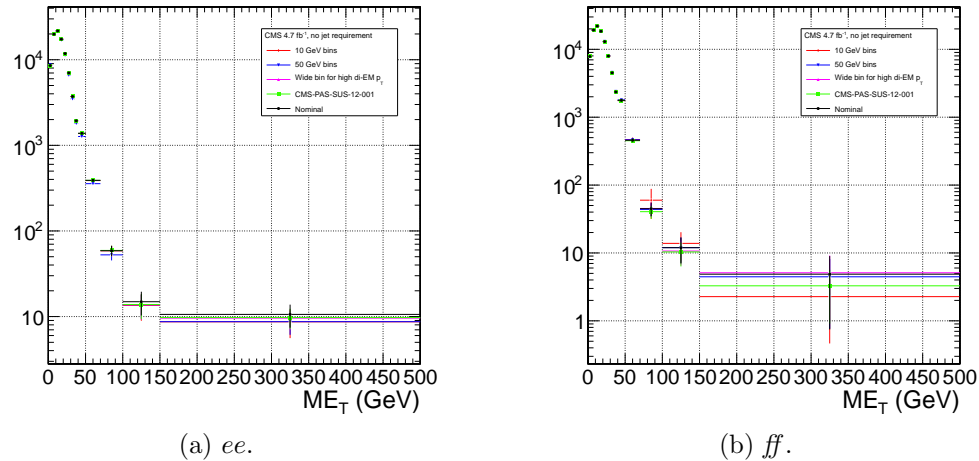


Figure 7.21: Comparison of \cancel{E}_T distributions for five different di-EM p_T bin definitions: uniform bins of width 10 GeV (red diamonds); uniform bins of width 50 GeV (blue downward-pointing triangles); bins with lower edges $\{0.0, 5.0, 10.0, 15.0, 20.0, 30.0, 40.0, 50.0, 60.0, 70.0, 80.0, 100.0, 750.0\}$ GeV for 0-jet events and $\{0.0, 5.0, 10.0, 15.0, 20.0, 30.0, 40.0, 50.0, 60.0, 70.0, 80.0, 100.0, 150.0\}$ GeV for ≥ 1 -jet events (magenta upward-pointing triangles), i.e. a single wide bin at high di-EM p_T ; bins with lower edges $\{0.0, 5.0, 10.0, 15.0, 20.0, 30.0, 40.0, 50.0, 60.0, 70.0, 80.0, 100.0, 150.0\}$ GeV for 0-jet events and $\{0.0, 5.0, 10.0, 15.0, 20.0, 30.0, 40.0, 50.0, 60.0, 70.0, 80.0, 100.0, 120.0, 150.0, 200.0\}$ GeV for ≥ 1 -jet events (green squares), i.e. the bins used in ref. [29]; and the nominal bin definitions shown in Fig. 7.14 (black circles).

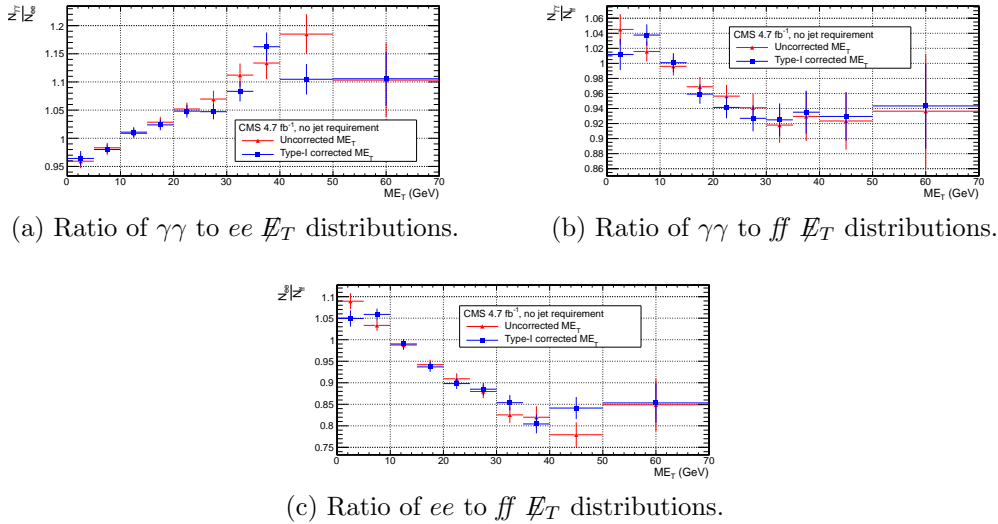


Figure 7.22: Agreement between $\gamma\gamma$, ee , and ff samples for uncorrected (red triangles) and corrected (blue squares) \not{E}_T .

1996 difference in the agreement of the background predictions and the search sample in
 1997 a control region at low \not{E}_T , as shown in Figure 7.22. Since the control samples are
 1998 derived from the same data as the search sample, any biases in the \not{E}_T reconstruction
 1999 due to jet energy scale are present equally in both samples.

2000 Tables 7.4 and 7.5 list all the errors on the ee and ff QCD background predictions,
 2001 respectively, for the \not{E}_T bins used in the search. Table 7.6 lists the errors on the
 2002 electroweak background prediction. Finally, Table 7.7 shows the errors on the total
 2003 QCD + electroweak background prediction, broken down by origin (statistical or
 2004 systematic) and QCD background estimation sample (ee or ff). In the final result,
 2005 only the ff QCD estimate is used.

2006 7.4 Results

2007 Figure 7.23(7.24) shows the \not{E}_T distribution of the inclusive(≥ 1 -jet) $\gamma\gamma$ search sample
 2008 along with the predicted \not{E}_T distributions of the QCD and electroweak backgrounds.
 2009 The observed number of two-photon events, background estimates and their errors,

Table 7.4: Errors on the ee QCD background prediction as a fraction of the ee prediction.

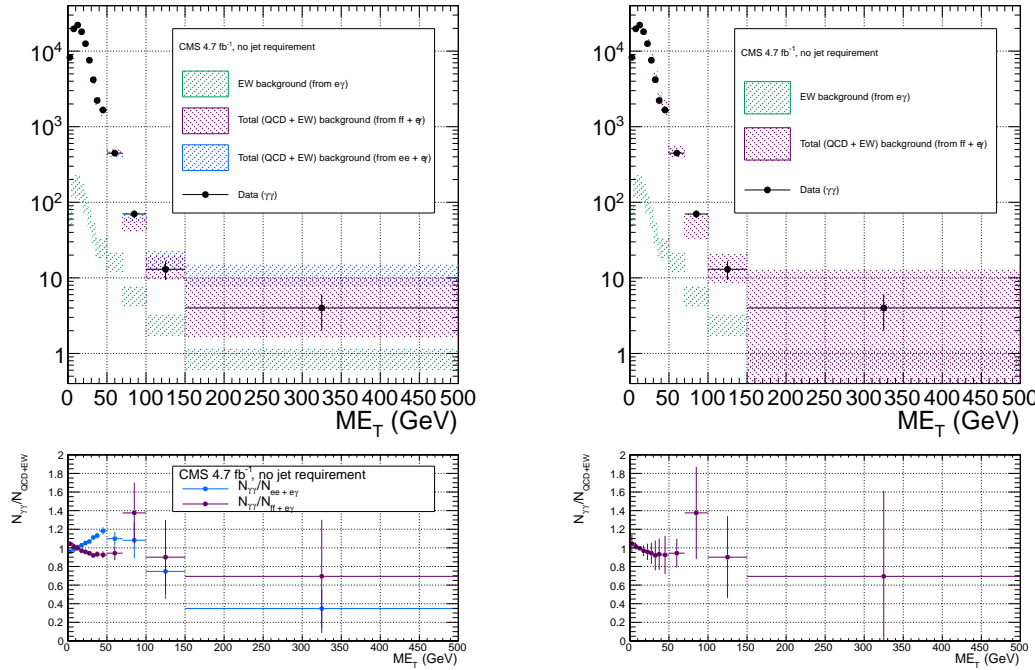
Source of error	Fractional uncertainty (%)				
	[50, 60)	[60, 70)	[70, 80)	[80, 100)	≥ 100
Total	3.9	8.1	16	25	25
Statistics	3.6	7.8	16	24	22
No. events	3.6	7.7	15	24	20
In norm. region	0.43	0.44	0.46	0.55	0.51
In this E_T bin	3.5	7.7	15	24	20
Reweighting	0.73	1.2	3.5	4.3	7.7
In norm. region	0.19	0.19	0.2	0.24	0.23
In this E_T bin	0.71	1.2	3.5	4.3	7.7
Systematics	2.6	4.4	1.2	7.5	14
$f_{e \rightarrow \gamma}$ (in norm. region)	0.0012	0.0012	0.0013	0.0015	0.0014
m_{ee} background shape	1.4	2	0.72	5.5	12
Jet energy scale	2.2	3.9	0.96	5.1	6.9

Table 7.5: Errors on the ff QCD background prediction as a fraction of the ff prediction.

Source of error	Fractional uncertainty (%)				
	[50, 60)	[60, 70)	[70, 80)	[80, 100)	≥ 100
Total	15	25	61	34	64
Statistics	7.2	14	30	33	38
No. events	7.1	14	29	33	36
In norm. region	0.64	0.64	0.64	0.64	0.64
In this E_T bin	7.1	14	29	33	36
Reweighting	0.85	2.7	5.1	6.9	13
In norm. region	0.27	0.27	0.27	0.27	0.27
In this E_T bin	0.81	2.6	5.1	6.9	13
Systematics	13	21	53	6.6	52
ee/ff difference	13	21	53	5.5	52
$f_{e \rightarrow \gamma}$ (in norm. region)	0.0012	0.0012	0.0012	0.0012	0.0012
Jet energy scale	0.099	1.7	1.8	3.5	1.8

Table 7.6: Errors on the $e\gamma$ electroweak background prediction as a fraction of the $e\gamma$ prediction.

Source of error	Fractional uncertainty (%)				
	[50, 60)	[60, 70)	[70, 80)	[80, 100)	≥ 100
Total	29	29	30	30	30
Statistics	3.6	5.2	6.7	7.2	6.5
Systematics ($f_{e \rightarrow \gamma}$)	29	29	29	29	29



(a) $ee + e\gamma$ and $ff + e\gamma$. The widths of the bands correspond to the errors given in Table 7.7, excluding the error associated with the difference between the ee and ff QCD estimates for the $ff + e\gamma$ E_T distribution.

(b) $ff + e\gamma$. The widths of the bands correspond to the errors given in Table 7.7, including the error associated with the difference between the ee and ff QCD estimates.

Figure 7.23: E_T distribution of the $\gamma\gamma$ search sample (black circles) along with the predicted E_T distributions of the QCD and electroweak backgrounds (blue band for ee QCD prediction + electroweak prediction, purple band for ff QCD prediction + electroweak prediction). The electroweak background prediction is shown in green. The bottom plots show the ratio of the $\gamma\gamma E_T$ distribution to the $ee + e\gamma$ background distribution (blue) and $ff + e\gamma$ background distribution (purple).

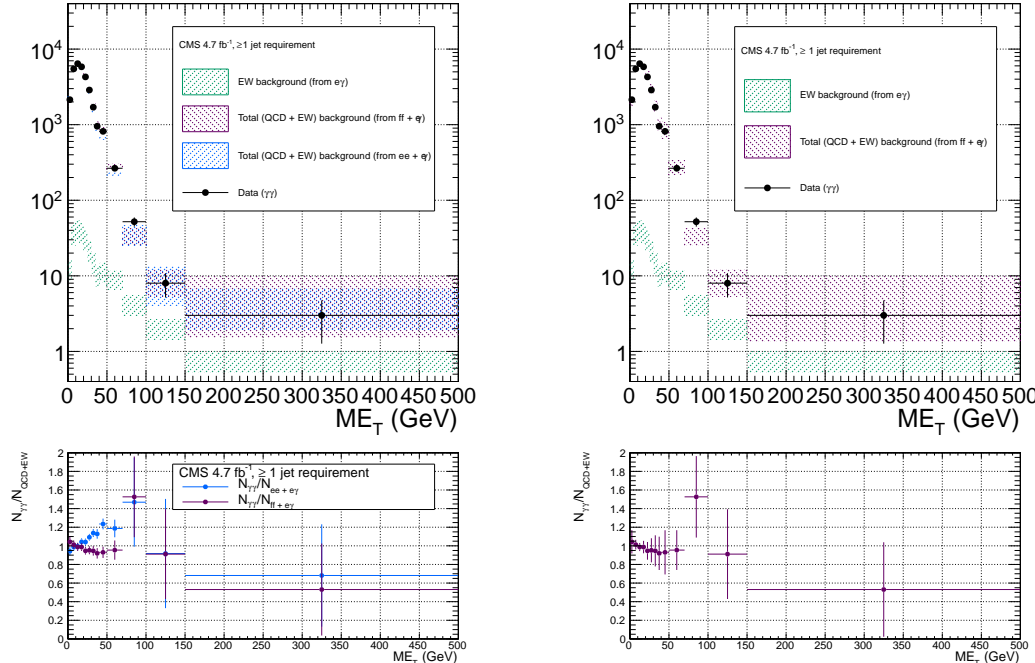
and expected number of inclusive(≥ 1 -jet) two-photon events from two representative GGM SUSY models are listed in Table 7.8(7.9). (Details of the SUSY MC production are given in Chapter 8 and App. A.) No deviation from the Standard Model prediction is observed in the $\gamma\gamma$ search sample.

Table 7.7: Errors on the total QCD + electroweak background prediction as a fraction of the total prediction.

Source of error	Fractional uncertainty (%)				
	[50, 60)	[60, 70)	[70, 80)	[80, 100)	≥ 100
Total ($ee + e\gamma$)	3.9	7.8	15	22	22
Statistics	3.4	7.3	14	21	18
QCD	3.4	7.3	14	21	18
Electroweak	0.13	0.3	0.53	0.79	0.76
Systematics	2.7	4.5	2.6	7.4	13
QCD	2.5	4.1	1.1	6.7	12
Electroweak	1	1.7	2.3	3.2	3.4
Total ($ff + e\gamma$)	14	24	54	30	54
Statistics	6.9	13	26	29	30
QCD	6.9	13	26	29	30
Electroweak	0.11	0.24	0.79	0.83	1.1
Systematics	12	20	47	6.7	43
QCD	12	20	47	5.8	43
Electroweak	0.9	1.3	3.4	3.4	4.8

Table 7.8: Observed numbers of two-photon events, background estimates and their errors, and expected numbers of two-photon events from two representative GGM SUSY models (details of MC simulation given in Chapter 8 and App. A) for the E_T bins used in the search. Errors on the background estimates are detailed in Tables 7.4, 7.5, 7.6, and 7.7. Errors on the expected numbers of GGM events are purely statistical.

Source	No. events				
	[50, 60)	[60, 70)	[70, 80)	[80, 100)	≥ 100
Observation ($\gamma\gamma$)	354	93	37	33	17
Predicted background ($ff + e\gamma$)	361 ± 51.5	113 ± 27.1	26.9 ± 14.5	23.9 ± 7.23	20.2 ± 10.9
$m_{\tilde{q}} = 720$ GeV $M_3 = 720$ GeV $M_1 = 375$ GeV	13.3 ± 2.13	17.7 ± 2.46	15.3 ± 2.33	42.9 ± 3.82	966 ± 18.3
$m_{\tilde{q}} = 1440$ GeV $M_3 = 1440$ GeV $M_1 = 375$ GeV	0.008 ± 0.003	0.009 ± 0.003	0.012 ± 0.003	0.030 ± 0.005	1.92 ± 0.04



(a) $ee + e\gamma$ and $ff + e\gamma$. The widths of the bands correspond to the errors given in Table 7.7, excluding the error associated with the difference between the ee and ff QCD estimates for the $ff + e\gamma$ E_T distribution.

(b) $ff + e\gamma$. The widths of the bands correspond to the errors given in Table 7.7, including the error associated with the difference between the ee and ff QCD estimates.

Figure 7.24: E_T distribution of the $\gamma\gamma + \geq 1$ jet search sample (black circles) along with the predicted E_T distributions of the QCD and electroweak backgrounds (blue band for ee QCD prediction + electroweak prediction, purple band for ff QCD prediction + electroweak prediction). The electroweak background prediction is shown in green. The bottom plots show the ratio of the $\gamma\gamma E_T$ distribution to the $ee + e\gamma$ background distribution (blue) and $ff + e\gamma$ background distribution (purple).

Table 7.9: Observed numbers of two-photon + ≥ 1 -jet events, background estimates and their errors, and expected numbers of two-photon + ≥ 1 -jet events from two representative GGM SUSY models (details of MC simulation given in Chapter 8 and App. A) for the \cancel{E}_T bins used in the search. Errors on the background estimates are detailed in Tables 7.4, 7.5, 7.6, and 7.7. Errors on the expected numbers of GGM events are purely statistical.

Source	No. events				
	[50, 60)	[60, 70)	[70, 80)	[80, 100)	≥ 100
Observation ($\gamma\gamma + \geq 1$ jet)	202	63	27	25	11
Predicted background ($ff + e\gamma$)	200 ± 35.4	77.7 ± 28.1	19.4 ± 8.55	14.7 ± 7.04	14.4 ± 5.59
$m_{\tilde{q}} = 720$ GeV $M_3 = 720$ GeV $M_1 = 375$ GeV	13.3 ± 2.13	17.7 ± 2.46	15.3 ± 2.33	42.9 ± 3.82	965 ± 18.3
$m_{\tilde{q}} = 1440$ GeV $M_3 = 1440$ GeV $M_1 = 375$ GeV	0.008 ± 0.003	0.009 ± 0.003	0.012 ± 0.003	0.031 ± 0.004	1.92 ± 0.04

2014 **Chapter 8**

2015 **Interpretation of Results in Terms
2016 of GMSB Models**

2017 As shown in Figs. 7.23 and 7.24 and Tables 7.8 and 7.9, no excess of events above
2018 the Standard Model expectation is found in either the ≥ 0 - or ≥ 1 -jet analyses for the
2019 GMSB-sensitive region $\cancel{E}_T \geq 50$ GeV. Therefore, upper limits on the production cross
2020 sections of various GMSB models are calculated and then translated into statements of
2021 exclusion. Section 8.1 describes the GMSB models that were generated with MC and
2022 tested for exclusion. The upper limit calculation and translation to model exclusions
2023 is laid out in Section 8.2. The upper limits themselves are presented in Section 8.3,
2024 and, finally, the exclusions are presented in Section 8.4.

2025 **8.1 Simplified Models**

2026 The exclusion reach of the two-photon search is presented for three different two-
2027 dimensional scans in GMSB parameter space. The first scan covers the bino NLSP
2028 scenario of Sec. 3.5. In this scan, M_2 , which controls the amount of wino mixing, is
2029 set to 3.5 TeV. M_1 , which controls the amount of bino mixing, is set to 375 GeV.
2030 This insures that all gauginos except the lightest neutralino are too heavy to be

2031 produced in significant numbers at the LHC. All other mass parameters except for
 2032 M_3 (\sim gluino mass) and $m_{\tilde{q}}$ (\sim first- and second-generation squark mass) are set to
 2033 3.5 TeV, which insures that squark/gluino decay to intermediate states such as third-
 2034 generation squarks or any flavor of lepton is strongly suppressed. M_3 and $m_{\tilde{q}}$ are
 2035 scanned over from $M_3 = m_{\tilde{q}} = 400$ GeV to $M_3 = m_{\tilde{q}} = 2$ TeV in 80-GeV steps.
 2036 The resulting simplified model consists only of a gluino, first- and second-generation
 2037 squarks, and the lightest neutralino and its decay products (the gravitino is forced to
 2038 be the LSP). The scan in M_3 - $m_{\tilde{q}}$ space illuminates the sensitivity of the two-photon
 2039 search to different levels of signal hadronic activity.

2040 The second scan is identical to the first except that the values of M_1 and M_2
 2041 are inverted ($M_1 = 3.5$ TeV and $M_2 = 375$ GeV). This corresponds to the wino
 2042 NLSP scenario of Sec. 3.5. Now, both the lightest neutralino and the lightest chargino
 2043 have masses of order 375 GeV, and are therefore produced with approximately equal
 2044 frequency in the gluino and squark decays. The chargino decays to $W + \tilde{G}$, so final
 2045 states in this scan often include leptons or large jet multiplicity. Since there is no
 2046 guarantee that two neutralinos will be produced and will decay to two photons, this
 2047 search is not well optimized for the wino NLSP scenario. However, a related CMS
 2048 search with one photon and ≥ 3 jets has an exclusion reach of ~ 1 TeV in M_3 and
 2049 $m_{\tilde{q}}$ for this scenario [29].

2050 The third scan is M_3 vs. M_1 for $m_{\tilde{q}}$, M_2 , and all other mass parameters equal to
 2051 2.5 TeV. M_3 is scanned from 160 GeV to 2 TeV in 80-GeV steps, while M_1 is scanned
 2052 from 150 GeV to 1050 GeV in 100-GeV steps. $M_3 < M_1$ is not allowed, as this would
 2053 imply that the gluino, not the lightest neutralino, is the NLSP. This scan highlights
 2054 the performance of the two-photon search as a function of M_1 (i.e. as a function of
 2055 decays open to the neutralino), whereas the previous two scans keep M_1 fixed.

2056 For each scan, the sparticle mass spectrum is generated with SuSpect 2.41 [123]
 2057 and the decay widths with SDECAY 1.3 [124]. The event data (including produc-

2058 tion, unstable particle decay, parton showering, and hadronization) is generated with
 2059 Pythia 6.422 [130], using the sparticle mass spectra and decay widths as inputs. The
 2060 gravitino is always forced to be the LSP. The simulated data are reconstructed with
 2061 CMSSWv4.2.2, which uses a detector simulation based on GEANT 4 [125]. Next to
 2062 leading order cross sections are calculated with PROSPINO 2.1 [126], and shown in
 2063 Figure 8.1 for the three signal MC scenarios.

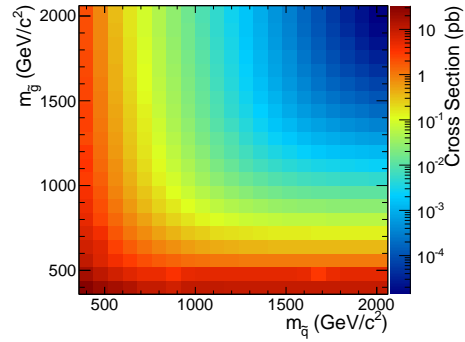
2064 8.2 Upper Limit Calculation and Model Exclusion

2065 The upper limits are calculated according to the prescription followed for the 2011
 2066 ATLAS + CMS Higgs limit combination [113]. This prescription utilizes the frequen-
 2067 tist CL_s method [114] with profile likelihood test statistic [115]. The CL_s method and
 2068 the profile likelihood are explained in Section 8.2.2, using specific signal MC points to
 2069 illustrate the procedure. First, however, the signal MC acceptance \times efficiency, which
 2070 is an input to the limit setting procedure, is presented in Section 8.2.1.

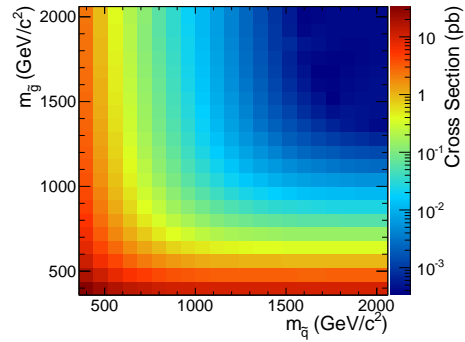
2071 8.2.1 Signal Acceptance \times Efficiency

2072 The signal acceptance \times efficiency (denoted $\mathcal{A} \times \epsilon$), defined for each signal point as
 2073 the number of $\gamma\gamma$ events selected with $\cancel{E}_T \geq 50$ GeV divided by the total number of
 2074 events generated, is shown in Figure 8.2 for the three different scenarios described in
 2075 Sec. 8.1.

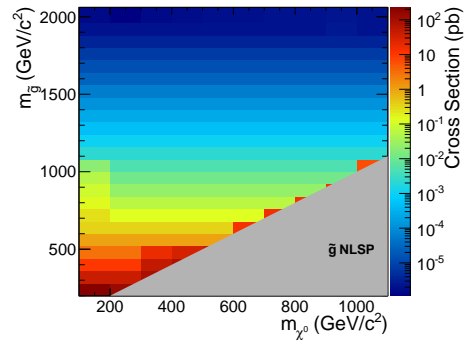
2076 In Figs. 8.2a and 8.2b, the large drop in $\mathcal{A} \times \epsilon$ for $m_{\tilde{q}} > M_3$ is due to an increase
 2077 in the number of jets produced per event and a consequent reduction in the number
 2078 of photons that pass the $I_{\text{comb}} < 6$ GeV cut. For $m_{\tilde{q}} > M_3$, there is more phase space
 2079 available to produce gluinos in the hard scatter than squarks. However, since gluinos
 2080 must decay via squarks, and in these models all squarks are heavier than the gluino,
 2081 only the two-jet decay $\tilde{g} \rightarrow qq\tilde{\chi}^0$ is available. Conversely, when $m_{\tilde{q}} < M_3$, there is



(a) M_2 decoupled ($M_2 = 3.5$ TeV), $M_1 = 375$ GeV, M_3 vs. $m_{\tilde{q}}$.



(b) M_1 decoupled ($M_1 = 3.5$ TeV), $M_2 = 375$ GeV, M_3 vs. $m_{\tilde{q}}$.



(c) $m_{\tilde{q}}$ decoupled ($m_{\tilde{q}} = 2.5$ TeV), M_3 vs. M_1 .

Figure 8.1: Next to leading order cross sections for the three different MC scenarios described in the text.

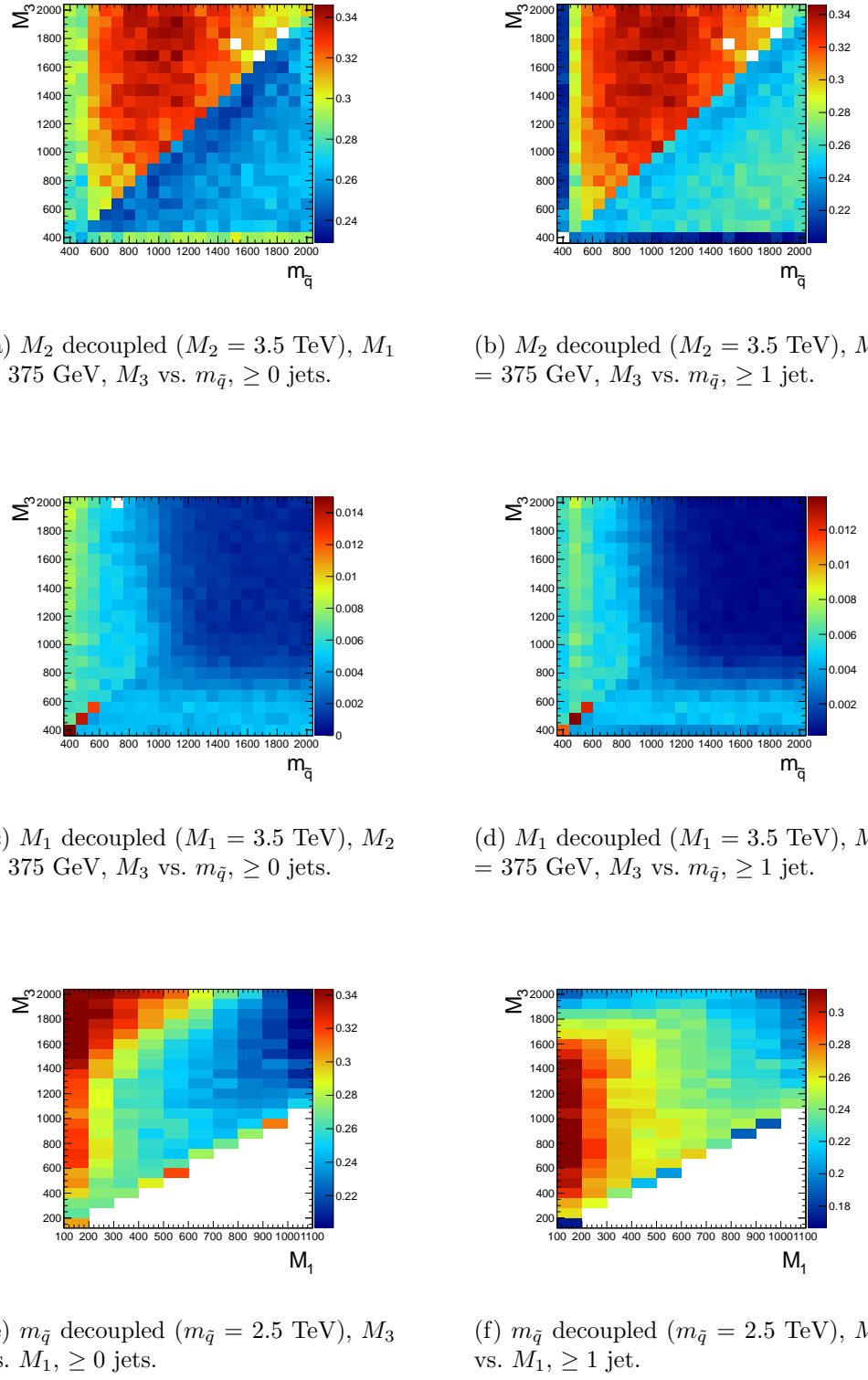


Figure 8.2: Signal acceptance \times efficiency (defined in the text) for the three different scenarios described in Sec. 8.1.

more phase space available to produce squarks, which may then decay via one jet as $\tilde{q} \rightarrow q\tilde{\chi}^0$. Jets in SUSY events may be very close to the neutralino decay photons, and as a result the photons may fail the strict isolation requirements, leading to lower $\mathcal{A} \times \epsilon$ for jet-rich events. The worsened acceptance along $M_3 = 400$ GeV and $m_{\tilde{q}} = 400$ GeV in Fig. 8.2b is due to efficiency of the jet cut, which decreases drastically as M_3 and $m_{\tilde{q}}$ approach M_1 because of shrinking phase space to produce hard jets in the squark and gluino decays to neutralinos.

The broad peak in $\mathcal{A} \times \epsilon$ shown in Fig. 8.2a for $m_{\tilde{q}} < M_3$ and ~ 600 GeV $< m_{\tilde{q}} < \sim 1600$ GeV is due to the $\cancel{E}_T > 50$ GeV cut. The efficiency of the cut decreases as $m_{\tilde{q}}$ decreases because of the fixed M_1 of 375 GeV. If the squark-neutralino mass splitting gets too small, the likelihood of producing an energetic enough gravitino to pass the \cancel{E}_T cut decreases.

$\mathcal{A} \times \epsilon$ is generally much lower for the $M_2 = 375$ GeV grid (Figs. 8.2c and 8.2d) due to the larger contribution from chargino decays to $W + \tilde{G}$, which do not give rise to photons in the final state. The increased acceptance for $M_3 > m_{\tilde{q}}$ is due to the same jet multiplicity issue affecting the $M_1 = 375$ GeV grid. As M_3 and $m_{\tilde{q}}$ increase relative to the fixed M_2 , the jets from squark and gluino decay get more energetic, increasing the chance that they will overlap with the neutralino decay photon and cause it to fail the isolation cut. For $m_{\tilde{q}} \gtrsim 1$ TeV and $M_3 \gtrsim 800$ GeV, the acceptance is so low that not enough events were simulated to see the acceptance decrease over the statistical error.

In Fig. 8.2e, the neutralino is always heavy enough to guarantee decay to a photon that can pass the 40 GeV p_T cut. $\mathcal{A} \times \epsilon$ increases as M_3 increases because the larger gluino-neutralino mass splitting gives the neutralino a larger kinetic energy, increasing the chance that it will decay to a photon with 40 GeV p_T or higher. After the bino mass increases beyond the threshold needed to produce high p_T photons, $\mathcal{A} \times \epsilon$ decreases with increasing M_1 , independent of gluino mass, because higher M_1 means more phase

2109 space is open to decays of the form $\tilde{\chi}_1^0 \rightarrow Z\tilde{G}$ and $\tilde{\chi}_1^0 \rightarrow H\tilde{G}$. The two-photon search
 2110 is naturally not as efficient for these decays.

Added

2111 There is a small chance that some real GMSB signal events could be reconstructed signal
 2112 as ff events in the data. To correct the signal acceptance for this effect, the number contamination
 2113 of signal events reconstructed as ff events is subtracted from the number of signal $\gamma\gamma$ ination
 2114 events, effectively reducing the signal acceptance. This is generally a small correction par.
 2115 ($\sim 5\%$).

2116 8.2.2 CL_s and the Profile Likelihood Test Statistic

2117 The process of setting a cross section upper limit entails (1) defining a test statistic,
 2118 (2) generating a distribution for that test statistic under the signal + background
 2119 and background-only hypotheses, and (3) deciding whether or not the observed value
 2120 of the test statistic is more compatible with the signal + background (i.e. weaker
 2121 upper limit) or background-only (i.e. stronger upper limit) hypotheses by considering
 2122 where it falls within the test statistic distributions. An important requirement on the
 2123 choice of test statistic is that it be able to effectively discriminate between the signal
 2124 + background and background-only hypotheses, i.e. the shape of its distribution for
 2125 these two hypotheses should be different. The procedure for determining the exclud-
 2126 ability of a particular model given the value of the test statistic observed should not
 2127 give rise to pathological behavior in the presence of small signals, low statistics, or
 2128 weak sensitivity to models, as is commonly the case in high energy physics. These
 2129 demands on the test statistic and the limit setting procedure itself dictate the choice
 2130 of the profile likelihood test statistic and CL_s procedure.

2131 In the remainder of this section, the notation is taken from ref. [113].

2132 **Profile Likelihood**

2133 For a specific model of GMSB, the limit setting procedure concerns the question of
 2134 whether to reject the signal + background hypothesis $\mu s + b$ in favor of the background-
 2135 only (Standard Model) hypothesis of b ($\mu = 0$). μ is a dimensionless signal strength
 2136 parameter. s is the expected number of signal events, calculated from MC simulated
 2137 signal events as in Secs. 8.1 and 8.2.1. b is the expected number of background events,
 2138 estimated in Chap. 7. By the Neyman-Pearson lemma [116], the ratio of the likelihood
 2139 of $\mu s + b$ to the likelihood of b is the test statistic with the highest power to reject $\mu s + b$
 2140 at whatever confidence level is desired. In practice, this means that the likelihood ratio
 2141 is the best discriminator between the GMSB and Standard Model hypotheses.

2142 The likelihood of the signal + background hypothesis as a function of the data
 2143 (either real or generated) is defined as

$$\mathcal{L}(\text{data}|\mu, \theta) = \prod_{i=1}^N \frac{(\mu s_i(\theta) + b_i(\theta))^{n_i}}{n_i!} e^{-\mu s_i(\theta) - b_i(\theta)} p(\tilde{\theta}|\theta) \quad (8.1)$$

2144 where $N = 5$ is the number of E_T bins used in the analysis ([50, 60) GeV, [60,
 2145 70) GeV, [70, 80) GeV, [80, 100) GeV, and [100, ∞) GeV); $s_i(\theta)$ and $b_i(\theta)$ are the
 2146 expected number of signal and background events in E_T bin i , respectively; n_i is the
 2147 number of events observed in E_T bin i ; and θ represents all the nuisance parameters
 2148 (uncertainties). $p(\tilde{\theta}|\theta)$ represents the product of probability distribution functions
 2149 (PDFs) for the nuisance parameters, where $\tilde{\theta}$ is the default value of the nuisance
 2150 parameter. In this analysis, there are eight experimental nuisance parameters per E_T
 2151 bin, given here as relative errors on the expected number of signal events:

- 2152 • Uncertainty on the measured integrated luminosity (4.5% in all bins) [117]
- 2153 • Uncertainty on the signal acceptance due to $\epsilon_e^{\text{data}}/\epsilon_e^{\text{MC}}$ and the pixel veto effi-
 2154 ciency error (cf. Sec. 6.4.2) (8% in all bins)

- 2155 ● Uncertainty on the signal acceptance due to imperfect pileup simulation (2.6%
2156 in all bins)

- 2157 ● Systematic uncertainty on QCD background prediction due to difference be-
2158 tween ff and ee estimates (5.5%-53% of the QCD background depending on
2159 bin)

- 2160 ● Systematic uncertainty on electroweak background prediction due to p_T depen-
2161 dence of $f_{e \rightarrow \gamma}$ (29%-30% of the electroweak background depending on bin)

- 2162 ● Statistical uncertainty on the signal acceptance (1.8%-100% depending on model
2163 and bin)

- 2164 ● Statistical uncertainty on the QCD background prediction (7.2%-38% of the
2165 QCD background depending on bin)

- 2166 ● Statistical uncertainty on the electroweak background prediction (3.6%-7.2% of
2167 the electroweak background depending on bin)

2168 and one very small theoretical nuisance parameter: the uncertainty on the signal
2169 acceptance due to underlying parton distribution function (PDF) uncertainties. In
2170 the limit-setting code, the uncertainties on signal acceptance due to photon efficiency
2171 and PDF errors are added in quadrature and treated as one. The uncertainty on the
2172 signal acceptance due to jet energy correction uncertainties is negligible, due to the
2173 presence of many hard jets in GMSB signal events. The uncertainties on integrated
2174 luminosity and pileup are 100% correlated between \cancel{E}_T bins, and the uncertainty on
2175 signal acceptance can usually be treated similarly because the error on $\epsilon_e^{\text{data}}/\epsilon_e^{\text{MC}}$ often
2176 dominates the PDF error on acceptance (although these three uncertainties are 0%
2177 correlated with each other).

2178 To estimate the uncertainty due to imperfect simulation of LHC pileup, the square
2179 of the average data efficiency for photons over the range 1-15 reconstructed primary

vertices (see Fig. 6.18a), weighted by the number of $\gamma\gamma$ events per primary vertex bin, is calculated. The efficiency per primary vertex bin is estimated from a linear fit to Fig. 6.18a. The process is repeated for MC using the entire range of primary vertices in Fig. 6.18a (all MC signal points have the same pileup simulation). The error is taken as $2 \times |\text{avg. data efficiency squared} - \text{avg. MC efficiency squared}| / (\text{avg. data efficiency squared} + \text{avg. MC efficiency squared})$.

Each nuisance parameter PDF is modeled by a log-normal distribution:

$$p(\tilde{\theta}|\theta) = \frac{1}{\sqrt{2\pi} \ln \kappa} \exp\left(-\frac{(\ln \tilde{\theta}/\theta)^2}{2(\ln \kappa)^2}\right) \frac{1}{\tilde{\theta}} \quad (8.2)$$

where $\tilde{\theta} = 1$ and $\kappa = 1 +$ the one-standard-deviation relative error on the nuisance parameter (e.g. for the 4.5% error due to integrated luminosity, $\kappa = 1.045$).

Similarly, the likelihood of the background-only hypothesis as a function of the data (either real or generated) is defined as

$$\mathcal{L}(\text{data}|0, \theta) = \prod_{i=1}^N \frac{b_i(\theta)^{n_i}}{n_i!} e^{-b_i(\theta)} p(\tilde{\theta}|\theta) \quad (8.3)$$

The profile likelihood test statistic is defined as

$$\tilde{q}_\mu = -2 \ln \frac{\mathcal{L}(\text{data}|\mu, \hat{\theta}_\mu)}{\mathcal{L}(\text{data}|\hat{\mu}, \hat{\theta})}, 0 \leq \hat{\mu} \leq \mu \quad (8.4)$$

where the $\hat{\theta}_\mu$ maximize $\mathcal{L}(\text{data}|\mu, \hat{\theta}_\mu)$ when it is evaluated at a particular μ , and $\hat{\mu}$ and $\hat{\theta}$ are the global maximum likelihood estimators of μ and θ . The condition $\hat{\mu} \leq \mu$ insures that the obtained cross section upper limit is one-sided, i.e. there is no possibility to find a lower limit on the cross section. The profile likelihood test

2196 statistic has the nice property that in the asymptotic (large statistics) limit its PDF
 2197 can be approximated by analytic formulae, eliminating the need to generate multiple
 2198 toy experiments to get the PDF. However, the approximation breaks down for small
 2199 numbers of observed events, so in practice the asymptotic limit is only used as a first
 2200 guess at the location of the true limit.

2201 The PDFs $f(\tilde{q}_\mu | \mu, \hat{\theta}_\mu^{\text{obs}})$ and $f(\tilde{q}_\mu | 0, \hat{\theta}_0^{\text{obs}})$ for the profile likelihood test statistic
 2202 under the signal + background and background-only hypotheses, respectively, are
 2203 obtained by generating toy MC pseudo-experiments. $\hat{\theta}_\mu^{\text{obs}}$ and $\hat{\theta}_0^{\text{obs}}$ maximize Eqs. 8.1
 2204 and 8.3, respectively, when they are evaluated for the observed data. For each μ (and
 2205 the background-only hypothesis $\mu = 0$), the pseudo-experiments are generated by
 2206 picking random values of s and b from a Poisson distribution with the θ fixed as just
 2207 described.

2208 **CL_s**

2209 In the classical frequentist approach, a signal model may be excluded at the 95%
 2210 confidence level (CL) if the probability of any measurement of the test statistic to be
 2211 greater than or equal to the observed value given the signal + background hypothesis
 2212 is 5%. This means that the observed value of the test statistic is so incompatible
 2213 with what one would expect to observe if the signal model were true that, under the
 2214 assumption that the signal model *is* true, the chance of observing a test statistic even
 2215 further afield from the signal expectation is only 5%. Mathematically,

$$\begin{aligned} p_\mu &\equiv P(\tilde{q}_\mu \geq \tilde{q}_\mu^{\text{obs}} | \mu s + b) = \int_{\tilde{q}_\mu^{\text{obs}}}^{\infty} f(\tilde{q}_\mu | \mu, \hat{\theta}_\mu^{\text{obs}}) d\tilde{q}_\mu \\ p_\mu &\leq 0.05 \Rightarrow \text{exclude } \mu \end{aligned} \quad (8.5)$$

2216 where $\tilde{q}_\mu^{\text{obs}}$ is the observed value of the test statistic and p_μ is the p-value. As indicated
 2217 in Eq. 8.5, the p-value is simply the integral of the PDF of \tilde{q}_μ from $\tilde{q}_\mu^{\text{obs}}$ to infinity.

2218 By construction, the classical 95% CL frequentist approach described above will
 2219 reject a true signal + background hypothesis 5% of the time. This can happen if the
 2220 experiment gets “unlucky” and the observation fluctuates low, causing $\tilde{q}_\mu^{\text{obs}}$ to fall in
 2221 the tail of the \tilde{q}_μ distribution. This poses a problem for the case of very weak signals
 2222 ($\mu \sim 0$), because it will lead to spurious exclusions of models to which the experiment
 2223 has little sensitivity. To avoid this pitfall, the CL_s limit setting method is used.

2224 In the CL_s method, the classical frequentist p-value of Eq. 8.5 is simply divided by
 2225 one minus the p-value of the background-only hypothesis, and it is this ratio, rather
 2226 than the p-value of the signal + background hypothesis alone, that is required to be
 2227 ≤ 0.05 . Mathematically,

$$1 - p_0 \equiv P(\tilde{q}_\mu \geq \tilde{q}_\mu^{\text{obs}} | b) = \int_{\tilde{q}_\mu^{\text{obs}}}^{\infty} f(\tilde{q}_\mu | 0, \hat{\theta}_0^{\text{obs}}) d\tilde{q}_\mu \quad (8.6)$$

$$\text{CL}_s(\mu) \equiv \frac{p_\mu}{1 - p_0} \quad (8.7)$$

$$\text{CL}_s(\mu) \leq 0.05 \Rightarrow \text{exclude } \mu$$

2228 where p_0 is the p-value for the background-only hypothesis ($\mu = 0$). In the case of
 2229 low sensitivity to μ , $p_\mu \lesssim 1 - p_0$, so $\text{CL}_s(\mu) \lesssim 1$ and μ will not be excluded. On the
 2230 contrary, for high sensitivity to μ ($\mu s \gg \sigma_b$), $p_\mu \ll 1 - p_0$, so models that can be
 2231 excluded by the criterion $p_\mu \leq 0.05$ will also be excluded by the criterion $\text{CL}_s \leq 0.05$.
 2232 Compared to the classical frequentist method, CL_s limits can be a little stronger in
 2233 the case of low signal sensitivity [113].

2234 To determine the upper limit on the cross section of a particular model, the lowest
 2235 value of μ for which $\text{CL}_s(\mu) \leq 0.05$, denoted $\mu^{95\% \text{CL}}$, is found. The cross section upper
 2236 limit of that model is then simply $\mu^{95\% \text{CL}}$ multiplied by the expected cross section of

2237 the model (cf. Fig. 8.1).

2238 In contrast to the observed upper limit, the expected upper limit is calculated from
 2239 an ensemble of background-only MC pseudo-experiments. The distribution $f(\mu_{\text{pseudo}}^{\text{95%CL}})$
 2240 is plotted (one entry per pseudo-experiment). The median expected upper limits and
 2241 $\pm 1\sigma$ and $\pm 2\sigma$ bands are defined as

$$0.5 = \int_0^{\mu_{\text{exp}}^{\text{95%CL}}} f(\mu_{\text{pseudo}}^{\text{95%CL}}) d\mu_{\text{pseudo}}^{\text{95%CL}} \quad (8.8)$$

$$0.16 = \int_0^{\mu_{-1\sigma,\text{exp}}^{\text{95%CL}}} f(\mu_{\text{pseudo}}^{\text{95%CL}}) d\mu_{\text{pseudo}}^{\text{95%CL}} \quad (8.9)$$

$$0.84 = \int_0^{\mu_{+1\sigma,\text{exp}}^{\text{95%CL}}} f(\mu_{\text{pseudo}}^{\text{95%CL}}) d\mu_{\text{pseudo}}^{\text{95%CL}} \quad (8.10)$$

$$0.025 = \int_0^{\mu_{-2\sigma,\text{exp}}^{\text{95%CL}}} f(\mu_{\text{pseudo}}^{\text{95%CL}}) d\mu_{\text{pseudo}}^{\text{95%CL}} \quad (8.11)$$

$$0.975 = \int_0^{\mu_{+2\sigma,\text{exp}}^{\text{95%CL}}} f(\mu_{\text{pseudo}}^{\text{95%CL}}) d\mu_{\text{pseudo}}^{\text{95%CL}} \quad (8.12)$$

2242 The technical procedure followed to calculate the 95% CL cross section upper
 2243 limits for each GMSB model tested is given below.

2244 1. Calculate a guess for the median expected limit and $\pm 2\sigma$ error bands ($\mu_{\pm 2\sigma,\text{guess}}^{\text{95%CL}}$)
 2245 using the asymptotic formulae for $f(\tilde{q}_\mu | 0, \hat{\theta}_0^{\text{obs}})$.

2246 2. Calculate observed ($\mu_{\text{obs,asym}}^{\text{95%CL}}$), median expected ($\mu_{\text{exp,asym}}^{\text{95%CL}}$), and $\pm 1\sigma$ ($\mu_{\pm 1\sigma,\text{asym}}^{\text{95%CL}}$)
 2247 and $\pm 2\sigma$ ($\mu_{\pm 2\sigma,\text{asym}}^{\text{95%CL}}$) expected CL_s limits using the asymptotic formulae for
 2248 $f(\tilde{q}_\mu | \mu, \hat{\theta}_\mu^{\text{obs}})$ and $f(\tilde{q}_\mu | 0, \hat{\theta}_0^{\text{obs}})$. Restrict the range of $\mu_{\text{obs,asym}}^{\text{95%CL}}$ and $\mu_{\text{exp,asym}}^{\text{95%CL}}$ to
 2249 $[0, 5 \times \mu_{\pm 2\sigma,\text{guess}}^{\text{95%CL}}]$ (this avoids pathological behavior of the limit-setting code
 2250 when the expected number of signal events is much greater than the observed
 2251 number of events and only introduces a $\sim 5\%$ upward bias in the observed limit,
 2252 well within the $\pm 1\sigma$ error bands).

2253 3. Calculate median expected ($\mu_{\text{exp}}^{\text{95%CL}}$) and $\pm 1\sigma$ ($\mu_{\pm 1\sigma}^{\text{95%CL}}$) and $\pm 2\sigma$ ($\mu_{\pm 2\sigma}^{\text{95%CL}}$) ex-

2254 pected CL_s limits using 100 toy MC pseudo-experiments to generate $f(\tilde{q}_\mu|\mu, \hat{\theta}_\mu^{\text{obs}})$
 2255 and $f(\tilde{q}_\mu|0, \hat{\theta}_0^{\text{obs}})$. Restrict the range of $\mu_{\text{exp}}^{95\%\text{CL}}$ to $[0, 5 \times \mu_{\pm 2\sigma, \text{guess}}^{95\%\text{CL}}]$.

2256 4. If $\mu_{\pm 2\sigma}^{95\%\text{CL}}$ could not be calculated, set $\mu_{\pm 2\sigma}^{95\%\text{CL}} = \mu_{\pm 2\sigma, \text{asym}}^{95\%\text{CL}}$ instead.

2257 5. If $\mu_{+2\sigma}^{95\%\text{CL}} \neq \mu_{-2\sigma}^{95\%\text{CL}}$ and $\mu_{\text{obs}, \text{asym}}^{95\%\text{CL}} > 0.0001$:

2258 • If $\mu_{\text{obs}, \text{asym}}^{95\%\text{CL}} > \mu_{+2\sigma}^{95\%\text{CL}}$, set $\mu_{+2\sigma}^{95\%\text{CL}} = 1.3 \times \mu_{\text{obs}, \text{asym}}^{95\%\text{CL}}$.

2259 • If $\mu_{\text{obs}, \text{asym}}^{95\%\text{CL}} < \mu_{-2\sigma}^{95\%\text{CL}}$, set $\mu_{-2\sigma}^{95\%\text{CL}} = 0.7 \times \mu_{\text{obs}, \text{asym}}^{95\%\text{CL}}$.

2260 6. If $\mu_{+2\sigma}^{95\%\text{CL}} = \mu_{-2\sigma}^{95\%\text{CL}}$, set $\mu_{\pm 2\sigma}^{95\%\text{CL}} = \mu_{\pm 2\sigma, \text{asym}}^{95\%\text{CL}}$ instead.

2261 7. Scan over 100 equally spaced test values of μ between $\mu_{-2\sigma}^{95\%\text{CL}}$ and $\mu_{+2\sigma}^{95\%\text{CL}}$ and,
 2262 if $\mu > 0.0001$, calculate the CL_s p-value (p_μ) for this test value of μ to 10^{-6}
 2263 precision using a minimum of 500 toy experiments to generate $f(\tilde{q}_\mu|\mu, \hat{\theta}_\mu^{\text{obs}})$ and
 2264 $f(\tilde{q}_\mu|0, \hat{\theta}_0^{\text{obs}})$.

2265 8. Determine the observed ($\mu_{\text{obs}, \text{scan}}^{95\%\text{CL}}$), median expected ($\mu_{\text{exp}, \text{scan}}^{95\%\text{CL}}$), and $\pm 1\sigma$ ($\mu_{\pm 1\sigma, \text{scan}}^{95\%\text{CL}}$)
 2266 and $\pm 2\sigma$ ($\mu_{\pm 2\sigma, \text{scan}}^{95\%\text{CL}}$) expected CL_s limits from the scan p-values for the signal
 2267 + background and background-only pseudo-experiments.

2268 Finally, a particular GMSB model is excluded if the upper limit on the cross
 2269 section for that model is less than the expected theoretical cross section.

2270 8.3 Cross Section Upper Limits

2271 Figure 8.3 shows the observed upper limits on the cross sections for the models de-
 2272 scribed in Sec. 8.1. In some ($\mathcal{O}(10^{-3})$) cases, the upper limit is zero due to a com-
 2273 putational failure. The upper limit for these points is estimated from the average of the
 2274 upper limits of the four neighboring points, as shown in Figure 8.4. If any of the four
 2275 points is also missing a valid upper limit, it is dropped from the average. The errors

2276 on the individual upper limits used in the estimate are propagated to the error on
 2277 the average.

2278 8.4 Exclusion Contours

2279 Exclusion contours for the GMSB models discussed above are shown in Figure 8.5. The
 2280 contours are derived from plots of predicted cross section minus cross section upper
 2281 limit ($\sigma \times (1 - \mu^{95\%CL})$), where σ is the nominal value of the predicted cross section
 2282 for a given GMSB model) vs. the two model parameters of interest, so the values are
 2283 either negative (not excluded) or positive (excluded). Sometimes, a particular point
 2284 may have a different sign than its four same-sign neighbors (cf. Fig. 8.4) due to a
 2285 fluctuation. In these cases, $\sigma \times (1 - \mu^{95\%CL})$ for the anomalous point is estimated
 2286 as the average $\sigma \times (1 - \mu^{95\%CL})$ of the four neighboring points. The errors on the
 2287 individual values of $\sigma \times (1 - \mu^{95\%CL})$ used in the estimate are propagated to the error
 2288 on the average.

2289 In the plots in Fig. 8.5, the expected limit (i.e. the contour derived from $\sigma \times (1 -$
 2290 $\mu_{\text{exp,scan}}^{95\%CL})$) is drawn in dark orange and the 1σ experimental band around the expected
 2291 limit (i.e. the shaded region between the contours derived from $\sigma \times (1 - \mu_{\pm 1\sigma, \text{scan}}^{95\%CL})$) is
 2292 drawn in light orange. The values of $\mu_{\text{exp,scan}}^{95\%CL}$ and $\mu_{\pm 1\sigma, \text{scan}}^{95\%CL}$ only reflect the experimental
 2293 uncertainties given in Sec. 8.2.2.

2294 The observed limits (derived from $\sigma \times (1 - \mu_{\text{obs,scan}}^{95\%CL})$) and 1σ theoretical error
 2295 bands around the observed limits in Fig. 8.5 are drawn in blue. The contours that
 2296 define this band are derived from $\pm(\sigma_{\pm 1\sigma} - \sigma \mu_{\text{obs,scan}}^{95\%CL})$, where $\sigma_{\pm 1\sigma}$ is the nominal
 2297 value of the predicted cross section \pm the one-standard-deviation theoretical error on
 2298 the predicted cross section. In this way, the experimental and theoretical errors, the
 2299 latter due to imperfect knowledge of the predicted cross section, are shown separately.
 2300 Comparing with Fig. 8.1, one can easily see that the shapes of the exclusion curves

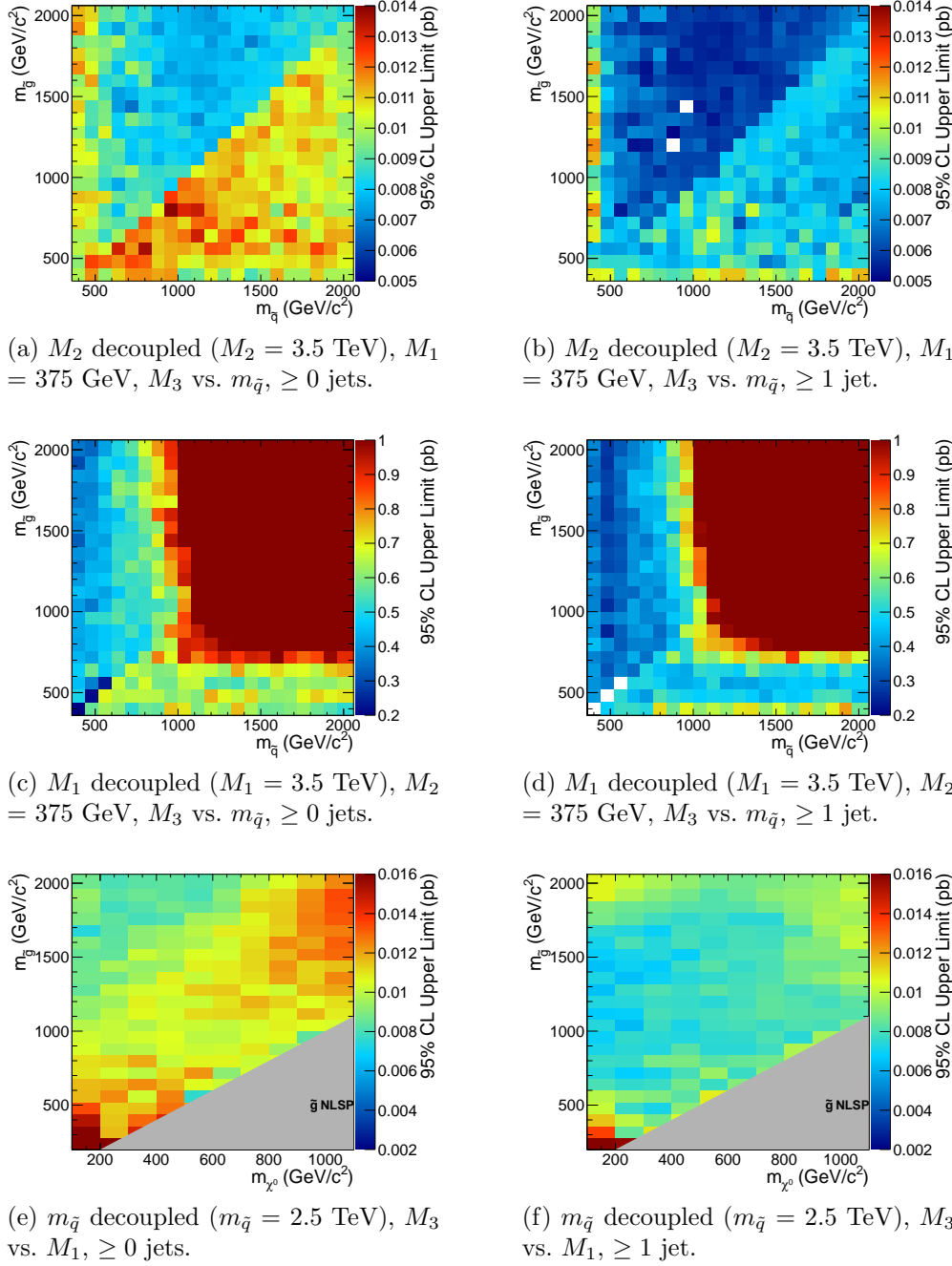


Figure 8.3: Cross section upper limits for the three different scenarios described in Sec. 8.1.

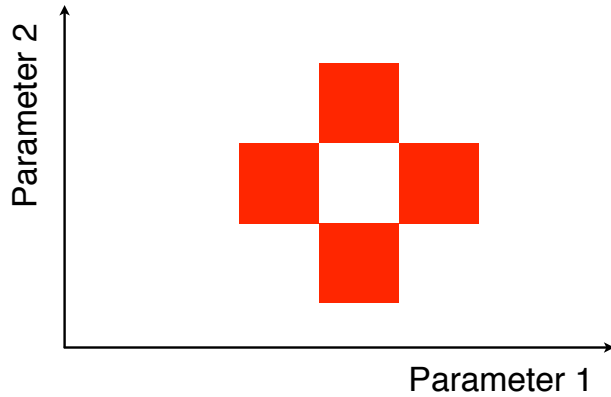


Figure 8.4: Diagram of the points (red squares) used in the estimation of an upper limit when a computational failure occurs (middle white square).

2301 are driven by the contours in the expected cross section plane.

2302 The dominant theoretical uncertainties on the GMSB cross sections are due to:

2303 • PDF uncertainty (4%-100% depending on model)

2304 • Renormalization scale uncertainty (0.036%-25% depending on model)

2305 The PDF4LHC [118] recommendations are used to calculate the effect of these un-
2306 certainties on the GMSB cross sections. The recommendations state that PDF sets
2307 from MSTW08 [119], CTEQ6.6 [120], and NNPDF2.0 [121] should be considered in
2308 the determination of the PDF uncertainties, because these three PDF sets include
2309 constraints from the Tevatron and from fixed target experiments, as well as from
2310 HERA [?], and are thus the most complete.

2311 Each collaboration's PDF prediction comes from a global fit to experimental data
2312 with a certain number of free parameters. The best fit parameters come from mini-
2313 mizing the χ^2 ; increasing the χ^2 by one from its minimum can be written in terms of
2314 the N -dimensional Hessian error matrix [?] where N is the number of free parameters.

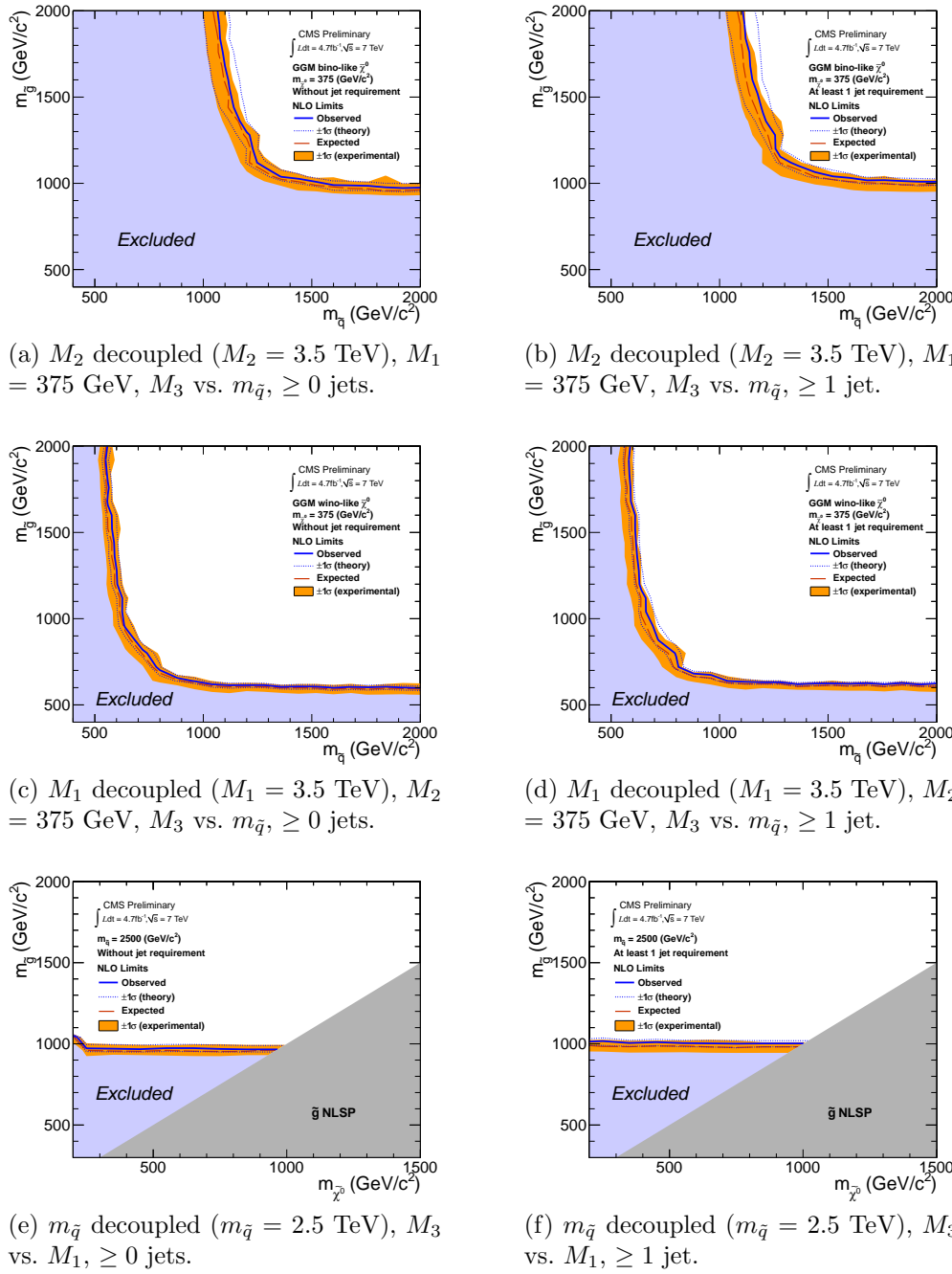


Figure 8.5: Exclusion contours for the three different scenarios described in Sec. 8.1.

2315 To form the i^{th} pair of members of the PDF set, the PDF is evaluated once at the
 2316 parameter values given by the i^{th} eigenvector of the Hessian matrix, and then again
 2317 at the parameter values given by the negative of the i^{th} eigenvector. Each PDF set
 2318 therefore contains $2N$ members, corresponding to the positive and negative values of
 2319 the N eigenvectors [122].

2320 To calculate the PDF uncertainties for a given GMSB model, the leading order
 2321 Pythia cross section is reweighted by a factor of the error PDF divided by the leading
 2322 order PDF with which the model was generated. This is repeated for each error PDF
 2323 in a given PDF set. The $\pm 1\sigma$ deviations are proportional to the maximum difference
 2324 between cross sections obtained this way. The actual equation for the $\pm 1\sigma$ errors is
 2325 Eq. (43) of ref. [122]. In the same way, the $\pm 1\sigma$ errors are calculated for the CTEQ6.6,
 2326 MSTW08, and NNPDF2.0 PDF sets. The total error is given by the half the difference
 2327 between the largest $+1\sigma$ deviation and the smallest -1σ deviation [118].

2328 The uncertainties on the signal cross sections due to the choice of renormaliza-
 2329 tion/factorization scale ($\alpha_S(M_Z)$) are evaluated by calculating the PROSPINO next
 2330 to leading order cross section once with $\alpha_S(M_Z)$ halved, then once with $\alpha_S(M_Z)$ dou-
 2331 bled. The lower error on the cross section is taken as the absolute difference between
 2332 the nominal and halved-scale values of the cross section, while the upper error is taken
 2333 as the absolute difference between the nominal and doubled-scale values. The PDF
 2334 and α_S uncertainties are added in quadrature to give the total PDF uncertainty.

2335 Note that the quoted GMSB cross sections are evaluated at next to leading order
 2336 using PROSPINO, but it is the leading order Pythia cross sections that are reweighted
 2337 to the next to leading order MSTW08, CTEQ6.6, and NNPDF2.0 PDFs to get the
 2338 error bands. In addition, since to a good approximation the GMSB production cross
 2339 sections for the M_3 - $m_{\tilde{q}}$ scans only depend on M_3 and $m_{\tilde{q}}$, the same PDF errors per
 2340 point are used for the \tilde{B} -like and \tilde{W} -like grids.

2341

Chapter 9

2342

Conclusion

2343 The results of a search for evidence of new particle production via final states with
2344 2 photons, large \cancel{E}_T , and ≥ 0 or ≥ 1 jet in pp collisions at $\sqrt{s} = 7$ TeV have been
2345 presented. No deviation in the production rate from that predicted by the Standard
2346 Model has been found. The null results were used to constrain general models of
2347 gauge mediated supersymmetry breaking. In these types of models, gluinos and first-
2348 and second-generation squarks are restricted to masses above ~ 1 TeV.

2349 These bounds on supersymmetry do not exclude it completely. The gluinos and
2350 first- and second-generation squarks can be a little bit heavier (but not too much
2351 heavier than a few TeV) and still imply an elegant supersymmetric solution to the
2352 hierarchy problem. More importantly, the bounds on the first- and second-generation
2353 squarks say nothing about the stop squark, which is intimately connected to the Higgs
2354 mass. At one loop order in the supersymmetric Standard Model, the lightest Higgs
2355 mass is given by [127]

$$m_h^2 \lesssim m_Z^2 + \frac{3g^2 m_t^4}{8\pi^2 m_W^2} \left[\ln \frac{M_S^2}{m_t^2} + \frac{X_t^2}{M_S^2} \left(1 - \frac{X_t^2}{12M_S^2} \right) \right] \quad (9.1)$$

2356 where g is the $SU(2)_L$ coupling constant, M_S^2 is the average of the two observable

2357 stop squared masses, and X_t is a parameter that characterizes stop mixing. The Higgs
 2358 mass is directly sensitive to the stop mass, for which the only current lower bound of
 2359 330 GeV [128] is much weaker than for the first- and second-generation squarks (and
 2360 highly model dependent). The current hints of a Higgs with mass ~ 125 GeV [15, 16]
 2361 point to a stop mass below 2 TeV if SUSY is really a symmetry of nature, depending
 2362 on model.

2363 Future searches for GMSB could look for either direct pair production of stops
 2364 decaying via top quarks to neutralinos that then decay to photons, or for stops pro-
 2365 duced in the decay of a heavier pair-produced particle like the gluino. Looking for a
 2366 final state containing a top, antitop, and ≥ 1 photon may be advantageous because
 2367 the expected SM background should be small.

2368 Top quark reconstruction depends heavily on b jet identification. The same b tag-
 2369 ging techniques needed to find stops could also be applied to a search for a Higgsino-
 2370 like neutralino decaying primarily to $b\bar{b}$. If gaugino mixing were in a certain corner of
 2371 parameter space, then photon + $b\bar{b}$ events might provide a window onto GMSB.

2372 There are a number of interesting possibilities for future GMSB searches in ad-
 2373 dition to those just outlined. SUSY searches will likely remain a fruitful avenue of
 2374 investigation throughout the lifetime of the LHC.

2375 **Appendix A**

2376 **Monte Carlo Samples**

2377 A number of MC samples are utilized in this analysis and referred to throughout the
2378 text. Below is a list of the MC samples used and an explanation of what the sample
2379 names mean.

2380 **A.1 List of Samples**

2381 1. Drell-Yan + up to 2 hard jets:

2382 /DYJetsToLL_TuneZ2_M-50_7TeV-madgraph-tauola/
2383 Fall11-PU_S6_START42_V14B-v1/AODSIM

2384 2. QCD enriched with B and D meson decays to electrons:

2385 /QCD_Pt-20to30_BCtoE_TuneZ2_7TeV-pythia6/
2386 Fall11-PU_S6_START42_V14B-v1/AODSIM,
2387 /QCD_Pt-30to80_BCtoE_TuneZ2_7TeV-pythia6/
2388 Fall11-PU_S6_START42_V14B-v1/AODSIM,
2389 /QCD_Pt-80to170_BCtoE_TuneZ2_7TeV-pythia6/
2390 Fall11-PU_S6_START42_V14B-v1/AODSIM

2391 3. Photon + jet doubly enriched with jets passing an EM filter:

2392 /GJet_Pt-20_doubleEMEnriched_TuneZ2_7TeV-pythia6/
 2393 Fall11-PU_S6_START42_V14B-v1/AODSIM

2394 4. W leptonic decays + up to 2 hard jets:

2395 /WJetsToLNu_TuneZ2_7TeV-madgraph-tauola/
 2396 Fall11-PU_S6_START42_V14B-v1/AODSIM

2397 5. $t\bar{t}$ + up to 2 hard jets:

2398 /TTJets_TuneZ2_7TeV-madgraph-tauola/
 2399 Fall11-PU_S6_START42_V14B-v2/AODSIM

2400 A.2 Explanation of Naming Conventions

2401 • L: charged lepton

2402 • B: B hadron

2403 • C: D , or charmed, hadron

2404 • E: electron or positron

2405 • G: photon

2406 • W: W boson

2407 • Nu: neutrino

2408 • T: top quark

2409 • TuneZ2: Pythia tune incorporating 2010 LHC data with CTEQ6L1 [120] PDFs

2410 [129]

2411 • M-50: Generated l^+l^- invariant mass threshold of 50 GeV

2412 • 7TeV: Generated center-of-mass energy 7 TeV

- 2413 • **pythia6**: Parton showering and hadronization simulated with Pythia v6.424
- 2414 [130]
- 2415 • **madgraph**: Hard interaction generated with MadGraph 5 [131]
- 2416 • **tauola**: τ decays generated with Tauola [132]
- 2417 • **PU_S6**: Generated with S6 pileup scenario, which has a mean between 6 and
2418 7 interactions per crossing, and includes pileup from the neighboring bunch
2419 crossings according to a Poisson distribution with mean equal to the number of
2420 interactions in the in-time crossing [133]
- 2421 • **START42_V14B**: Reconstructed with best alignment and calibration constants
2422 and magnetic field conditions as of August 3, 2011
- 2423 • **Pt_XtoY**: $X \leq$ generated $\hat{p}_T < Y$
- 2424 • **BCToE**: Only keeps events if they contain at least one electron with $E_T > 10$
2425 GeV in $|\eta| < 2.5$ that came from a b or c quark
- 2426 • **doubleEMEnriched**: Enriched in photons, electrons, electrons from b/c decay,
2427 and electromagnetic jets [134]
- 2428 • **AODSIM**: Run through full CMS reconstruction algorithm based on a GEANT 4
2429 [125] detector simulation; AOD data tier, including generator-level information

2430

Bibliography

- 2431 [1] <http://cms.web.cern.ch/news/cms-detector-design> (2011).
- 2432 [2] S.L. Glashow, J. Iliopoulos, and L. Maiani, *Phys. Rev. D* **2** (1970) 1285; S.L. Glashow, *Nucl. Phys.* **22(4)** (1961) 579; J. Goldstone, A. Salam, and S. Weinberg, *Phys. Rev.* **127** (1962) 965; S. Weinberg, *Phys. Rev. Lett.* **19** (1967) 1264; A. Salam and J.C. Ward, *Phys. Lett.* **13(2)** (1964) 168.
- 2436 [3] M. Gell-Mann, *Phys. Lett.* **8** (1964) 214; G. Zweig, *CERN 8419/TH. 412* (1964) (unpublished).
- 2438 [4] J. Drees, *Int. J. Mod. Phys.* **A17** (2002) 3259.
- 2439 [5] P.W. Higgs, *Phys. Lett.* **12(2)** (1964) 132; P.W. Higgs, *Phys. Rev. Lett.* **13** (1964) 508; P.W. Higgs, *Phys. Rev.* **145** (1966) 1156.
- 2441 [6] I. Aitchison, *Supersymmetry in Particle Physics: An Elementary Introduction* (Cambridge University Press, Cambridge 2007), p. 4.
- 2443 [7] C. Quigg, in *Flavor Physics for the Millennium: TASI 2000, Boulder, 2000*, edit by J. L. Rosner (World Scientific, Singapore, 2001), p. 3.
- 2445 [8] L. Álvarez-Gaumé and J. Ellis, *Nature Phys.* **7** (2011) 2.
- 2446 [9] G. Arnison et al. (UA1 Collaboration), *Phys. Lett.* **B122** (1983) 103.
- 2447 [10] G. Arnison et al. (UA1 Collaboration), *Phys. Lett.* **B126** (1983) 398.

- 2448 [11] J. Gunion, H.E. Haber, G. L. Kane, and S. Dawson, *The Higgs Hunter's Guide*,
 2449 (Addison-Wesley, Redwood City, 1990).
- 2450 [12] S. P. Martin, *A Supersymmetry Primer* **v4** (2006) 86. [arXiv:hep-ph/9709356](#).
- 2451 [13] K. Nakamura et al. (Particle Data Group), *J. Phys.* **G37** (2010) 075021.
- 2452 [14] G. Jungman, M. Kamionkowski, and K. Griest, *SU* **4240-605** (1995).
- 2453 [15] S. Chatrchyan et al. (CMS Collaboration), *Phys. Lett.* **B710** (2012) 26.
- 2454 [16] G. Aad et al. (ATLAS Collaboration), *Phys. Lett.* **B710** (2012) 49.
- 2455 [17] M. Dine and W. Fischler, *Phys. Lett.* **B110** (1982) 227; C.R. Nappi and B.A.
 2456 Ovrut, *Phys. Lett.* **B113** (1982) 175; L. Alvarez-Gaumé, M. Claudson, and M.B.
 2457 Wise, *Nucl. Phys.* **B207** (1982) 96; M. Dine and A.E. Nelson, *Phys. Rev.* **D48**
 2458 (1993) 1277; M. Dine, A.E. Nelson, and Y. Shirman, *Phys. Rev.* **D51** (1995)
 2459 1362; M. Dine, A.E. Nelson, Y. Nir, and Y. Shirman, *Phys. Rev.* **D53** (1996)
 2460 2658.
- 2461 [18] A.H. Chamseddine, R. Arnowitt, and P. Nath, *Phys. Rev. Lett.* **49** (1982) 970; R.
 2462 Barbieri, S. Ferrara, and C.A. Savoy, *Phys. Lett.* **B119** (1982) 343; L.E. Ibáñez,
 2463 *Phys. Lett.* **B118** (1982) 73; L.J. Hall, J.D. Lykken, and S. Weinberg, *Phys. Rev.*
 2464 **D27** (1983) 2359; N. Ohta, *Prog. Theor. Phys.* **70** (1983) 542; J. Ellis, D.V.
 2465 Nanopoulos, and K. Tamvakis, *Phys. Lett.* **B121** (1983) 123; L. Alvarez-Gaumé,
 2466 J. Polchinski, and M. Wise, *Nucl. Phys.* **B221** (1983) 495.
- 2467 [19] P. Meade, N. Seiberg, and D. Shih, *Progr. Theor. Phys. Suppl.* **177** (2009) 143.
- 2468 [20] G. Aad et al., *CERN-PH-EP-2011-160* (2011).
- 2469 [21] T. Aaltonen et al., *Phys. Rev. Lett.* **104** (2010) 011801.
- 2470 [22] CMS Collaboration, *CMS-PAS-SUS-11-009* (2011).

- 2471 [23] <http://en.wikipedia.org/wiki/Tevatron>.
- 2472 [24] E. Fernandez et al., *Phys. Rev. Lett.* **54** (1985) 1118; E. Fernandex et al., *Phys.*
 2473 *Rev.* **D35** (1987) 374; D. Decamp et al., *Phys. Lett.* **B237(2)** (1990) 291; F.
 2474 Abe et al., *Phys. Rev. Lett.* **75** (1995) 613; S. Abachi et al., *Phys. Rev. Lett.* **75**
 2475 (1995) 618; G. Alexander et al., *Phys. Lett.* **B377(4)** (1996) 273; S. Aid et al.,
 2476 *Z. Phys.* **C71(2)** (1996) 211; S. Aid et al., *Phys. Lett.* **B380(3-4)** (1996) 461; B.
 2477 Aubert et al., *Phys. Rev. Lett.* **95** (2005) 041802.
- 2478 [25] O. Buchmueller et al., *CERN-PH-TH/2011-220* (2011).
- 2479 [26] <https://twiki.cern.ch/twiki/bin/view/CMSPublic/PhysicsResultsSUS>.
- 2480 [27] G. Aad et al., *JINST* **3** (2008) S08003.
- 2481 [28] B.C. Allanach et al., *Eur. Phys. J.* **C25** (2002) 113.
- 2482 [29] CMS Collaboration, *CMS-PAS-SUS-12-001* (2012).
- 2483 [30] A. Boyarsky, J. Lesgourgues, O. Ruchayskiy, and M. Viel, *CERN-PH-TH/2008-*
 2484 *234* (2009).
- 2485 [31] E. Komatsu et al., *Astrophys. J. Suppl. Ser.* **180** (2009) 330.
- 2486 [32] C.-H. Chen and J.F. Gunion, *Physical Review* **D58** (1998) 075005.
- 2487 [33] F. Staub, W. Porod, J. Niemeyer, *JHEP* **1001** (2010) 058.
- 2488 [34] L. Evans and P. Bryant (eds.), *JINST* **3** (2008) S08001.
- 2489 [35] <http://cms.web.cern.ch/news/summary-2011-p-p-running> (2011).
- 2490 [36] <http://public.web.cern.ch/public/en/lhc/Facts-en.html> (2008).
- 2491 [37] CERN, <http://cdsweb.cern.ch/record/833187> (2005).

- 2492 [38] RGBStock.com, <http://www.rgbstock.com/photo/n7EsabW/Airplane> (2011).
- 2493 [39] R. Flükiger, S. Y. Hariharan, R. Küntzler, H. L. Luo, F. Weiss, T. Wolf, and J.
2494 Q. Xu, in *Landolt-Börnstein: Numerical Data and Functional Relationships in*
2495 *Science and Technology*, edited by R. Flükiger and W. Klose (Springer, 2012).
- 2496 [40] Y.-P. Sun, F. Zimmermann, and R. Tomás, in Proceedings of the 23rd Particle Ac-
2497 celerator Conference, Vancouver, 2009, <http://accnet.web.cern.ch/accnet/>
2498 Literature/2009/TH5PFP016-Sunpdf.pdf (unpublished).
- 2499 [41] O.S. Brüning et al. (eds.), *CERN-2004-003-V-1*, <http://lhc.web.cern.ch/lhc/LHC-DesignReport.html> (2004).
- 2500 [42] CERN, <http://cdsweb.cern.ch/record/841568/files/> (1993).
- 2501 [43] P. Komorowski and D. Tommasini, in *Proceedings of the 1998 International*
2502 *Computational Accelerator Physics Conference, Monterey, 1998*, edited by K.
2503 Ko and R. Ryne (SLAC, Stanford, 1998), p. 192, http://www.slac.stanford.edu/econf/C980914/papers/ICAP98_eConf.pdf.
- 2504 [44] <http://lhc-machine-outreach.web.cern.ch/lhc-machine-outreach/components/magnets.htm> (2008).
- 2505 [45] S. Chatrchyan et al. (CMS Collaboration), *JINST* **3** (2008) S08004.
- 2506 [46] G.L. Bayatian et al. (CMS Collaboration), *CERN/LHCC* **2006-001**, edited by
2507 D. Acosta (2006).
- 2508 [47] M. Ivova, talk given at the Swiss Ph.D. School on Particle and Astroparticle
2509 Physics (CHIPP), Monte Verita' (2010).
- 2510 [48] G. Bolla et al., *Nucl. Instr. Meth. Res.* **A461** (2001) 182.

- 2514 [49] https://twiki.cern.ch/twiki/pub/CMSPublic/DPGResultsTRK/_imgf9e0ee48ebca770d7774454532b4b4ee.png (2011).
- 2515
- 2516 [50] https://twiki.cern.ch/twiki/pub/CMSPublic/DPGResultsTRK/_img7569b7652b3f7c15030a11a4223e631c.png (2011).
- 2517
- 2518 [51] https://twiki.cern.ch/twiki/pub//CMSPublic/DPGResultsTRK/hv11_d1.png (2011).
- 2519
- 2520 [52] https://twiki.cern.ch/twiki/pub/CMSPublic/DPGResultsTRK/_imga571742cbcd3a14a9e2581ae95efa54c.gif (2011).
- 2521
- 2522 [53] <https://twiki.cern.ch/twiki/pub//CMSPublic/DPGResultsTRK/StripHitRes2.gif> (2011).
- 2523
- 2524 [54] https://twiki.cern.ch/twiki/pub//CMSPublic/EcalDPGResults/histories2_laser.png (2012).
- 2525
- 2526 [55] https://twiki.cern.ch/twiki/pub//CMSPublic/EcalDPGResults/electronres_eb_inclusive.png (2012).
- 2527
- 2528 [56] https://twiki.cern.ch/twiki/pub//CMSPublic/EcalDPGResults/electronres_ee_inclusive.png (2012).
- 2529
- 2530 [57] <https://twiki.cern.ch/twiki/pub//CMSPublic/EcalDPGResults/seed-time.EEEE.png> (2012).
- 2531
- 2532 [58] N. Akchurin and R. Wigmans, *Rev. Sci. Instrum.* **74** (2003) 2955.
- 2533 [59] CMS Collaboration, *CMS-DP 2010-025* (2010).
- 2534 [60] https://twiki.cern.ch/twiki/pub/CMSPublic/PhysicsResultsMUO/dimuMass_2011Run_1fb_20July2011.pdf (2011).
- 2535
- 2536 [61] S. Chatrchyan et al. (CMS Collaboration), *JHEP* **4** (2012) 33.

- 2537 [62] W.H. Smith, P. Chumney, S. Dasu, F. Di Lodovico, M. Jaworski, J.R. Lackey, and
 2538 P. Robl in *Proceedings of the 7th Workshop on Electronics for LHC Experiments,*
 2539 *Stockholm, 2001*, edited by C. Isabella (CERN, Geneva, 2001), p. 238.
- 2540 [63] R. Alemany et al., *IEEE Trans. Nucl. Sci.* **52**(5) (2005) 1918.
- 2541 [64] R. Brun and F. Rademakers, *Nucl. Inst. Meth. Res.* **A389** (1997) 81. See also
 2542 <http://root.cern.ch/>.
- 2543 [65] J. Gutleber and L. Orsini, *Cluster Comput.* **5** (2002) 55.
- 2544 [66] D. Box, D. Ehnebuske, G. Kakivaya, A. Layman, N. Mendelsohn, H.F.
 2545 Nielsen, S. Thatte, and D. Winer, *W3C Note 08*, <http://www.w3.org/TR/2000/NOTE-SOAP-20000508/> (2000).
- 2547 [67] R. Arcidiacono et al., talk given at the 10th ICAL-EPCS International Conference
 2548 on Accelerator and Large Experiment Physics Control Systems, Geneva (2005).
- 2549 [68] J. Knobloch et al., *CERN-LHCC-2005-024* (2005).
- 2550 [69] R. Brunelière, *Nucl. Instr. Meth. Res.* **A572** (2007) 33.
- 2551 [70] S. Chatrchyan et al. (CMS Collaboration), *JINST* **5** (2010) T03011.
- 2552 [71] CMS Collaboration, *CMS PAS EGM-10-002* (2010).
- 2553 [72] P. Meridiani and C. Seez, *CMS IN-2011/002* (2011).
- 2554 [73] P. Adzic et al. (CMS Electromagnetic Calorimeter Group), *Eur. Phys. J.* **C44S2**
 2555 (2006) 1.
- 2556 [74] P. Adzic et al. (CMS Electromagnetic Calorimeter Group), *JINST* **3** (2008)
 2557 P10007.

- 2558 [75] M. Malberti, *Nuc. Sci. Symposium Conference Record NSS/MIC IEEE* (2009)
 2559 2264.
- 2560 [76] S. Chatrchyan et al. (CMS Collaboration), *JINST* **5** (2010) T03010.
- 2561 [77] R. Paramatti, *J. Phys. Conf. Ser.* **293** (2011) 012045.
- 2562 [78] Y. Yang, http://www.hep.caltech.edu/cms/posters/Pi0Poster_CMSWeekDec2011.pdf (2011).
- 2564 [79] M. Anderson, A. Askew, A.F. Barfuss, D. Evans, F. Ferri, K. Kaadze, Y. Maravin,
 2565 P. Meridiani, and C. Seez, *CMS IN-2010/008* (2010).
- 2566 [80] <https://twiki.cern.ch/twiki/bin/view/CMS/ECALEnergyScaleCorrections>.
- 2567 [81] The $H \rightarrow \gamma\gamma$ working group, *CMS AN-2011/426* (2011).
- 2568 [82] M. Cacciari, *LPTHE-P06-04* (2006).
- 2569 [83] M. Cacciari, G.P. Salam, and G. Soyez, *CERN-PH-TH-2011-297* (2011).
- 2570 [84] S. Chatrchyan et al. (CMS Collaboration), *Phys. Rev. Lett.* **106** (2011) 082001.
- 2571 [85] A. Askew, B. Cox, D. Elvira, Y. Gershtein, M. Hildreth, D. Jang, Y.-F. Liu, D.
 2572 Mason, D. Morse, U. Nauenberg, M. Paulini, R. Stringer, R. Yohay, and S.L.
 2573 Zang, *CMS AN-2011/515* (2011).
- 2574 [86] F. Beaudette, D. Benedetti, P. Janot, and M. Pioppi, *CMS AN-2010/034* (2010).
- 2575 [87] M. Konecki, in Proceedings of the European Physical Society Europhysics Con-
 2576 ference on High Energy Physics, Krakow, 2009, Eur. Phys.Soc. Mulhouse (ed.)
 2577 (unpublished).
- 2578 [88] W. Adam, R. Früwirth, A. Strandlie, and T. Todorov, *J. Phys.* **G31** No. 9 (2005).
- 2579 [89] CMS Collaboration, *CMS PAS PFT-09-001* (2009).

- 2580 [90] CMS Collaboration, *CMS PAS PFT-10-002* (2010).
- 2581 [91] S. Chatrchyan et al., *JINST* **6** (2011) P11002.
- 2582 [92] CMS Collaboration, *CERN-PH-EP 2011-102* (2011).
- 2583 [93] M. Cacciari, G.P. Salam, and G. Soyez, *JHEP* **0804** (2008) 063.
- 2584 [94] G. Salam, talk given at CERN Theory Institute: SM and BSM Physics at the
2585 LHC (2009).
- 2586 [95] C.W. Fabjan and R. Wigmans, *Rep. Prog. Phys.* **52** (1989) 1519.
- 2587 [96] <http://www-cdf.fnal.gov/physics/new/top/2004/jets/cdfpublic.html>
2588 (visited on 16 January 2011).
- 2589 [97] S. Chatrchyan et al. (CMS Collaboration), *JINST* **6** (2011) P09001.
- 2590 [98] CMS Collaboration, *CMS PAS JME-09-002* (2009).
- 2591 [99] T. Sjöstrand, S. Mrenna, and P. Z. Skands, *Comput. Phys. Commun.* **178** (2008)
2592 852.
- 2593 [100] S. Chatrchyan et al. (CMS Collaboration), *JINST* **5** (2010) T03014.
- 2594 [101] <https://twiki.cern.ch/twiki/bin/view/CMS/PVTMain> (2011).
- 2595 [102] J. P. Chou, S. Eno, S. Kunori, S. Sharma, and J. Wang, *CMS IN-2010/006*
2596 (2010).
- 2597 [103] Y. Chen, talk given at a meeting of the CMS JetMET group (2011).
- 2598 [104] R. Korzekwa et al., *iEEE Trans. Elec. Dev.* **38** (1991) 745.
- 2599 [105] W. Adam, Th. Speer, B. Mangano, and T.Todorov, *CMS NOTE 2006/041*
2600 (2006).

- 2601 [106] G. Daskalakis, D. Evans, C.S. Hill, J. Jackson, P. Vanlaer, J. Berryhill, J. Haupt,
 2602 D. Fulyan, C. Seez, C. Timlin, and D. Wardrope, *CMS AN-2007/019* (2007).
- 2603 [107] F. James and M. Roos, *Comput. Phys. Commun.* **10** (1975) 343.
- 2604 [108] W. Verkerke and D.P. Kirkby, *CHEP-2003-MOLT007* (2003).
- 2605 [109] J.E. Gaiser, Ph.D. thesis, Stanford University (1982).
- 2606 [110] A. Askew, S. Arora, Y. Gershtein, S. Thomas, G. Hanson, R. Stringer, W.
 2607 Flanagan, B. Heyburn, U. Nauenberg, S.L. Zang, R. Nandi, D. Elvira, D. Mason,
 2608 M. Balazs, B. Cox, B. Francis, A. Ledovskoy, and R. Yohay, *CMS AN* **2010/271**
 2609 (2010).
- 2610 [111] Information about all CMS datasets is available from the CMS Data Aggrega-
 2611 tion System (DAS), located at the URL <https://cmsweb.cern.ch/das/>.
- 2612 [112] S. Chatrchyan et al., *Phys. Rev. Lett.* **106** (2011) 211802.
- 2613 [113] G. Aad et al. (ATLAS Collaboration), S. Chatrchyan et al. (CMS Collabora-
 2614 tion), and LHC Higgs Combination Group, *CMS-NOTE-2011/005* (2011).
- 2615 [114] A.L. Read, in *Proceedings of the First Workshop on Confidence Limits, Geneva,*
 2616 *2000*, edited by L. Lyons, Y. Perrin, and F.E. James (CERN, Geneva, 2000), p.
 2617 81.
- 2618 [115] G. Cowan, K. Cranmer, E. Gross, and O. Vitells, *Eur. Phys. J.* **C71** (2011)
 2619 1554.
- 2620 [116] J. Neyman and E.S. Pearson, *Phil. Trans. R. Soc. Lond.* **A231** (1933) 289.
- 2621 [117] CMS Collaboration, *CMS PAS EWK-11-001* (2011).

- 2622 [118] S. Alekhin et al. (The PDF4LHC Working Group), arXiv:1101.0536 [hep-ph];
 2623 M. Botje et al. (The PDF4LHC Working Group), arXiv:1101.0538 [hep-ph];
 2624 <http://www.hep.ucl.ac.uk/pdf4lhc/index.html>.
- 2625 [119] A.D. Martin, W.J. Stirling, R.S. Thorne, and G. Watt, *Eur. Phys. J.* **C63**
 2626 (2009) 189.
- 2627 [120] P. M. Nadolsky, H.-L. Lai, Q.-H. Cao, J. Huston, J. Pumplin, D. Stump, W.-K.
 2628 Tung, and C.-P. Yuan, *Phys. Rev.* **D78** (2008) 013004.
- 2629 [121] R.D. Ball, L. Del Debbio, S. Forte, A. Guffanti, J.I. Latorre, J. Rojo, and M.
 2630 Ubiali, *Nucl. Phys.* **B838** (2010) 136.
- 2631 [122] J.M. Campbell, J.W. Huston, and W.J. Stirling, *Rep. Prog. Phys.* **70** (2007) 89.
- 2632 [123] A. Djouadi, J.-L. Kneur, G. Moultaka, arXiv:hep-ph/0211331 (2005).
- 2633 [124] M. Muhlleitner, A. Djouadi, Y. Mambrini, *Comput. Phys. Commun.* **168** (2005)
 2634 46.
- 2635 [125] J. Allison et al., *IEEE Trans. Nucl. Sci.* **53**(1) (2006) 270.
- 2636 [126] W. Beenakker, R. Hoepker, M. Spira, arXiv:hep-ph/9611232 (1996).
- 2637 [127] M. Carena, J.S. Conway, H.E. Haber, and J.D. Hobbs, *FERMILAB-Conf-00*
 2638 **279-T** (2000). arXiv:hep-ph/0010338
- 2639 [128] ATLAS Collaboration, *ATLAS-CONF 2012-036* (2012).
- 2640 [129] R. Field, talk given at LHC Physics Centre at CERN Minimum Bias and Un-
 2641 derlying Event Working Group Meeting (2011).
- 2642 [130] T. Sjöstrand, S. Mrenna, and P. Z. Skands, *JHEP* **0605** (2006) 026.

2643 [131] J. Alwall, M. Herquet, F. Maltoni, O. Mattelaer, and T. Stelzer, *JHEP* **1106**
2644 (2011) 128.

2645 [132] Z. Was, *Nucl. Phys. Proc. Suppl.* **98** (2001) 96.

2646 [133] <http://cmslxr.fnal.gov/lxr/source/SimGeneral/MixingModule/python/>
2647 `mix_E7TeV_Fall2011_Reprocess_50ns_PoissonOOTPU_cfi.py` (2011).

2648 [134] <http://cmslxr.fnal.gov/lxr/source/GeneratorInterface/GenFilters/>
2649 `src/doubleEMEnrichingFilterAlgo.cc` (2011).